

Hybrid manufacture of Precision 3D ceramic components

Jack Hinton

Submitted in accordance with the requirements for the
degree of Doctor of Philosophy in Mechanical Engineering

The University of Leeds
School of Mechanical Engineering

January 2020

The candidate confirms that the work submitted is their own, except where work, which has formed part of jointly authored publications has been included. The contribution of the candidate and the other authors to this work has been explicitly indicated below. The candidate confirms that appropriate credit has been given within the thesis where reference has been made to the work of others.

The work in Chapter 3-5 Process development and Chapter of the thesis has appeared in publication as follows:

Hybrid Additive Manufacturing of Precision Engineered Ceramic Components, Rapid Prototyping Journal, July 2019, **J. Hinton**, D. Basu, M. Mirgkizoudi, D. Flynn, R.A. Harris, R.W. Kay.

I was responsible for the writing of the publication and the fabrication of demonstrators and subsequent characterisation.

The contribution of the other authors was D. Basu, working on a paid placement provided technical support for the integration and setup of the machining spindle and sacrificial support extruder. M. Mirgkizoudi provided technical guidance and completed preliminary work for this publication. D. Flynn, R.A. Harris, R.W. Kay were in supervisory roles during this work.

The work in Chapter 6 of the thesis has appeared in publication as follows:

Extreme environment interconnects and packaging for power electronics. The Journal of Engineering, 2019, A. Campos-Zatarain, **J. Hinton**, M. Mirgkizoudi, J. Li, R. A. Harris, R. W. Kay, D, Flynn,

I was responsible for the manufacture of the electronic circuits. The contribution of the other authors was M. Mirgkizoudi, J. Li and A. Campos-Zatarain provided technical support for the design and testing of ceramic electronics. M. Mirgkizoudi provided expertise relating to reliability testing with A. Campos-Zatarain providing guidance for asset management applications. D. Flynn, R. A. Harris, R. W. Kay were in supervisory roles during this work.

This copy has been supplied on the understanding that it is copyright material and that no quotation from the thesis may be published without proper acknowledgement

The right of Jack Hinton to be identified as Author of this work has been asserted by him in accordance with the Copyright, Designs and Patents Act 1988.

Acknowledgements

I would firstly like to acknowledge and thank my supervisor, Dr Robert Kay, for his ongoing support and guidance throughout the last five years and for the opportunities that he has provided. This work would not have been possible without his positive outlook and enthusiasm. I would also like to thank the continued support of Christopher Hampson, who has guided and advised this work, providing me with numerous opportunities that have been invaluable in expanding my knowledge of this area of research.

I would like to thank the contributions and support of my colleagues in the Future Manufacturing Processes Research Group. In particular, I would like to thank Nathan Wilkinson for the many hours he has spent advising and reviewing my research. I would also like to thank Dejan Basu for his help with building the manufacturing platform and for his unwavering optimism and humour.

A number of technicians and support staff at both the University of Leeds and Morgan Advanced Materials have been instrumental throughout this work and have provided valuable guidance throughout this work.

Finally, I would like to thank my family and friends, in particular, my parents Lynn and Malcolm. They have always been there for me and enabled me to get to where I am today.

Abstract

Advanced ceramic materials and ceramic thick-film electronics are used across a diverse range of industries including aerospace, automotive, medical and power generation. Digitally driven fabrication techniques such as Additive Manufacturing (AM) present an alternative way to manufacture parts from advanced ceramic materials. However, standalone ceramic AM has a number of shortcomings that limit its use within commercial and end-user applications.

This thesis presents the development of a new digitally driven manufacturing process, which combines high viscosity paste extrusion, sacrificial support extrusion and micromachining in a hybrid manufacturing platform. This was achieved using a commercial feedstock formulation composed of 96wt% alumina, using existing material formulation and post-processing operations.

The resultant process was implemented using a 3-axis CNC, benchtop platform, using a positive displacement pumping system, machining spindle with an automatic tool changer and Fused Filament Fabrication (FFF) sacrificial support extruder. The fabrication of 3D ceramic component featuring spanning, overhanging and conformal geometries with densities of up to 99.93% and shrinkages of 15-19%. The synergistic use of AM and subtractive processing resulted in the reduction of surface roughness from R_a 34.3 μm (R_q 42.4 μm) down to 0.5 μm (R_q 0.6 μm). Flexural testing of the fabricated samples demonstrated an average strength of 221 MPa, but as high as 252 MPa.

Functionalisation of these parts was achieved with a ceramic thick-film process depositing a Low-Temperature Co-fire Ceramic (LTCC) silver conductor using Direct Ink Writing (DIW). The deposited tracks had a measured resistivity of 8.4937×10^{-08} - 1.1383×10^{-07} Ωm . The production of a functional 555-timer circuit on planar and 3D ceramic alumina substrates that were made using the hybrid manufacturing platform demonstrate the feasibility of this approach. The production of co-fireable ceramic electronics was also demonstrated with the extrusion of LTCC dielectric and conductor materials that were subsequently co-fired. This presents an alternative approach for the fabrication of multilayer ceramic electronics for harsh environment applications.

Table of Contents

Acknowledgements	iii
Abstract	iv
Publications	ix
Journal Papers	ix
Conference Proceedings	ix
Poster Presentations	ix
List of Figures	x
List of Tables	xxi
Abbreviations	xxiii
1 Introduction	25
1.1 Advanced Ceramic Materials	25
1.2 Research Motivation	31
1.3 Research Intentions	32
1.3.1 Aims and Objectives	32
1.3.2 Research Novelty	33
1.4 Thesis Structure	35
2 Literature Review	37
2.1 Additive Manufacturing of Ceramics	37
2.1.1 Suspension-based Processes	38
2.1.2 Powder based processing	45
2.1.3 Material Extrusion	54
2.1.4 Sheet Lamination	59
2.2 Process comparison	62
2.3 Process Selection	66
2.4 Thermal Processing post-fabrication	68
3 Process Development	71
3.1 Process flow	71
3.2 Print materials and characterisation	73
3.3 Extrusion system	75
3.4 Forced Convection Drying	81
3.5 Substrate and Support Material	84

3.5.1	Substrate	84
3.5.2	Sacrificial Support	87
3.6	Ceramic AM Machining	90
3.6.1	Feature Production	100
3.7	Post processing	104
3.8	Process selection and Conclusion	106
4	Machine Development.....	110
4.1	Motion Platform	112
4.2	AM hardware	115
4.2.1	Ceramic Extruder	115
4.2.2	Accelerated Forced Convection Drying	117
4.2.3	Sacrificial Support	119
4.3	Machining Hardware	121
4.3.1	Spindle	121
4.3.2	Automatic Tool changer	123
4.4	Hardware Integration	124
4.4.1	Fixture Design	124
4.5	Control Software and Integration	126
4.6	System commissioning and validation	127
4.6.1	Bed Levelling	127
4.6.2	Z-axis repeatability	128
4.6.3	X-Y axis repeatability	130
4.7	Component Toolpath generation	138
4.8	Conclusion	142
5	3D structures and characterization	145
5.1	3D ceramic Components	145
5.2	Ceramic Feedstock Extrusion	145
5.3	Fabrication of 3D ceramic srtructures	147
5.3.1	Square 2.5D geometries	147
5.3.2	Tapered Tile Geometries	150
5.3.3	Pyramid Geometries	153
5.3.4	Enclosed geometries	156
5.3.5	Conformal Geometries	158
5.4	Mechanical Characterisation	161
5.5	Process Summary	165

6 Ceramic electronics	168
6.1 Extrusion of LTCC Ag Paste	172
6.2 Ceramic electronic circuits	177
6.2.1 Process Summary	181
6.3 Co-fire Ceramics	182
7 Conclusion and Future Work.....	186
7.1 Conclusion	186
7.2 Future work	190
7.2.1 Materials and feedstock development	190
7.2.2 Process Optimisation	191
8 References	194
Appendix A.....	221
Appendix B.....	222
Appendix C.....	223
Appendix D.....	227
Appendix E	228
Z-Axis	228
X-Axis	229
Y-Axis	230
Repeatability for X and Y axes at a constant acceleration of 300ms ⁻²	231
9.1 Variable Acceleration at target feedrate of 1,600 mm/min	233
9.2 Variable Acceleration at target feedrate of 3,200 mm/min	234
Appendix F	235
Appendix G.....	236
9.3 Non-machined Sample	236
9.4 Machined Sample	237
Appendix H	239
9.5 Non-machined Sample	239
9.6 Machined Sample	240
Appendix I.....	242
Appendix J.....	243

Appendix K	245
Appendix L.....	246
Appendix M	247

Publications

Journal Papers

J. Hinton, D. Basu, M. Mirgkizoudi, D. Flynn, R.A. Harris, R.W. Kay. *Hybrid Additive Manufacturing of Precision Engineered Ceramic Components*, Rapid Prototyping Journal, 2019

A. Campos-Zatarain, **J. Hinton**, M. Mirgkizoudi, J. Li, R. A. Harris, R. W. Kay, D, Flynn, *Extreme environment interconnects and packaging for power electronics*. The Journal of Engineering, 2019

DOI: 10.1049/joe.2018.8118

Conference Proceedings

J. Hinton, R. A. Harris, R. W. Kay, *Hybrid Additive Manufacturing of Precision Engineered Ceramic Components*, IOP PGS Conference: Printing for the future, 2018

J. Hinton, D. Basu, D. Flynn, R. A. Harris, R. W. Kay, *A Digitally-Driven Hybrid Manufacturing Process For The Flexible Production Of Engineering Ceramic Components*, Proceedings of the 29th Annual International Solid Freeform Fabrication Symposium, 2018

J. Hinton, M. Mirgkizoudi, A. Campos-Zatarain, D. Flynn, R.A. Harris, R.W. Kay, *Digitally-Driven Hybrid Manufacture Of Ceramic Thick-Film Substrates*, 7th Electronic System-Integration Technology Conference (ESTC), 2018

DOI:10.1109/ESTC.2018.8546388

Poster Presentations

J. Hinton, Mechanical Engineering PGR Poster 2019, University of Leeds, 2019

List of Figures

Figure 1-1 - Shows the process chain fo manufacturing advanced ceramic parts usingr a) conventional manufacturing techniques b) Indirect AM techniques and c) direct AM techniques.....	28
Figure 1-2 – Predicted market value of advanced ceramic markets between 2017 and 2028 [8]	29
Figure 1-3 – Shows a visualisation of the proposed hybrid manufacturing process to produce precision 3D ceramic components. The process combines selective material deposition (additive), accelerated drying, planarising machining (subtractive) and post-process machining (subtractive).....	33
Figure 2-1 – Shows the process categories that have been used to demonstrate the fabrication of components using advanced ceramic materials	37
Figure 2-2 – illustrates a typical configuration of CSL hardware in a) top-down configuration and b) bottom-up setup. Both setups are showing the fabrication of a pyramid geometry.....	39
Figure 2-3 – Illustration of a typical PBF system showing a pyramid geometry being fabricated.....	47
Figure 2-4 – Illustration of a typical binder jetting setupwith a pyramid geometry being fabricated.....	50
Figure 2-5 – Schematic of a direct drive ME using a filament feedstock.....	55
Figure 2-6 – Illustration of a typical LOM system using a “Stack then cut” approach	60
Figure 2-7 - Assessment of the various AM processes at fabricating key geometries from advanced ceramic materials. Adapted from [208]	63
Figure 2-8 –IT-classes for conventional and Additive manufacturing techniques [214].....	67

Figure 2-9 – Shows a visualisation of indirect processing of advanced ceramic materials, highlighting the thermal processing that is used to transition from the green state to the fired state.	68
Figure 2-10 – Shows the recommended firing profile for Heraeus TC0306A silver conductor as an example of a thermal profile used to sinter ceramic materials	70
Figure 3-1 – Process flow for the hybrid manufacture of components	71
Figure 3-2 – Illustrates the effect of implementing the surface milling operation to remove the convex surface of the deposited tracks to eliminate porosity in the intertrack regions	72
Figure 3-3 – The shear thinning behaviour averaged from 6 samples across a shear range of 100-1,000s ⁻¹ using a measurement spacing of 1.5mm	74
Figure 3-4 – Shows the shear relaxation of the material after applying shear of to 1,000 s ⁻¹ for 30s.....	75
Figure 3-5 – Illustration of three extrusion mechanisms: (a) Ram extruder (b) Shutter valve (c) Screw-based extruder [172]	76
Figure 3-6 – Illustration of a) Auger screw extrusion mechanism [227] b) material Flow of material through a PC pump [228].....	78
Figure 3-7 – Illustration of the ceramic feedstock being extruded through nozzle of different sizes and profiles using a pneumatic ram extuder (left to right) 233 µm tapered, 437 µm tapered, 220 µm straight, 254 µm straight, 330 µm straight, 510 µm straight, 210 µm and 250 µm polymer taper.....	78
Figure 3-8 – a) Shows flow of material through the material reservoir, die (material compression) and material outlet (agglomerate breakdown). b) shows the process of extruding high solids loading material and the affect of agglomerate breakdown [229].....	80
Figure 3-9 - Illustration of the ceramic feedstock being extruded through various nozzle sizes and profiles using an ecoPEN300 extuder (left to right) 233 µm tapered, 437 µm tapered, 220 µm straight, 254 µm straight,	

330 μm straight, 510 μm straight, 210 μm , 250 μm polymer taper.	81
Figure 3-10 – Illustrates the visual difference between a) dried material and b) drying material	82
Figure 3-11 – shows a) poor machining characteristics o a part that was insufficiently dried 60 seconds using fan speed of 3, with the cooling override activated at a distance of 150 mm b) Shows the result of rapid drying on the surface of a component.	83
Figure 3-12 – Shows the configuration that was used to chaacterise the parameters of the handheld forced convection drying unit	83
Figure 3-13 – The measured temperature at 0 mm, 50 mm, 100 mm and 150 mm from the handheld drying unit	84
Figure 3-14 - The measured air speed at 0 mm, 50 mm, 100 mm and 150 mm from the handheld drying unit	84
Figure 3-15 – Shows parts that were fabrciated in a layerwise process using the developed hybrid manufacturing platform on different substrate materials includeing a) cullulose sheet b) polyethene sheet c) standard printing paper and d) FFF PLA raft.....	86
Figure 3-16 – Shows a prefabricated support structure being used to test the production of an overhanging geometry	88
Figure 3-17 – Deposition of PLA onto a ceramic part fabricated directly on a metal substrate using an Ultimaker 2.....	89
Figure 3-18 – (left) a spanning structure that was fabricated using a prefabricated PLA support structure. (right) shows the same sample post sintering.	89
Figure 3-19 - a) shows the casting mould following the production of ceramic samples, the removable floor of the top right cavity has been removed to show the orifice for releasing the samples. b) shows the samples that were produced using the mould.....	90

Figure 3-20 – Validation of the ceramics machinability was undertaken on cast samples using a Europa Milltech 2000VS Turret Milling Machine	91
Figure 3-21 – Shows the direction of the cutter relative to the feed direction for conventional and climb milling operations [233]	92
Figure 3-22 – (a) shows the use of a fluted carbide end mill machining slots into cast alumina tiles. (b) shows a ceramic sample having undergone side milling at 2310 RPM at 475mm	93
Figure 3-23 – (a) Material deposits left from a HSS end mill when end milling the top surface of the cast tile. (b) Large scale machining demonstrate the capability to remove significant amounts of material from a cast ceramic tile This was machined at 3750RPM at 475mm/min.....	94
Figure 3-24 – A range of PCD tooling with a range of cutter profiles.....	95
Figure 3-25 – Validation of in-situ machining following the drying of deposited ceramic material. Note: the machining was undertaken using course diamond coated end mill.	96
Figure 3-26 – Shows the accumulation of machining debris on a PCD machining tool following a side milling operation.....	96
Figure 3-27 – Range of fluted CVD diamond tooling (left to right) 1 mm ball nose cutter, 1 mm end mill, 1.5 mm end mill, 2 mm end mill, 2.5 mm end mill, 3 mm end mill and 4 mm end mill. The 4 mm end mill was used throughout this work for interlayer machining on all parts and during post process machining of vertical sides.....	97
Figure 3-28 - Shows the edge of a ceramic tile that has been machined using a side milling operation	98
Figure 3-29 - Shows the identification of side numbers based on the width of cut which was to investigated various feedrates using a spindle speed of 10,000 RPM.....	98

- Figure 3-30 – shows sample 1, sample 2 and sample 3. Sample 1 was machined on 2 complete side before becoming detached whilst machining the third 99
- Figure 3-31 – Shows the surface roughness Ra for side and end milling operations at variable feedrates using a constant spindle speed of 10,000 RPM 100
- Figure 3-32 – Shows the Ø0.7 mm fluted drill bits that are coated in coarse PCD diamond..... 101
- Figure 3-33 – Shows the part following the drilling operations and the corresponding hole numbers on a tile geometry produced in a layerwise manner using the developed manufacturing apparatus102
- Figure 3-34 – Shows the sample used to validate slot milling operations. (left) shows the 12 mm slot, (centre) 11 mm slot and (right) 10 mm slot. The defect on the 10 mm was caused by by misalignment of the cutting tool103
- Figure 3-35 – (Top) shows the green state parts that were produced during the characterisation of the machining parameters. (Bottom) shows the samples following thermal processing using conventional backend processing. 104
- Figure 3-36 – SEM image of a section taken from a fabricated part. Discrete layers are not visible in the top section of the part, although defects within the bottom of the image indicate the layer orientation. the layers show the orientation of the layers.105
- Figure 4-1 – a) shows a configuration using an automatic tool changer. b) shows a configuration using a permanent fixture [238].....113
- Figure 4-2 – Low cost, non-branded 3+2 axis CNC router provided a suitable platform to develop the additive-subtractive hybrid manufacturing system114
- Figure 4-3 – Sectional view of the high-viscosity paste extruder. Attached is a pre-packaged EFD syringe116

- Figure 4-4 – Shows the characterisation of the 150 W enclosure heater with the anemometer and thermocouple in the same configuration shown previously 118
- Figure 4-5 – Shows the measured heat and airspeed of the enclosure heater at distances of 0 mm, 50 mm, 100 mm and 150 mm 118
- Figure 4-6 – (left) shows a CAD representation of the mounting fixture (right) shows the manufacturing apparatus mounted in the fixture on the motion platform 12
- Figure 4-7 – Shows the input-output block diagram for the proposed hybrid manufacturing system..... 126
- Figure 4-8 – Shows the process of levelling the build plat relative to the Z axis motion platform with the DTI zeroed in the centre of the bed that is moved to the positions shown by the insert 128
- Figure 4-9 – Shows the validation of the distance moved using a 5 mm slip block 129
- Figure 4-10 – a) shows the setting on the DTI in the datum position. b) shows the checking of the distance using slip blocks with the same value as the nominal distance. c) shows the slip blocks with the required width to zero the DTI 131
- Figure 4-11 – Shows the average deviation stage from the nominal for various accelerations with a target speed of 1,600 mm/min on the X-axis motion stage. Error bars have been omitted for clarity 132
- Figure 4-12 – Shows the average deviation stage from the nominal for various accelerations with a target speed of 1,600 mm/min on the Y-axis motion stage Error bars have been omitted for clarity. y Error bars have been omitted for clarity 132
- Figure 4-13 – Shows the average deviation stage from the nominal for various accelerations with a target speed of 3,200 mm/min on the X-axis motion stage Error bars have been omitted for clarity 134

- Figure 4-14 - Shows the average deviation stage from the nominal for various accelerations with a target speed of 3,200 mm/min on the Y-axis motion stage Error bars have been omitted for clarity.....134
- Figure 4-15 - Shows the average deviation stage from the nominal for various feedrates using an acceleration of 300 ms^{-2} on the X-axis motion stage Error bars have been omitted for clarity Error bars have been omitted for clarity.....136
- Figure 4-16 - Shows the average deviation stage from the nominal for various feedrates using an acceleration of 300 ms^{-2} on the Y-axis motion stage Error bars have been omitted for clarity Error bars have been omitted for clarity Error bars have been omitted for clarity136
- Figure 4-17 - Shows the deviation from the nominal for all of the data collected during the aforementioned tests 137
- Figure 4-18 - Illustrates the process for generating manufacturing toolpaths for the various processes on the hybrid manufacturing process.....141
- Figure 4-19 - Shows a) ecoPEN 300 PC extrusion system b) FFF hotend mounted on a linear solenoid c) Nakanishi Micromachining spindle (1) with ATC (2) d) enclosure heater for accelerated drying142
- Figure 4-20 - Shows the hybrid manufacturing process to fabricate components from advanced ceramic materials. The part shown demonstrates all elements of the process including extrusion of the ceramic feedstock, accelerated drying, sacrificial support deposition and machining. Once the green state part is fabricated, the part is thermally processed (fired) by Morgan Advanced Materials.....144
- Figure 5-1 - Shows the profiles generate for tracks produced with a $250 \mu\text{m}$ straight-profile nozzle and constant printing height of $125 \mu\text{m}$ on uncoated paper using a) Flowrate rate $40\mu\text{l}/\text{min}$, Printing speed $650\text{mm}/\text{min}$ b) Flow rate $33\mu\text{l}/\text{min}$, Printing speed $725\text{mm}/\text{min}$ w146
- Figure 5-2 -a) shows the post-process machining of the green state tile using a $\text{Ø}4 \text{ mm}$ fluted CVD end mill b) shows the sintered tiles with (1)

being machined on the top and side surfaces and (2) that was machined on the top surface only. Both tiles underwent a measure X-Y shrinkage of ~16%..... 148

Figure 5-3 – Shows the profiles generated from the side surface of the parts. a) Shows side B of the non-machined tile b) shows side D of the machined sample. The machined sample shows a more consistent profile..... 149

Figure 5-4 – illustrates the reduction in surface roughness R_a and R_q achieved by implementing a post-process machining operation 150

Figure 5-5 – (top) shows the taper tiles that were fabricated with different degrees of post processing. Sample a has undergone no post processing. Sample b was machined used a \varnothing 1 mm ball nose cutter with a stepdown height of 1 mm. Sample c was machined used a \varnothing 1 mm ball nose cutter with a stepdown height of 0.01 mm. (botton) shows the sintered samples..... 151

Figure 5-6 – Shows the height maps generated for a) sample b with a stepdown height of 1 mm and b) sample c with a stepdown height of 0.01 mm 152

Figure 5-7 - Shows a comparison of the measured surface roughness of the samples following post process machining with a \varnothing 1 mm ball nose cutter using variable stepdown heights..... 153

Figure 5-8 – a) shows the deposition of a new layer of ceramic during the fabrication of the pyramids b) shows the post process machining of the left hand pyramid using a \varnothing 1 mm ball nose cutter and a stepdown height of 0.2 mm..... 154

Figure 5-9 a) shows the sintered non-machined pyramid that exhibits a number of surface defects. b) shows the sintered machined pyramid..... 154

Figure 5-10 – a) shows the height map generated for Side C of the non-machined pyramid. b) shows the height map generated for Side D of the machined pyramid 155

- Figure 5-11 – Comparison of the surface roughness of the non-machined and machined pyramids156
- Figure 5-12 a) shows the placement of the prefabricated PLA support structures within the internal cavities. b) shows the enclosed geometries with the corresponding infill densities engraved on the top surface ... 157
- Figure 5-13 – shows the delaminated samples post sintering where samples 20, 40, 60 and 80 sintered in the orientations shown. Samples 0 and FL split into two separated pieces.158
- Figure 5-14 – Inspection of the internal cavities shows that both infill densities resulted in the formation of the internal cavity. Debris and other artefacts are visible in the base of the FL sample158
- Figure 5-15 a) shows the support structure for the overhanging section of the conformal geometry during layer surface machining. b) shows the conformal geometries post fabrication before post process machining. c) shows the conformal after post process machining with a $\varnothing 1$ mm ball nose cutter and stepdown height of 0.2mm. d) shows a sintered non-machined and machined conformal geometry side-by-side with the internal structures shown below.159
- Figure 5-16 a) shows the height map generated for the non-machined dome. b) shows the height map for the machined dome with a stepdown height of 0.2 mm160
- Figure 5-17 – a) shows the deposition of the ceramic feedstock during the production of the bend test samples. b) shows the post process machining of the bend test samples162
- Figure 5-18 – Shows the measured surface roughnesses of the bend test samples. The bottom surface has a higher surface roughness due to the infill pattern of the substrate163
- Figure 5-19 – Shows the orientation of the bend test samples during the flexural strength testing.....163
- Figure 5-20 – shows the fracture surface of the bend test sample using SEM at 220 \times magnification165

Figure 5-21 – Shows an overview of the various processing stages used to fabricate the hollow hemisphere using the hybrid manufacturing process.	167
Figure 6-1 – (a) shows the screen printing process [251] (b) shows a planar circuit produced using screen-printed silver-Palladium conductor plus resistor materials [252]	171
Figure 6-2 – Shows a summary of process used to digitally fabricate electronic features on the sintered alumina substrates.....	173
Figure 6-3 - (a-c) shows the unsintered Ag conductor deposited onto alumina substrates. (d-f) shows the sintered Ag conductor	174
Figure 6-4 – Shows the manufacturers thermal profile for the Ag conductor paste (TC0306A, Heraeus, Germany)	175
Figure 6-5 – shows the variation in conductivity across the three test samples post sintering.	176
Figure 6-6 - shows the surface roughness of the 4-pt probs disks with sample 1 having an R_a of 14.4 μm , sample 2 with a surface roughness R_a 8.1 μm , sample 3 with a surface roughness R_a of 6.2 μm	177
Figure 6-7 – Shows the profile of a sintered track on the alumina substrate ...	178
Figure 6-8 – Shows an alumina substrate with sintered LTCC Ag tracks and 1210 components that have been reflowed with SAC solder at a peak temperature of 249 °C	179
Figure 6-9 – Shows a functioning 555-timer circuit on a planar alumina substrate	180
Figure 6-10 – Shows LTCC silver conductor being deposited onto a 3D geometry using topographical mapping generated by a Keyence.....	180
Figure 6-11 a) shows the sintered 3D thick film circuit produced using DIW of LTCC Ag conductor b) shows the circuit with the 1210.....	181
Figure 6-12 – Shows a summary of the process used to fabricate a 3D ceramic thick-film device on a sintered alumina substrate that was produced using the hybrid manufacturing platform	182

- Figure 6-13 – a) shows the process of fabricating ceramic electronics when depositing thick-film materials onto sintered substrates b) shows the process of fabricating ceramic electronics using HTCC and LTCC materials183
- Figure 6-14 – shows the deposition of Ag conductor onto a substrate made from extruded LTCC dielectric material with Ag conductor that was co-fired at a peak temperature of 865°C185
- Figure 7-2 – Shows the range of parts that were fabricated as part of the validation of the hybrid manufacturing process188
- Figure 7-1 – Shows an overview of the hybrid manufacturing process with the incorporation of digitally-driven, 3D thick-film electronics.....189
- Figure 7-3 – a) shows a hollow hemisphere fabricated from silicon carbide using the hybrid manufacturing process. b) shows a tube geometry fabricated from silicon carbide. The base of the part was post-process machined whilst the top was not.....191

List of Tables

Table 2-1 – Summary of the Ceramic AM categories, the materials and densities that have been demonstrated plus a rating of the process’s multi-material compatibility[205], [206].....	62
Table 2-2 – Summary of the advantages and disadvantages of ceramic AM processes [206], [209]–[213].....	65
Table 3-1 – The feedrates used the machine the sides of the tile.....	99
Table 3-2 – Shows the parameters used during the investigation of Ø0.7 mm and Ø 2.00 mm drill bits	101
Table 3-3 – Shows the parameters used to investigate plunge rate during slot milling operations using a spindle speed of 10,000 RPM and a feedrate of 330 mm/min	103
Table 3-4 – Shows the measured dimensions of the machined slots.....	104
Table 4-1 – Initial deisgn specification used to guide and inform the selection of suitable machine hardware and software	110
Table 4-2 – Shows the specified parameters of the low cost 3+2 axis CNC router	114
Table 4-3 – Shows the repeatability data obtained for the Z axis – showing the average of 10 measurements for each set of parameters.....	130
Table 4-4 – Shows the average deviation from the nominal distance and the range of values that were recorded for the X and Y axis accelerating at various accelerations to a maximum feedrate of 1,600 mm/min. The calculated standard deviation are also shown.....	133
Table 4-5 - Shows the average deviation from the nominal distance and the spread of measurements that were recorded for the X and Y axis accelerating at various accelerations to a maximum feedrate of 3,200 mm/min. The calculated standard deviation are also shown.	135
Table 4-6 - Shows the average deviation from the nominal distance and the spread of measurements that were recorded for the X and Y axis	

accelerating to various feedrates at an acceleration of 300 ms^{-2} The calculated standard deviation are also shown.	137
Table 5-1 - average measured surface roughness of the tapered tile samples. Sample size $n = 5$	152
Table 5-2 – Measured surface roughness of the bend test samples.....	162
Table 5-3 – Cross sectional measurements of the bend test samples and the recorded F_{\max} value output during the flexural tests.....	164
Table 6-1 – Measurement of the unsintered and sintered diameter and thickness with the calculated shrinkage	175

Abbreviations

ABS	Acrylonitrile Butadiene Styrene
AM	Additive Manufacturing
ATC	Automatic Tool Changer
BJ	Binder Jetting
CAD	Computer Aided Design
CAGR	Compound Annual growth Rate
CAM	Computer Aided Manufacture
CAM-LEM	Computer-Aided Manufacturing of Laminated Engineering Materials
CIP	Cold Isostatic Pressing
CNC	Computer Numerical Control
CSL	Ceramic Stereolithography
CVD	Chemical vapour Deposition
DED	Directed Energy Deposition
DIW	Direct Ink Writing
DTI	Dial Test Indicator
FDC	Fused Deposition of Ceramic
FDM	Fused Deposition Modelling
FEF	Freeze-from Extrusion Fabrication
FFF	Fused Filament Fabrication
HSS	High Speed Steel
HTCC	High Temperature Co-fire Ceramic
IJP	Inkjet printing
LOM	Laminated Object Manufacture
LTCC	Low-Temperature Co-fire Ceramic
ME	Material Extrusion
MJ	Material Jetting
PBF	Powder Bed Fusion
PC	Progressive Cavity
PCD	Polycrystalline Diamond

PD	Positive Displacement
PDC	Polymer-Derived Ceramics
PI	Polyimide
PLA	Polylactic Acid
PLC	programmable logic controller
PVA	Polyvinyl Alcohol
PZT	Lead Zirconia Titanate
QIP	Quasi Isostatic Pressing
RC	Robocasting
RPM	Revolutions per Minute
SEM	Scanning Electron Microscope
SL	Sheet Lamination
SLM	Selective Laser Melting
SLS	Selective Laser Sintering
SMU	source measurement unit
TD	Theoretical Density
UI	User Interface
VP	Vat Photopolymerisation
WIP	Warm Isostatic Pressing

1 Introduction

1.1 Advanced Ceramic Materials

Advanced ceramic materials are extensively used across a range of industrial sectors including medical, dental, power generation, chemical and processing, automotive and aerospace. Operating conditions often involve combinations of high operating temperatures, pressure, radiation, areas of high erosion, corrosion, wear requiring chemical inertness and biocompatibility. A range of applications are shown in Appendix A.

Advanced ceramic materials are defined as “inorganic, non-metallic elements, basically crystalline material of rigorously controlled composition and manufactured with detailed regulation from highly refined and/or characterised raw materials giving precisely specified attributes” [1]. Classification of advanced ceramic materials is broadly; oxide ceramics such as Alumina (Al_2O_3) and Zirconia (ZrO_2); and non-oxide ceramics such as Silicon Nitride (Si_3N_4), Silicon Carbide (SiC) and Magnesium Diboride (MgB_2). These materials typically exhibit low toughness and ductility, high hardness and melting points while being susceptible to thermal shock. Although attractive in end use applications, these characteristics present significant manufacturing challenges. [2].

The manufacture of parts using advanced ceramic materials involves the synthesised ceramic powder, with a controlled particle size distribution using processes such as spray drying or sieving. The subsequent powder can either be directly used as a dry powder feedstock or homogeneously dispersed within a binder matrix to form a manufacturing feedstock that exhibit non-Newtonian, pseudoplastic behaviour. Subsequent processing using a number of shaping and forming techniques result in the creation of a green-state part. Thermal processing through a controlled heating cycle causes decomposition of the binder matrix, whilst simultaneously inducing sintering and densification of the remaining elements. This yields a high-density monolithic ceramic part that has the required material properties but has undergone a measured

shrinkage of 16-18% [3]. Post sintering, the hard and brittle nature of the ceramic prevents further processing involving significant deformation or material removal such as pressing or machining. Grinding, polishing and lapping can be used to remove surface defects or create features that could not otherwise be produced using the previous forming processes.

Predominant methods of shaping and forming the green state ceramic part within conventional manufacturing chains are reliant on template-based techniques such as Cold Isostatic Pressing (CIP), uniaxial pressing, slip casting and injection moulding. However, these template-based production methods necessitate high production volumes, large capital investment and long development lead times due to the need to manufacture moulds and tooling. This imposes a number of limitations in terms of flexibility and responsiveness of the manufacturing process to iterative design changes. Furthermore, the design of components is also hampered by the inability of these conventional forming processes to create internal features and functionally graded components with dynamically changing material composition.

Green state CNC machining of preformed billets of ceramic material is used to during low volume production for high-value end-user applications such as aerospace or for prototyping and developmental purposes. A significant shortcoming of subtractive manufacturing processes is the volume of material that is removed and subsequently wasted, which can be up to 98% [4]. This requires the billet preform to be considerably larger than the final component, particularly if an assembly stage cannot be implemented. The inclusion of an assembly step may provide additional design freedoms to reduce the volume of material required to create the intended geometry. Removing large volumes of material is not only inefficient in terms of resource utilisation and machining time, but also increases tool wear. 5-axis CNC machining facilitates the production of a range of intricate features and geometries, although design and manufacturing limitations do still prevail. This is apparent when machining components with overhanging and enclosed geometries with restricted access due to the size and length of the cutting tools and machining spindle. Furthermore, subtractive machining operations cannot produce fully enclosed

cavities without the inclusion of a joining or assembly stage. This prevents the alteration of internal structures for weight reduction and thermal management purposes. Finally, subtractive manufacturing does not enable the material composition of a part to be dynamically altered, preventing the creation of functionally graded structures. Functionally graded structures enable the combined use of multiple materials providing a number of benefits such as weight and cost saving and improved thermal regulation.

Digitally driven fabrication techniques such as Additive Manufacturing (AM) offer a way in which to manufacture parts from advanced ceramic components without the need for templates, whilst imposing fewer geometric design limitations than subtractive manufacturing techniques. The ISO/ASTM 52900 standard defines AM as “the process of joining materials to make objects from 3D model data, usually layer upon layer, as opposed to subtractive manufacturing methodologies”. The standard aims to classify the various processes into 7 fundamental categories; vat photopolymerisation (VP), material extrusion (ME), powder bed fusion (PBF), material jetting (MJ), binder jetting (BJ), sheet lamination (SL) and directed energy deposition (DED). The development of AM feedstocks has enabled the fabrication of parts from polymers, waxes, metals and advanced ceramic materials. The absence of part-specific tooling enables economic low-volume production for the manufacture of high-value end-user components and prototypes for research and development purposes. The layerwise manufacture overcomes the restriction of subtractive and conventional forming processes for the production of enclosed internal cavities and functionally graded parts. Ceramic AM processes can be broadly classified as direct and indirect methods. Direct fabrication techniques fuse the ceramic powder feedstock, forming the geometric shape and final material properties simultaneously, whereas indirect techniques form a green part that is thermally processed to produce monolithic ceramic. Direct processes have a number of ongoing challenges such as cracking and distortion due to thermally induced stresses, resulting in indirect ceramic AM being most common, which also have closer affinity to conventional manufacturing of ceramics. Figure 1-1 shows the manufacturing process chains

for fabricating components from advanced ceramic materials using (a) conventional manufacturing techniques (b) Indirect AM, (c) direct AM.

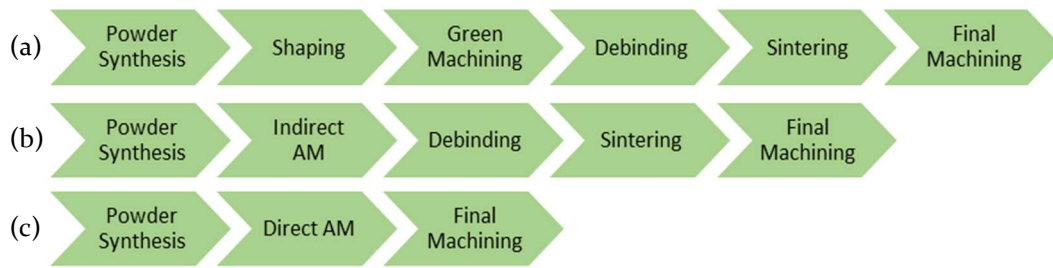


Figure 1-1 - Shows the process chain for manufacturing advanced ceramic parts using a) conventional manufacturing techniques b) Indirect AM techniques and c) direct AM techniques

Despite the benefits of AM, the uptake of ceramic AM has been limited due to a number of processing challenges and incompatibilities with conventional manufacturing process chains. Ceramic AM systems have typically been developed by the adapting AM processes designed for polymers and metals, often using the conventional AM feedstock as the binder matrix to fabricate a green state ceramic part. This has a number of implications during the formation of materials and suitable feedstocks (frontend processing) and the debinding, sintering and densification stages post-fabrication (backend processing). The need to incorporate additional elements within the ceramic AM feedstock, such as photo-curable monomers for VP processes prevents the use of conventional feedstock formulations. This reduces the coherence between parts fabricated using ceramic AM and conventional processes, which reduces the ability to produce representative parts during research and development cycles. Moreover, the formulation and characterisation of alternative feedstocks, increases the cost of integrating ceramic AM. Furthermore, retaining suitable process dependent characteristics such as rheology and curing depth restricts the volume and types of ceramic material that can be dispersed within the feedstock. This has a number of implications, with parts often exhibiting combinations of insufficient density, inferior resolution and high shrinkages compared to conventional processes.

Despite these challenges, the potential added-value of AM [5] is generating continued growth and investment. In 2015 the overall AM market was valued at \$5.3 billion and is expected to increase to \$21.5 billion by 2025, representing a

Compound Annual growth Rate (CAGR) of 15.03% [6]. In 2018 the technical ceramic AM market was valued at \$20.6 million with a value of \$159.5 million by 2025, representing a CAGR of 34% [7]. Figure 1-2 shows the predicted growth of the ceramics AM market between 2017 and 2028, with a predicted value of \$1.89 billion by 2025 and \$3.6 billion by 2028. The largest growth is anticipated to be in the technical parts segment.

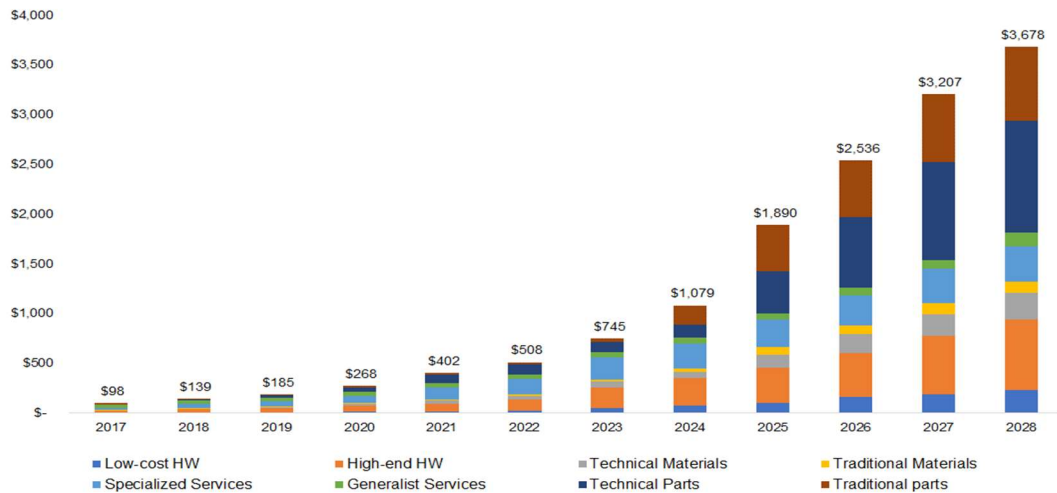


Figure 1-2 – Predicted market value of advanced ceramic markets between 2017 and 2028 [8]

A limitation of AM processes in general (including polymer and metal AM) is the functionalisation of fabricated parts. Material limitations often result in the production of non-functional parts from a single material class i.e. polymers. However, the creation of functional parts with elements such as electronics is an ongoing development for AM technology, requiring the use of multiple material classes in a single part such as polymers and ceramics. Ceramic thick-film electronics are widely used within industries such as the automotive sector to fabricate devices for engine and gearbox controls, tyre pressure sensors and airbag ignitors. These applications are required to have long-term reliability in harsh environments that undergo thermo-cycling beyond the operational temperature ranges of conventional electronics (-65 to 125°C) plus exposure to vibrations, corrosive agents and humidity [9]. A common dielectric material within thick-film substrates is alumina with a purity of 94-98% [10].

Conventional manufacturing approaches of ceramic thick film electronics are template-based using processes such as screen printing. These have similar constraints in terms of responsiveness as the aforementioned processes used to

fabricate advanced ceramic materials, but also restrict the thick-film circuits to 2.5D planar geometries. Direct Ink Writing (DIW) of thick-film materials have been demonstrated with conventionally manufactured planar substrates [11], although this process has not been applied to 3D AM substrates.

Templateless deposition of conductive materials and inks has been shown to create 3D electronic circuits on additively manufactured parts fabricated using polymer-based materials [12], [13]. The combination of ceramic AM with 3D DIW has the potential to enable the functionalisation of ceramic AM parts with thick-film ceramic electronics. The combination of AM and DIW of ceramic thick film electronics have a number of benefits in terms of more versatile packaging configurations and device form factor for industrial sectors such as communications and automotive.

In 2018 the electronic components and equipment industries accounted for over 70.0% of total demand for advanced ceramic materials. The electronics industry is expected to grow by ~13% between 2017 and 2022 [14]. The largest growth is anticipated to be within communications, automotive and control sectors [15]. This is due to the increasing automation within the automotive industry and growing demand for personal transport. This is complimented by the evolution of wireless communication networks and RF devices for applications such as 5G data networks and Industry 4.0. [16] [17].

To overcome the limitations of standalone AM and enable increased functionality, multiple manufacturing processes are being combined into a single hybridised system. Currently, no definitive definition of hybrid manufacturing exists, although an open definition was refined by the International Academy for Production Engineering defines it: “a hybrid manufacturing process combines two or more established manufacturing processes into a new combined set-up whereby the advantages of each discrete process can be exploited synergistically” [18]. Whilst this is not a conclusive definition of hybrid manufacturing, this will be used throughout the course of this thesis. Merz *et al.* demonstrates the merits of hybrid manufacturing in 1994 with the development of Shape Deposition Manufacturing (SDM) [19]. SDM combines

AM, 5 axis CNC machining, shot peening and micro-casting. More recent examples of hybrid manufacturing approaches include the work of Song *et al*, combining Gas Metal Arc Welding (GMAW) with a commercial 3-axis milling system. A 75 × 75 × 50 mm mild steel cube was fabricated using GMAW only, with a resolution of ±0.5 mm and surface R_a of 150 μm . Hybridisation using both GMAW and 3-axis milling resulted in a resolution of ±0.01 mm with a surface R_a of 2 μm [20]. Alternatively, Li *et al*. combined a polymer-based VP process with DIW of an electrically conductive adhesive to fabricate a multilayer 555-timer circuit, which was embedded within a polymer AM part [21]. However, the additional complexity of fabricating parts from advanced ceramic materials has resulted in these approaches not yet being applied.

1.2 Research Motivation

The rapidly evolving technological and manufacturing environment is necessitating the implementation of flexible and responsive manufacturing strategies, which are capable of processing a range of materials including advanced ceramic materials. Digital fabrication approaches enable the production of intricate geometries as near-net-shape and final parts, minimising material waste, cost and the environmental impact of manufacture. The absence of templates and tooling streamlines product development whilst providing greater design freedoms, particularly in the production of overhanging and enclosed geometries. Functionalisation of these geometries with elements such as electronics requires the use of multiple material types, such as polymers, metals and ceramics. This represents an ongoing challenge for AM processes, due to material compatibility issues and component performance. There are four motivating factors that support the need for the research and development of a digitally driven, hybrid manufacturing process using advanced ceramic materials:

- Overcoming the manufacturing limitations of conventional and existing ceramic AM processes to produce full density, geometrically complex parts using advanced ceramic materials

- Reducing the waste generated during the development and manufacture of complex 3D ceramic components
- Processing of feedstocks that are compatible with existing front and backend processes used within existing ceramic production chains
- Overcome some of the challenges associated with the production of functionalised components using multiple material types such as advanced ceramics and metals.

1.3 Research Intentions

1.3.1 Aims and Objectives

This PhD thesis documents the development of a fully integrated additive/subtractive hybrid manufacturing process for the production of high density, advanced ceramic components. Using a conventional injection moulding feedstock containing 96wt% alumina with an average primary particle size of 2-3 μ m and a measured moisture content of between 18-22% aims to streamline the integration with existing manufacturing process chains. The capabilities of the process are validated by the production of demonstrators featuring filled (fully dense), overhanging, spanning and conformal geometries. The use of a digitally driven DIW process depositing a silver-based conductor indicate the capabilities of creating 3D thick-film ceramic electronics on the fabricated ceramic parts. This required a number of objectives:

- To develop an additive/subtractive hybrid process flow using feedstocks derived from commercial formulations.
- Design, assemble and test a hybrid manufacturing platform featuring additive, subtractive and ancillary elements.
- Determine a suitable processing window to enable the fabrication of 3D geometries using advanced ceramic materials.
- Fully characterise the fabricated components in terms of density, surface roughness and resolution.

- Demonstrate the feasibility of producing 3D circuits on the sintered ceramic geometries using a commercially available LTCC conductor material.

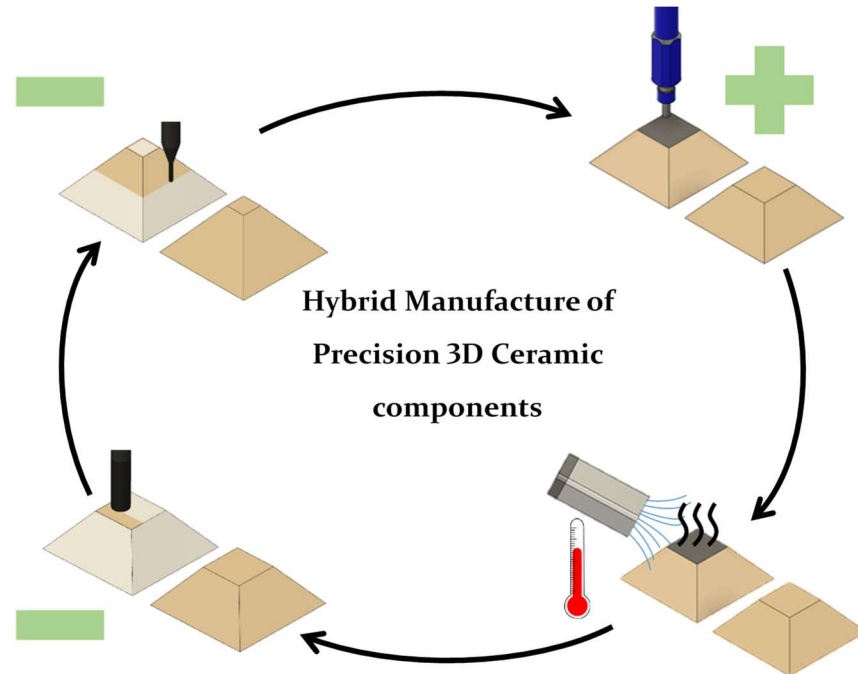


Figure 1-3 – Shows a visualisation of the proposed hybrid manufacturing process to produce precision 3D ceramic components. The process combines selective material deposition (additive), accelerated drying, planarising machining (subtractive) and post-process machining (subtractive)

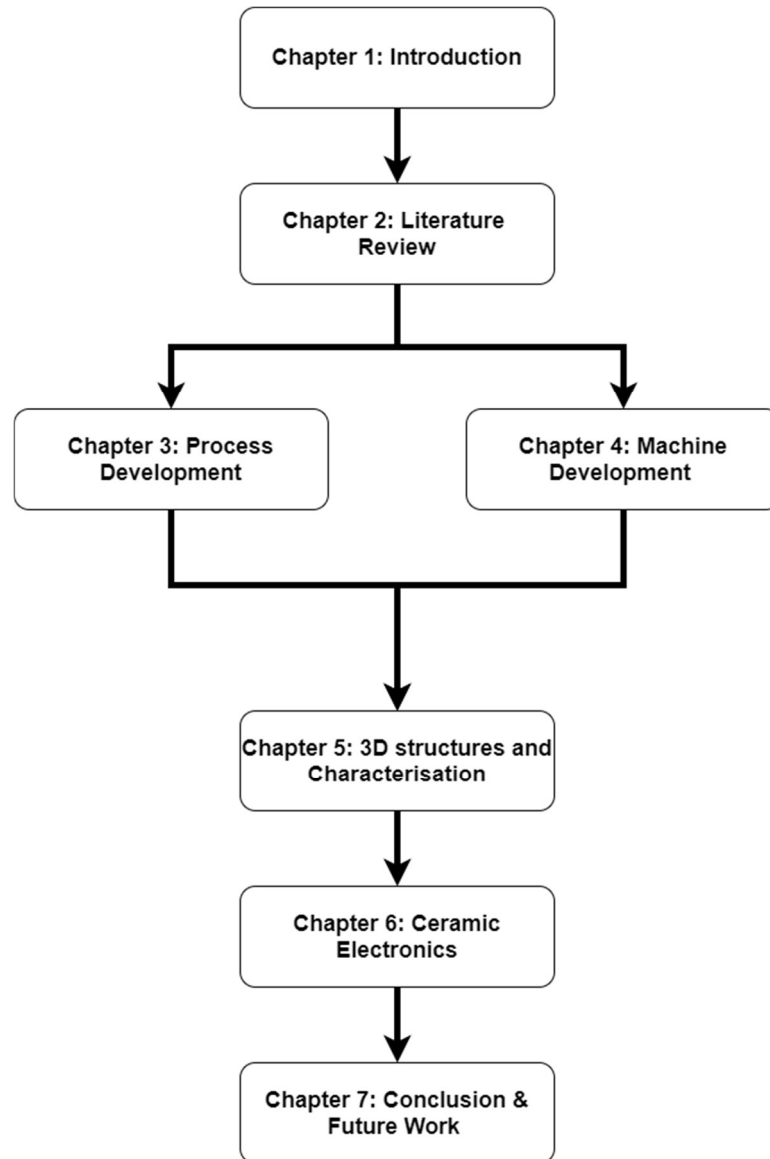
1.3.2 Research Novelty

Combining additive and subtractive processes into a single integrated manufacturing process has a number of benefits, which have been demonstrated. However, this approach has not previously been used to produce parts from advance ceramic materials. The use of feedstocks developed for conventional injection moulding process limits the disruption to established manufacturing process chains by using the same front and backend processing, obtaining comparable densities and shrinkage. The subtractive elements of the process enable the creation of high-fidelity features with manufacturing tolerances that are comparable to conventional and existing AM processes. Furthermore, the subtractive machining capability provides in-situ post-processing and rework, enabling the removal of defects that would otherwise the result in the part being scrapped, thus reducing waste. The use of 3D DIW

using LTCC silver conductor demonstrates one of the first instances of digitally fabricated thick-film ceramic electronics. The work undertaken during this thesis has approached the digital fabrication of advanced ceramic components with integrated electronics from a different perspective by:

- Processing of ceramic feedstocks derived from conventional formulations, which are compatible with conventional front and backend processes.
- Combination of additive and subtractive manufacturing apparatus into a single digitally driven process capable of using a range of ceramic feedstocks.
- Creation of a versatile and adaptable manufacturing platform with comparable results to conventional and existing AM processes.
- Fabrication of 3D ceramic components with densities of up to 99.93% with shrinkages comparable to conventional manufacturing processes.
- Production of planar and 3D thick film ceramic electronics using a commercially available LTCC conductor on substrates fabricated using a digitally driven approach.

1.4 Thesis Structure



Chapter 2 provides a comprehensive Literature review of the available literature on ceramic AM techniques. A critical review of each process identifies the relative benefits and shortcomings of each process, with a comparison of the various processes. The findings from this were used to guide and inform the development of the hybrid manufacturing process.

Chapter 3 documents the development of the hybrid manufacturing process covering the characterisation of the ceramic feedstock's rheological properties, which were used to guide and inform the identification of suitable extrusion apparatus. An investigation of PLA support structures for the creation of overhanging geometries and raft substrates is presented, determining the

feasibility of this approach. Characterisation of the green state ceramics machinability is presented to identify suitable processing parameters that can be used to post-process the ceramic part and create high-fidelity features.

Chapter 4 details the selection of suitable manufacturing hardware for the hybrid platform including motion platform, high viscosity paste extruder, FFF extruder, accelerated drying fan and machining spindle. This chapter documents the integration of the manufacturing processes with the control software and the process of generating toolpath to enable manufacturing precision 3D components using the hybrid manufacturing platform. Characterisation of the motion platform's repeatability is also presented to determine the capabilities and limitations of the system.

Chapter 5 presents the characterisation of 3D ceramic geometries that were used to validate the capabilities of the hybrid manufacturing platform. The fabrication of 2.5D and 3D geometries are investigated with varying degrees of post-process machining to determine the change in surface roughness, part density and manufacturing resolution.

Chapter 6 documents the functionalisation of the fabricated ceramic substrates using a DIW process to deposit a high viscosity LTCC silver paste to form planar and 3D ceramic electronics. The fabrication of a functional 555-timer is presented as evidence of the feasibility of this approach.

Chapter 7 concludes the key findings from this body of work with suggestions of future work to expand the range of process compatible materials and increase the capabilities of the hybrid manufacturing platform.

2 Literature Review

This literature review explores how AM approaches have been used to manufacture parts from advanced ceramic materials covering process hardware configurations, material formulations and post-processing techniques. A critical review of each ceramic AM processes covering the benefits and shortcomings of the various ceramic AM processes will be used to guide and inform the development of the proposed hybrid process. Conventional shaping and forming techniques will not be covered in this literature review as the intention is to develop a digitally driven manufacturing process.

2.1 Additive Manufacturing of Ceramics

Additive manufacturing of advanced ceramic material has been an ongoing evolution of AM since its initial inception in the mid 1980's, although the added complexity of processing ceramic materials results in it being less developed than polymer and metal AM. All seven process categories have been used to manufacture parts from advanced ceramic materials. However, the available literature surrounding the use of DED is limited and will therefore not be covered in this literature review. Figure 2-1 shows six ASTM defined categories that have been used to manufacture ceramic parts and will be reviewed during this literature review.

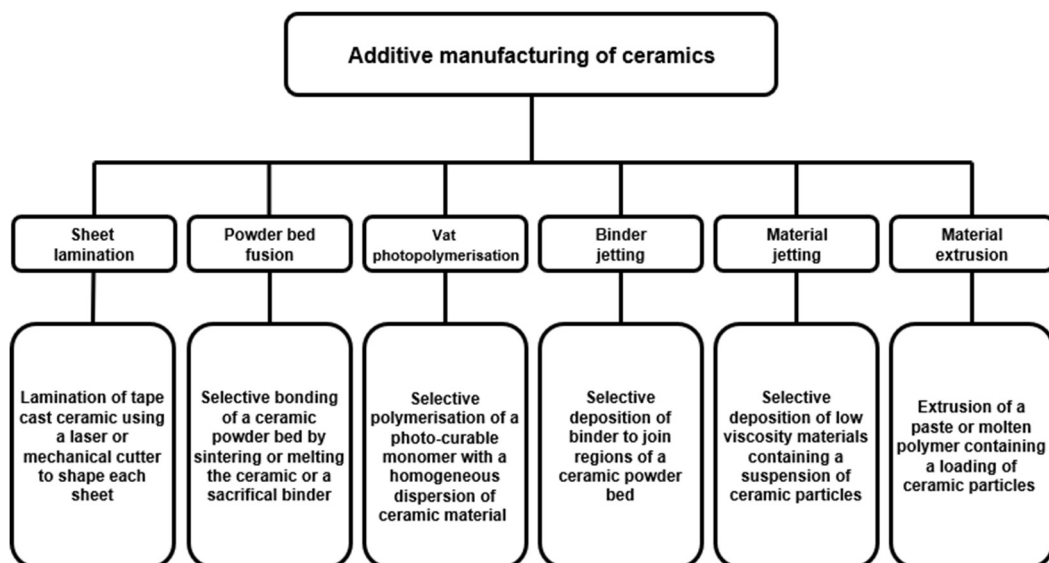


Figure 2-1 – Shows the process categories that have been used to demonstrate the fabrication of components using advanced ceramic materials

The classification of ceramic AM processes covered in this literature review will be categorised based on the feedstock form such as suspension-based processes, powder-based processes, material extrusion and sheet lamination. Both direct and indirect AM fabrication techniques will be reviewed although the majority of ceramic AM processes are indirect processes.

2.1.1 Suspension-based Processes

Suspension-based ceramic AM approaches, which include VP and MJ, use a liquid resin or slurry feedstock containing a homogeneous dispersion of ceramic material. VP is one of the most prevalent ceramic AM processes used to produce high density parts from advanced ceramic materials. This is due to the fine features, low surface roughness and high densities that can be achieved [22]. VP uses a liquid photo-curable monomer that is selectively irradiated with light, often in the UV spectrum, to induce crosslinking (polymerisation) of the monomer to form the layer cross section. This process is repeated until the 3D geometry is formed.

Ceramic Stereolithography (CSL) is the predominant VP process used to fabricate ceramic parts. CSL was originally demonstrated during the 1990s by selectively cured photo-curable monomers containing 10 - 50 vol% ceramic using a high-intensity UV lamp [23]. It has since been implemented by a number of commercial ceramic AM systems such as the CeraFab7500 (Lithoz, Austria) and Admaflex 130 (Admatec, Netherlands). CSL has been used to process materials such as Alumina, Zirconia and Silicon Nitride [24]. Examples of fabricated parts include cellular structures [25], turbine blades [26] and dental crowns [27], with typical layer thicknesses of 10-200 μm , resulting in measured surface roughness R_a of 0.3 – 3.0 μm and minimum feature sizes of 100-125 μm [22], [28], [29]. Alumina-based feedstocks resulted in parts with sintered densities of 90.5- 99.3% [22], [30]–[32] and flexural strength of 275 - 476 MPa [22], [28], [33], [34].

The CSL hardware can use either top-down or bottom-up configurations. Top-down configurations position the polymerising light source above the material

vat, which is irradiated over the top surface of the resin to selectively induce polymerisation. Once the layer is formed, the build plate lowers by one-layer thickness, using a doctor blade to create a uniform layer of material before patterning the next layer. The process is repeated until the 3D part is fabricated. Alternatively, bottom-up setups position the light source beneath the build area, selectively curing the material that is formed between the part and the vat by projecting through a transmissive window. The polymerisation process can result in the adhesion between the part and vat bottom, requiring a detachment movement to “peel” the part off the vat, before the build platform raises by one-layer thickness. The process repeats until the part is fabricated. Figure 2-2 illustrates a side-by-side comparison of *a)* top-down CSL setup and *b)* bottom-up CSL setup. The top-down setup would normally feature a layer recoating mechanism such as a doctor blade, which has been omitted from this figure for clarity.

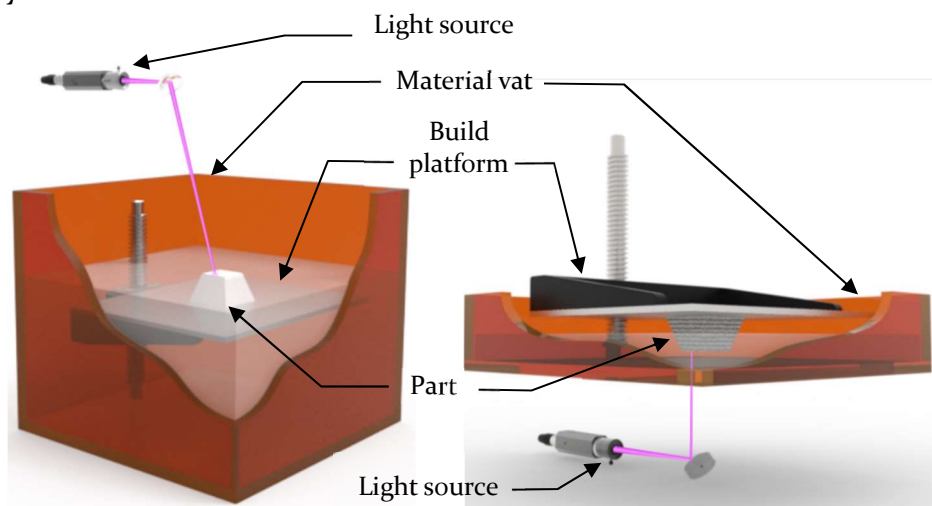


Figure 2-2 – illustrates a typical configuration of CSL hardware in a) top-down configuration and b) bottom-up setup. Both setups are showing the fabrication of a pyramid geometry

Whilst CSL can produce high density parts with fine features, existing feedstock formulations and light-based patterning are restrictive, resulting in a number of shortcomings such as high shrinkages and limited material compatibility. The layer recoating mechanism for both top-down and bottom-up systems is reliant on the feedstock having a suitable viscosity and pseudoplastic behaviour. However, the addition of ceramic material to the photo-curable monomer, causes an increase in viscosity affecting its processability [23]. The magnitude of the increase is dependent on a number of variables such as particle size and

morphology, although the volume of dispersed ceramic has the most profound effect. Despite attempts to exceed 65 vol% [35], feedstocks typically contain 30-60 vol% ceramic with measured viscosities of 100 – 1,400 mPa.s at 100s⁻¹ [22], [36]–[38]. This results in measured linear shrinkages of up to 35% during the debinding and sintering stages of manufacture [39], [40]. These shrinkages restrict the size of components that can be fabricated due to the possibility of cracking, delamination and distortion of the part [38]. The high volume of binder within the feedstock, can also cause porosity within the sintered part reducing the mechanical strength. This restricts the types of applications where these parts can be used such as non-functional prototypes. Consequently, parts fabricated using CSL are typically limited to <10 mm in size [34] and require high levels of process control over the rate of drying, debinding and densification to avoid distortion and defects within the part [41].

To ensure the fabrication of green parts with sufficient strength, the polymerising radiation is required to penetrate through the material to the previous layer, to ensure that the new layer adheres to it. However, the inclusion of ceramic material reduces the penetration depth as a result of scattering caused by mismatched refractive indexes [42]–[45]. Griffith *et al.* noted that when processing feedstocks containing 30 vol% submicron silicon nitride particles, cure depth was reduced from 200 µm for the unfilled monomer to 60 µm [46]. This issue is further compounded by the effects of other variables such as particle morphology and colour which alters the absorption characteristics of the material [47]. This imposes further restrictions the range of materials that can be practicably processed and preventing the use of materials such as silicon carbide [46], [48]. Additionally, the scattering of the polymerising radiation often results in “overgrowth” of the polymer relative to the projected pattern, reducing the resolution of the process.

A largely undocumented, but critical step in the CSL process is the post-fabrication washing stage prior to thermal processing. The washing stage removes uncured feedstock from the part that would cause a reduction in manufacturing tolerances. However, the viscosity and surface tension of the feedstock may require mechanical or ultrasonic agitation to achieve sufficient

cleaning. The additional agitation can damage the parts, due to the low green-part strength [49], [50]. Furthermore, this washing stage increases the complexity and cost of incorporating secondary materials to create functionalised parts and electronics.

Variations of the CSL process have also been developed to overcome some of the material challenges and reduce the minimum feature size. Micro-stereolithography (μ SL) uses improved optics to achieve a smaller spatial resolution, whilst reducing layer thicknesses to 1 - 10 μ m [51]. μ SL was demonstrated by Zhang *et al.* using feedstocks containing 33 vol% alumina to fabricate gears with diameters of 400 and 1000 μ m. Sintering of the parts resulted in a measured linear shrinkage of 16% with parts exhibiting 56% TD. Furthermore, the thinner layers and focused light source increase fabrication time, making this inappropriate for the production of large components [51].

Alternative feedstock formulations such as Polymer-Derived Ceramics (PDC) have been investigated to overcome the challenges of dispersing ceramic material. PDCs were discovered in the 1960s and rely upon the pyrolytic decomposition of a preceramic polymer to produce ceramics such as SiC, SiOC, BN, BCN and Si₃N₄ [52]. PDCs have been shown to have a broad range of mechanical, electrical, optical and chemical properties and are currently used in the production of ceramic fibres [53]. PDCs have been combined with photocurable elements, enabling them to be processed using ceramic AM processes [54]. In 2016 Zanchetta *et al.* demonstrated the production of an intricate lattice structure from SiOC ceramic from PDCs processed using CSL by combining photocurable elements with the inorganic PDC precursor [25]. This approach was further validated by Eckel *et al.* later in 2016 by the fabrication of a twisted lattice structure using SiOC ceramic [54]. Although these approaches have shown promise, the pyrolysis of PDCs into ceramic materials resulted in shrinkages of between 25% and 70% [55]–[57]. Whilst this approach is not strictly suspension-based, its use with CSL may facilitate the digital fabrication of certain advanced ceramic materials. However, PDCs are not available for many commonly used advanced ceramic materials and have limited compatibility with existing ceramic manufacturing chains.

Material Jetting (MJ) processes, often referred to as Inkjet printing (IJP), is a suspension-based ceramic AM process that involves the deposition of a liquid material in droplet form. Once deposited, the material coalesces to form a solid layer, which then solidifies due to the evaporation of solvent, cooling or polymerisation. The process is repeated in a layerwise manner until the geometry is produced.

IJP of ceramics was first alluded to in the patent “Three-dimensional printing techniques” by Sachs *et al.* in 1989, with reference to the dispersion of powder within “a liquid vehicle” [58]. Blazdell *et al.* first demonstrated the application of direct IJP of ceramic materials in 1995, depositing inks formulated using 60 vol% Zirconia before dilution with solvents (prior to printing) [59]. The diluted ink had a viscosity of less than 10 mPa s, with a corresponding ceramic content of 5.3 vol%. The ink was deposited through selectable 50 and 75 μm nozzles onto a substrate consisting of ashless filter paper with a porous nitrocellulose membrane. A Zirconia wafer consisting of 65 layers was produced with a sintered thickness of 50 - 70 μm . The part was shown to be free from macro defects and did not distort during thermal processing, although the topography of the part exhibits signs of the droplet deposition.

IJP has been used to deposit inks containing ceramic materials such as Alumina [60], Zirconia [61], Barium Titanate [62], Lead Magnesium Niobate [63], PZT [64] and Silicon Nitride [65]. Inks are often formulated and diluted using volatile solvents to achieve the necessary fluid characteristics, exploiting Rayleigh instability of the inks to eject the material through fine nozzles that typically range from 30 - 120 μm [66]. This results in the formation of droplets with diameters slightly larger than the nozzle [67]. IJP has been used to fabricate parts with layers as low as 0.3 μm [68], although examples typically quote layer thicknesses of 3 - 4 μm [69], [70].

Noguera, Lejeune and Chartier demonstrate the production of 3D fine scale features in the form of a PZT pillar array. The manufacturing apparatus was determined to have an X-Y resolution of ± 10 μm and a Z resolution of ± 1 μm . The print head consisted of 60 μm nozzle orifices processing feedstocks with a

viscosity of 5 - 20 mPas. Inks formulated with 50 vol% PZT were diluted to a relative loading of 10 vol% PZT with a measured viscosity of 10 mPas. The fabricated pillars consisted of a base and rod section with a measured base of 110 μm and an average cross-section of 90 μm . The rods were fabricated using a 3 μm layer thickness, with each rod being approximately 400 μm in height [70].

Cappi *et al.* demonstrates the production of a gear structure from an ink containing 32.5 vol% silicon nitride with a median particle size of 0.4 μm , which was deposited using a printhead with 30 μm nozzles. The fabricated gear had 10 printed layers with no visible surface defects. Sintering of the fabricated parts caused no delamination or warping, however no quantitative discussion of shrinkages is provided, although comparison of figure scale bars would imply a linear shrinkage of $\sim 30\%$. This work provides no discussion of component density, although it is unlikely to be comparable to conventional manufacturing densities [65].

Ainsley, Reis and Derby demonstrated the fabrication of an impeller with a diameter of 28 mm and height of 10 mm. Unlike the aforementioned approaches that have deposited inks containing a volatile solvent, this approach relies on the solidification of a binder vehicle with a melting temperature of 50 - 60°C. The fabrication of the part was achieved using an ink containing 40 vol% alumina powder with a median particle size of 0.3 μm and 90th quartile size of 1.8 μm . The resultant ink had a viscosity of ~ 102 mPa s at a shear rate of 20 s^{-1} , which produced droplets of ~ 33 - 52 μm dependent upon the ejection frequency, which was between ~ 1.5 -18 kHz. During the production of this part, the authors note the need to dynamically change the frequency of droplet generation to account for the X-Y acceleration and deceleration of the print head. Whilst this demonstrates the fabrication of a 3D geometry the sintered part had a sintered density of 80% after undergoing a linear shrinkage of 18% [60]. This indicates that higher shrinkages would be experienced when producing parts with high densities $>99\%$.

The fabrication of 3D geometries is restricted by sensitive processing parameters, complex droplet ejection, formation and impact characteristics, slow build rates and high shrinkages during post-deposition drying and thermal processing [71]. Therefore, maximum size of parts that can be fabricated with high densities is limited to typically $< 1 \text{ cm}^3$ [72].

The narrow processing window in terms of viscosity, surface tension and minimum nozzle diameter, necessitates the use of fine powders, typically between $0.1 - 1.5 \mu\text{m}$, within ink formulations [73] [74]. This has previously been shown to alter the viscosity of the feedstocks and cause the formation of agglomerates, resulting in frequent nozzle blockages. Furthermore, the increased viscosity requires higher actuation pressure to eject material from the printhead. This can result in the formation of satellite articles and non-uniform droplets due to the complex formation dynamics of droplet formation, which result in defects and reduce manufacturing resolution [74]. The challenges of ink formulation and viscosity are further complicated by the need to dilute inks with solvents to temporarily reduce viscosity. This results in inks with ceramic content as low as 4 vol%, which adversely affects the long-term stability. This can result in sedimentation, agglomeration and premature drying, leading to parts with inhomogeneous compositions and nozzle blockages.

The need to compensate for the effect of acceleration and deceleration of the printhead, further complicates the control of the process by necessitating the use of variable ejection frequencies. Varying the frequency of droplet ejection can alter the size of droplets due to the sensitive droplet formation process. Furthermore, certain frequencies are within the anti-resonance region, resulting in wetting of the outer face of the nozzle, which prevents the deposition of material [60].

The wettability of the ink to the substrate and previously deposited material is necessary to ensure the formation of a uniform layer. However, the ballistic impact of the droplets can cause an uneven, ripple effect, resulting in increased surface roughness [75]. This alters the wettability of the surface, with the increased roughness reducing the effective receding contact angle, which also

improves the stability of features [76]. This change in surface roughness also alters the drying characteristics of the ink, causing inhomogeneous material deposits, due to the phenomena referred to as the coffee staining effect [77]. The addition of additives to the inks has been shown to reduce this phenomena, although an increase in ink viscosity was also observed, which may alter the processability of the ink [78].

IJP therefore has limited application within many conventional manufacturing processes, due to the challenges in fabricating 3D geometries. However, potential applications of IJP include the creation of thin functionalised layers or functionally-graded components such as electrodes in energy storage devices [79]–[82].

2.1.2 Powder based processing

Powder-based ceramic AM processes include Powder Bed Fusion (PBF) and Binder Jetting (BJ), which fabricate parts by selectively joining regions of a dry powder feedstock that has been formed into a uniform layer. The process is repeated in a layerwise manner until a 3D geometry is formed. Powder-based processes have been used to fabricate parts from alumina [83]–[85], zirconia [84], Zirconium Diboride [86], Silicon Carbide [87], [88], hydroxyapatite [89] and calcium phosphate [90].

The synthesis of ceramic powder often involves processes such as ball milling or spray drying, which result in the ceramic powders having an irregular particle morphology. This causes the powders to exhibit poor flowability and prone to the formation of agglomerates [91], particularly if the particles are $< 20 \mu\text{m}$ [34]. The flowability of the powder and packing density of the powder bed is dependent on the particle size distribution and the particle morphology of ceramic particles, which have Powders composed of the same particle size exhibit poor flowability and prevent the theoretical density of fabricated components exceeding 74% [92]. Therefore, a suitable particle size distribution and morphology is required in order to achieve sufficient part density [93], [94].

PBF processes include Selective Laser Sintering (SLS) and Selective Laser Melting (SLM). SLS is often used as an indirect method by sintering a secondary materials that has either been combined with the ceramic powder or coated onto the ceramic powder feedstock [95] whereas, SLM is often use as a direct fabrication approach [96]. PBF processes form a uniform layer of powder using a roller or recoating blade, within a build environment that typically heated to a temperature close to the sintering temperature of the feedstock. A laser is selectively rastered over the surface of the powder bed to selectively fuse regions to form the profile of the layer, after which a new layer of powder is deposited. The process is repeated until the 3D geometry has been fabricated.

SLS was developed in 1986 using wax-based materials but has since been expanded to use a range of polymeric materials [97], [98] and higher melting point materials such as aluminium and copper. Lakshminarayan *et al.* demonstrated the feasibility of indirect ceramic SLS in 1990 with the production of a gear and complex bridge structure using a layer thickness of 127 μm (5 mils) from a binary mix of alumina and ammonium phosphate. Ammonium phosphate has a melting temperature of $\sim 190^\circ\text{C}$, which melts and forms a glassy phase around the alumina particles. The resultant green parts had sufficient strength to withstand removal from the build environment and thermal processing to yield a monolithic ceramic part. The fabrication of separate density and shrinkage samples that were processed at temperatures exceeding 1500°C had sintered densities of 32 - 52% with linear shrinkages determined to be between 5 - 10% [99].

The hardware configuration for SLS/SLM systems typically consist of a laser source module, build platform, powder recoating mechanism, area preheating and material store. Figure 2-3 shows a schematic of a typical SLS/SLM process setup. The high processing temperatures of ceramics results in a number of hardware design challenges relating to the containment and maintaining the high processing temperatures. Consequently, direct SLM approaches often use a secondary laser source to preheat the feedstock ahead of the raster laser.

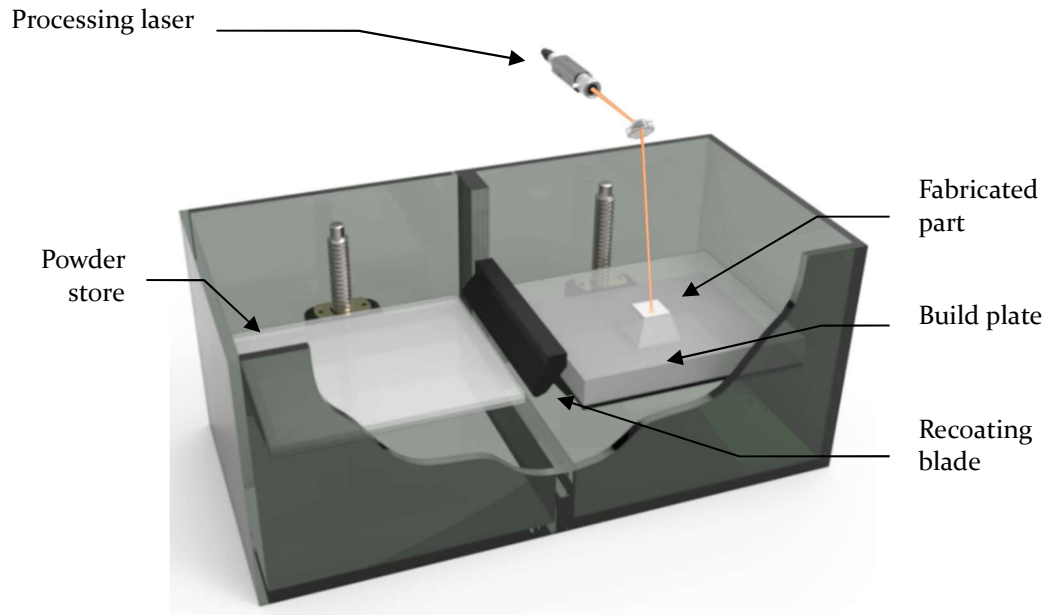


Figure 2-3 – Illustration of a typical PBF system showing a pyramid geometry being fabricated

SLM has been used within ceramic AM to directly process ceramic materials. Direct processing of advanced ceramic materials streamlines the supply and manufacturing chains by reducing the need to develop binder materials, resulting in lower simpler manufacturing process chains. SLM has been demonstrated with ceramic materials including alumina [100], zirconia [101], Silica, silicon carbide, aluminium titanate (Al_2TiO_5) and zirconium silicate (ZrSiO_4) [96], [102], [103].

Wilkes *et al.* initial investigations focused on the use of powders consisting entirely of alumina and entirely of zirconia, though issues relating to crack formation and coarse microstructures resulted in the use of 58.5 wt% Alumina and 41.5wt% zirconia. Feedstocks composed of 20 – 70 μm particles with irregular and spherical morphologies were used to fabricate parts by preheating a 20 \times 30 mm area of the powder bed using a 1,000W CO_2 laser, whilst melting of the ceramic powder was achieved using a 150W Nd: YAG-laser. The high melting temperatures of advance ceramic materials results in the heating of an entire build volume impractical, with systems often using a laser preheat instead. Preheating the material from ambient room temperature to 1,800°C revealed that heating to at least 1,600°C was necessary to avoid crack formation. The authors note that crack free specimens with a volume up to $\sim 400\text{mm}^3$ can

be fabricated, although larger parts exhibit cracks due to stresses caused by the deposition of cold powder onto the part. Parts fabricated from powders with an irregular morphology contained porosity, whereas parts fabricated from spherical particles were high density, although specific values are not provided. The additional heat required to prevent cracking of the part caused larger melt pools, resulting in an increase in surface roughness [103].

The processability of ceramic materials using SLM is dependent on the absorption of the laser radiation to cause localised heating of the material. Scattering and reflection of the incident radiation causing non-uniform heating and inefficiencies with alumina-based materials absorbing less than 10% of laser energy at wavelengths around 1000 nm [104]. Non-uniform heating of the material is exacerbated by the formation of grain boundaries and other defects, which have higher laser absorption coefficients, resulting additional residual stresses.

Juste *et al.* incorporated 0.1 vol% graphite to an alumina powder feedstock to improve the optical coupling between the powder and laser as graphite has a absorption of >90%. Samples measuring 10 × 10 × 10 mm were fabricated using a 200W laser, with sintered parts densities between 92.9 - 97.5%. However, all of the samples fabricated using these processing parameters exhibited distortion in the Z direction due to the melting and subsequent solidification of the alumina feedstock.

Indirect PBF techniques such as SLS use powder feedstocks that contain the ceramic material and a low melting point binder, which is used to fabricate a green state part [105]. The secondary material can be either organic, such as polymers and waxes [106], [107] or inorganic such as low-melting point metals and glasses [108].

Liu *et al.* combined alumina powder with a particle size of 0.4 µm with stearic acid to create a feedstock consisting of 50 vol% stearic acid. The fabrication of the green part occurred in a build chamber that was held at 60°C as the melting temperature of stearic acid is 67 - 69°C, using layer thicknesses of 100-200 µm. The green parts had a post-fabrication density of 45-49%, which corresponds to

a sintered density of ~88% density and a four-point flexural strength of 255 ± 17 MPa [109].

Deckers et al. fabricated $10 \times 10 \times 10$ mm cubic parts from alumina powder, with a binder content of 53-71 vol% in a build environment held at 75-175°C. The green state parts had measured densities of 37-66%, which resulted in the production of sintered parts with densities of 39-77% undergoing linear shrinkages of 20-31% in the X-Y and 21-44% in the Z [110]. This approach was determined to have a build accuracy of $\pm 250 \mu\text{m}$ [111].

Binder jetting (BJ) fabricates parts from a uniform layer of powder, which is selectively bonded by the deposition of a binder solution. The permeating liquid binder encapsulates the powder feedstock, creating a solid layer after which a new layer of powder is formed; with the process repeating until a green state part is formed.

BJ with ceramic materials was first reported by Sachs *et al.* [112] in 1991 with the production of a 3D ceramic part featuring eight intersecting planes using a powder composed of 0-100 μm alumina/silica spheres. The liquid binder was deposited through a 50 μm glass nozzle into a powder bed with a layer thickness of ~100 μm . However, the author does not state whether the fabricated part was sintered, although it is likely to have resulted in porous parts due to the packing density of the powder bed.

BJ systems can be configured to dispense either an organic glue [113] or an agent that reacts with a polymer component of the feedstock [114]. A typical binder jet setup features a print head, which is similar to an inkjet printer head used within document printing. The build plate, powder store and layer recoating mechanism are similar to those used within SLS processes, although heating of the build area is not required due to the solidification mechanisms of the binder. Figure 2-4 illustrates a typical BJ setup.

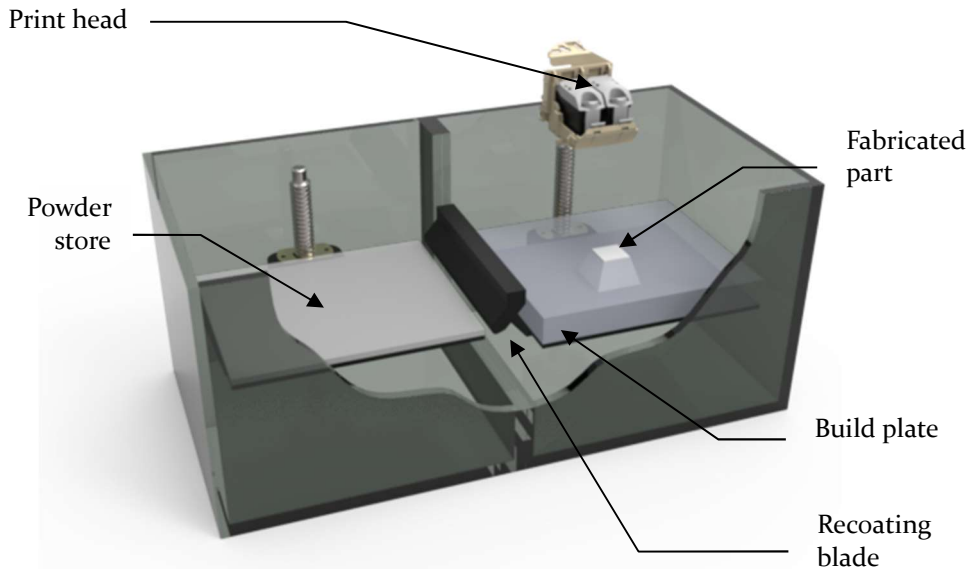


Figure 2-4 – Illustration of a typical binder jetting setup with a pyramid geometry being fabricated

Hotta et al. fabricated components from an alumina powder with an average particle size of $\sim 60 \mu\text{m}$ containing 4.2 vol% organic water-soluble binder and a layer thickness of $500 \mu\text{m}$. The fabrication process selectively spraying water onto the powder bed to dissolve the water-soluble binder, which was dried for 10 minutes before the build platform descended and a new powder layer formed. The fabricated part had a thickness of 5 mm with a green state density of 45% and a sintered density of 48%. The porosity of the sintered part is attributed to the large spaces between particles preventing sufficient material diffusion between adjacent particles [115].

The absence of heat to enable the diffusion of material during the BJ forming process results in no residual stresses within the part, preventing distortion and cracking of the green state part. The deposition of binder decouples the effects of thermal coefficients and refractive indexes that are problematic during PBF and VP processes, enabling the processing of materials such as alumina without the use of absorption additives. BJ processes use layer thicknesses that range from $50 - 500 \mu\text{m}$ [116], [117] resulting in parts with minimum feature sizes of $350 - 500 \mu\text{m}$ [118], [119]. However, fabricated green parts often exhibit poor mechanical strength, which can be problematic during the removal of the part from the powder bed and subsequent post processing. The low sintered parts

typically have densities of 22.5 - 73% [120], which adversely affects the mechanical strength, with alumina parts demonstrating flexural strengths of 3 - 32.8% bulk strength [120].

The complex ejection and droplet formation dynamics are affected by the rheological properties of the binding agent, requiring variable droplet deposition rates to account for the acceleration and deceleration of the printhead. The impaction and penetration characteristics of the binder causes considerable complexity due to the number of interdependent variables such as powder morphology, binder viscosity and surface tension [121]. The binder needs to penetrate to a sufficient depth to ensure adhesion with the previous layer, which is a result of capillary effect. Capillary forces are complex and often uncontrollable particularly when using powders that may contain inhomogeneities [122]–[124].

Despite the problems relating to individual processes, a fundamental challenge with powder-based ceramic AM processes is the insufficient density of the green and sintered components due to the challenges associated with processing dry powder feedstocks. Parts fabricated from alumina typically exhibit green state densities of 21 - 50% [83], [125] with post sintered parts having densities of between 39 - 96% [83], [110], [115], [126]–[129]. This corresponds to a flexural strength of between 12 - 131 MPa, which is 3 - 32.8% of the flexural strength of bulk alumina [129]–[131]. The high porosity is a result of the low packing density of the powder bed and feedstock flowability, which is affected by particle size distribution, particle morphology and the formation of agglomerates that cause large inter-agglomerate pores [132]. Furthermore, the mechanism of sintering relies on the capillary forces between adjacent particles resulting in insufficient diffusion of material to form high density parts [92]. Therefore, Parts fabricated using powder-based processes cannot be used within applications requiring high-density, low surface roughness parts [102], [125], [133]–[136].

A number of approaches have been attempted to increase the packing density, stability and flowability of the powder bed to increase the density of fabricated parts. Compression rollers that apply a vertical compaction force in addition to

the lateral spreading motion have been investigated as a means of increasing powder bed density. The authors state that an increase in packing density was achieved, although little quantitative discussion is provided regarding the effectiveness of this approach [92], [134]. Misting the powder bed with water was undertaken as a method of reducing shear stresses during layer recoating to enable the production of thinner layers whilst improving the stability of the powder bed, particularly when using fine powders. The water forms a liquid bridge between adjacent particles, meaning the particles are able to slip past one another with reduced friction, enabling layer thicknesses of 44 μm to be reliably produced, with the authors noting the improved manufacturing resolution and reduced surface roughness, although specific values are omitted [137]. Material flowability is noted as being a particular challenge, particularly for feedstocks composed of powder particles $<20 \mu\text{m}$. Several approaches have been investigated in an attempt to improve the flowability of these powders including the use of plasma treatment [138], lubricants [139] and the formation of ceramic slurries [140].

Gahler *et al.* demonstrated the fabrication of ceramic parts using aqueous slurries containing between 63 ($\text{Al}_2\text{O}_3\text{-SiO}_2$ mixtures) and 87 wt% (pure Al_2O_3) yielding parts with densities of between 86% and 92% TD resulting in samples of up to 90% density post sintering. These approaches provided an incremental increase in the packing density of the powder bed, although packing density remains insufficient to enable the fabrication of full density ceramic parts. Furthermore, the additives and treatments to improve flowability can have a detrimental effect on the process resolution due to the modification of the interaction between the feedstock and binding mechanism.

Alternatively, post-processing of the green-state parts using secondary manufacturing operations such as Cold Isostatic Pressing (CIP) [141], Warm Isostatic Pressing (WIP) [142], quasi isostatic (QIP), infiltration [130], [143] remelting and infiltration [144], [145] have also been investigated. Deckers *et al.* investigated the use of CIP, QIP and WIP on $10 \times 10 \times 10 \text{ mm}$ Alumina cubes. The pressing processes resulted in a decrease in porosity within the green state parts by 42%, 54% and 29% respectively, resulting in sintered densities of 64%,

88% and 83%. Atmospheric, pressure and vacuum infiltration were also investigated by infiltrating the parts with an Al_2O_3 solution of between 30 - 40 vol%. Pressure and vacuum infiltration were noted as causing a more appreciable reduction in porosity compared to atmospheric infiltration. However, a combination of infiltration followed by WIP was found to cause the largest reduction in porosity, producing crack and defect free sintered geometries with densities of up to 88% [110]. Alternatively, Yoo et al. used a modified press-rolling technique to produce the components from pure submicron alumina powders. The alumina powders formed agglomerates ranging from 75-150 μm , resulting in parts with an as-printed density of between 33 - 36%. Components fabricated from a binder containing 6wt% binder resulted in as printed densities of 36%. CIP resulted in the density increasing to 54% with a sintered density of 95.9%. WIP at 80°C resulted in the density increasing to 56% with a sintered density of 97.8%. Doping the samples with MgO to inhibit grain growth during sintering resulted in an as-printed density of 34% which increased to 61% following WIP at 80°C. The sintered components underwent linear shrinkages of 22.2 - 31.2% but exhibited a density of 99.2% with a flexural strength of 324 MPa.

Despite increasing the density of the sintered components, the additional post processing further complicated the manufacturing process and introduces additional constraints such as high shrinkages, which have been shown to be detrimental. Isostatic pressing cause additional shrinkage whilst potentially causing cracking of the part. Liu demonstrated the fabrication of Al_2O_3 components with densities of between 31% and 34%. CIP at 50 MPa and 35 MPa increased to 40% and 54% respectively. However, the increasing pressure resulted in linear shrinkage of the green components of between 2.5 - 5% at 50 MPa and 14 - 17% at 335 MPa. This resulted in sintered components with densities of 92% whilst undergoing an additional shrinkage of between 28.3 - 32.5% [146].

2.1.3 Material Extrusion

Material extrusion (ME) ceramic AM processes continuously extrude a liquid feedstock containing ceramic material through a nozzle to form a bead of material. The translation of the nozzle forms the layer cross-section by producing an outline geometry that is filled using a predetermined infill pattern. The process repeats in a layerwise manner until the 3D geometry is formed. Ceramic ME feedstocks include thermoplastic filaments containing ceramic material [147], ceramic slurries [148] and sol-gels containing ceramic powder [149]. The liquid feedstocks are required to exhibit pseudoplastic behaviour to ensure that the material can be extruded without forming a large backpressure. Ceramic ME feedstocks contain similar volume loading of ceramic to those used by conventional manufacturing processes, which typically contain between 45-70 vol% ceramic [150]–[152].

Ceramic ME was first used to fabricate parts using thermoplastic filament feedstocks containing ceramic material was first demonstrated by Danforth in 1995, terming the process Fused Deposition of Ceramic (FDC) [153]. The filaments were produced using a binder specifically designed for ceramic AM containing between 50-65 vol% silicon nitride and alumina materials, which were processed using a commercial FDM system (3D modeler™, Stratasys, Inc., USA). Filaments have since been produced containing ceramic materials such as Tungsten Carbide, PZT [154], Silicon dioxide and silicon nitride [155]. Unlike polymer ME processes, the ceramic thermoplastic filaments are less flexible, which prevents a continuous supply of material, due to the filament breaking. The fabricated parts showed no signs of delamination with sintered densities of >95%.

A number of ceramic ME processes have been developed, demonstrating a range of extrusion and solidification mechanisms. Ceramic ME processes typically consists of an extrusion mechanism, build plate, feedstock delivery system and nozzle. Figure 2-5 shows a typical configuration of a ceramic ME system using a filament feedstock, which also acts as the plunger mechanism. Slurry-based

feedstocks are typically extruded using a plunger or screw-based extrusion system [156].

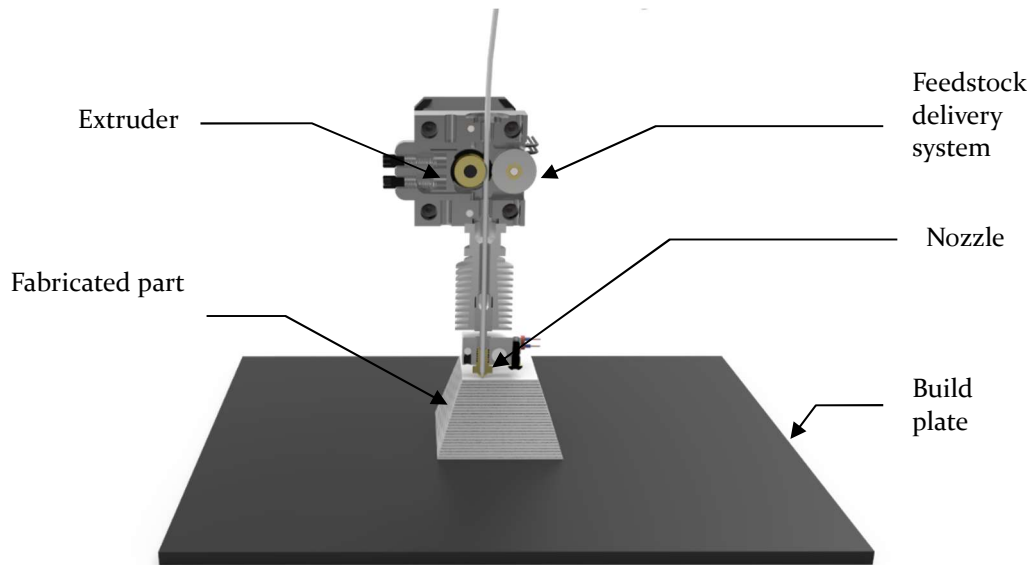


Figure 2-5 – Schematic of a direct drive ME using a filament feedstock

2.1.3.1 Filament-based feedstock

Filament based feedstocks have been investigated by a number of researchers such as Griffin and McMillin who demonstrated the fabrication of a gear, pyramid and C-shaped part using filaments containing between 45-55% Alumina. The filaments had a diameter of 0.070" (1.778 mm) and were between 6 and 8" long, due to the poor flexibility of the filament preventing the material being spooled on a reel. Post sintering the alumina parts were determined to have sintered densities of between 96.2 and 97.6 %TD [157]. Agarwala demonstrated the production of silicon nitride parts defect containing parts exhibiting green densities of between 85-90%. Defects such as sub-perimeter voids are caused by incomplete filling of areas within the perimeter whilst Inter-road voids are a result of inconsistent material flow during the extrusion process [158]. Optimisation of the extrusion process plus defect removal strategies enable the production of green parts with densities >96%. Post sintering, the defective parts had densities of <95% having undergone a linear shrinkage of between 12-15% in X – Y and between 17-20% in Z. The defect free parts had densities >98% having undergone 15.3-17.9% shrinkage in X – Y and between 17.7 – 20.9 % in Z [159]. However, the use of filament feedstocks has a number

of processing challenges relating to material formulation, debinding and manufacturing defects. The high loading of ceramic material within the filament often results in poor flexibility causing the filament to break, which interrupts the material flow, leading to voids and porosity. Furthermore, the production of the ceramic filament requires several manufacturing stages whilst maintaining a <2% variation in filament diameter [160]–[162]. Inconsistencies in the filament diameter results in variations in material flow rate that can lead to voids and excess material deposits, which reduce the density and tolerance of the manufactured part. Moreover, ME based processes have the potential to fabricate multi-material and functionally graded components by dynamically changing the feedstock feed. However, filament ME processes often lack the control to achieve the dynamic transition between materials to create functionally graded parts, although multi-material parts are possible to produce, particularly if multiple extrusion systems are available [163]. Debinding and sintering of the fabricated parts is both difficult and time consuming due to the high volume of binder within the filament, often resulting in severe warping and cracking [164].

2.1.3.2 Slurry-based feedstock

Alternatively, a slurry-based process termed “Robocasting” (RC) was developed and patented by Cesarano at the Sandia National Laboratories in 1997 [34], [165]. The feedstocks contained 50-65 vol% ceramic material, which were formulated from alumina powder with an average particle size of 2.2 μm . RC relies on the rheological properties of the feedstock and partial evaporation of the solvent to retain the deposited shape [166]. The process was used to fabricate a hollow part consisting of 20 layers, which had a post sintered density of 96% with no signs of delamination or cracking.

Consequently, slurry-based feedstocks are more prevalent within the ME ceramic AM processes due to the diverse range of hardware configurations and versatility of slurry feedstocks. Furthermore, Slurry feedstocks are extensively used within conventional ceramics manufacturing, with AM slurry feedstocks

containing binder contents of <10 wt% binder compared to >30 wt% for thermoplastic feedstocks [167].

Denham, Cesarano and King demonstrated the fabrication of alumina bars using RC of a slurry feedstock composed of 60 vol% alumina with an average particle size of 2.4 μm , through an 834 μm nozzle onto a build plate held at a temperature of 40°C. The parts were determined to have an average green density of 68.4% compared to parts produced using uniaxial pressing, isostatic pressing and slip casting, which had green densities of 64.5%, 69.3% and 71.3% respectively. Post sintering the RC samples had a density of 93.7% with the conventional processes achieving 93.4%, 95.2% and 93.0% respectively. The slip cast samples had an average flexural strength of 309.80 MPa. Flexural testing of the RC samples highlighted the variation in mechanical properties based on the direction of the infill. Bars that had infill running lengthways had an average flexural strength of 302.82 MPa whereas parts with infill running widthways had an average flexural strength of 242.07, which represents ~20% difference [168]. Slurry-based processes have also been shown to process multiple materials through a single nozzle to functionally grade a part. Cesarano demonstrated the use of up to 4 material feeds that were extruded through a single nozzle to produce multi-material and functionally graded parts. A kaolin slurry feedstock was used in conjunction with a fugitive, sacrificial material to produce a 90° overhanging structure [166]. Leu *et al.* demonstrate the production of parts featuring discrete and graded layer compositions from alumina and zirconia slurries using a triple extrusion mechanism [169].

Despite the high densities, low shrinkages and capability to produce multi-material and functionally graded parts, slurry-based AM processes have a number of limitations compared to filament-based ME processes. This is primarily due to the separation and sedimentation of particles during high stress and convergent flow and whilst stationary [170]. This can result in a non-uniform distribution of material throughout the fabricated parts, resulting in anisotropic shrinkage and porosity hotspots. Air entrapment during the formulation of the ceramic feedstock is a particular challenge as it can be difficult to completely remove, but will reduce the density and strength of the

fabricated parts [162]. The evaporation of volatile solvents post deposition to form a dilatant mass is an important stage during the fabrication of components. However, controlling this transition is challenging as faster evaporation rates can result in the cracking of the part whilst slower rates can result in slumping and deformation of the deposited material. Furthermore, non-uniform evaporation can cause residual stresses within the part that can lead to cracking and warping of the fabricated part, subsequently affecting the scalability of the process [168].

A number of approaches have been investigated to overcome the challenges relating to uncontrolled drying of the material during fabrication. Ghazanfaril *et al.* developed a screw-based extrusion process where an aqueous paste containing >50 vol% ceramic and 1-4 vol% organic additives is deposited onto a substrate inside a watertight tank. The tank is filled with a dissimilar fluid, typically oil, which is maintained just below the topmost layer. Infrared radiation is then used to uniformly dry the deposited layer, preventing distortion and cracking of the part. This process has been used to fabricate parts from alumina, zirconium diboride, boron carbide and zirconium carbide with sintered densities >98%TD with measured shrinkages of between 15 - 18.1% [171], [172]. Despite providing greater control over the drying process, the need to use a tank containing a secondary fluid may adversely affect the scalability of the process due to the size of the tank and volume of secondary fluid required to fabricate part. Furthermore, the immersion of the part in a secondary fluid will require additional washing prior to debinding and sintering whilst potentially impeding the compatibility of the process with secondary materials.

Huang *et al.* demonstrated the production of alumina parts using aqueous pastes containing 50 vol% alumina with an average particle size of 0.4 μm . The material is deposited into a build environment that is maintained at -20°C using a ram extruder with a 580 μm nozzle, fabricating parts using a layer height of 500 μm . The green parts had a density of 50% with a sintered density of 98% TD. The parts had a surface roughness of between 100-200 μm with a 4-pt flexural strength of 219 MPa and 198 MPa for samples with infill running lengthways and widthways respectively [173]. However, the use of freeze-drying

potentially introduces additional defects and porosity attributable to dendrite formation in the freezing binder [174], [175].

Slurries formulated using photopolymerizable elements have also been investigated as a means of overcoming the challenges with non-uniform drying. Stuffle *et al.* demonstrated the fabrication of acrylic based pastes containing 53 vol% Al₂O₃ – 0.5wt% MgO. The material was deposited through a 330 µm nozzle onto a heated bed that was held at 120°C. The green components were determined to have a green density of ~60% with sintered parts having densities between 90-99% [176]. The author provides no discussion of manufacturing resolution, although shrinkage and deformation can occur during the polymerisation of the photocurable elements.

An overarching challenge of ME processes is the large manufacturing tolerances, high surface roughness and frequency of defects during the manufacture. ME processes typically have the largest manufacturing tolerances and minimum feature size of ceramic AM processes. This is due to the minimum nozzle diameter required to process slurry feedstocks, which need to be between 10-200 times the average particle size [177]. The suitability of different nozzle sizes is further compounded by the rheological characteristics of the feedstock and the effect of the nozzle size and profile on shear forces during extrusion, often results in parts with features ±400 µm [178]–[180].

2.1.4 Sheet Lamination

Sheet lamination (SL), also known as Laminated Object Manufacture (LOM) is a process in which sheets of material are bonded together to form an object. Sheet lamination processes are extensively used within electronics manufacturing to fabricate ceramic multilayer circuits [181] and passive components such as capacitors [182]. This approach has been used since the 1960s but unlike ceramic AM derivatives, this approach is reliant on template and tooling-based production methods such as pressing and stamping. LOM can be subdivided into traditional LOM and Computer-Aided Manufacturing of Laminated Engineering Materials (CAM-LEM). CAM-LEM has its roots in the fabrication of multi-layer ceramic substrates for microelectronic packaging

[183]. Traditional LOM consists of a roll of tape cast ceramic material onto which the outline of the layer is cut using a CO₂ laser. A heated roller moves across the part activating the adhesive deposited on the ceramic sheet, affixing it to the previous layer [184]. The unused material is cut into blocks to aid removal from the part after fabrication. Alternatively, CAM-LEM uses a similar approach but instead of “stack then cut” approach, the material is pre-cut then robotically stacked, using a “cut then stack” process. Once the green component has been produced, it is thermally processed to remove the binder material and sinter the remaining ceramic.

The configurations of LOM and CAM-LEM differ due to the different strategies used to cut and stack layers. Traditional LOM setups, depicted in Figure 2-6 typically have a roll or mechanism to create entire layers that is adhered using the heated roller then cut with the processing laser. Alternatively, a CAM-LEM system features multiple stations within an enclosed workstation with automated transfer between stations. The workstations include a material store for the sheet feedstock, a cutting station and assembly station with a heated roller to activate the adhesive on the feedstock.

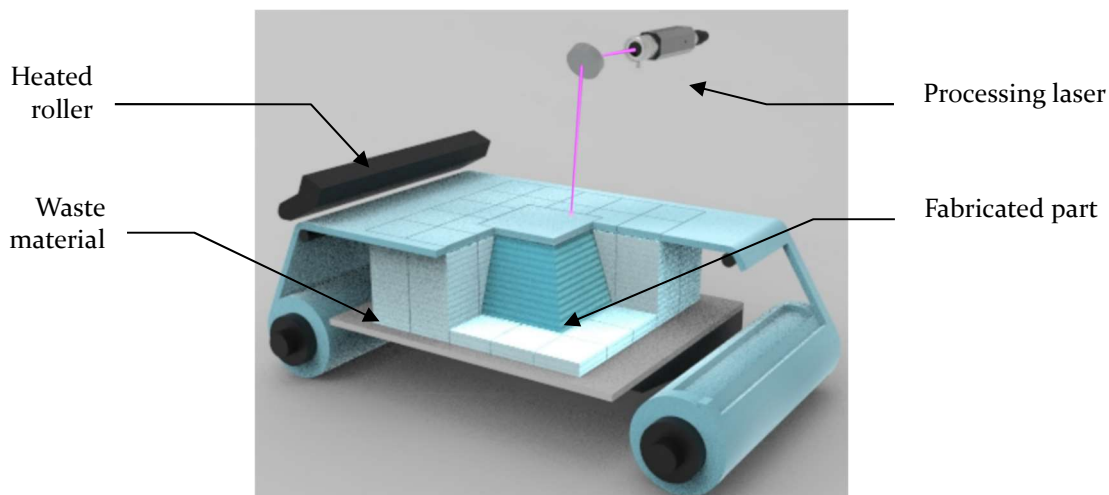


Figure 2-6 – Illustration of a typical LOM system using a “Stack then cut” approach

LOM feedstock comprises a ceramic material within a polymer matrix that has been tape cast into a sheet that has been covered with a thermally activated adhesive. Critical factors affecting the performance of the feedstock include the suitability of the tape for laser cutting, development of an efficient tacking mechanism, post assembly lamination to create a monolithic part, preservation

of dimensions during firing [185]. The ceramic tapes are typically between 150 – 700 μm thick containing ~55 vol% ceramic with a particle size distribution of between 0.5 - 60 μm [186]–[189]. LOM and CAM-LEM processes have been shown to fabricate components from Alumina [190], Zirconia [191], [192], Silicon Nitride [193], [194] PZT [195] and silicon carbide [196], [197].

Zhang *et al.* demonstrated the fabrication of alumina components using 760 μm thick tape cast sheets containing 7 wt% binder with an average particle size of 2 μm . The green components were determined to have a green density of 65.4% and a sintered density of 97.1% undergoing a measured linear shrinkage of 34% in the X – Y plane and 8% in the Z (build) direction. Evaluation of flexural strength using 3-pt bending resulted in an average strength of 145 MPa when the load was applied parallel to the layers and 228 MPa when the load was applied perpendicular to the layers [186]. These results are consistent with other examples that have shown anisotropic properties with linear shrinkages of between 17 – 25% and sintered densities of up to 98.16% [193], [198]

A benefit of this approach is that the production of the ceramic sheets is separate to the fabrication of the component, minimising the inclusion of defects associated with individual layers [199]. The stacking of discrete layers using the CAM-LEM process enables the creation of multi-material parts by combining two or more different tapes [192]. Whilst classified as an AM process, SL processes generate more waste compared to other ceramic AM processes, which increases cost and diminishes some of the benefits of AM such as reduced material waste. Furthermore, functionally grading material compositions by dynamically transitioning between materials is not possible with SL processes. A more discernible limitation of SL however, is the fundamental manufacturing challenges persist that restrict geometric freedoms and resolution. The encapsulation of the fabricated part during traditional LOM process makes part removal difficult, often causing the parts to exhibit rough surface finishes with poor dimensional accuracy, typically around 250 μm [200]. This has several implications for the creation of hollow structures or fine features such as thin channels [196], [201], [202]. A more considerable challenge occurs during the debinding and densification stages of production. The pyrolytic decomposition

of the binder and subsequent degassing can result in bloating of the part causing density gradients, delamination, anisotropic material properties [203]. To counteract this and the relaxation of residual stresses, the pressure is applied to the thermal processing, which can limit geometric design freedoms and result in damage to the part [204].

2.2 Process comparison

The production of ceramic components using ceramic AM processes has been demonstrated using both direct and indirect techniques. Despite this, direct manufacturing approaches have a number of ongoing challenges relating to the density, surface finish and integrity of fabricated parts plus processing challenges due to the high temperatures required to directly process ceramic materials. Consequently, indirect AM approaches have been pursued, with a number of commercial vendors supply AM systems and materials for the production of ceramic components. Table 2-1 shows the different indirect ceramic AM processes and the materials that have been processed to fabricate ceramic parts and the maximum density that has been achieved. A list of commercial vendors is also provided, with VP, PBF and BJ having the some of the most prominent ceramic AM vendors.

Table 2-1 – Summary of the Ceramic AM categories, the materials and densities that have been demonstrated plus a rating of the process’s multi-material compatibility[205], [206]

	Material	Maximum reported density	Commercial systems
VP	Al ₂ O ₃ , ZrO ₂ , Si ₃ N ₄ , SiO ₂ TiO ₃ , SiC (PDC),	99.3%	Lithoz 3DCeram Admatec Prodways Tethon
MJ	Al ₂ O ₃ , ZrO ₂	N/A	Xjet
PBF	Al ₂ O ₃ , ZrO ₂ , Si ₃ N ₄ , SiO ₂ , ZrB ₂ BaTiO ₃ , SiC (PDC), SiSiC, PZT	85% (SLM) 80% (SLS)	3D Systems
BJ	Al ₂ O ₃ , ZrO ₂ (Beta), SiC (Beta) B ₄ C (Beta)	76%	VoxelJet ExOne ComeTrue M10
ME	Al ₂ O ₃ , ZrO ₂ , Si ₃ N ₄ , ZrB ₂ , SiC, ZrC, BaTiO ₃ , PZT, PMN, ITO	>98%	3D-figo Aim3D WASP
SL	Al ₂ O ₃ , ZrO ₂ , Si ₃ N ₄ , SiO ₂ , PZT	98.16%	CAM-LEM

Despite the number of commercial ceramic AM systems, the uptake of ceramic AM within commercial manufacturing chains has been limited to a small number of companies serving specific markets [207]. The disruptive potential of AM technology has yet to be realised due to challenges relating to combinations of high shrinkages, density, part integrity, manufacturing tolerances, scalability, processable materials, multi-material compatibility and minimum feature size [34]. These challenges typically occur as a result of AM feedstock formulations and the process-specific requirements that have limited affinity with conventional feedstocks. This results in incompatibilities between conventional front and backend processes with parts fabricated using ceramic AM, making the integration of AM processes expensive with a number of incompatibilities.

Ceramic AM seeks to overcome some of the design limitations associated with template-based production, enabling economic small batch production and mass customisation. However, ceramic AM is not without design constraints due to factors such as support structures and distortion and cracking caused by anisotropic shrinkages. Feilden provides an assessment of ceramic AM processes for the production of filled, spanning, overhanging, floating and closed cavity geometries. Figure 2-7 shows a graphical summary of the results, which applies exclusively to ceramic AM processes [208].

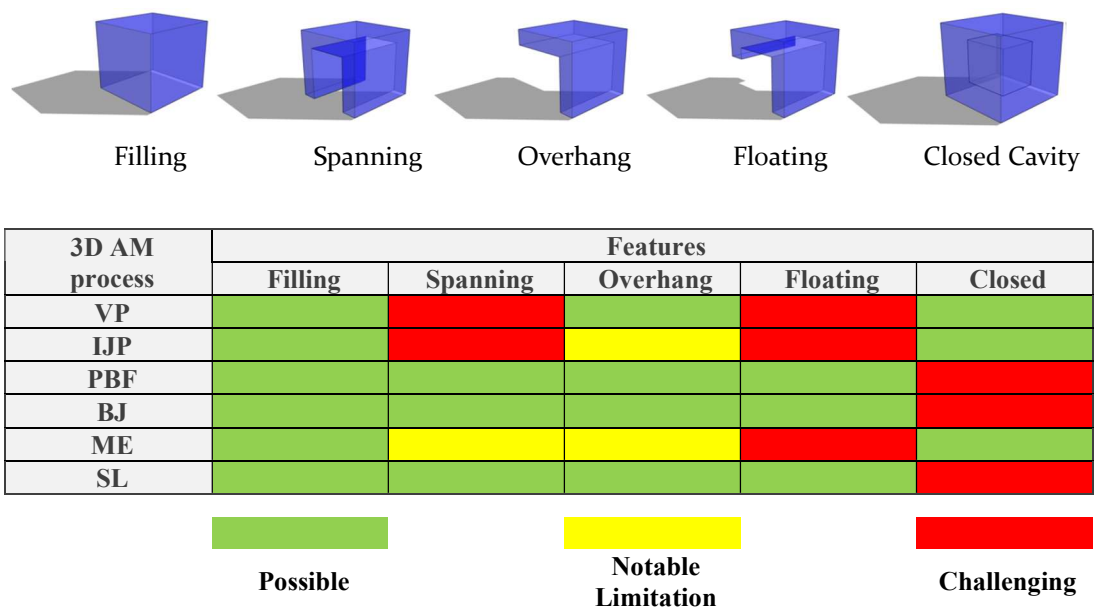


Figure 2-7 - Assessment of the various AM processes at fabricating key geometries from advanced ceramic materials. Adapted from [208]

Based on this evaluation, PBF, BJ and SL have the fewest restrictions in terms of the geometries that can be produced, whilst VP, IJP and ME have either notable or challenging limitations. This evaluation shows that all ceramic AM processes are capable of fabricating filled geometries, although this evaluation is independent of the density of the fabricated component. As previously discussed, PBF and BJ processes cannot produce parts of a sufficient density to be used within structural, engineering applications. The inclusion of additional processing such as isostatic pressing and infiltration has been shown to increase the density of fabricated parts, although these processes increase the complexity of the manufacturing process and cause further design restrictions due to shrinkage and low green part strength. Whilst SL is capable of achieving the required density for structural engineering applications, the resolution of the parts is limited by the minimum layer thickness of the sheets and stacking resolution of the process. Furthermore, the anisotropic shrinkage of parts often causes warping and cracking during thermal processing, imposing a number of design limitations. The challenges relating to the production of spanning, overhanging and floating geometries using VP, IJP and ME are a result of cracking and distortion during thermal processing. For VP and IJP this is due to the large anisotropic shrinkages as a result of the limited solid loading within the feedstock. The limitations of ME arise from the need to use support structures, which cannot be created using the process feedstock. Despite this, VP and ME ceramic AM processes are capable of producing parts with sufficient green and sintered densities to be used within end-user applications. VP processes have demonstrated the production of parts with the smallest manufacturing tolerance and features size with the lowest surface roughness. However, retention of suitable feedstock rheological characteristics places significant restrictions on the volume of ceramic material that can be loaded within the photocurable monomer. Consequently, these processes have some of the highest shrinkages of up to 35%, which restricts the size of parts that can be fabricated owing to the probability of cracking and deformation of the part. Moreover, the hardware configurations of SL setups further limit the size of parts that can be fabricated due to spreading and diffraction of the polymerising

radiation. ME processes offer the most versatile and scalable hardware configurations, whilst enabling the use of feedstocks with closest affinity to conventional feedstocks. ME processes are not constrained by the restrictive build environments required for processes such as VP and PBF. Slurry-based ME feedstocks provide greater versatility compare to thermoplastic filaments due to the improved capability to functionally grade parts by dynamically altering the composition of the extruded materials. Moreover, slurry feedstocks often contain a lower volume of binder, thus reducing the debinding and sintering shrinkages whilst overcoming defects caused by inconsistent material flow due to variations in filament diameter and filament breakages. However, parts fabricated using ME processes often have large manufacturing resolutions and high surface roughness compared to other ceramic AM processes. Figure 2-4 shows a summary of the key advantages and disadvantages associated with the various ceramic AM processes.

Table 2-2 – Summary of the advantages and disadvantages of ceramic AM processes [206], [209]–[213]

Process	Advantages	Disadvantages
Vat Photopolymerisation	<ul style="list-style-type: none"> • High resolution • Excellent surface finish • High density parts can be produced • Intricate parts can be produced 	<ul style="list-style-type: none"> • Affected by colour and morphology of the material • Restrictive rheological requirements resulting in high shrinkages • Post-fabrication washing required • Requires support • Limited multi-material compatibility
Inkjet Printing	<ul style="list-style-type: none"> • High accuracy due to thin layers • Good surface finish • Multi-material compatibility • Ability to functionally grade materials 	<ul style="list-style-type: none"> • Post processing may damage fine features • Low volume of dispersed ceramic • Limited to thin layers
Powder Bed Fusion	<ul style="list-style-type: none"> • Geometrically complex parts can be fabricated • Does not require support materials • Nesting of parts within the build volume 	<ul style="list-style-type: none"> • Rough surface finish • High degree of porosity due to the challenges of using dry powders • Expensive machines requiring environmental control •
Binder Jetting	<ul style="list-style-type: none"> • Does not require support structures due to the self- 	<ul style="list-style-type: none"> • Rough appearance • Challenges surrounding the use of dry powders

	supporting nature of the powder	<ul style="list-style-type: none"> • Issue surrounding the infiltration of the deposited binder • High degree of porosity within the fabricated parts
Material Extrusion	<ul style="list-style-type: none"> • High density parts can be produced • Faster fabrication rates by increasing the size of the nozzle • Decouple the effects of colour and morphology on the processing parameters. • functionally graded parts 	<ul style="list-style-type: none"> • Defects are common and often difficult to predict • The large nozzles reduce resolution and increase surface roughness • Requires support structures to produce certain geometries
Sheet Lamination	<ul style="list-style-type: none"> • High build rates can be achieved • Low warping and residual stresses • Functionally graded materials are possible • No support structure is required 	<ul style="list-style-type: none"> • Difficulty removing material from internal cavities (traditional LOM) • Alignment of layers (CAM-LEM) • Potential for warping • Limited resolution due to tape thickness • Potential for delamination

2.3 Process Selection

The extrusion of slurry-based feedstocks represents the most feasible solution with which to produce full density, ceramic parts feature intricate geometries that cannot be produced using conventional manufacturing techniques. Despite the poor manufacturing tolerances compared to other ceramic AM processes, all AM processes have larger manufacturing tolerances compared to conventional manufacturing approaches. Lieneke *et al.* sought to determine the tolerances of AM compared to conventional manufacturing approaches by measuring linear dimensions of samples produced using ME and PBF processes. These processes were classified into the IT-classes that are defined by DIN EN ISO 286-1, whereby a higher IT-class represents coarser tolerances. Appendix B shows the table for determining the IT-classes according to DIN EN ISO 286-1. Figure 2-8 shows the IT classification of the selected AM processes against conventional manufacturing approaches such as casting, milling, drilling and turning.

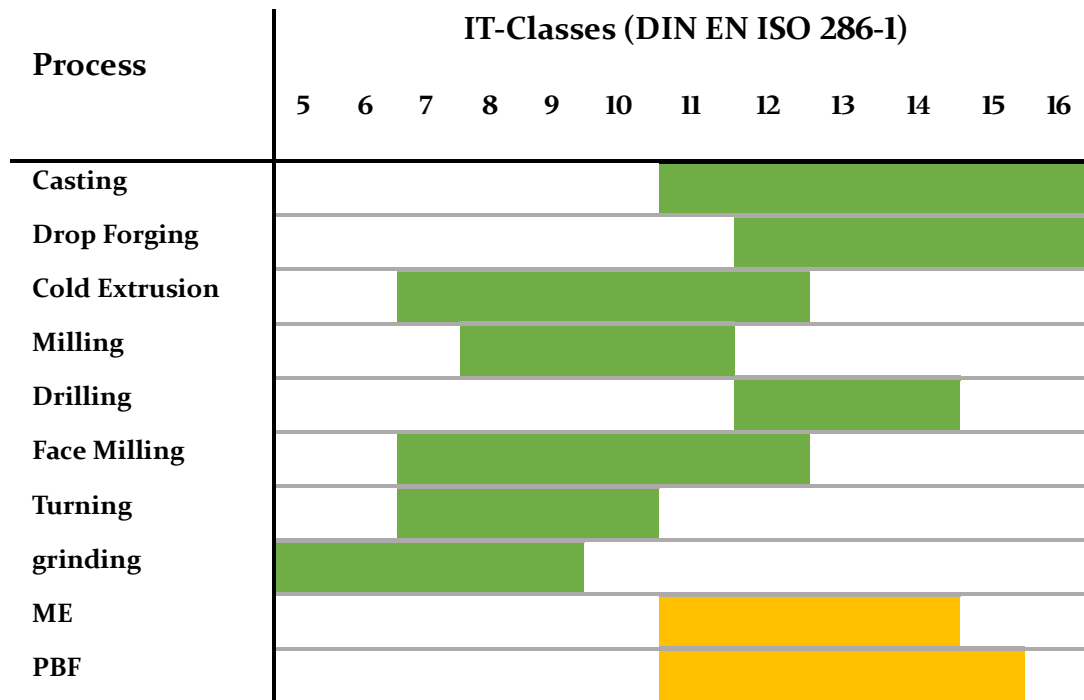


Figure 2-8 –IT-classes for conventional and Additive manufacturing techniques [214]

AM processes have comparable resolution to casting, drop forging, drilling and cutting. Yet, processes such as milling, face milling, turning and planing can achieve finer tolerances, often with lower surface roughness than AM processes.

Machining of preformed, green state ceramic billets is used within conventional ceramic manufacturing to obtain low volume production of high value components. The extrusion of feedstocks derived from conventional feedstock formulations should retain the necessary machining characteristics to enable in-situ machining of the deposited material. Therefore, the integration of conventional machining processes alongside the ceramic AM process will provide the design freedoms and economic small-batch production of AM whilst overcoming the challenges relating to the large manufacturing tolerances and high surface roughness associated with ME processes.

Soares *et al.* demonstrated the used of ME with machining to fabricate gypsum moulds for large scale tooling [215]. The combination of additive and subtractive processes has been shown to achieve an order of magnitude improvement in tolerances and surface finish compared to standalone AM [216]. In addition to reducing the manufacturing tolerances and surface roughness, a subtractive machining capability provides the opportunity for in-situ rework to remove

defects, which have been noted as being a challenge for ME ceramic AM processes. To date, there is a limited number of hybrid manufacturing approaches being used with ceramic materials, none of which have been used to directly fabricate ceramic parts for end user applications [217]. This is due to the complexity of manufacturing advanced ceramic materials that arise due to the multiple manufacturing stages, material compatibility, abrasive nature of ceramic feedstocks and susceptibility to thermal shock. The combination of suitable processing hardware with an appropriate ceramic feedstock should enable the digitally driven, hybrid manufacture of precision 3D ceramic components.

2.4 Thermal Processing post-fabrication

The indirect fabrication of parts from advanced ceramic materials involves multiple processing stages, with the state of the parts being categorised as either green or sintered. Once shaped and formed, the green state ceramic parts are thermally processed to produce the sintered parts with the required material properties. Figure 2-9 shows a simplified visualisation of indirect fabrication of parts using advanced ceramic materials.

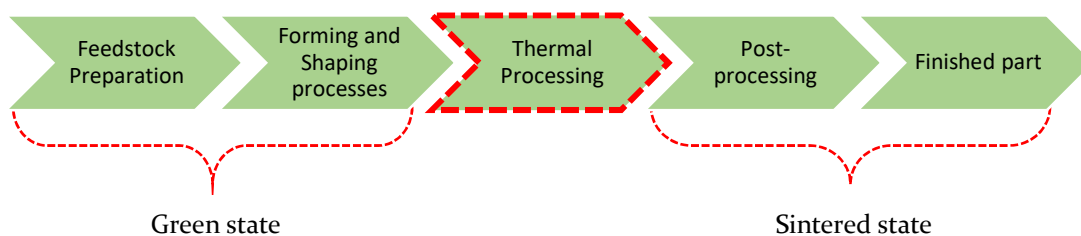


Figure 2-9 – Shows a visualisation of indirect processing of advanced ceramic materials, highlighting the thermal processing that is used to transition from the green state to the fired state.

Thermal processing involves a number of stages including drying, debinding, sintering and densification [218]. The thermal process follows a controlled profile to ensure that the ceramic parts are fully dried, organic binder elements are removed by pyrolytic decomposition and sintering of the non-organic elements such as the ceramic and additives. Within commercial manufacturing of ceramics, thermal processing is often achieved using a tunnel kilns, due to the high throughput that can be achieved compared to chamber furnaces [219].

Tunnel kilns work by transiting a carriage along the tunnel, passing through various temperature zones to control the heating of the part, enabling the continuous loading, and unloading of parts, providing the required throughput capacity for commercial manufacturing. For lower volume production, chamber furnaces, which have an enclosed cavity that is lined with refractory material and heating elements can be used instead. However, chamber furnaces need to complete the entire thermal profile before the processing of a second batch can begin, reducing its overall throughput capacity.

The drying of the green state part prior to debinding and sintering is necessary to avoid differential shrinkages that can cause distortion and warping of the part. Convection drying is the most commonly used method, although radiation drying using microwave or infrared radiation can also be used. Convection drying is often preferred as this can be done in the same tunnel kiln as the other thermal processing steps, using the recovered heat from the cooling zone of the kiln.

The debinding step, also referred to as pre-sinter thermal processing, is done at temperatures well below firing temperatures. Pre-sintering provides additional drying and to vaporise or decompose organic elements and impurities. Pre-sinter thermal processing can be applied in a separate step, referred to as bisque firing, or gradually increasing and holding the temperature in several stages.

The sintering and densification (firing) stage consolidates the ceramic material into a dense, cohesive body with the required material properties required in the final application. The firing profile is dependent on a number of factors such as particle size, firing temperature, time and pressure., sintering requires the green state part to be heated to approximately two-thirds of the melting point of the material in ambient pressure. Sintering and densification results in an inherent degree of shrinkage, which is typically between 16 and 18% [3]. Figure 2-10 shows the recommended thermal profile for the Ag conductor (TC0306A, Heraeus, Germany) used in Chapter 6 for example. The drying process begins by ramping from ambient temperature at 3 °C/min to 100 °C, after which it increases to 450°C at 1°C/min. This pre-sintering stage decomposes the binder material and

prevents thermal shock to the remaining inorganic material. The temperature ramp then increases to 865 °C at 8.0 to 10 °C/min, where it is maintained for 20 to 30 minutes to sinter and densify the ceramic material, after which it is cooled back to ambient conditions at 10 °C/min [220].

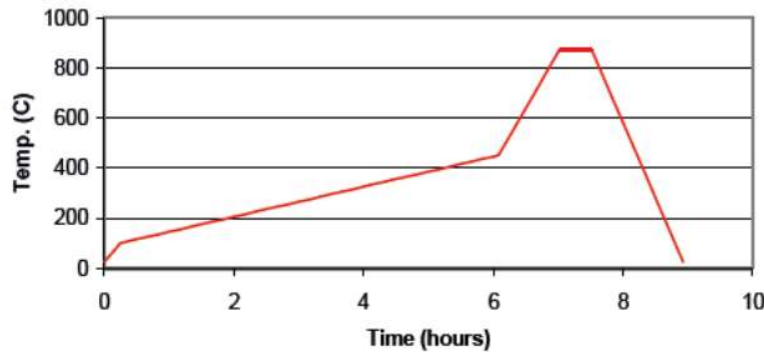


Figure 2-10 – Shows the recommended firing profile for Heraeus TC0306A silver conductor as an example of a thermal profile used to sinter ceramic materials

Throughout this work, the thermal processing of the fabricated ceramic parts was undertaken by Morgan Advanced Materials using a commercial tunnel kiln. The alumina parts that were fabricated during this work were thermally processed alongside conventionally manufactured parts using a thermal profile with a peak temperature exceeds 1,400°C. The thermal processing of other materials used throughout this work, such as the sintering of the Ag conductor, was achieved using a benchtop chamber furnace (RHF 16/3, Carbolite, UK). A tunnel kiln was unsuitable for these processes due to the low volumes and different thermal profile to the alumina substrates. The temperature and heating rate of the chamber furnace is programmed using a multi-segment controller, which was located in the Future Manufacturing Processes Research Laboratory.

3 Process Development

This chapter focuses on the characterisation of the process feedstock, which was used to guide and inform the selection of suitable process hardware. Evaluation of the hardware for the extrusion of the ceramic feedstock, accelerated drying, substrate and sacrificial support plus subtractive machining enabled the creation of the hybrid manufacturing platform. The development and validation of the resultant manufacturing platform are covered in Chapter 4. Details of the fabrication process used for each part shown in this chapter is documented in Appendix C.

3.1 Process flow

The proposed hybrid manufacturing process will be based around a ME process extruding a high viscosity paste. The system will combine a number of additive, subtractive and ancillary elements into a single integrated system. Figure 3-1 shows the envisaged process flow for the hybrid fabrication of 3D ceramic parts.

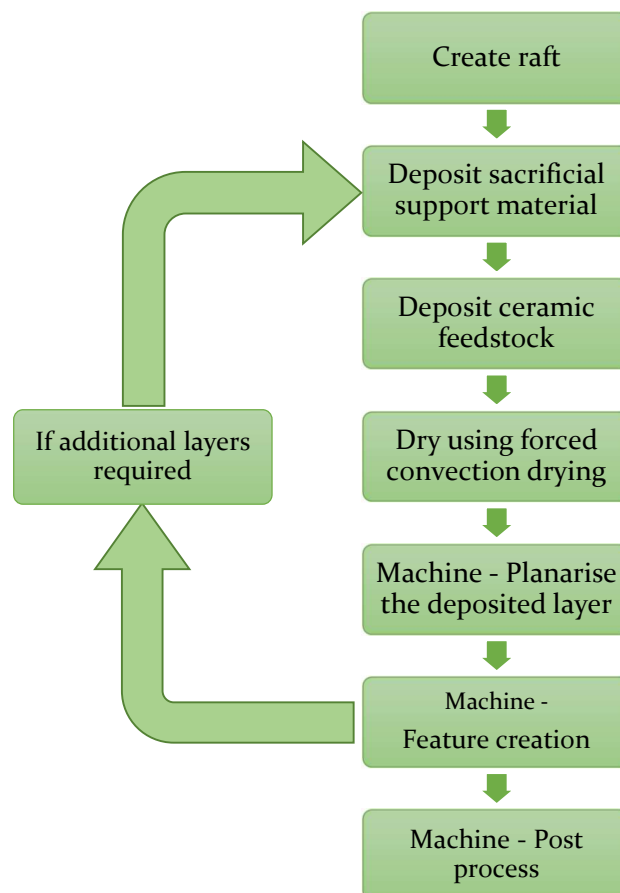


Figure 3-1 – Process flow for the hybrid manufacture of components

The feedstock used throughout the development of the hybrid manufacturing process is derived from a commercial injection moulding formulation, with an increased moisture content, which is a proprietary formulation of Morgan Advanced Materials. The modified feedstock contains 96wt% alumina with an average primary particle size of 2-3 μm and a secondary particle size <30 μm and moisture content of between 18-22 vol%. Additives to improve processability make up the remaining 4 wt%. The extruded ceramic feedstock lacks sufficient strength to create intricate features with overhanging geometries, therefore requiring the use of sacrificial support material. Furthermore, the ceramic feedstock will be reliant on the evaporation of aqueous solvents to form a dilatant mass to retain its shape and withstand further processing. Controlling the rate of evaporation is a key parameter in reducing manufacturing times, without causing defects such as cracking of the fabricated parts. The deposition of material using an ME process can result in beads of material with a domed top surface, leading to porosity within the fabricated parts due to incomplete filling of the voids between adjacent beads of material, as shown by Figure 3-2a. Once the deposited material is sufficiently dry, the subtractive manufacturing process will be used to ensure the uniformity of the layer by using a surface machining operation to planarize the dried layer. The planarizing operation is intended to remove a sufficient amount of material to mitigate any potential porosity within the part. Figure 3-2b illustrates the benefits of implementing interlayer machining of the part to remove the convex top surfaces on the previous layer. This prevents the formation of porosity caused by incomplete filling of voids between adjacent beads.

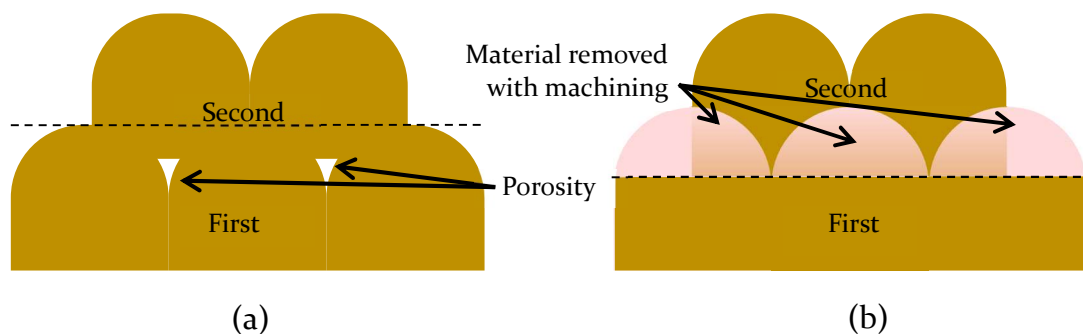


Figure 3-2 – Illustrates the effect of implementing the surface milling operation to remove the convex surface of the deposited tracks to eliminate porosity in the intertrack regions

Subtractive machining will improve the repeatability of the individual layer heights, enabling the creation of fine features with tolerances that are beyond the resolution of the AM elements used in isolation. After the 3D form of the component has been achieved, the machining process will be used to remove “stair – stepping” and other surface defects. Throughout the fabrication process, the machining element will be used for in-situ rework with the removal of defective layers, ensuring the integrity of fabricated parts whilst increasing the manufacturing yield.

3.2 Print materials and characterisation

The modified ceramic feedstock was characterised to ensure suitable rheological behaviour to be extruded using a micro-extrusion system. The feedstock is required to exhibit pseudoplastic behaviour, in which shear stress generated by the nozzle causes a reduction in apparent viscosity, reducing back pressure and enables the use of nozzles down to 150 μm . Once extruded, the shear force will dissipate, causing a rapid increase in viscosity due to the thixotropic response of the material, forming a dilatant mass that retains the extruded profile. The rheological behaviour was characterised, using a parallel plate rheometer (Anton Paar Physica MCR 301, Austria) and a $\text{\O}50$ mm parallel plate with a slope angle of 1° , with the assistance of laboratory technicians at the University of Leeds. Testing was carried out in ambient laboratory conditions, with the rheometer plate maintained at 24°C , as this was deemed to be representative of the intended operating conditions of the manufacturing process. The ceramic material was deposited using a manual syringe, with sufficient quantity to ensure the correct operation when using measurement height of 1.5 mm above the bed. Excess material was removed from the edges of the plate as this may affect the measurements. Depositing the material from a syringe causes a degree of shear thinning to the material prior to testing. Postponing the test to allow the material to undergo shear relaxation and exhibit a similar viscosity to the static material within the syringe, would result in the evaporation some of the solvent. This would cause an increase to the material’s apparent viscosity, preventing the original static viscosity from being obtained.

Therefore, the material was sheared at a rate of 100s^{-1} for 15 seconds prior to the test commencing to homogenise the deposited material and minimise potential variations between tests. The materials rheological response was characterised over a shear range of $100\text{-}1,000\text{s}^{-1}$ for a total time of 315s [221], [222]. Six tests were completed with the averages shown in Figure 3-3. During the test, balling of material along the edge of the shear plate was observed, which may be a result of material drying and its pseudoplastic response. This demonstrates that the modified feedstock has suitable pseudoplastic behaviour, to be extruded using a micro extrusion system without the creation of large back pressures.

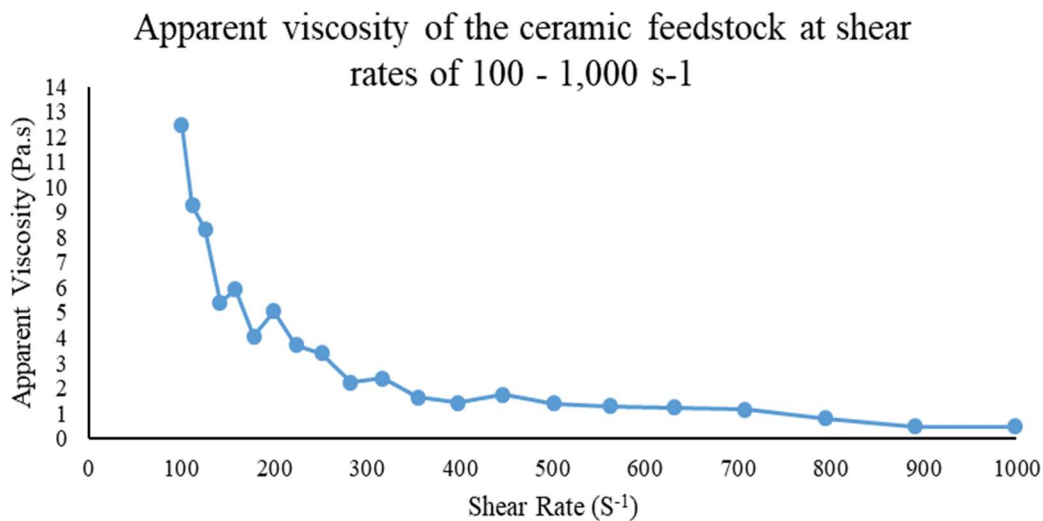


Figure 3-3 – The shear thinning behaviour averaged from 6 samples across a shear range of $100\text{-}1,000\text{s}^{-1}$ using a measurement spacing of 1.5mm

The feedstock is required to demonstrate a thixotropic response once the shear force is removed, causing a rapid increase in apparent viscosity. The material was subjected to a shear of 1 s^{-1} for 10s, which was rapidly increased to $1,000\text{ s}^{-1}$ for a period of 30s after which the shear was reduced to 1 s^{-1} for 300s. Figure 3-4 shows the average plot from 5 tests that were undertaken. Reducing the shear from $1,000\text{ s}^{-1}$ to 1 s^{-1} caused a rapid increase in apparent viscosity from $<1\text{ Pa}\cdot\text{s}$ to $>60\text{ Pa}\cdot\text{s}$ in a 10 s, demonstrating that the material can be used as an AM feedstock.

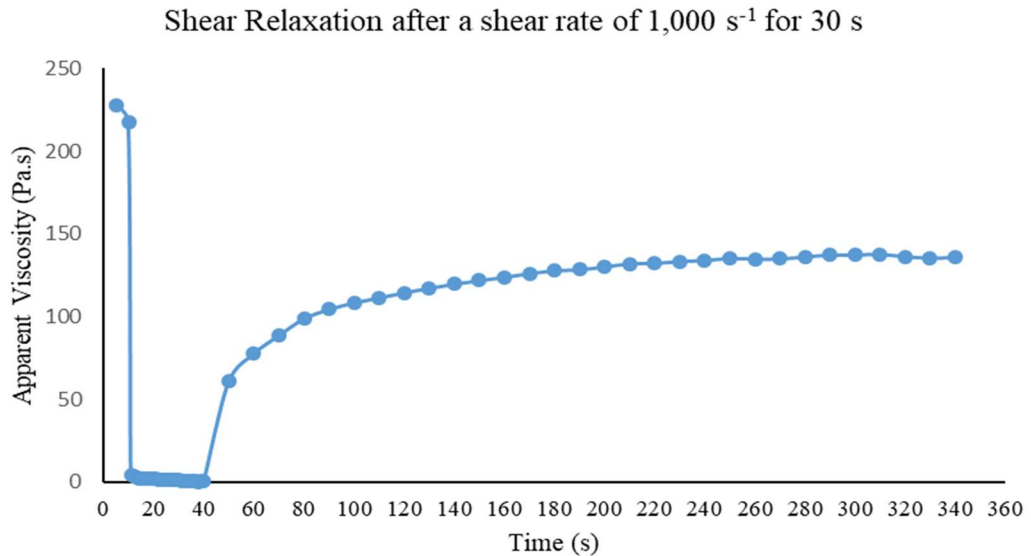


Figure 3-4 – Shows the shear relaxation of the material after applying shear of to $1,000 \text{ s}^{-1}$ for 30s

During these tests, a drier surface layer was formed on the edges that were exposed to the atmosphere. This drier layer rapidly formed on the upper surface of the material when the cone was raised after the testing had finished.

3.3 Extrusion system

The extrusion of high viscosity, pseudoplastic materials containing solid particles is used within a number of conventional manufacturing processes such as solder deposition in the manufacture of electronics. There are numerous systems that can continuously extrude high viscosity materials, broadly classified as either pneumatically or mechanically actuated.

Pneumatically actuated systems are often simpler and use the controlled application of pressure either directly to the material or to a “floating” piston that is in contact with the material. These types of system are capable of achieving faster deposition rates and enable the use of a wide range of material viscosities. However, pneumatic systems are limited by maximum pressure that can be applied by the compressor and hardware pressure ratings [223]. Pneumatically actuated systems are classified as time/pressure dispensing systems, resulting in a delay when initiating and terminating the extrusion process, due to the accumulation and dissipation of pressure within the system [224]. Furthermore, as the material barrel empties the ratio of air to material

changes altering the dispensing characteristics. This is exacerbated by the accumulation of heat from pulsing or extended actuation, which changes the viscosity of the fluids resulting in inconsistent dispensing characteristics.

Mechanically actuated systems use motors and transmission elements to drive a piston, gear or screw mechanisms, which typically provide more control over the extrusion parameters compared to pneumatic systems. The direct drive from mechanical systems circumvents the delay when initiating and terminating the extrusion process. However, mechanically-actuated systems generate larger pressure gradients which can cause significant variation in the shear stress applied to the materials resulting in inconsistent flow [223], [225]. Screw-based mechanisms provide finer spatial control than piston-driven systems and are typically used to extrude higher viscosity materials due to the additional shear-thinning generated by the screw mechanism. However, these mechanisms exacerbate the pressure gradients within the material, resulting in large pressure drops at the nozzle, which can disrupt material flow [223]. Figure 3-5 show a range of extrusion systems including (a) ram extruder, (b) Shutter valve extruder and (c) auger valve.

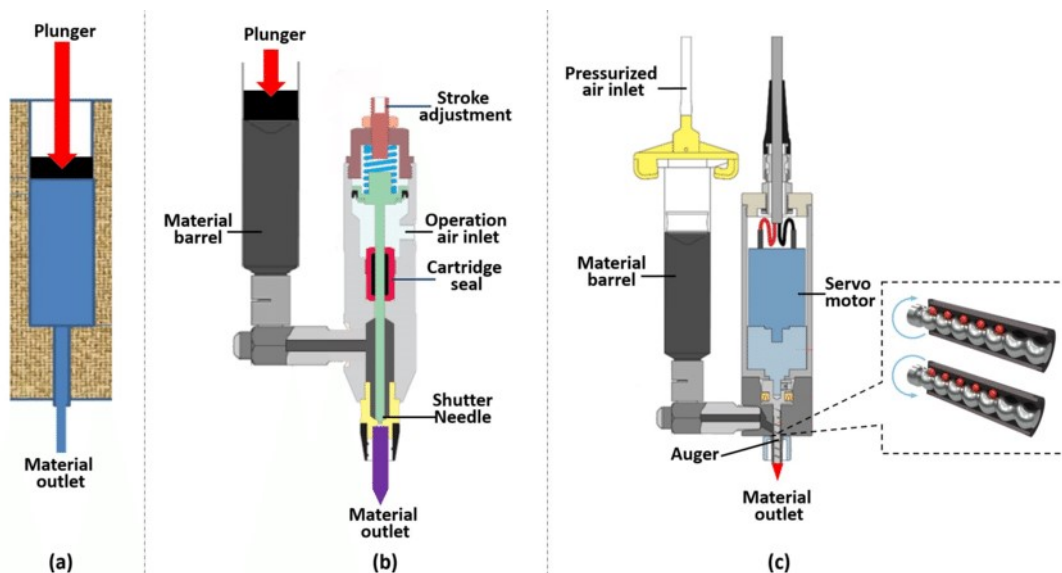


Figure 3-5 – Illustration of three extrusion mechanisms: (a) Ram extruder (b) Shutter valve (c) Screw-based extruder [172]

Ram extruders can be mechanically or pneumatically actuated to control the displacement of a plunger that is in direct contact with the feedstock, causing it to flow through the material outlet. Ram extruders are simple in design, but the

extrusion of high viscosity materials often requires high torque motors and complex gearing mechanisms, which increased weight and bulk but have a limited viscosity range. Pneumatically actuated systems provide the lightest and most compact configuration as the control unit can be located separately from the material reservoir. However, the design of this extruder can result in significant back pressures due to the formation of pressure gradients caused by the friction between the paste and extruder wall resulting in the formation of plug and slip flow [226]. The implementation of a shutter mechanism such as a needle valve shown in Figure 3-5*b*, can be used to reduce the delay in terminating extrusion by preventing the deposition of excess material. Constant pressure can be maintained within the material reservoir to reduce the delay when initiating the extrusion process.

Screw-based systems rely on the displacement of material produced by the rotation of a screw, which generates additional shear are more suitable for high viscosity materials. However, the control of the material flowrate is more challenging compared to piston-based mechanisms, typically resulting in reduced spatial control. Various screw-based mechanisms are available including auger screw mechanisms and progressive cavity (PC) pumps. Auger screw mechanisms as shown by Figure 3-6*a* use a rotating helical screw, which is sometimes tapered, to drive material from the reservoir to the nozzle. The extrusion flow rate is controlled by the RPM of the screw, resulting in slower flowrates compared to pneumatically driven extrusion systems. Progressive Cavity (PC) Pumps, shown by Figure 3-6*b* are a form of PD pumps that comprise a metallic rotor with a helical profile within an elastomeric stator that has a double helix profile. Material is extruded by a volumetric transfer of fluid between the fixed cavities formed between the helix and stator.

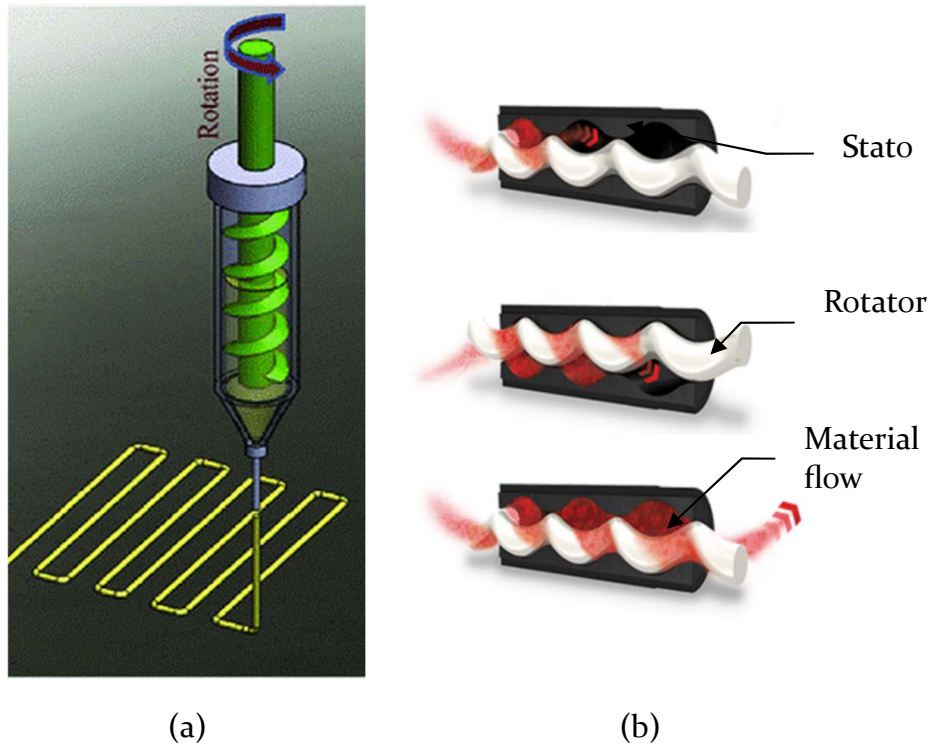


Figure 3-6 – Illustration of a) Auger screw extrusion mechanism [227] b) material Flow of material through a PC pump [228]

The ceramic feedstock was loaded into 10cc material syringes that were backed with a piston and connected to a pneumatic dispensing system with a maximum pressure of 5 bar. The syringe barrels have a standard luer lock connection allowing a range of compatible nozzles to be used. Figure 3-7 shows the ceramic feedstock being successfully extruded through various nozzle sizes ranging from 220 μm to 510 μm with tapered and straight nozzle profiles using a pneumatic ram extruder.

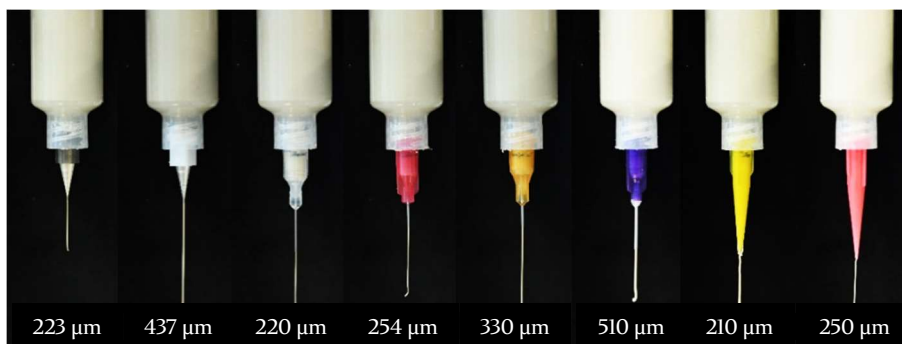


Figure 3-7 – Illustration of the ceramic feedstock being extruded through nozzle of different sizes and profiles using a pneumatic ram extuder (left to right) 233 μm tapered, 437 μm tapered, 220 μm straight, 254 μm straight, 330 μm straight, 510 μm straight, 210 μm and 250 μm polymer taper.

The straight profile nozzles caused more shear thinning compared to the tapered nozzles, due to the additional shear generated during extrusion. Furthermore, frequent nozzle blockages occurred with the hard agglomerates being located close to the middle of the profile. A pneumatically actuated shutter valve system (Pico SV-060, Nordson, USA) designed to deposit solder paste, silver epoxies and other filled materials was investigated alongside the basic ram extruders. The system uses straight profile nozzles with diameters ranging of 150-400 μm . The shutter valve system had a short delay when initiating the extrusion process, with no material deposits after the extrusion process had been terminated. The shorter nozzles cause less shear thinning of the extruded material, resulting in less slumping of the deposited material.

Despite the improved extrusion characteristics, non-uniform flow and blockages were a frequent occurrence. These disruptions are likely to be caused by the drying of material within the nozzle, entrapped air release and the effects of agglomerate break down. The preparation and loading of the feedstock into the material barrels causes a degree of entrapped air due to the high viscosity of the paste. During extrusion, increased pressure from the die causes compression of entrapped air bubbles due to the buoyancy affects from the surrounding material. Air bubbles subsequently merge to form larger air bubbles, which expand and burst when exiting the material outlet causing a large pressure release that disrupts the material flow.

Agglomerate breakdown is also attributable to some of the flow disruptions that were observed. This phenomenon occurs due to the compression of interlocking agglomerates, creating a backpressure that increases until the agglomerates disintegrate and break down. However, agglomerate breakdown is difficult to predict, resulting in force spikes that cause fluctuations in material flowrate and defects within the fabricated parts. Figure 3-8 illustrates the mechanism of agglomerate breakdown, which is caused by the material compression within the extruder die. The disintegration of the larger agglomerates into smaller one, alleviates the generated back pressure but alters the flowrate through the material outlet [229].

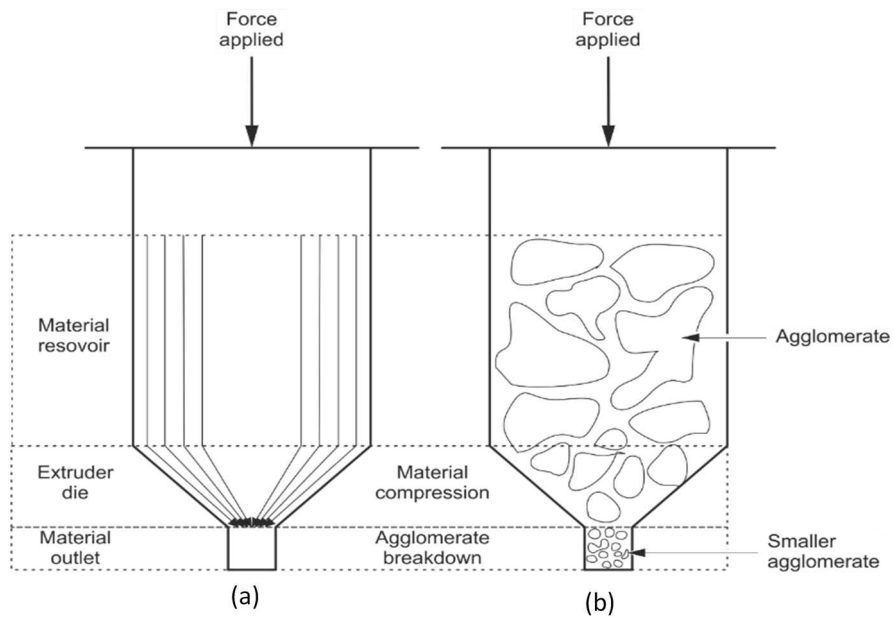


Figure 3-8 – a) Shows flow of material through the material reservoir, die (material compression) and material outlet (agglomerate breakdown). b) shows the process of extruding high solids loading material and the affect of agglomerate breakdown [229].

Screw-based extrusion systems reduce the effects of agglomerate breakdown by causing the agglomerates to disintegrate, before generating large backpressure. The additional mixing and shear improve the homogeneity of the extruded material. Auger screw mechanisms are dependent on consistent viscosity to achieved stable extrusion flowrates. However, the viscosity of pseudoplastic material changes dynamically throughout the extrusion process, which may restrict the compatibility of other feedstocks formulations [172]. This results in auger screw dispensing systems being less versatile than PC pumps, which are more resilient to changes in viscosity [230]. Therefore, auger screw pumping systems were not suitable for the proposed process.

A volumetric dosing PC pump (Preeflow ecoPEN 300, ViscoTec, Germany) with a dosing precision of 1 μl was used to deposit the feedstock through a range of luer lock nozzles. The material was extruded using a volumetric flowrate of 300 $\mu\text{l}/\text{min}$, applying a retraction of 3 $\mu\text{l}/\text{min}$ when the process is terminated. A delay of 2 - 5s was observed when initiating the extrusion, which is due to the retraction of the material. The PC system resulted in consistent material flowrates with no notable flow disruptions such as the nozzles blockages or entrapped air release. Figure 3-9 shows the ceramic feedstock being successfully

extruded by the ecoPEN300 PC extruder through various nozzle sizes ranging from 220 μm to 510 μm with tapered and straight nozzle profiles.

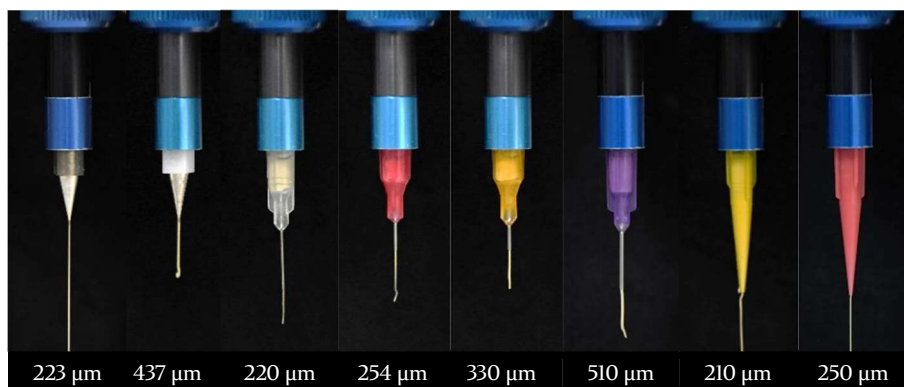


Figure 3-9 - Illustration of the ceramic feedstock being extruded through various nozzle sizes and profiles using an ecoPEN300 extruder (left to right) 233 μm tapered, 437 μm tapered, 220 μm straight, 254 μm straight, 330 μm straight, 510 μm straight, 210 μm , 250 μm polymer taper.

Qualitative assessment of the nozzles was used to select the nozzles that would be used to fabricate the ceramic components. This was sufficient as notable differences were observed between the different nozzles, the exploratory nature of this work not warranting further investigation of nozzles. These tests resulted in the metal tapered nozzles being selected for the fabrication of ceramic parts due to the more responsive extrusion characteristics compared to the straight profile nozzles. This was determined by the shorter delay when initiating the extrusion process, with smaller material deposits after terminating due to less shear-thinning of the feedstock. The polymer tapered nozzle visibly flexed during the extrusion process, with material curling and deforming around the end of the nozzle as shown by the 210 μm nozzle.

3.4 Forced Convection Drying

Accelerated drying of the extruded feedstock will reduce fabrication times by shortening the time to achieve suitable machining characteristics. Drying of materials within conventional ceramic manufacturing often use convective and radiation heating techniques. Convective heating is used to dry a large number of parts simultaneously prior to debinding and sintering. Heated forced convection enables faster drying rates to be achieved, whilst providing directional control of heating. However, the accelerated airflow of forced convection can cause deformation of the drying material. Investigation of

accelerated drying using this method was based on visual observation of the part and the resultant machining characteristics. Figure 3-10 shows the visual transformation between the dried ceramic material and undried material. The fabrication of this part are documented in Chapter 5.3.5 (page 158).

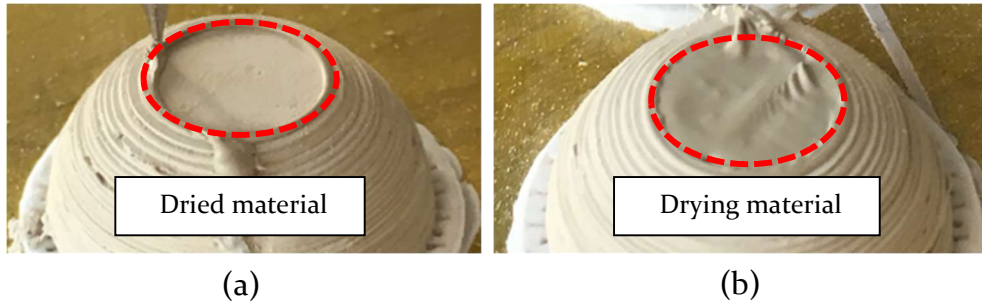


Figure 3-10 – Illustrates the visual difference between a) dried material and b) drying material

A 2000W handheld forced convection drying unit (Fast Dry, TRESemme, US) with the concentrator nozzle removed was used to dry deposited material. The unit has three speed/heat settings, plus a manual override to turn off the heating element. The unit was mounted on a laboratory clamp stand and angled downward towards the build plate. The drying unit was investigated using the different temperature settings at 50, 100 and 150mm from the part. The time required to produce a uniformly matte surface, which was determined to be a sufficiently dry state to have suitable machining characteristics.

The tiles measured $25 \times 25 \times 7$ mm, which were fabricated on the hybrid manufacturing platform as documented in Section 5.3.1, required a drying time of ~25s when using speed setting 2 at a distance of 50 mm. Figure 3-11a shows a part that demonstrated poor machinability due to insufficient drying, resulting in inconsistent edge retention and high surface roughness due to the cutting faces of the tool becoming blocked with undried ceramic material. Alternatively, Figure 3-11b demonstrates a layer that was dried for 60s using a fan speed setting of 3, with the cooling override deactivated at a distance of 50 mm. These settings resulted in the formation of bubbles on the top surface of the layer, causing large pores in the machined surface of the part.

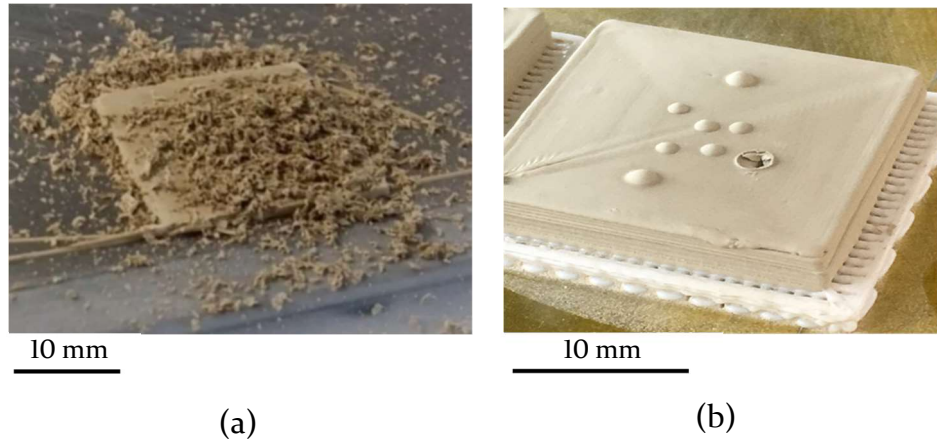


Figure 3-11 – shows a) poor machining characteristics of a part that was insufficiently dried 60 seconds using fan speed of 3, with the cooling override activated at a distance of 150 mm b) Shows the result of rapid drying on the surface of a component.

The handheld forced convection drying unit was characterised in ambient laboratory conditions using a handheld anemometer (AVM-03, Prova, Taiwan) and a calibrated multimeter with a K-type thermocouple attachment (116 digital multimeter, Fluke, US). Figure 3-10 shows the setup that was used to characterise the different temperature and air speed settings in the drying unit. Measurements were acquired 30s after the fan was started and allowed to cool to ambient temperature in between measurements.



Figure 3-12 – Shows the configuration that was used to characterise the parameters of the handheld forced convection drying unit

Measurements of fan speed and temperature were taken at 0mm, 50mm, 100mm and 150 mm from the front face of the drying unit. Figure 3-13 shows the temperature profiles for the different settings on the unit, whilst Figure 3-14 shows the measured airspeeds. Speed setting 2 at a distance of 50 mm from the

part was found to provide the most efficient drying, which equates to a measured temperature of 58.7 °C with a corresponding air speed of 12.1 m/s.

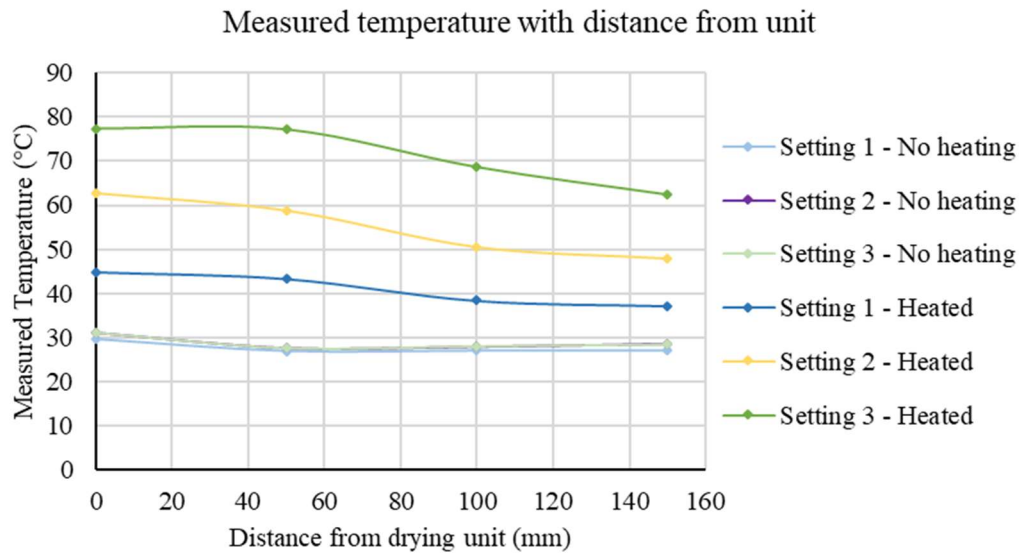


Figure 3-13 - The measured temperature at 0 mm, 50 mm, 100 mm and 150 mm from the handheld drying unit

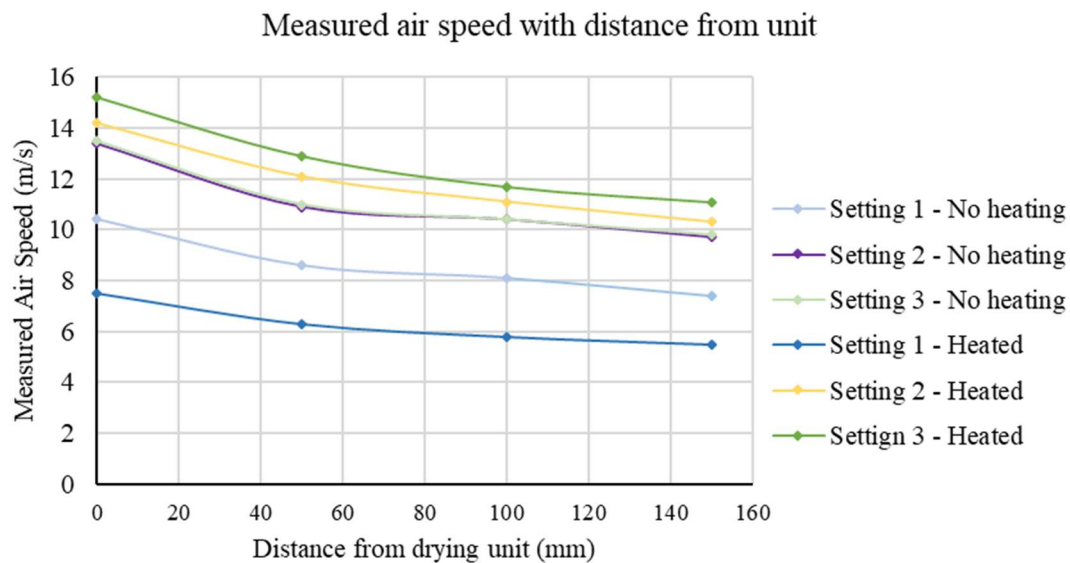


Figure 3-14 - The measured air speed at 0 mm, 50 mm, 100 mm and 150 mm from the handheld drying unit

3.5 Substrate and Support Material

3.5.1 Substrate

The substrate is the interface between the build plate and the green ceramic part during the manufacturing process. It is required to have sufficient adhesion

with the green state part to withstand the various manufacturing processes but enable removal without causing damage to the part or contamination of the equipment. The material needs to demonstrate dimensional stability under the processing conditions, including moisture and heat. The substrate materials were investigated with the fabrication of a square tile, which measured $25 \times 25 \times 7$ mm, involving the deposition of the feedstock, accelerated drying and subsequent machining. A key differentiator between types of substrate material are reusable and sacrificial.

Reusable substrates are intended to be reused during multiple fabrication cycles, with the fabricated part being removed prior to thermal processing. These substrates can be in direct contact with the fabricated part or via an intermediate layer such as polymer tape i.e. Polyimide (PI) tape. Reusable substrates such as glass and metal sheet are commonly used within other AM processes such as FFF and SLA. The intention to incorporate machining processes makes glass substrates unsuitable due to the risks of breaking the substrate as a result of coming into contact with the cutting tool during subtractive machining operations. Therefore, glass substrates were not investigated as part of this work.

Metal substrates formed from 5 mm thick aluminium sheet were investigated, demonstrating sufficient adhesion to the part with no signs of detachment or warping. However, part removal post fabrication was challenging, with the part remaining attached despite multiple attempts to remove it mechanically using a scraper. Heating and freezing of the part and substrate were also attempted, however this also failed to detach the part from the substrate.

The application of an adhesive-backed (PI) tape and PVA glue was used to form a sacrificial intermediate layer to facilitate the removal of the part post-fabrication. The PI tape demonstrated sufficient adhesion to withstand the various manufacturing operations, although some parts did become detached during side milling operations when the parts exceeded 5 mm in height.

Separation of the part from the substrate occasionally resulted in damage to the underside of the part. Applying PVA glue improved adhesion, with fewer

occurrences of part detachment during fabrication. Separation of the part and substrate was achieved by misting the PVA with water to dissolve the material, although the removal of parts with large footprints were limited due to penetration depth of the water. Misting water did result in the deformation of the ceramic part due to weak green strength.

Alternative sacrificial substrates, which are intended to remain attached to the part during fabrication and thermal processing such as uncoated printing paper, polymer sheet and extruded PLA rafts, were investigated. Sacrificial substrates are intended to pyrolytically decompose during thermal processing. Figure 3-15 shows a range of parts that were fabricated using the developed hybrid manufacturing platform on a range of substrate materials including *a)* Cellulose sheet, *b)* 400-gauge polyethylene sheet *c)* standard printing paper and *d)* PLA raft, which are low cost and readily available.

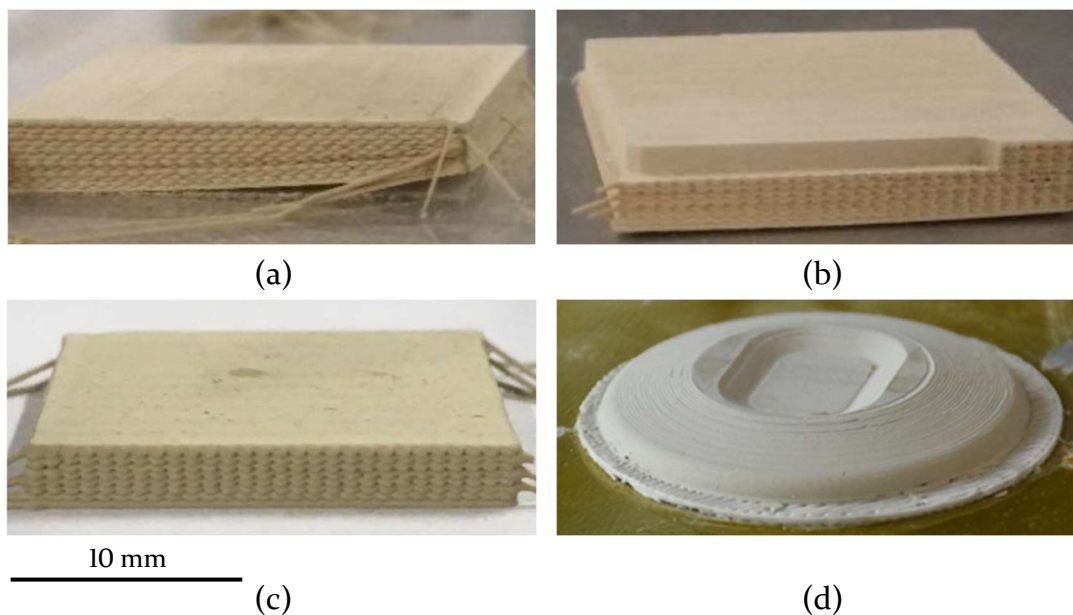


Figure 3-15 – Shows parts that were fabricated in a layerwise process using the developed hybrid manufacturing platform on different substrate materials including a) cellulose sheet b) polyethylene sheet c) standard printing paper and d) FFF PLA raft

The cellulose and Polyethylene sheets exhibited sufficient adhesion to the ceramic part to withstand the sequential deposition of material and surface machining operations. Side milling operations frequently caused the part to become detached from the substrate. Both substrate materials demonstrated poor dimensional stability when heated during the drying process, resulting in warping and detachment of the samples. Clamping of the polymer sheet using

a metal frame and toggle clamps proved ineffective at reducing the warping, with the base surface of fabricated parts being visibly bowed.

Standard printer paper is low cost and readily available was affixed to the build plate using masking tape on the edges of the sheet. The paper showed sufficient dimensional stability in these processing conditions with the part showing no signs of warping or distortion. However, paper has limited compatibility with materials that are likely to be used as sacrificial support. Removal of the part from the substrate sometimes resulted in damage to the underside of the part. Also, there are a number of safety concerns surrounding the pyrolytic decomposition of the paper during the thermal process such as the smoke generation. Moreover, kaolin within the paper poses a significant contamination risk to both the ceramic part and thermal processing equipment [231].

Polymer FFF systems create a sacrificial raft structure to improve bed adhesion and reduce the possibility of warping during fabrication, whilst reducing the risk of damage during part removal post fabrication. The implementation of a sacrificial support extruder represents a convenient method of producing raft substrates that provides better protection against mechanical handling compared to thin sheet substrates. Using the same process for substrate and support fabrication causes no compatibility issues that may arise by using dissimilar materials.

3.5.2 Sacrificial Support

Various thermoplastic filaments are available in filament form including PLA, ABS, Poly Carbonate (PC) and other specialist materials that are designed for applications such as investment casting. The sacrificial support material is required to enable the fabrication of overhanging and spanning geometries with sufficient adhesion to the green ceramic part to withstand the various manufacturing processes. The support material needs to be capable of being deposited onto the dried green ceramic part in order to support geometries that are not accessible from the substrate.

PLA is one of the most widely available FFF filament material, which is produced from fermented plant starch and is the second most used bioplastic [232]. PLA

has fewer health and safety considerations than materials such as ABS and does not necessitate the implementation of heated build plates to prevent warping during cooling. However, PLA may lack sufficient rigidity in certain processing conditions such as extended drying due to it having a glass transition temperature T_g of $\sim 60^\circ\text{C}$. Furthermore, this T_g temperature results in poor machining characteristics, preventing the removal of defects and stair stepping, which may be transferred onto the ceramic part. To determine the suitability of PLA support, a wedge structure was fabricated using a commercially available FFF system (Ultimaker2, Ultimaker, Netherlands) using a hotend temperature of 210°C and a heated bed temperature of 45°C . The wedge had a footprint of $15 \times 15 \text{ mm}$ and an angle of 30° onto which, the ceramic feedstock was deposited. Figure 3-16 shows the PLA pyramid onto which the ceramic feedstock was deposited onto the PLA wedge using the ecoPEN300 and a $200 \mu\text{m}$ polymer tapered nozzle with a specified layer thickness of $200 \mu\text{m}$. Insufficient drying of layers resulted in excessive slumping of the material, although the ceramic and PLA had sufficient adhesion to enable the production of this overhanging geometry.

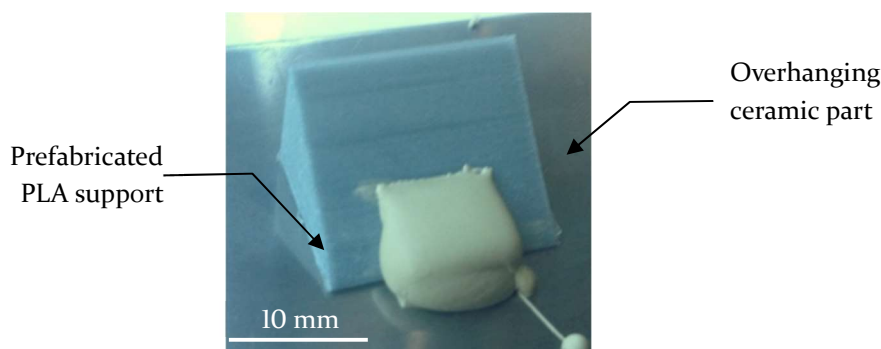


Figure 3-16 – Shows a prefabricated support structure being used to test the production of an overhanging geometry

During the fabrication of complex geometries, it is not always possible to have the support material in contact with the substrate. Therefore, the direct deposition of support material onto the green state ceramic was investigated. Five layers of PLA were sequentially deposited onto the ceramic part, with a delay of three minutes between each layer, to replicate the time taken for the other processes of the hybrid manufacturing process. Figure 3-17 shows the PLA being deposited directly onto the ceramic part with the detailed image showing the final part, which consisted of five layers.

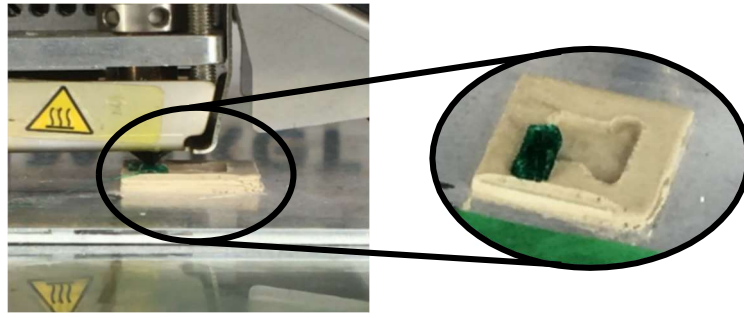


Figure 3-17 – Deposition of PLA onto a ceramic part fabricated ~~directly~~ on a metal substrate using an Ultimaker 2

A spanning structure with a total width of 18 mm and height and depth of 5 mm was fabricated using the developed hybrid manufacturing platform. The material was deposited through a 223 μm metal tapered nozzle using the ecoPEN300. The part was fabricated directly on a 4 mm aluminium sheet. The PLA support structure was produced separately on a commercial FFF system (Ultimaker2) using PLA with 40% infill (Grey filament, Ultimaker). The FFF system was configured with a 0.4 mm nozzle with a nozzle temperature of 210°C and bed temperature of 60°C. The support structure was manually placed and aligned during the fabrication process once the upright sections of the part had been fabricated. Once placed, the process was resumed to fabricate the spanning section of the geometry. Figure 3-18a shows the green-state structure with the support structure in place. The part was sintered in an industrial tunnel kiln in the orientation shown, with the support material in place. Figure 3-18b shows the sintered monolithic ceramic structure.



Figure 3-18 – (left) a spanning structure that was fabricated using a prefabricated PLA support structure. (right) shows the same sample post sintering.

Inspection of the sintered part showed minimal residue, thus demonstrating that PLA was a suitable support material to enable the development of the hybrid manufacturing process.

3.6 Ceramic AM Machining

Investigation of the machinability of the green-state ceramic parts, which were fabricated in a layerwise manner covered the suitability of tooling materials and designs, whilst determining appropriate processing parameters. Machining of preformed green-state ceramic billets is used within conventional ceramic manufacturing, although these parts are devoid of discrete layers. The sequential deposition and drying of the feedstock during the hybrid manufacturing process, may result in defects or anisotropic properties that may affect the parts machinability. A casting mould was produced using a commercial stereolithography AM system (Viper SLA, 3D systems) to enable the fabrication of multiple ceramic test specimens. The mould consisted of 4 segments of equal size, which measured $25 \times 25 \times 5$ mm. The moulds were filled in five stages to form discrete layers that were fully dried between each deposition. To prevent contamination of the ceramic feedstock, mould release agent was not applied, although this resulted in some of the samples becoming damaged when removed from the mould. The cast samples were sufficient to proceed with the initial machining feasibility tests. Figure 3-19a shows the casting mould following the removal of the parts. The top right cavity shows the mould without the removable floor, showing the orifice used to remove the floor and component. Figure 3-19b shows some of the components that were produced using the casting mould.

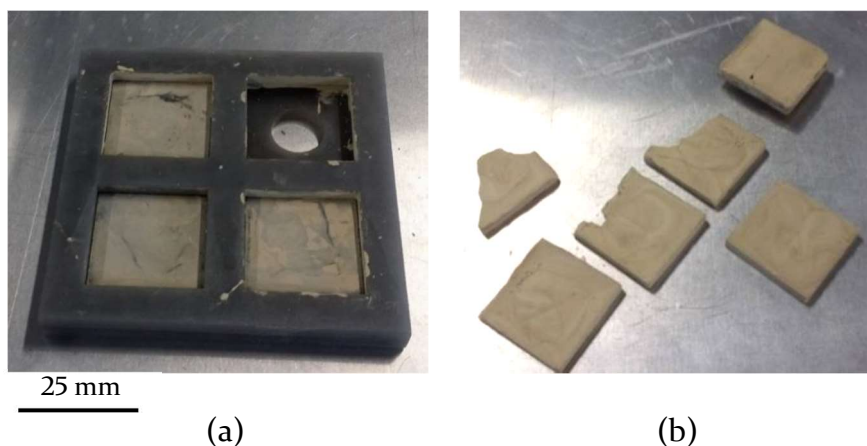


Figure 3-19 - a) shows the casting mould following the production of ceramic samples, the removable floor of the top right cavity has been removed to show the orifice for releasing the samples. b) shows the samples that were produced using the mould

The cast ceramic parts were machined using a manual turret mill (Milltech 2000VS, RK International, UK) with a spindle speed of 50 - 4,500RPM and a powered auto feed bed. Control of the spindle speeds involved the transfer of belts between pulleys within the turret of the milling machine, which prevented the fine adjustment of spindle speeds. The cast parts lacked sufficient strength to withstand clamping in the machining vice and were therefore mounted to a block of stainless steel using double sided tape. Figure 3-20 shows the cast ceramic affixed to the stainless-steel mount in the machining vice, with a $\text{Ø} 1.5$ mm high speed steel (HSS) fluted cutter.

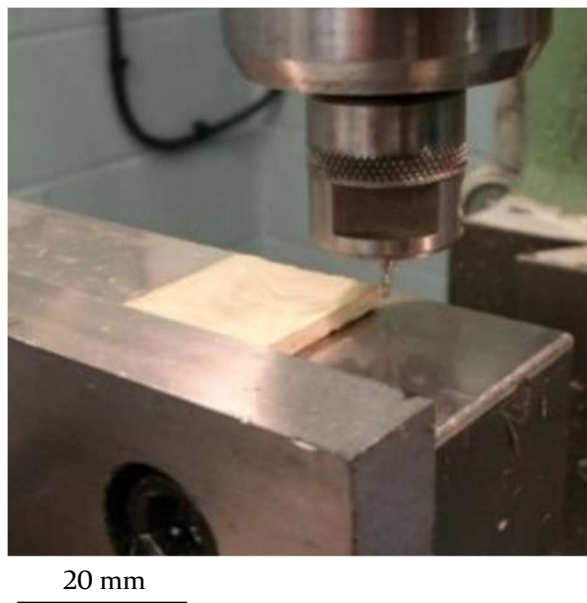


Figure 3-20 – Validation of the ceramics machinability was undertaken on cast samples using a Europa Milltech 2000VS Turret Milling Machine

These tests were used to confirm that green state ceramic parts formed of discrete parallel layers had sufficient strength to withstand subtractive machining operations. The presence of discrete layers within the part may have resulted in poor machining characteristics due to delamination and cracking as a result of weak interlayer adhesion. However, the parts were machined with no signs of cracking or delamination, indicating the feasibility of implementing the machining process with the additively manufactured parts. During these initial tests, both conventional and climb milling operations were evaluated. Conventional milling operations rotate the cutting tool against the direction of the feed, whereas climb milling operations rotate the cutting tool with the

direction of feed. Figure 3-21a shows a diagram illustrating the climb milling strategy with, Figure 3-21b illustrating the conventional milling strategy.

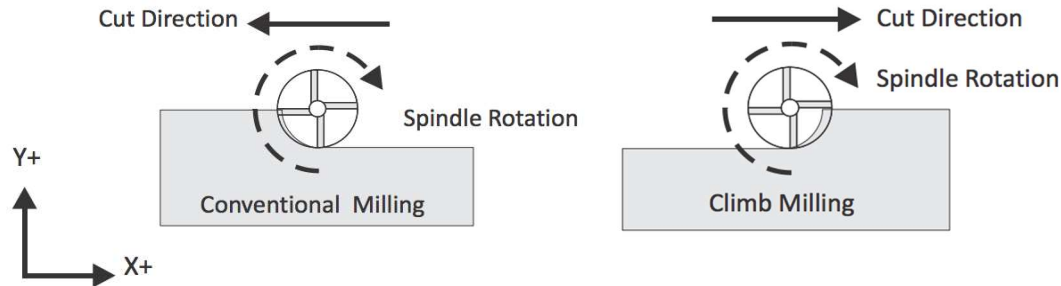


Figure 3-21 – Shows the direction of the cutter relative to the feed direction for conventional and climb milling operations [233]

Climb milling operations are typically preferred due to the alternative shear planes resulting in lower surface roughness, whilst cutting debris falls behind the cutter, which reduces tool rub and increases tool life. However, climb milling operations require machining platforms that counteract backlash, which is caused by play between the lead nut and screw. The cast samples were machined using a fixed feedrate of 475 mm/min (7.9 mm/s) using spindle speeds of 2,310 and 3,750 RPM. Climb and conventional milling operations were characterised on the same sample by traversing the cutting tool in both directions. For example, slot milling operations were investigated by machining a slot running parallel to the Y-axis. Once clear of the part, the cutter was offset along the X-axis before creating a second slot alongside. The production of adjacent slots facilitated the direct comparison of climb and conventional machining during feature production slot milling operations. Figure 3-22 shows samples that have undergone slot, side and end milling operations using both conventional and climb milling strategies.

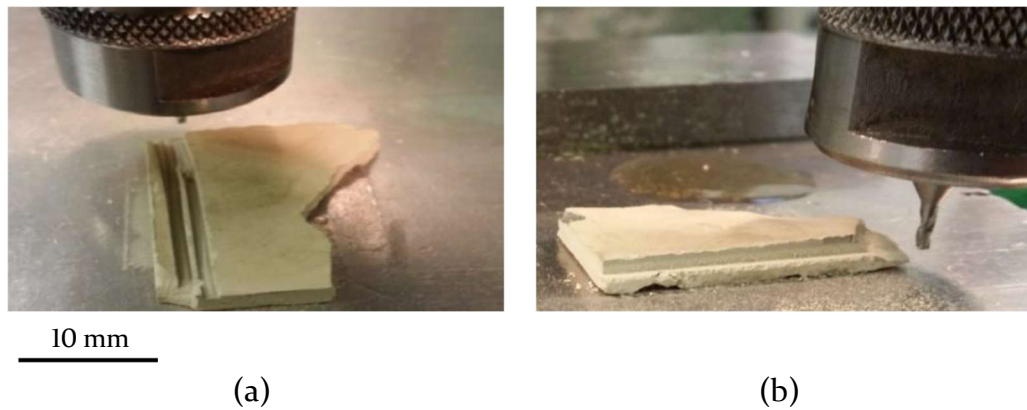


Figure 3-22 – (a) shows the use of a fluted carbide end mill machining slots into cast alumina tiles. (b) shows a ceramic sample having undergone side milling at 2310 RPM at 475mm

Degradation of the HSS cutting tool was observed throughout the preliminary machining operations. This was due to the presence of surface striations and deteriorating edge retention as the number of machining passes increased. Literature on the machining of green-state ceramic preforms advocate the use of diamond coated tooling at faster spindle speeds and feedrates. Dhara *et al.* investigated green state machining of alumina samples formed using gel-casting, protein coagulation casting and gel forming. The preliminary study was undertaken using HSS, carbide- and diamond-coated tooling using a spindle speed of 12,000 RPM and feedrate of 10 mm/s. Both the HSS and carbide-coated tooling exhibited signs of rapid wear with material dark deposits on the machined surfaces that was determined to have originated from the cutting tool. The machined surfaces also turned a brownish black colour due to partial burning of the organic binders due to the heating of the carbide tooling during machining. Tool wear poses a considerable problem due to the adverse effects that can occur to the ceramic body due to contamination with metallic impurities. This was in contrast to the ceramic parts that were machined using the diamond-coated tooling, which exhibited no burning or material deposits even after extended machining operations [234]. Figure 3-23a shows dark deposits that were visible on the ceramic part following the machining operation. Inspection of the tools after the machining operations showed rounding of the cutting face, which is the cause of the poor machining characteristics. Figure 3-23b shows a part with deteriorating edge retention and increased surface roughness that occurred due to tool wear.

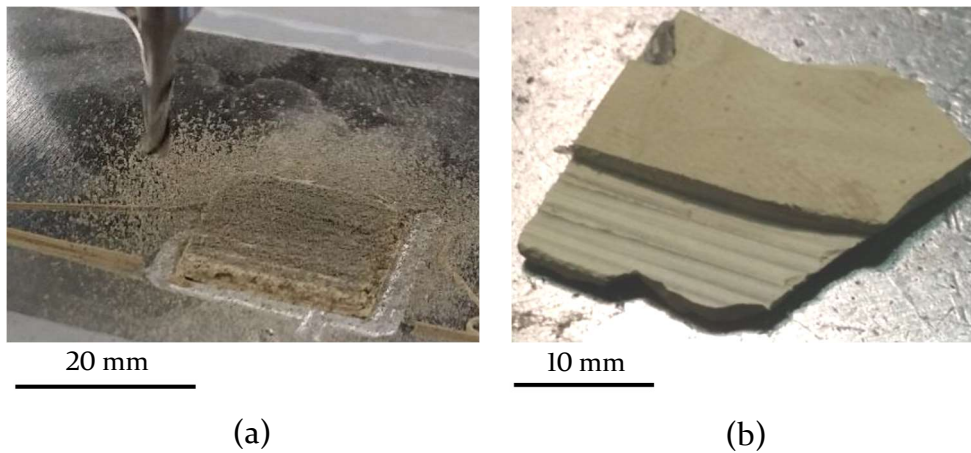


Figure 3-23 – (a) Material deposits left from a HSS end mill when end milling the top surface of the cast tile. (b) Large scale machining demonstrate the capability to remove significant amounts of material from a cast ceramic tile This was machined at 3750RPM at 475mm/min.

Furthermore, Mohanty *et al.* investigated the machining of green ceramic compacts formed from slurries containing 55 vol% alumina. The machining tools consisted of mild steel flat and pointed end conical tools that were formed using either $\sim 117 \mu\text{m}$ or $\sim 20 \mu\text{m}$ diamond particles. The diamond particles were randomly distributed over the steel body. Surfacing, roughing and finishing machining operations were investigated on the ceramic preforms using a bench-top CNC milling machine using a spindle speed of 10,000 RPM, X-Y feedrate of 8-10 mm/s and Z feedrate of 4-5 mm/s. The depth of cuts varied from 0.2-0.5 mm, with the shallower cuts and slower feedrates being used by the finishing operations. Parts fabricated during this work include a cylinder, 3D micro pattern with a $15 \times 15 \text{ mm}$ footprint and a dental crown (incisor). Tooling formed using $\sim 117 \mu\text{m}$ particles offered higher material removal rate compared to the tooling formed from $\sim 20 \mu\text{m}$ particles, owing to the increased surface roughness of the larger particles, though similar material removal rates were obtained using identical machining parameters. Clogging of the cutting tool with machining debris was noted as being insignificant even during extended machining operations. Although the depth of cut was limited due to the absence of a helical flute to facilitate debris removal during certain machining operations such as pocketing and slot machining. The green state parts were determined to have a surface roughness perpendicular to the tool path of $0.82 \pm 0.03 \mu\text{m}$ and $0.42 \pm 0.04 \mu\text{m}$ with spikes of $\sim 2 \mu\text{m}$ and $\sim 0.1 \mu\text{m}$ for the tools produced using $\sim 117 \mu\text{m}$ and $\sim 20 \mu\text{m}$ particles respectively. Post sintering, the

samples had an average surface roughness perpendicular to the tool of $0.59 \pm 0.08 \mu\text{m}$ and $0.20 \pm 0.06 \mu\text{m}$. Along the tool path, the sintered parts had an average surface roughness of $\sim 0.19 \pm 0.06 \mu\text{m}$ and $0.10 \pm 0.03 \mu\text{m}$ respectively. The sintered samples had an average density of $>98\%$ TD with an average flexural strength determined by 3-pt bending of $289 \pm 33 \text{ MPa}$ for parts fabricated using the $\sim 117 \mu\text{m}$ tooling and $319 \pm 28 \text{ MPa}$ for the samples produced using the $\sim 20 \mu\text{m}$ [235].

Polycrystalline diamond (PCD) typically consist of a metal shank that has been coated with a metallic matrix, containing a random scattering of PCD. This tooling is low cost and readily available in a number of profiles, enabling the production of a range of geometries and feature sizes. Investigation of this type of tooling was undertaken using low cost, unbranded tooling shown by Figure 3-24.



Figure 3-24 – A range of PCD tooling with a range of cutter profiles

A $\text{Ø}4 \text{ mm}$ straight flanked end mill was used during the initial tests as this was the most suitable tool for planarizing and finishing operations for straight sided 2.5D geometries. Square samples measuring $20 \times 20 \times 5 \text{ mm}$ produced in a layerwise manner using the developed manufacturing platform were machined using a spindle speed of 10,000 RPM and feedrates of 10 mm/s. The tooling was capable of machining the additively manufactured parts without causing damage. No deposits were visible on the machined part, compared to the sample machined using HSS tooling investigated previously. This suggests that the tooling is not being abraded at an excessive rate or burning the organic elements. This is beneficial as material deposits from the tooling can result in contamination of the ceramic part, which may affect the final parts

performance. Figure 3-25a shows the surfacing function by using the tool as an end mill. The chip formation mechanism results in the generation of fine particles that needed to be frequently removed. Figure 3-25b shows a sample following a surfacing operation on the top face and side milling operation using a climb milling strategy on the top half of the edges.

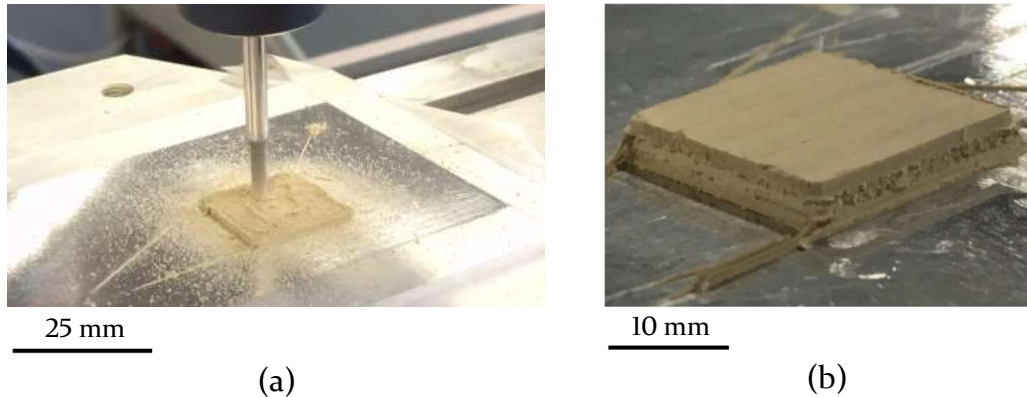


Figure 3-25 – Validation of in-situ machining following the drying of deposited ceramic material. Note: the machining was undertaken using coarse diamond coated end mill.

The edges of the part exhibit a number of defects, which become more pronounced throughout the machining operation. The lack of flutes and spacing between the coarse diamond particles on the cutting tool result in the accumulation of debris on the cutting tool, reducing the effectiveness of the cutting surface. Figure 3-26 shows the accumulation of debris on the cutting tool following the machining of a single side during a side milling operation. Due to the amount of debris generated by the machining operations, regular cleaning of the machining tool would be necessary to retain suitable machining characteristics.



Figure 3-26 – Shows the accumulation of machining debris on a PCD machining tool following a side milling operation

The rapid clogging of the tool may prove problematic when machining enclosed geometries, where efficient debris removal is required. As noted by Mohanty *et al.* the maximum depth of cut is inhibited by the lack of helical flutes, which may reduce the capability of the tool to produce certain geometries. Diamond coated fluted tooling produced using chemical vapour deposition (CVD), are readily available but at an increased cost compared to PCD tooling. Although, fluted tooling can enable a broader range of machining operations by overcoming the limitations of insufficient debris removal and cutting surface degradation.

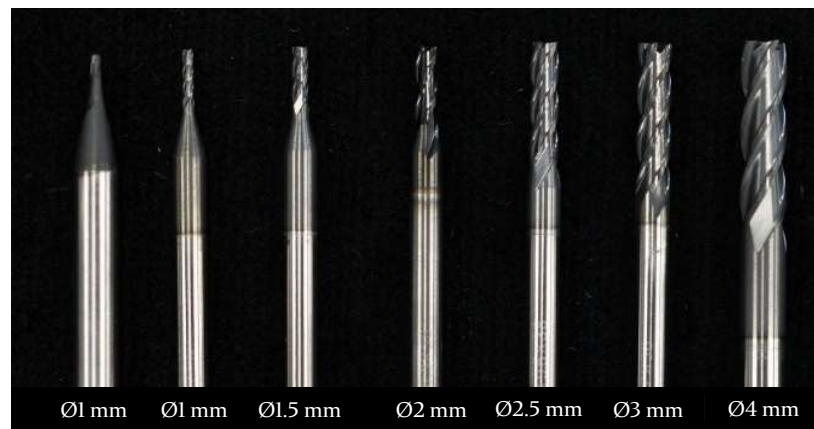


Figure 3-27 – Range of fluted CVD diamond tooling (left to right) 1 mm ball nose cutter, 1 mm end mill, 1.5 mm end mill, 2 mm end mill, 2.5 mm end mill, 3 mm end mill and 4 mm end mill. The 4 mm end mill was used throughout this work for interlayer machining on all parts and during post process machining of vertical sides.

Investigation of the CVD fluted tooling used a Ø4mm, four flute end mill using a spindle speed of 10,000 RPM and feedrates of 10 mm/s. The debris produced by the fluted tooling was coarser due to the cutting surface of the flutes on the tooling. No material deposits were visible on the machined surfaces that could be attributed to tool wear or the burning of organic elements. Side milling operations using a climb milling strategy demonstrated better edge retention with no cracking or defects that are attributable to the machining process. Figure 3-28 shows the edge of a sample that has undergone a side milling operation using fluted tooling under SEM at a magnification of 50x. The edges of the part do not exhibit any defects that can be attributed to the machining process or poor machining characteristics, whilst the discrete layers are not visible on the machined surface.

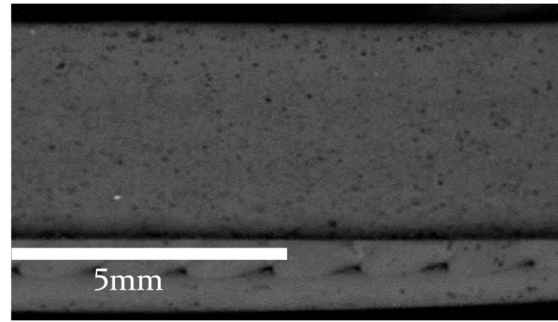


Figure 3-28 - Shows the edge of a ceramic tile that has been machined using a side milling operation

Further characterisation of the fluted tooling was undertaken in order to quantify the effect of feedrate on the machining characteristics. A further five samples were produced in a layerwise manner using the developed manufacturing apparatus using a $\text{Ø}4$ mm CVD end mill as shown in Figure 3-27 during the machining elements of the process. To investigate feedrates of 150 - 800 mm/min (2.5 - 13.3 mm/s) during surfacing and side milling operations To identify the corresponding sample and feedrate that was used on each side, the depth of the side milling operation was varied. Figure 3-29 illustrates the machining strategy used to identify the different feedrates.

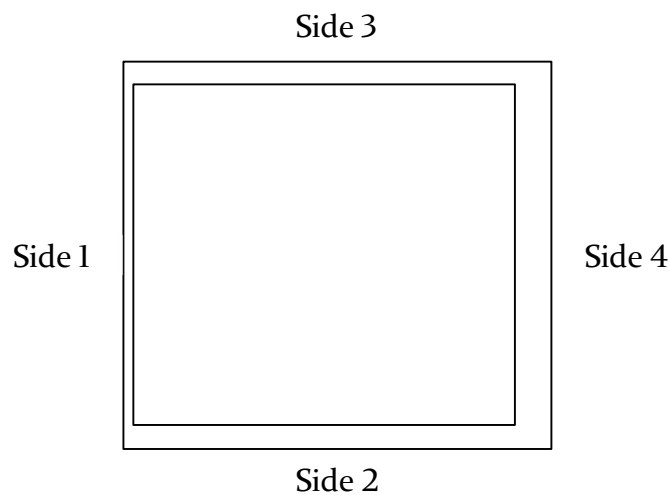


Figure 3-29 - Shows the identification of side numbers based on the width of cut which was to investigate various feedrates using a spindle speed of 10,000 RPM

Table 3-1 shows the feedrates that were used on the different sides during the side milling operations, with Figure 3-30 showing the corresponding samples post machining. Figure 3-30a shows sample 1, which became detached from the

substrate during the machining of side 1. Despite this, samples 2 and 3 shown by Figure 3-30b and Figure 3-30c were successfully machined on all sides.

Table 3-1 – The feedrates used the machine the sides of the tile

Sample	Spindle speed			
	Side 1 (mm/min)	Side 2 (mm/min)	Side 3 (mm/min)	Side 4 (mm/min)
1	150	400	650	800
2	200	330	460	600
3	250	400	550	700

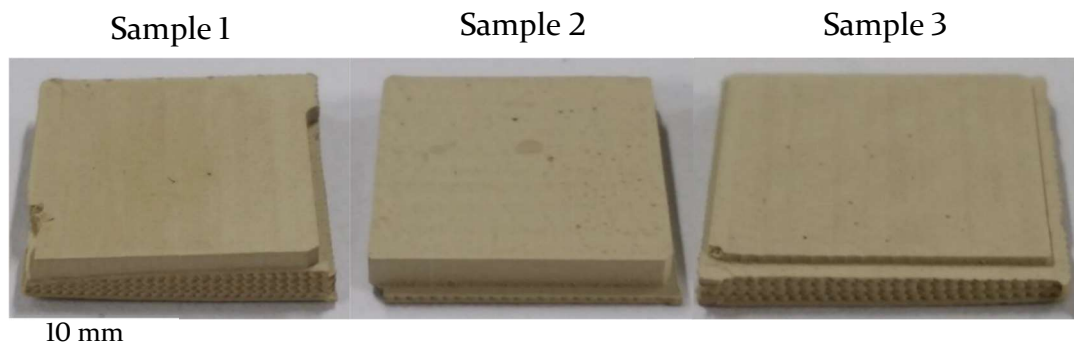


Figure 3-30 – shows sample 1, sample 2 and sample 3. Sample 1 was machined on 2 complete side before becoming detached whilst machining the third

The edges of the samples were visually inspected for defects such as chipping, striations, which would indicate poor machining characteristics. The use of faster spindle speeds will increase the material removal rate, enabling faster feedrates to be used. Although, faster spindle speeds will increase the accumulation of heat between the part and tool that may adversely affect the part such as burning of the organic elements. End milling operations were investigated using feedrates ranging from 150 – 800 mm/min that were incremented in 50 mm/min increments, using a spindle speed of 10,000 RPM. All of the samples remained attached to the substrate with no visible defects that are attributable to the machining operation. Sample 2 displayed in Figure 3-30 show some open pores on the top surface, which were a result of the machining process exposing entrapped air pockets within the top layer of the part. Measurement of surface roughness on the ceramic parts using non-contact profilometry (Talysurf CLI 2000, Taylor Hobson, USA) are displayed in Figure 3-31. Measurements of surface roughness after end milling operations

were obtained from the top surface of the part, whereas measurement of surface roughness due to side milling operations was obtained from vertical sides of the part. The data shows that the lowest surface roughness values of $1.11 \mu\text{m}$ and $1.62 \mu\text{m}$ were achieved for side and end milling operations at feedrates of 330 and 350 mm/min respectively.

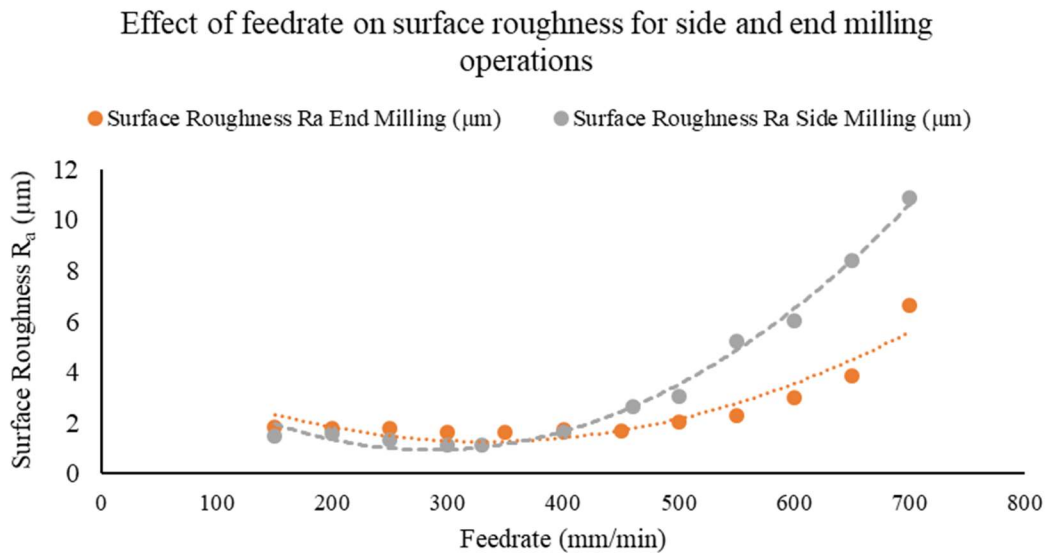


Figure 3-31 – Shows the surface roughness Ra for side and end milling operations at variable feedrates using a constant spindle speed of 10,000 RPM

3.6.1 Feature Production

Drilling

Machining of the green ceramic part can also be used to produce features with smaller spatial resolutions than can be achieved using the AM process. Drilling can be used to accurately produce round holes or channels. Drills feature a conical cutting face with helical flutes to remove material away from the cutting face. Spindle speed and plunge rate are key parameters during drilling operations, which are affected by the efficiency of the material removal of the tool. Investigation of the drilling characteristics used low cost PVD diamond drill bits that had diameters of $\text{Ø}0.7 \text{ mm}$ and $\text{Ø}2 \text{ mm}$, shown by Figure 3-32.

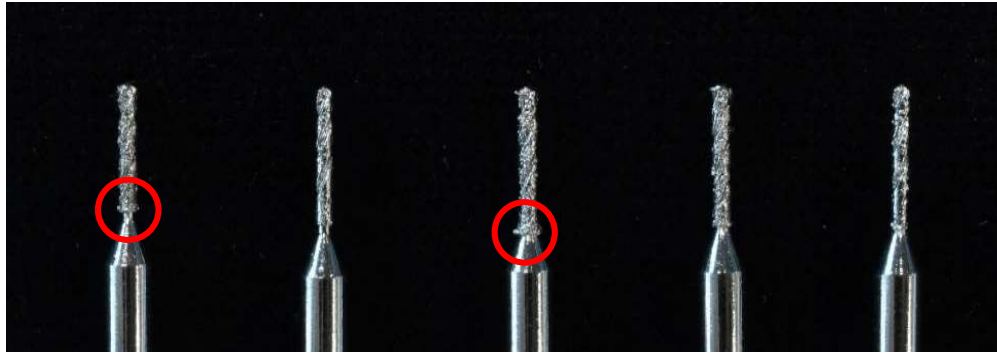


Figure 3-32 – Shows the Ø0.7 mm fluted drill bits that are coated in coarse PCD diamond

Comparison of the tools shown in Figure 3-32 show that there are a number of inconsistencies and manufacturing defects on the tooling. Red circles identify some of these defects, which are present on all of the tooling, causing in inaccuracies during machining operations.

The tests were carried out on a sample that measured $25 \times 25 \times 5$ mm, which was fabricated in a layerwise manner using the developed manufacturing apparatus. Due to the spatial limitations of the selected sample ten holes were drilled using the Ø0.7 mm bit and eight using the Ø2 mm bit. The holes were drilled to a depth of 3 mm. Table 3-2 shows the parameters that were used during the investigation of drilling. Figure 3-33 shows the location of the holes that correspond to the specified parameters. Machining tables designed for metals were used to guide the selection of suitable parameters.

Table 3-2 – Shows the parameters used during the investigation of Ø0.7 mm and Ø 2.00 mm drill bits

0.7mm drill bit

Hole Number	Spindle Speed (RPM)	Plunge Rate (mm/min)
1	7,000	45
2	7,000	130
3	7,000	215
4	7,000	300
5	7,000	385
6	4,000	215
7	6,000	215
8	8,000	215
9	10,000	215
10	12,000	215

2mm drill bit		
Hole Number	Spindle Speed (RPM)	Plunge Rate (mm/min)
11	8,000	45
12	8,000	130
13	8,000	215
14	8,000	300
15	4,000	215
16	6,000	215
17	10,000	215
18	12,000	215

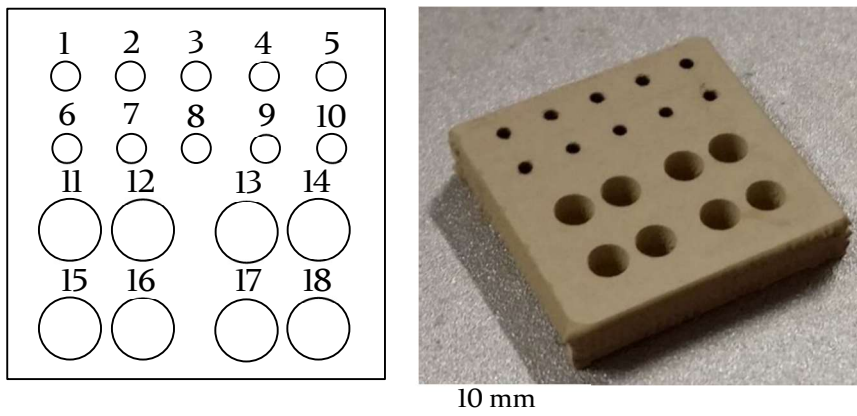


Figure 3-33 – Shows the part following the drilling operations and the corresponding hole numbers on a tile geometry produced in a layerwise manner using the developed manufacturing apparatus

During the drilling operation a significant amount of debris accumulated on top of the part, which was removed using compressed air in the interim period between each hole being drilled. The removal of the machining debris is a key consideration to avoid ingress of ceramic debris within the motion platform. Inspection of the holes showed an accumulation of machining debris that would need to be removed prior to sintering as this would affect the manufacturing tolerances. Analysis of the hole dimensions on one sample using non-contact profilometry – focus variation measurements (Talysurf CLI 2000, Taylor Hobson, USA) showed that the 0.7 mm tool had an average diameter of 0.728 ± 0.054 mm whereas the 2mm holes had an average diameter of 2.09 ± 0.032 mm.

Milling

The production of channels can be achieved using slot milling operations, whereby an end mill is plunged into the part and traversed to create a channel.

The validation of slot milling operations was achieved by the creation of 1 mm deep channels with a length of 12 mm, 11 mm and 10 mm. The spindle speed and feedrate were based on the parameters that resulted in the lowest surface roughness in previous tests. The selection of plunge rates was guided by the use of machining tables designed for metals, which are lower than the plunge rates for drilling operations due to the use of end mills that have a lower material removal rate in the Z direction. Table 3-3 shows the machining parameters that were used during this test.

Table 3-3 – Shows the parameters used to investigate plunge rate during slot milling operations using a spindle speed of 10,000 RPM and a feedrate of 330 mm/min

Slot Milling

Slot Number	Slot Length (mm)	Spindle Speed (RPM)	Feedrate (mm/min)	Plunge Rate (mm/min)
1	12	10,000	330	30
2	11	10,000	330	50
3	10	10,000	330	70

Figure 3-34 shows the three channels that were successfully machined into the top surface of the part. The channels show no defects that are attributable to inappropriate machining characteristics, although slot 3 does have a defect that occurred due to misalignment of the cutting tool.

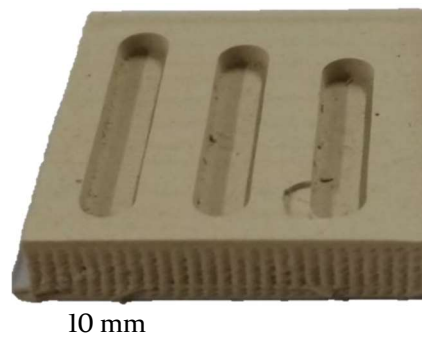


Figure 3-34 – Shows the sample used to validate slot milling operations. (left) shows the 12 mm slot, (centre) 11 mm slot and (right) 10 mm slot. The defect on the 10 mm was caused by by misalignment of the cutting tool

Analysis of the machined slots using non-contact profilometry (Talysurf CLI 2000, Taylor Hobson, USA) showed that the slots had a manufacturing resolution $\pm 35\mu\text{m}$. Table 3-4 shows the measured pocket dimensions against the specified dimensions.

Table 3-4 – Shows the measured dimensions of the machined slots

Slot	Slot Length (mm)	Measured Length (mm)	Slot Milling		Pocket depth (mm)	Measured Depth (mm)
			Desired pocket width (mm)	Measured pocket width (mm)		
1	12	12.2±0.05	4	4.06	1	0.935 ±0.02
2	11	11.1±0.07	4	4.06	1	0.936 ± 0.05
3	10	10.1 ±0.02	4	4.07	1	0.948 ±0.02

3.7 Post processing

Processing of the green ceramic parts in an industrial tunnel furnace was done at Morgan Advanced Materials production facility, following a controlled profile with a peak temperature exceeding 1,400°C, resulted in the production of monolithic alumina. Visual inspection of the parts showed no signs of warping or delamination between layers, validating the compatibility of the modified feedstock and hybrid manufacturing process with conventional manufacturing backend processes. Geometric measurements of the green and sintered samples to determine the relative shrinkage was provided by production staff at Morgan Advanced Materials. The samples underwent a calculated shrinkage of ~17-19%, which is consistent with conventionally manufactured parts. Figure 3-35 shows the green state ceramic parts above the sintered monolithic parts.

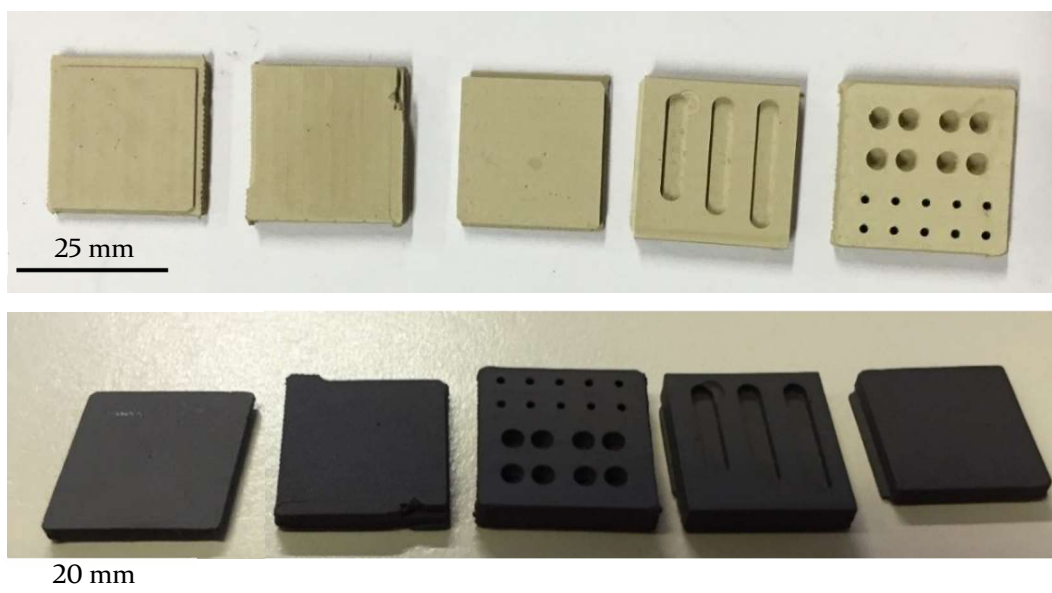


Figure 3-35 – (Top) shows the green state parts that were produced during the characterisation of the machining parameters. (Bottom) shows the samples following thermal processing using conventional backend processing.

Analysis of part density using an Archimedes density determination kit (Sartorius, Germany) in conjunction with a $\pm 0.1\text{mg}$ accuracy (Practum®, Sartorius, Germany) showed the parts had an average sintered density of $97 \pm 1.2\%$. Inspection of a sectioned part using SEM confirms the production of monolithic alumina, with no visible discrete layers, suggesting that layerwise fabrication does not adversely affect the debinding and sintering processes. Figure 3-36 shows the SEM image acquired from one of the fabricated parts which confirms the production of a monolithic part. The part was prepared by being sputter coated with gold. Defects are present within the part, which also highlight the orientation of the layers within the part, thus confirming the absence of discrete layers. Furthermore, a number of cavities are visible within the part, which is due to entrapped air within the ceramic feedstock, providing an explanation for the lower measured densities.

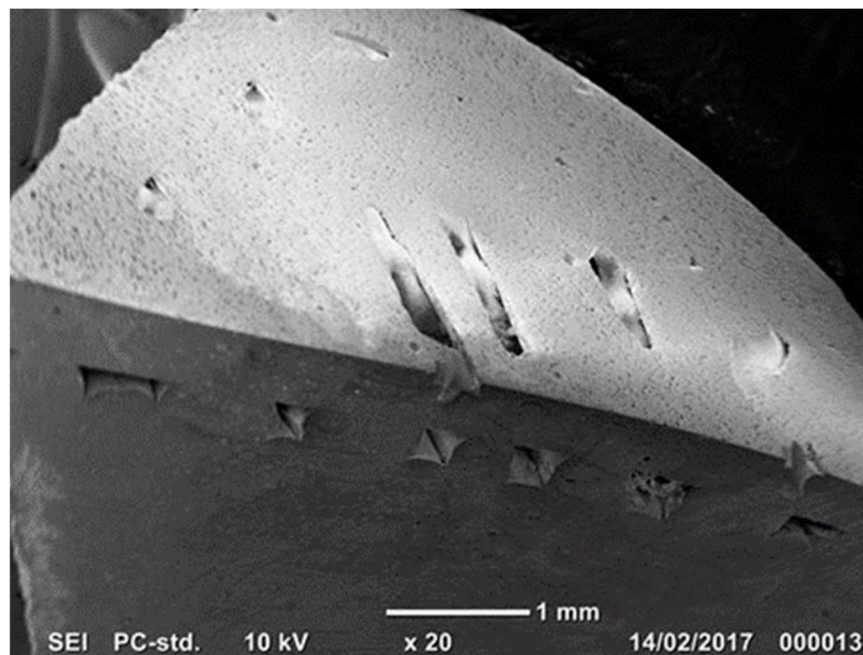


Figure 3-36 – SEM image of a section taken from a fabricated part. Discrete layers are not visible in the top section of the part, although defects within the bottom of the image indicate the layer orientation. the layers show the orientation of the layers.

The combined use of high viscosity paste extrusion, sacrificial polymer support and milling/drilling operations have demonstrated a number of benefits compared to standalone ceramic ME. The implementation of these processes into a laboratory scale, bench top manufacturing platform enables the fabrication of low volume, 3D ceramic structures.

3.8 Process selection and Conclusion

The suitability and performance of different process hardware, tooling and materials have been investigated to enable the hybrid manufacture of advanced ceramic components. The characterisation of the alumina feedstock derived from a commercial formulation using a parallel plate rheometer confirmed that the material had the necessary shear-thinning, pseudoplastic behaviour. The lack of templates within the hybrid manufacturing process requires the material to rapidly form a dilatant mass to achieve sufficient shape retention. This is achieved in part by the evaporation of volatile solvents and the shear relaxation of the binder, which was confirmed using a parallel plate rheometer.

Based on the result of the literature review of suitable ceramic AM processes, the hybrid manufacturing process was focused around a high viscosity paste extruder. A range of actuation mechanisms were investigated including pneumatically actuated ram and shutter-valve extrusion systems in addition to mechanically actuated, screw-based extrusion systems. Using these systems, the ceramic feedstock was successfully extruded through a range of luer lock nozzles including straight and tapered nozzles with diameters ranging from 210 to 510 μm . The test indicated that straight profile nozzles resulted in excessive shear thinning of the material compared to the tapered nozzles. However, the pneumatically actuated systems were noted as having less responsive extrusion characteristics compared the mechanically actuated screw-based extrusion processes. This was attributed to the formation of large back pressures, resulting in variable delays when initiating extrusion and excess material deposits when terminating the extrusion process. The inclusion of a mechanical “shutter” improved the responsiveness of the extrusion process, although was hampered by flow disturbances caused by the effects of agglomerate breakdown and nozzle blockages. Therefore, a mechanical, screw-based extrusion system was deemed most appropriate for this application due to additional shear, which improved the uniformity and homogeneity of the extruded material. A positive displacement screw extrusion mechanism was selected as these are more resilient to changes in viscosity compared to auger-screw mechanisms.

The alumina feedstock relies on the evaporation of an aqueous solvent to form a dilatant mass and create a green state part with sufficient mechanical strength to withstand further processing. To reduce manufacturing times, an accelerated drying stage was investigated. Forced convection drying is preferred over radiative heating as it is independent on the absorption characteristics of the material, enabling a broader range of feedstock materials to be used. The suitability of heated force convection drying was confirmed by using a 2,000 W forced convection drying unit to dry the deposited material. Qualitative assessment of machining characteristics was used to determine suitable drying parameters. This investigation showed that insufficient drying resulted in poor machining properties, whilst intense heating of the part could result in the formation of bubbles on the part. A temperature of 58.7 °C with a corresponding air speed of 12.1 m/s achieved suitable machining characteristics in the shortest time, without creating defects on the green state parts.

A range of materials for substrate and sacrificial support were investigated to enable the convenient removal of the green state part post-fabrication and production of parts with overhanging geometries. Substrate materials were categorised as either reusable or sacrificial. Direct deposition onto the reusable substrates demonstrated sufficient adhesion to withstand all of the manufacturing. However, removal of the fabricated part from the substrate often resulted in parts becoming damaged. Alternatively, sacrificial substrates such as cellulose sheet, 400-gauge polyethene sheet, standard printing paper and PLA (deposited using an FFF hotend) were also investigated. These sacrificial substrates demonstrated sufficient adhesion to withstand the various processes, although unintentional detachment of the part was observed with all sacrificial substrates. PLA substrates, that were created using an FFF process were subsequently used during the fabrication of parts due to its versatility, convenient removal and compatibility with the sacrificial support material. FFF was also used for the production of sacrificial support structures. PLA was used as a sacrificial support material as it can be directly deposited onto the dried feedstock material with sufficient mechanical strength to enable the fabrication

of a range of geometries. PLA is also low cost and readily available with fewer health and safety concerns compared to materials such as ABS.

To validate the machining characteristics of parts formed of discrete parallel layers, test samples were produced using a multi-step casting approach. This involved filling a casting mould in several intervals to create parts with 5 discrete layers. Machining of these samples using a 3-axis turret mill and fluted HSS cutter confirmed the viability of this approach, although rapid degradation of the HSS tooling was also observed.

Various tooling geometries and materials were investigated including non-fluted PCD diamond and fluted CVD diamond tooling. Non-fluted PCD diamond tooling demonstrated adequate machining capabilities for planarizing the deposited layers. However, the lack of fluting resulted in the coarse coating of the tools becoming saturated with machining debris, causing the cutting performance of the tool to deteriorate. Fluted CVD diamond tooling was noted as providing more consistent machining performance, particularly during extended machining operations. Investigation of spindle speed and feedrate on the surface roughness of the green state part showed that the surface roughness measurements of $1.11 \mu\text{m}$ and 1.62 were achieved using a spindle speed of 10,000 RPM and feedrates of 330 and 350 mm/min for side and end milling operations, respectively. The transition to fluted cutting tools enables the creation of high-fidelity features using processes such as drilling and slot milling. Drilling operations were investigated on parts using a 0.7 and 2 mm fluted PCD drill bits resulting in holes with an average diameter of 0.728 ± 0.054 mm and 2.09 ± 0.032 mm. The production of 1 mm deep slots using a CVD diamond end mill confirmed the capability of using the subtractive processes to create high fidelity features.

Based on this evaluation, the hybrid manufacturing platform will use a positive displacement pump to deposit the ceramic feedstock onto a substrate produced from PLA using an FFF process. Heated forced convection drying of the deposited material reduced the time required to achieve suitable green state machining characteristics. When required, sacrificial support will be created

from PLA using the in-situ FFF system. Subtractive machining operations will use a high-speed machining spindle in conjunction with fluted CVD diamond tooling.

4 Machine Development

The hybrid manufacture of ceramics needs to enable the production of high-density parts with low surface roughness and fine spatial resolution. Therefore, the system needs to be capable of fabricating parts of a comparable size, shrinkage and density to those currently produced by conventional manufacturing. The system also needs to enable the production volumes and geometries that cannot currently be achieved. Application of this technology is expected to be within low-volume, high-value manufacturing such as prototyping and development. The system should therefore be operable within a laboratory environment using 220V single phase power sources. Proximity with other laboratory equipment and people means that the system should not generate excessive noise, vibration and debris, principally airborne particulates. Table 4-1 shows a summary of key requirements for the various elements of the hybrid manufacturing platform.

Table 4-1 – Initial design specification used to guide and inform the selection of suitable machine hardware and software

System Element	Requirement	Justification
General system	<ul style="list-style-type: none"> • Bench top size • Powered using 220V single phase power. • Retraction/tool change mechanism to avoid interference from inactive process hardware. 	<ul style="list-style-type: none"> • Convenient to be used within most laboratory/research environments.
Motion Platform	<ul style="list-style-type: none"> • Axis minimum with capability to incorporate additional axes. • Repeatability of $\pm 25 \mu\text{m}$ • Maximum speed of 50 mm/s. 	<ul style="list-style-type: none"> • Based on the requirements of industrial end-users
Build Plate	<ul style="list-style-type: none"> • Sufficient size to enable the fabrication of parts measuring $150 \times 150 \times 100\text{mm}$. 	<ul style="list-style-type: none"> • Based on feedback from industrial manufacturers of parts using advanced ceramic materials.

	<ul style="list-style-type: none"> • Heating temperature of 35-60°C 	<ul style="list-style-type: none"> • Comparable to other ceramic AM systems.
Ceramic Extruder	<ul style="list-style-type: none"> • Capable of processing a range of material viscosities. • Withstand the processing of abrasive materials. • PC pumping mechanism. • Compatible with luer lock nozzles. 	<ul style="list-style-type: none"> • Ensures that the system can be used by multiple end users with a range of feedstock materials.
Accelerated Drying	<ul style="list-style-type: none"> • Provide an outlet temperature of ~60°C. • 12/24V DC power. • Compact design 	<ul style="list-style-type: none"> • Based on the findings documented in chapter 3.4.
Support Extruder	<ul style="list-style-type: none"> • Capable of processing standard Ø1.75 mm filament. • Enable the use of alternative materials. 	<ul style="list-style-type: none"> • Availability of materials from commercial suppliers.
Machining Spindle	<ul style="list-style-type: none"> • Spindle speed of 5,000-30,000 RPM • Low run out • Use tooling with a shaft diameter of Ø2-8 mm • Retraction or tool change function • Debris suppression/removal 	<ul style="list-style-type: none"> • Based on the findings documented in Chapter 3.6.
Software and control	<ul style="list-style-type: none"> • Control the various manufacturing processes • Facilitate closed-loop control • Provide feedback to the operator regarding machine status. 	<ul style="list-style-type: none"> • To ensure sufficient overhead for future upgrades and adaptations of the system.
Toolpath Generation	<ul style="list-style-type: none"> • Production of parts using a single toolpath file (amalgamation of additive and subtractive toolpaths into a single machine file). 	<ul style="list-style-type: none"> • To streamline machine operation to ensure maximum impact is achieved.

4.1 Motion Platform

The motion platform of the hybrid manufacturing platform provides the translational movement to the manufacturing processes whilst forming the main structure onto which elements are mounted. The requirement of the hybrid manufacturing process is to be a benchtop system that can operate using single-phase power, guided the identification of suitable motion stages. The manufacturing platform is required to be a minimum of 3-axis (X, Y and Z) to enable the production of 3D geometries. Most ME systems are configured using 3-axis as this generally does not impose unworkable design constraints but does necessitate the use of support structure for overhanging features. A number of research institutes [236] and commercial vendors such as HAGE3D GmbH [237] have developed ME systems with 3+ axis, although these are polymer ME processes. CNC milling machines, however, are typically configured as either 3+ axis systems due to the increased degrees of freedom required to produce internal and overhanging geometries. Therefore, the manufacturing platform is required to be a minimum of 3-axis but would also benefit from the additional degrees of freedom afforded by the additional axis, particularly when undertaking finishing or feature creation operations. However, 5-axis requires additional process control, to ensure that the required manufacturing tolerances can be achieved.

Another difference between ME and CNC machining is the suitability of different transmission elements, which convert the motor rotation into linear motion. The two primary transmissions classes include belt-driven and leadscrew driven.

The low mass of the extrusion head and minimal forces during production are amenable to the use of belt and pulley driven systems. These transmission elements are suited to faster feedrates that can exceed 7,200 mm/min (100 mm/s). However, the higher forces experienced during machining operations makes belt and pulley transmission unsuitable due to the stretching of the belt and slippage between the belt and pulley. Therefore, leadscrew transmission is most appropriate for the additive/subtractive hybrid manufacturing platform.

The manufacturing platform needs to be capable of fabricating components that measure $150 \times 150 \times 100\text{mm}$. Therefore, the effective stroke of the platform required to achieve this, is dependent on the method of transitioning between the different manufacturing processes. Figure 4-1a illustrates a system that has a single tool holder, with the transition between the manufacturing processes being achieved using an automatic tool changer (ATC). The use of an ATC requires the smallest effective stroke distance, due to the minimal offset distances between tools. Furthermore, the use of a standard mounting fixture will streamline the future integration of additional processes, increasing the versatility of the manufacturing platform. However, this mechanism adds to the complexity of the overall platform and introduces additional variables that can reduce the manufacturing resolution such as the repeatability when switching between processes. Alternatively, Figure 4-1b shows a system where the various manufacturing elements are permanently mounted adjacent to one another. Permanently mounting the tools is the simplest method of mounting tools, applying a predetermined offset to transition between processes. The permanent mounting of tools can achieve more rigid fixtures, which will reduce the possibility of cumulative errors. However, this configuration increases the effective stroke of the machine to achieve the required build environment.

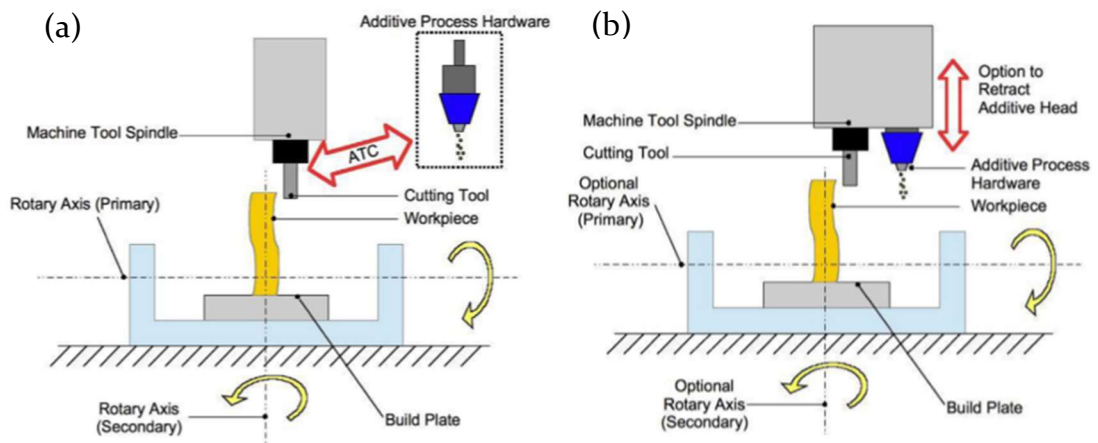


Figure 4-1 – a) shows a configuration using an automatic tool changer. b) shows a configuration using a permanent fixture [238]

The simpler integration of the permanent fixture was preferred for the initial development of the hybrid manufacturing platform. Therefore, a non-branded 5-axis CNC engraver, shown by Figure 4-2 was acquired for approximately

£1,000 and used as the motion stage for the hybrid manufacturing platform. The system is setup as a 3-axis platform with 2 additional axes, resulting in a 3+2 axis system.

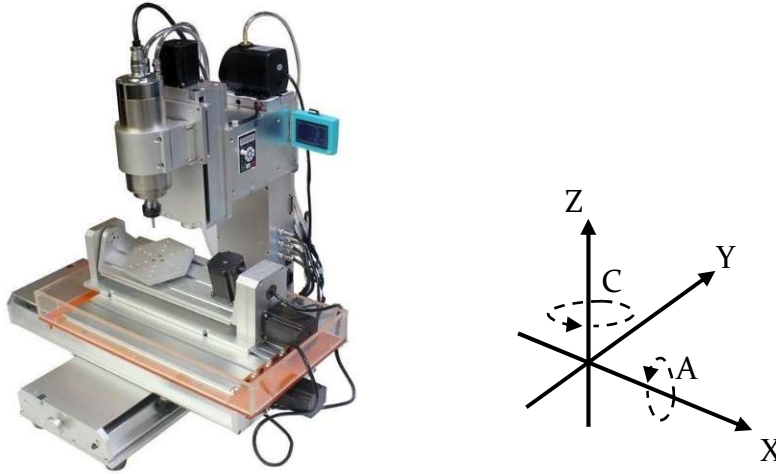


Figure 4-2 – Low cost, non-branded 3+2 axis CNC router provided a suitable platform to develop the additive-subtractive hybrid manufacturing system

Table 4-2 shows a summary of the stage parameters, which are consistent with the aforementioned requirements. The 3+2 axis setup as this would enable the development of the process using the simpler 3 axis configuration but provide increased versatility of the additional axes should the need arise.

Table 4-2 – Shows the specified parameters of the low cost 3+2 axis CNC router

Parameter	
Machine Dimensions	715 × 699 × 610 mm
Number of Axes	3+2
Effective Stroke	400(X) × 300 (Y) × 150 (Z)
Feedrate	0-4,000 mm/min
Power Supply	24V 350W connected to 230V single phase mains
Repeat positioning accuracy	0.01 mm
Repeat positioning precision	0.02 mm

The standard stage is capable of self-homing using the mechanical switch end stops positioned at the furthest point on each of the individual axis. However, homing positions were often inconsistent with switch detection being

unreliable, resulting in collisions between the carriage and stage structure. The inclusion of optical IR light switches with a 5.08 mm gate spacing (OPB916BZ, Optek, Germany) at the midpoint of the X and Y axis provided a more reliable self-homing function. The switches were mounted internally on the respective stages to provide protection from machining debris and dust. An interrupter flag was permanently mounted on the motion carriage, which would approach from the same direction during the homing function, thus improving the repeatability of the automated homing function. An additional connector breakout board was implemented to increase the number of available connections to interface with the different manufacturing processes.

4.2 AM hardware

4.2.1 Ceramic Extruder

The Preeflow volumetric PC pumping system was identified as a suitable micro extrusion system. The ecoPEN range of extruders use an “endless piston” PC mechanism that enables the continuous extrusion of materials with volume flows of 0.12 - 60.0 ml/min with minimum dispensing 0.001-0.06 ml with a repeat accuracy of >99%. The Preeflow dispensing system consists of two elements; the dispenser and the controller unit. The extrusion process is actuated by an integrated motor within the extruder that is controlled by the control unit (ecoCONTROL, ViscoTec, Germany). The extrusion process and process parameters can be controlled manually using the control unit’s user interface (UI), operator footswitch (initiation and termination only) and with a programmable logic controller (PLC). Manual initiation and termination of the extrusion process is unsuitable as the process needs to operate autonomously, without operator intervention. However, the use of constant flowrates throughout the fabrication process enables the programming of extrusion parameters using the controller UI, actuating the extrusion process using remoted control of the footswitch function. PLC control enables autonomous operation of the entire extrusion process including the programming of flowrates, although the additional cost and complexity of implementing PLC control was beyond the requirements for this work. Therefore, the control unit

was interfaced with the connector breakout board using the operator footswitch port, enabling the extrusion process to be initiated and terminated remotely.

The ecoPEN300 (ViscoTec, Germany) is the smallest dispenser in the ecoPEN range measuring $29 \times 29 \times 206$ mm and weighing 280g. The system has an adjustable flowrate of between 0.12 - 1.48ml/min with a minimum dosing volume of 0.001 ml and dosing accuracy of $\pm 1\%$. This volumetric dispensing capacity of this system are consistent with the anticipated volumetric flowrates required for the ceramic AM element of the hybrid manufacturing process. The supply of medium/high viscosity material to the extruder from a material tank or disposable syringe is through a material inlet with a standard G 1/8" connector and is controlled using pneumatic pressures of 0-6 bar. Figure 4-3 shows a CAD model of the eco-PEN300 with connected material barrel and pneumatic connector. The material reservoir, stator and nozzle have been sectioned to show the internal workings.

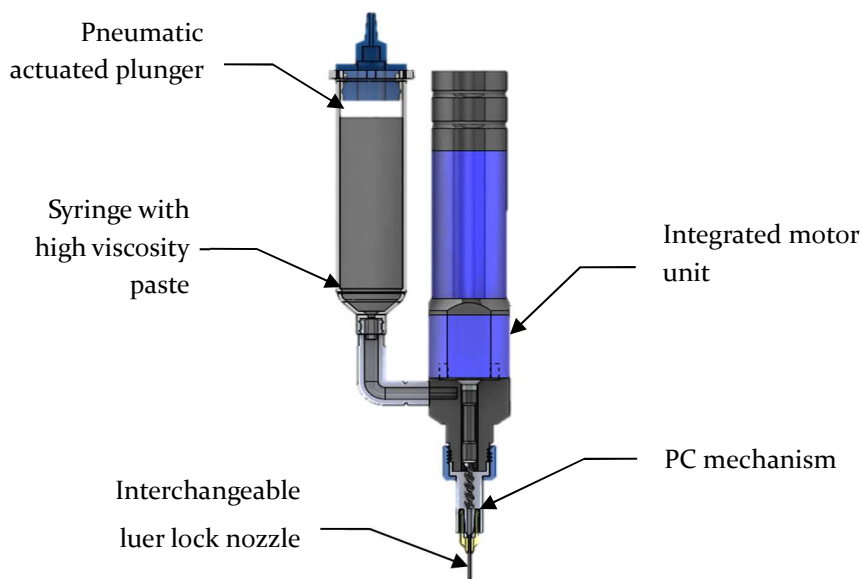


Figure 4-3 – Sectional view of the high-viscosity paste extruder. Attached is a pre-packaged EFD syringe

The material reservoir and PC mechanism of the standard ecoPEN300 is constructed from a mix of polymers such as Delrin (HD-POM) and metal such as stainless steel. As these components are in direct contact with the ceramic feedstock, the wear on the tooling is likely to be greater due to the hard nature of the ceramic material, which can reduce tooling life and increase operating

costs. Measurements of the tooling diameters such as the stator and material reservoir were taken before loading the ceramic feedstock and following the use of ten, 10cc syringes. This was done to monitor any wear on the tooling that may arise from the processing of slurries and pastes containing abrasive material. During the processing of the alumina-based materials, no scratches and striations were visible on the Delrin components. The stainless-steel screw mechanism appeared to become polished after the processing of the ceramic feedstock, which does indicate some abrasion, although this was difficult to quantify by measuring the parts using a digital Vernier callipers (CD-6" ASX, Mitutoyo, Japan). Regular cleaning of the extruder was implemented following the use of 10 syringes or after one week to ensure that the material reservoir did not become contaminated. During this cleaning process, the wear on components was monitored to ensure consistent and reliable material extrusion. Transitioning to harder ceramic materials such as silicon carbide, will require more frequent inspection of the tooling. Excessive tool wear could be problematic due to the increased cost of tooling and the potential contamination of fabricated parts.

4.2.2 Accelerated Forced Convection Drying

The Cirrus series of enclosure heaters (DBK Solutions, Germany) have a compact form factor and a temperature range of 35-120°C, which can be implemented as an accelerated drying mechanism. The Cirrus 40/2 form factor measures 42 × 42 × 112 mm and weighs 260g, which features a 12V axial fan with a 230V heater cartridge. Independent control of the fan and heater cartridge provides greater versatility, such as enabling the fan to be run separately as part of a debris removal system. The 150W variant was selected as this could achieve a surface temperature of 72°C with an airflow of 12.4m³/h. Characterisation of the heaters performance was achieved using a handheld anemometer (AVM-03, Prova, Taiwan) and a calibrated multimeter with a K-type thermocouple attachment (116 digital multimeter, Fluke, US). Figure 4-4 shows the setup that was used to determine the temperature and air speed produced by the selected heating unit. The air speed and temperature measurements were recorded 30

seconds after the heater had been initiated. The heater was allowed to cool to ambient temperature of 19.8°C. The heater was characterised at a distance of 0 mm, 50 mm, 100 mm and 150 mm from the finger guard on the front face of the heater unit. Figure 4-5 shows the results from the characterisation of the heating unit, which achieved a maximum temperature of 74°C at a distance of 0 mm from the unit, which decreased to ~71°C at 50 mm and ~63°C at a distance of 150 mm. The unit achieved a maximum fan speed of 1.7 m/s at 0 mm from the unit, which reduced to 1.5 m/s at 50mm and 1.3 m/s at 150mm. The lower fan speeds are preferred for laboratory environments as residual machining debris is less likely to become airborne. Airborne particulate poses a potential health and safety risk to other laboratory users and may result in ingress of ceramic debris within other elements of the manufacturing platform resulting in increased wear of on components. Moreover, the slower fan speeds generate less noise, which is beneficial within a laboratory environment.

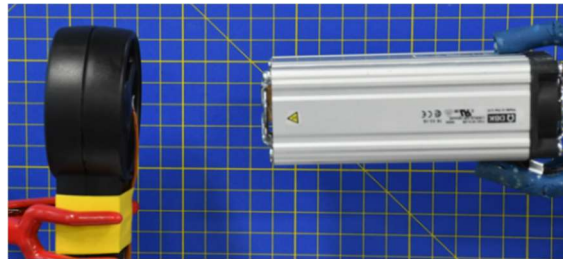


Figure 4-4 – Shows the characterisation of the 150 W enclosure heater with the anemometer and thermocouple in the same configuration shown previously

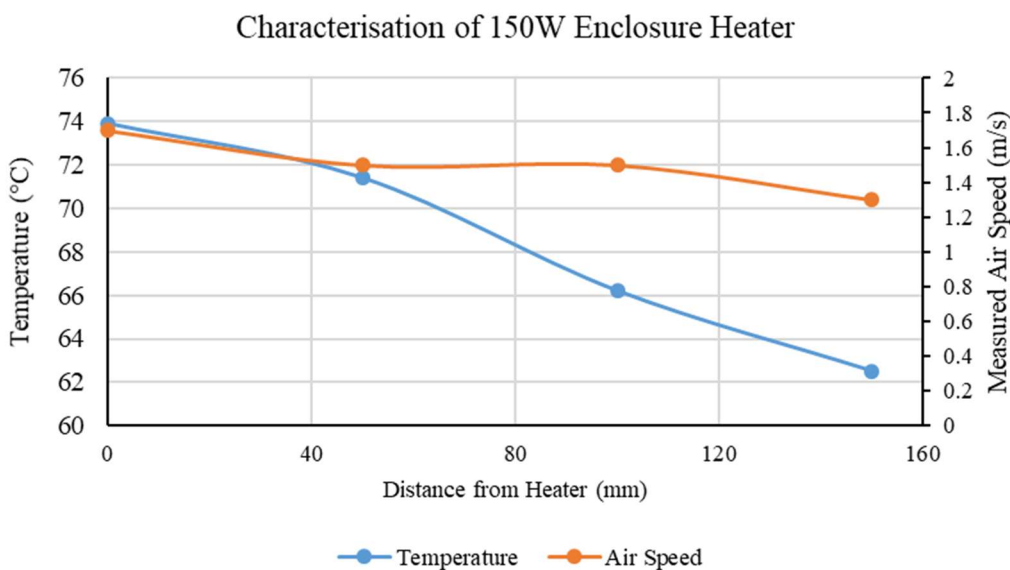


Figure 4-5 – Shows the measured heat and airspeed of the enclosure heater at distances of 0 mm, 50 mm, 100 mm and 150 mm

Characterisation of the units drying with the ceramic feedstock showed comparable drying rates with the handheld unit whilst less particulates were seen becoming airborne. However, this does prevent the unit from being implemented as part of a debris removal system.

4.2.3 Sacrificial Support

A commercial FFF system was used to validate the production of sacrificial support using PLA filament feedstocks, which enabled the production of a spanning bridge structure. FFF hardware is often low cost, readily availability and can be setup in a number of configurations, which often have small form factors. A range of FFF filament feedstocks are readily available including PLA, ABS, PC and specialist filaments which are designed for specific applications such as investment casting. A typical FFF system consists of a hotend, extruder mechanism and build plate, which process either 1.75 mm or 2.85/3 mm diameter filaments. The hotend normally consists of an interchangeable nozzle, heater cartridge, cooling fan and heat break. The heat break is designed to prevent premature melting of the filament feedstock, which would prevent the filament acting as the plunger mechanism. The extruder mechanism consists of a motor that is attached to a hobbled gear and tensioning mechanism to hold the filament. If additional torque or finer spatial resolution is required, gearing mechanisms can be implemented to adapt the extrusion characteristics.

FFF systems are setup as either a direct drive or bowden tube system. Direct drive sees the hotend and extruder positioned adjacent to one another on the print head, with the extruder directly feeding material into the hotend. The short distance between the extruder and the hotend achieves more responsive extrusion characteristics, which reduces the delay between motor input and the effect at the nozzle. However, extruder mechanisms add additional weight and bulk to the print head, which can have a number of adverse effects on the motion platform performance such as reducing accuracy and affecting the acceleration and deceleration of the platform. Furthermore, the additional bulk of direct drive systems may also change the effective stroke/work area of the platform. Alternatively, bowden tube configurations have the extruder and hotend

assemblies positioned away from each other but are connected with a semi-rigid tube, which guides the filament feedstock between extruder and hotend. The hotend is located on the print head of the system whilst the extruder is often located externally to the build environment. Locating the components separately shrinks the form factor of the print head, whilst reducing weight and bulk on the motion platform. Moreover, locating the extrusion system away from the build environment can provide greater protection from the ingress of ceramic debris generated by the machining process, which may result in additional wear of transmission components. Moreover, locating the extruder elsewhere enables better placement of the system to improve accessibility for maintenance and material changes. However, the bowden tube system is likely to reduce the responsiveness of the extrusion mechanism, which may cause defects such as increased surface roughness within the support structures that may be transferred onto the ceramic parts. Furthermore, the increased friction between the filament and the tube necessitates the use of higher torque extruders, which typically increases the size and complexity of the extruder.

An aluminium/stainless steel hotend (V6 hotend, E3D, UK) configured to use 1.75 mm filament, which measured $30 \times 31 \times 62.3$ mm (including 12V cooling fan) and weighs 45.4g was implemented using a bowden tube configuration. The standard hotend is capable of operating at a maximum working temperature of 285°C using a thermistor (400°C if used with thermocouple), which enables the processing of an extensive range of FFF filament feedstock materials including PLA. The hotend is a modular construction with a number of components that are upgradable and modifiable, enabling repair and upgrade, which increases the versatility of the system. This was implemented in conjunction with an open source direct drive extruder (Bulldog Lite Extruder, Plugit Ltd, Hong Kong) that was configured to use 1.75 mm filament in a bowden tube setup. The actuation motor is a Nema 17 stepper motor, which enables direct integration with the manufacturing platform. A Ø220 mm aluminium heated build plate (Sintron, Taiwan) with a maximum temperature of 110°C was also implemented as part of the sacrificial support extrusion system to increase the range of materials that can be processed. Materials such as ABS and PC

require a heated build plate to improve adhesion and prevent distortion. Furthermore, the heated build plate can be operated during the ceramic deposition process to decrease drying times and to improve the uniformity of the rate of evaporation, which has been noted as potentially causing damage to green state parts.

Temperature control of the hotend and the heated bed is achieved using two manually programmable PID controller (Thermostat ITC-100VH, Inkbird, China) connected through the additional connector breakout board. This enables the remote initiation and termination of the hotend and heated bed, whilst temperature control is done by the PID controllers. The controllers have an accuracy of $\pm 0.2\%$ ($< 1,000^{\circ}\text{C}$) and temperature compensation of $0 - 50^{\circ}\text{C}$ with a sample period of 0.5s [239]. The controllers are manually programmed using the user interface, providing control over the max temperature, drift and heating rates.

PLA is a low cost, readily available aliphatic polymer that is derived from fermented plant starch, is which widely used by many FFF systems. The sacrificial support system was used to process 1.75 mm white PLA filament (RS Pro, RS components, UK), which has a manufactured tolerance of $\pm 0.05\text{mm}$ and a melting temperature of $145-160^{\circ}\text{C}$ and a softening temperature of 60°C . The filament can be printed without the use of a heated bed, but if required a heated bed temperature of $\pm 35-60^{\circ}\text{C}$ is recommended. This specification is compatible with the hardware implemented as part of the sacrificial support extruder and

4.3 Machining Hardware

4.3.1 Spindle

The machining spindle is required to enable the surface machining of individual layers and facilitate the creation of high-fidelity features and removal of defective layers, which will typically involve more substantial material removal than surfacing operations. To fulfil these requirements the spindle needs to be capable of achieving spindle speeds of 5,000 – 30,000 RPM with sufficient

torque and minimal spindle run out. Additionally, the system needs to have a compact form factor to maximise the production volume, be suitable to be operated within a laboratory environment and be compatible with a range of tooling.

A low-cost engraving spindle that was supplied with the motion platform had a diameter of 52 mm and a length of 200 mm and weighed 1.2 kg. The spindle could achieve speeds of 3,000-12,000 RPM with a maximum power of 400W. Runout is the rotational inaccuracy caused misalignment along the central axis, which causes inaccuracies when machining. The spindle collet had a measured runout of $\pm 28 \mu\text{m}$, which would equate to a $\sim 10\%$ error when using tooling with a diameter of 0.3mm. The spindle has a fixed collet system that uses ER11 standard tooling collets, which are compatible with cutting tools with shanks diameters of 1-7 mm.

Alternatively, a precision micromachining system was identified, which could provide spindle speeds of up to 80,000 RPM with a maximum power of 350W and measured collet runout of $\sim 1 \mu\text{m}$. The system consists of an electric motor, spindle and controller. A pneumatically actuated ATC spindle (NR50-5100 ATC, Nakanishi, Japan) would provide increased manufacturing capability by enabling the switching of cutting tools without operator intervention. The spindle has a diameter of $\text{Ø}50$ mm and length of 116 mm and weighs 1,370g. The spindle uses collets that can hold tools with a shank diameter of $\text{Ø}2$ -6.35 mm and achieve a maximum speed of 50,000 RPM. Both the NR-3060S and NR50-5100 use ceramic bearings, which offer increased tooling life, which is an important factor when machining ceramic materials.

The low-cost spindle, whilst capable of machining the ceramic parts, provides insufficient spindle speeds and has a large form factor that reduces the effective build area of the manufacturing platform. A more considerable shortcoming however, is the spindle runout that will adversely affect manufacturing resolution and the minimum feature size. Therefore, the high precision spindle is most appropriate for the hybrid manufacturing platform due to the smaller spatial resolution that can be achieved. The fixed collet spindle provides the

smallest form factor with the highest spindle speeds, although the inability to autonomously switch between cutting tools offsets these benefits by reducing the versatility of the machining element. While the ATC spindle setup is the heaviest, with a large form factor, the ability to remotely switch tooling expands the feature production capability of the manufacturing platform. However, the collet remains fixed within the ATC during tool changes, meaning that the cutting tools are required to have the same diameter shank to switch between tooling without operator intervention.

4.3.2 Automatic Tool changer

The implementation of an ATC machining spindle necessitates the implementation of a tool storage system that contains a range of cutting tools to enable repeatable transition between different cutting tools. Conventional CNC milling machines often use a tool storage bandolier, with an indexing mechanism enabling tool deposition and collection to occur at the same location. Furthermore, these systems often use removable collet mechanisms, whereby the collet is permanently attached to the cutting tool, enabling the use of tooling with different shank diameters. However, the permanent collet fixture means that tools in the tool holder need to be the same diameter. Furthermore, the $\text{\O}50$ mm ATC spindle requires a minimum of 25 mm spacing between tools to avoid interference when depositing and collecting tools. Investigation of cutting tools that are compatible with the ATC spindle and capable of machining ceramic materials revealed that tools typically used shank diameters of $\text{\O}3 - 4$ mm. The storage block was manufactured from Delrin due to its dimensional stability and low friction, which will aid tool removal and prevent wear due to being softer than the tool bits. The block measures $40 \times 180 \times 50$ and is permanently mounted alongside the build plate to provide convenient access during fabrication. The tool storage solution features nine $\text{\O}4 \times 15$ mm holes in two rows at a pitch of 40 mm.

4.4 Hardware Integration

4.4.1 Fixture Design

Mounting of the aforementioned processes necessitated the design and manufacture of a bespoke fixture assembly. The assembly structure was designed to minimise the spacing between the various processes in order to maximise the available build space, whilst aligning the central axis of the processes along the X axis to simplify the commissioning and validation stages. The ecoPEN was selected to be the primary manufacturing system on the manufacturing platform and was therefore used as the datum reference when mounting the other manufacturing processes. Therefore, the ecoPEN300 was rigidly mounted onto the motion platform without any Z retraction mechanism.

The rigid mounting of tooling adjacent to one another has been applied on FFF systems to enable the use of dual extrusion heads. However, collisions between inactive tooling and the work piece are a common occurrence, resulting in damage to the part and/or detachment from the build plate. Therefore, many dual extrusion systems implement a retraction mechanism to provide additional clearance between the inactive tooling and the work piece. Rigid mounting of the ecoPEN ceramic extrusion system requires the spindle and sacrificial support extruder to be positioned above the height of the ecoPEN when inactive and lower when active. Therefore, a retraction distance of ~10 mm between active and inactive positions would provide sufficient clearance to the other manufacturing elements to prevent collisions with the work piece.

The implementation of the ATC spindle provides a convenient mechanism with which to provide additional clearance during periods of inactivity. The ATC collet cannot be closed without a tool being present due to excessive compression of the collet causing damage to the spindle bearings. Therefore, a blanking mechanism with the same diameter as the cutting tools was inserted into the collet during periods of inactivity. Decreasing the length of the blanking adapter by ~12mm was sufficient to achieve the required clearance between the spindle and the ecoPEN nozzle.

The lightweight of the sacrificial support hotend enabled the use of a linear, push-action solenoid with a maximum stroke distance of 15 mm (Z857AA62, Mecalectro, France). The solenoid measures $32 \times 27 \times 60.5$ mm providing a maximum force of 5.9N, with an internal spring to retract the solenoid when power is terminated. The push bar on the solenoid was integrated into the attachment bracket for the hotend that was designed around the mounting connector used for direct mount applications. Mounting of the hotend attachment onto a linear slide assembly (ER513+40L, THK, Japan) with vertical running straightness of $2 \mu\text{m}$ and horizontal running straightness of $4 \mu\text{m}$ over <20 mm stroke length. Figure 4-6a shows the CAD design of the mounting bracket that was designed to replace the front face of the Z axis. The mounting bracket aligns the central axis of the manufacturing processes along the X axis to streamline the commissioning process. Figure 4-6b shows the ecoPEN mounted centrally on the motion platform alongside the sacrificial extruder attached to the linear solenoid and the machining spindle with ATC.

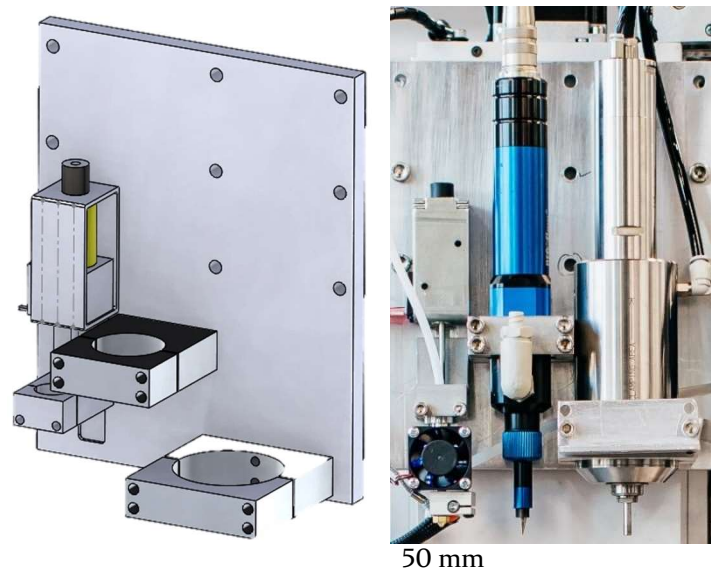


Figure 4-6 – (left) shows a CAD representation of the mounting fixture (right) shows the manufacturing apparatus mounted in the fixture on the motion platform

The use of interchangeable nozzles necessitated the calibration of the extruder to the build plate, each time the nozzle was removed or replaced. Calibration to the build plate when switching between nozzles of the same length was done using a $25 \mu\text{m}$ slip gauge that was slid between the nozzle and the build plate, applying the offset within the control software. Switching between nozzles of

significantly different lengths, for example switching from a ¼” nozzle to a ½” required the extruder to be manually moved within the mount before calibrating with the bed.

4.5 Control Software and Integration

The control software is intended to operate on a dedicated computer running a standard operating system (Windows 7, Microsoft, US). An additional parallel port PCIe card was added to the computer to provide two parallel port connections that were connected to the motion platform controller and the additional breakout connector board. The Motion control board was used to control the 3 axis motion platform with the 4th axis being used to drive the FFF extruder stepper motor. The connector breakout board connector was interfaced with remaining elements of the system such as the ceramic extruder controller, spindle controller, FFF hotend and heated bed and the solenoids used to retract the FFF head and open/close the ATC collet. Appendix D shows a schematic of the hardware that is used to interface the various manufacturing elements. Figure 4-7 shows a block diagram representing the interfacing of the control software with the manufacturing platform.

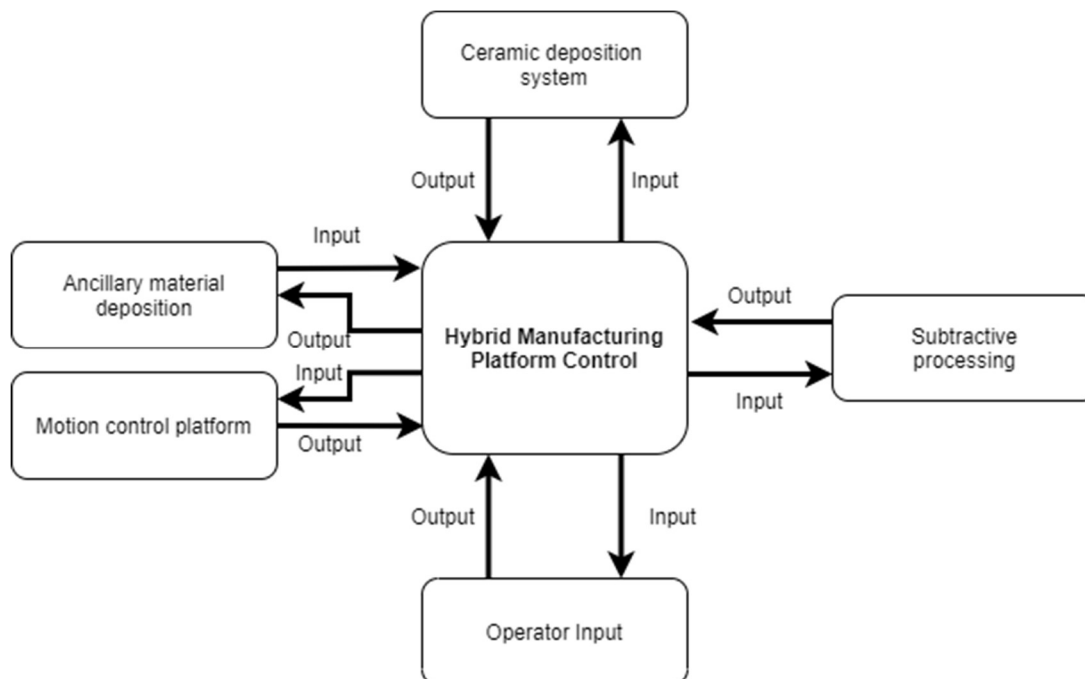


Figure 4-7 – Shows the input-output block diagram for the proposed hybrid manufacturing system

The control software of the hybrid manufacturing platform provides a number of functions including:

- Sending command signals to the manufacturing hardware to control motion and initiate/terminate manufacturing processes.
- Providing a user interface so the operator can interact with the system.
- Reading and interpreting the G code commands within the toolpath file.
- Store and apply tool offsets and tool change locations

A number of open source CNC control software packages are available such as DesKam (DAKEngineering,US), LinuxCNC 2.7 (Linux, US) and Mach3 (Newfangled Solutions, US). Both software packages are designed to control a range of manufacturing equipment including milling machines, lathes, 3D printers and plasma cutters. The intention to utilise an existing PC running Windows 7 resulted in Mach3 being the preferred option as this avoid altering the operating system. Mach3 is capable of controlling up to 6 axis CNC machines, enabling the implementation of a 5-axis motion platform whilst retaining the existing control interface of the FFF extruder. The software enables the implementation of full closed-loop control should the need arise, which can be achieved by the inclusion of encoded stepper motors or DC servo motors on the motion platform. Mach3 has a fully customisable user interface, with the facility to create custom M-codes and macros using VBscript. This feature enabled the creation of macros for functions such as tool changes with a visual display on the user interface indicating the status of manufacturing processes and the tool that is currently within the machining spindle.

4.6 System commissioning and validation

4.6.1 Bed Levelling

The system commissioning and validation of the manufacturing platform involved a number of elements to ensure the correct function of manufacturing elements, whilst determining the repeatability of the 3 axis motion platform. Bed levelling of the build plate was undertaken using an analogue dial test indicator (DTI) (DG-M, Linear Tools, UK) with a stroke length of 10 mm,

resolution of 0.01 mm and an accuracy of ± 0.020 . The DTI was mounted within a Delrin mount that was located in the mounting bracket of the ecoPEN, which was positioned centrally to the build plate. The DTI was lowered to the build plate, until the dial indicated 2.0 mm, to provide sufficient preload to prevent errors that may arise from the DTI bottoming out. Figure 4-8a shows the DTI positioned centrally on the build plate. Figure 4-8b shows the DTI at the maximum $-Y$ position, the position of which is indicated by the red dot on the inset diagram. The DTI was traversed to the furthest \pm locations on the build plate along the X and Y planes as indicated by inset Figure 4-8b.

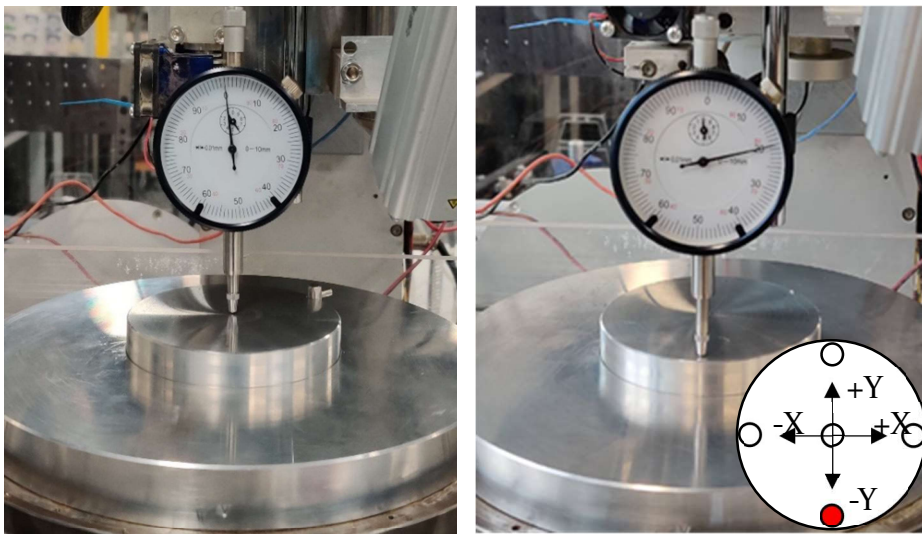


Figure 4-8 – Shows the process of levelling the build plat relative to the Z axis motion platform with the DTI zeroed in the centre of the bed that is moved to the positions shown by the insert

Correction of the measured offsets was achieved using metal shims located under the main build plate. The build plate was determined to have a levelness of $\pm 10 \mu\text{m}$ between the furthest points along the X and Y planes.

4.6.2 Z-axis repeatability

Determining the repeatability of Z axis motion was achieved using the DTI (DGM, Linear Tools, UK) with a stroke length of 10 mm, resolution of 0.01 mm and an accuracy of ± 0.020 and slip blocks with a resolution of 0.005 mm ($5 \mu\text{m}$). The default motor control parameters within the control software enable a maximum feedrate of 800 mm/min with an acceleration 300 ms^{-2} . The software enables a maximum feedrate of 3,200 mm/min with a maximum acceleration of 800 ms^{-2} . The orientation of the motion stage causes the driving force to be

applied to the same face of the ball screw, removing the need to account for backlash within the system. A preload value of 4 mm was applied to the DTI to provide sufficient travel to enable the use of the slip blocks, with the smallest denomination block measuring 1.000 mm. During the fabrication of a part, the Z axis will be moved incrementally such as layer changes during AM processes or dynamically over short distances <5 mm when completing machining operations. Therefore, characterisation of the Z axis accuracy and repeatability was undertaken using actuation distances of 0.2 mm, 0.5 mm, 1 mm, 2 mm, 3mm, 4mm and 5mm as these were consistent with Z moves associated with AM and subtractive manufacturing processes. Feedrates of 800 mm/min, 1,600 mm/min, 2,400 mm/min and 3,200 mm/min were investigated in conjunction with accelerations of 300 ms⁻², 550 ms⁻² and 800 ms⁻². Figure 4-9 shows the measurement of the travelled distance using a DTI in conjunction with a slip block. A distance of 5 mm was travelled using a feedrate of 800 mm/min using an acceleration of 300 ms⁻², which demonstrates that the Z axis travelled 5 ± 0.01 mm.



Figure 4-9 – Shows the validation of the distance moved using a 5 mm slip block

Table 4-3 shows the repeatability of the Z axis travelling 0.2 – 5 mm using constant acceleration of 300 ms⁻². 10 measurements were taken for each distance at each feedrate. These tests demonstrate that the Z axis had a minimum accuracy of 35 µm. The full dataset for this test are shown in Appendix E.

Table 4-3 – Shows the repeatability data obtained for the Z axis – showing the average of 10 measurements for each set of parameters

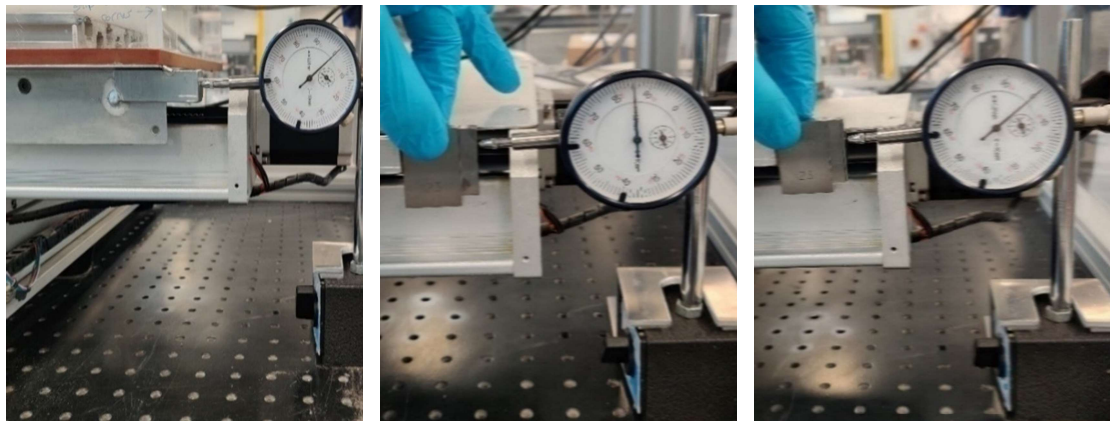
Distance	Repeatability (μm)			
	800 mm/min	1600 mm/min	2400 mm/min	3200 mm/min
0.2	± 0	± 7.5	± 0	± 0
0.5	± 2.5	± 2.5	± 2.5	± 0
1	± 2.5	± 2.5	± 0	± 0
2	± 15	± 12.5	± 7.5	± 10
3	± 17.5	± 10	± 2.5	± 10
4	± 17.5	± 0	± 5	± 0
5	± 7.5	± 2.5	± 5	± 0

4.6.3 X-Y axis repeatability

The accuracy and repeatability of the X and Y was determined using a DTI with a resolution of 0.01 mm and an accuracy of ± 0.020 and slip blocks with a minimum resolution of 0.005 mm (5 μm). Backlash is defined as “the maximum distance or angle through which any part of a mechanical system may be moved in one direction without applying appreciable force or motion to the next part in mechanical sequence” [240]. Backlash can cause accuracy errors when reversing the direction of the transmission elements, as there is a delay between the motor input and the stage moving, resulting in the stage being shorter than the specified distance. This can have a number of implication in the production of circular/round geometries, which can exhibit a more elliptical geometry as a result of the backlash. Backlash is often eliminated by the inclusion of a backlash pre-tensioning nut, which eliminates the delay between motor and stage movement. However, the motion platform did not have such as feature, which therefore required the backlash to be determined. For the X axis, the DTI was configured in the datum position as illustrated by Figure 4-10a, with a preload of 4 mm. The motion stage was moved to a specified distance from the datum then returned to the original position with the DTI value being recorded. The specified travel distances were 30 mm, 60 mm, 90 mm, 120 mm and 150mm as these were representative of the distances to be travelled during the fabrication of precision 3D ceramic parts. The stage was reset to ensure that the ball-nut was in contact with the leading edge of the ball screw, after which the

DTI was zeroed. This process was repeated for the Y axis, with both axes having a measured backlash of between 40 - 60 μm .

The accuracy and repeatability of the stages was determined by moving the stage to a specified distance, using slip blocks to determine the offset between the specified and actual distance travelled. Figure 4-10a shows the DTI in the datum position, which has been zeroed against the measurement surface of the motion stage. The slip blocks are wrung together by sliding the edges of two adjacent blocks together, which causes them to adhere together. Figure 4-10b shows the motion stage after it has been travelled 30.000 mm along the X axis, with 30.000 mm slip (23 mm and 7 mm blocks wrung together) blocks placed between the measurement point and the DTI, which indicates that the stage is $\sim 150 \mu\text{m}$ short of the desired location. Zeroing of the DTI was achieved using 30.170 slip blocks that were formed from a 23.000 mm, 6.000 mm and 1.170 mm slip blocks.



a) Datum Position b) 30.00 mm slip block c) 30.17 mm slip block

Figure 4-10 – a) shows the setting on the DTI in the datum position. b) shows the checking of the distance using slips blocks with the same value as the nominal distance. c) shows the slip blocks with the required width to zero the DTI

Accuracy and repeatability were determined over distances of 30 mm, 60 mm, 90 mm, 120 mm and 150 mm at feedrates of 800 mm/min, 1,600 mm/min, 2,400 mm/min and 3,200 mm/min using accelerations of 300 ms^{-2} , 550 ms^{-2} and 800 ms^{-2} . Ten repeat measurements were taken for each feedrate at each distance, with the difference between the specified distance and the slip block value being recorded. Between each test an adjustment movement was included to mitigate the effects of backlash on the measurement. The adjustment

movement involved returning the motion stage to a value of -2.00 mm, after which it was returned to 0.00 mm and the DTI were zeroed. This removes the backlash error from the positional measurements. If the stage failed to reach the nominal distance a value of N/A was recorded, and the platform was reset. The full dataset for this test is shown in Appendix E.

The effect of acceleration on repeatability was investigated using feedrates of 1,600 mm/min and 3,200 mm/min using accelerations of 300 ms⁻², 550 ms⁻² and 800 ms⁻². Figure 4-11 and Figure 4-12 shows the average distance from the nominal of the X and Y axes respectively accelerating to a target feedrate of 1,600 mm/min.

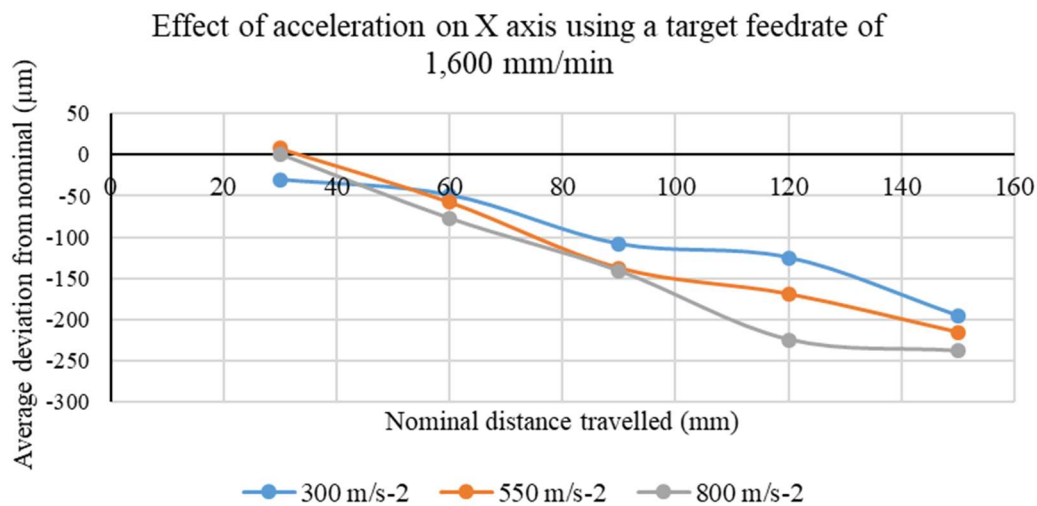


Figure 4-11 – Shows the average deviation stage from the nominal for various accelerations with a target speed of 1,600 mm/min on the X-axis motion stage. Error bars have been omitted for clarity

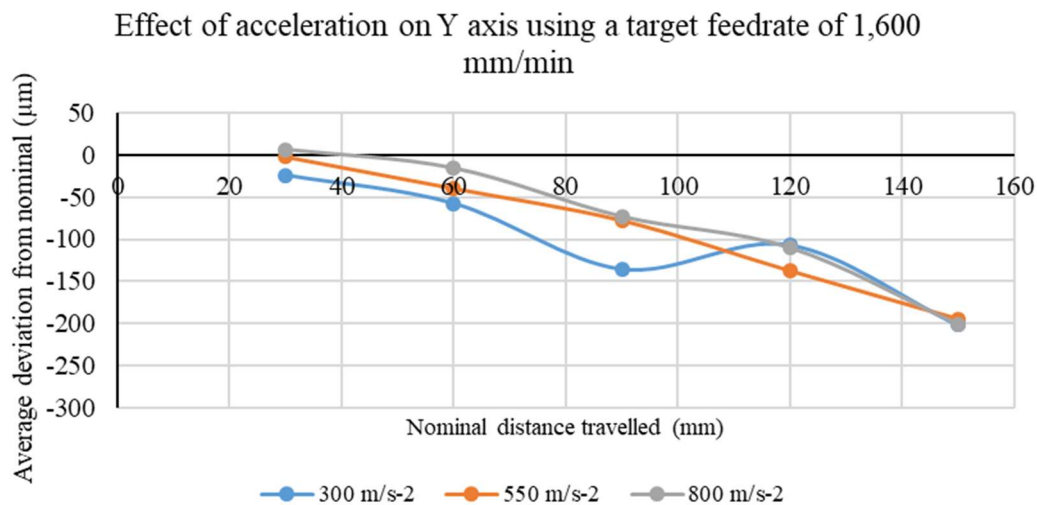


Figure 4-12 - Shows the average deviation stage from the nominal for various accelerations with a target speed of 1,600 mm/min on the Y-axis motion stage. Error bars have been omitted for clarity.

The general trend indicates that increasing the nominal distance causes an increase in the deviation from the nominal. The trend shown by Figure 4-11 indicates a systematic error within the system, due to the comparable magnitude of deviation at all distances. It also shows that increasing the rate of acceleration results in an increase in the deviation from the nominal. Further investigation into this error and optimisation of the motion platform should result in a reduction of this error. However, the trend shown in Figure 4-12 indicates the presence of a potential random error in addition to a systematic error due to the shift in the deviation measured at 90 and 120 mm distances. During the tests, both the X and Y axis experienced intermittent stalling of the motion platform when moving to nominal distances >90 mm.

Table 4-4 shows a summary of the average data for the X and Y axes. Positive values within this table signify that the measured distance exceeded the nominal distance.

Table 4-4 – Shows the average deviation from the nominal distance and the range of values that were recorded for the X and Y axis accelerating at various accelerations to a maximum feedrate of 1,600 mm/min. The calculated standard deviation are also shown.

Acceleration	Nominal Distance (mm)	Average Deviation (μm)		Spread of Measurements (μm)		Standard Deviation (μm)	
		X	Y	X	Y	X	Y
300	30	-31	-24	55	80	16	26
	60	-49	-58	45	35	17	11
	90	-109	-136	35	75	13	20
	120	-125	-107	55	145	19	45
	150	-196	-202	45	60	13	16
550	30	8	-2	90	35	26	11
	60	-58	-40	40	55	12	14
	90	-138	-78	50	80	17	22
	120	-169	-137	50	80	16	23
	150	-216	-195	45	120	14	39
800	30	1	7	45	35	16	11
	60	-77	-16	60	45	19	13
	90	-141	-73	60	45	16	12
	120	-224	-110	55	85	16	27
	150	-238	-201	80	75	29	23

Figure 4-13 and Figure 4-14 shows the average distance from the nominal of the X and Y axes respectively accelerating to a target feedrate of 3,200 mm/min respectively.

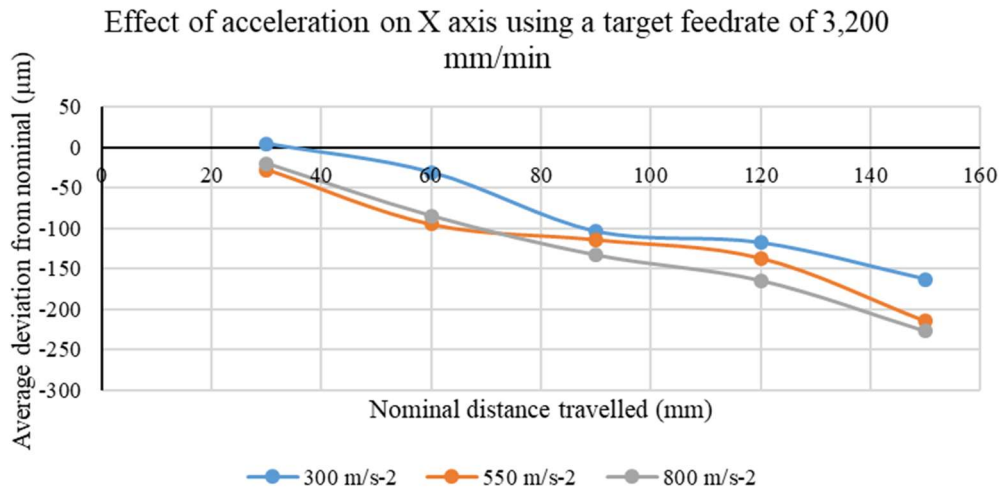


Figure 4-13 - Shows the average deviation stage from the nominal for various accelerations with a target speed of 3,200 mm/min on the X-axis motion stage Error bars have been omitted for clarity

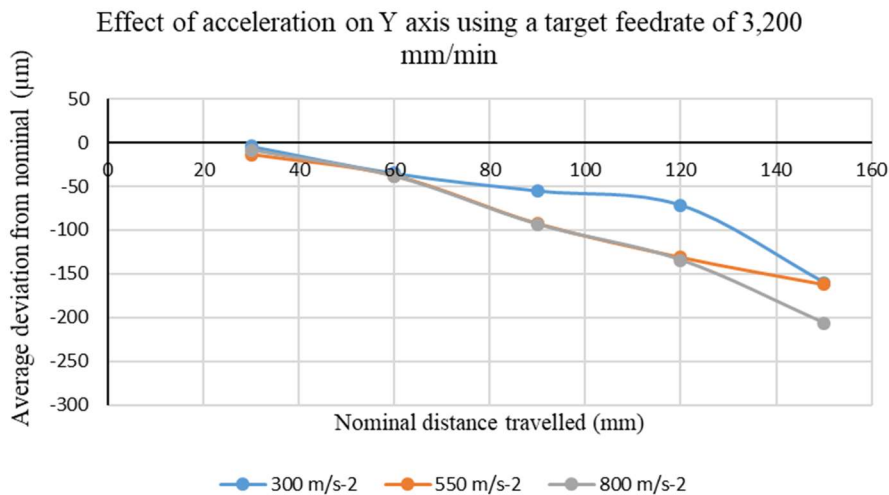


Figure 4-14 - Shows the average deviation stage from the nominal for various accelerations with a target speed of 3,200 mm/min on the Y-axis motion stage Error bars have been omitted for clarity

Figure 4-13 and Figure 4-14 show the same trend, where increasing the nominal distance results in a larger deviation from the nominal distance. The trends indicate that accelerating at 300 ms⁻² resulted in the lowest deviation from the nominal value. Furthermore, accelerating at 300 ms⁻² did not result in the stalling of the motion stage on either the X or Y axis.

Table 4-5 shows a summary of the parameters measured during the investigation of acceleration with a target feedrate of 3,200 mm/min.

Table 4-5 - Shows the average deviation from the nominal distance and the spread of measurements that were recorded for the X and Y axis accelerating at various accelerations to a maximum feedrate of 3,200 mm/min. The calculated standard deviation are also shown.

Acceleration	Nominal Distance (mm)	Average Deviation (μm)		Spread of measurements (μm)		Standard Deviation (μm)	
		X	Y	X	Y	X	Y
300	30	5	-4	60	35	23	13
	60	-31	-35	25	40	9	14
	90	-104	-55	70	65	22	22
	120	-118	-71	80	120	28	51
	150	-163	-160	50	160	20	54
550	30	-28	-14	35	35	10	10
	60	-95	-38	50	70	15	22
	90	-114	-93	95	60	25	20
	120	-137	-131	70	70	23	25
	150	-214	-162	45	135	15	54
800	30	-20	-9	35	45	9	16
	60	-85	-39	80	55	23	19
	90	-133	-94	50	60	17	20
	120	-164	-134	100	130	37	50
	150	-227	-207	100	175	32	58

Characterising the effects of feedrate on the repeatability of the motion stage were undertaken using a constant acceleration of 300 ms^{-2} as this was determined to be the most repeatable acceleration. Various feedrates of 800 mm/min, 1,600 mm/min, 2,400 mm/min and 3,200 mm/min was investigated on both X and Y axes. Figure 4-15 and Figure 4-16 shows the average deviation from the nominal distance using the aforementioned feedrates.

Distance from nominal at increased travel distances for multiple feedrates
- X axis

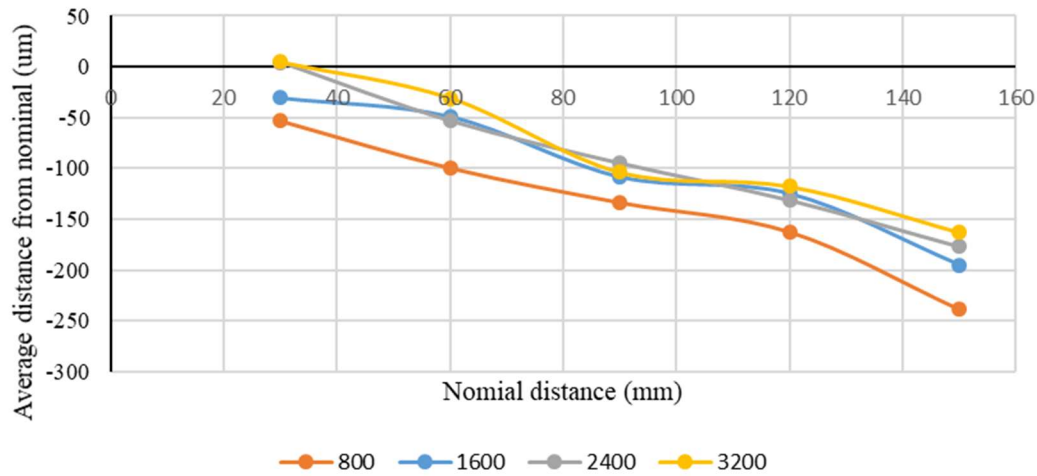


Figure 4-15 – Shows the average deviation stage from the nominal for various feedrates using an acceleration of 300 ms^{-2} on the X-axis motion stage Error bars have been omitted for clarity
Error bars have been omitted for clarity

Distance from nominal at increased travel distances for multiple feedrates
- Y axis

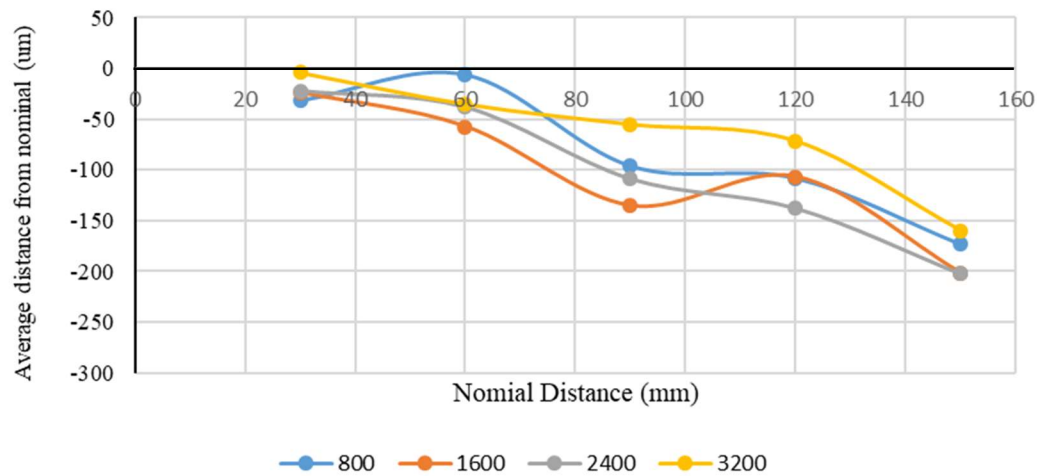


Figure 4-16 - Shows the average deviation stage from the nominal for various feedrates using an acceleration of 300 ms^{-2} on the Y-axis motion stage Error bars have been omitted for clarity
Error bars have been omitted for clarity Error bars have been omitted for clarity

The trends shown by Figure 4-15 and Figure 4-16 indicate a negligible effect of feedrate on the repeatability of the motion platform. Figure 4-15 indicates the same systematic error as shown previously, whilst Figure 4-16 indicates the presence of both systematic and random errors. Both X and Y stages demonstrate comparable repeatability across the feedrates that were investigated. However, both X and Y stages would stall intermittently when

exceeding distances >70 mm at feedrates of 2,400 mm/min and 3,200 mm/min. Table 4-6 shows a summary of the measured deviation values for the aforementioned feedrates with the average and standard deviation shown.

Table 4-6 - Shows the average deviation from the nominal distance and the spread of measurements that were recorded for the X and Y axis accelerating to various feedrates at an acceleration of 300 ms^{-2} . The calculated standard deviation are also shown.

Nominal Distance (mm)	Average distance from the nominal (μm)		Spread of measurements (μm)		Standard Deviation (μm)	
	X	Y	X	Y	X	Y
30	-19	-21	200	85	38	23
60	-58	-34	200	110	37	25
90	-110	-101	175	170	32	37
120	-136	-109	175	180	34	42
150	-198	-185	145	210	37	37

Figure 4-17 shows the averaged repeatability of the X and Y axes for all feedrates and a constant acceleration of 300 ms^{-2} . A maximum of 40 data points is included in each box plot, with some plots containing fewer points due to the stalling of the motion stage.

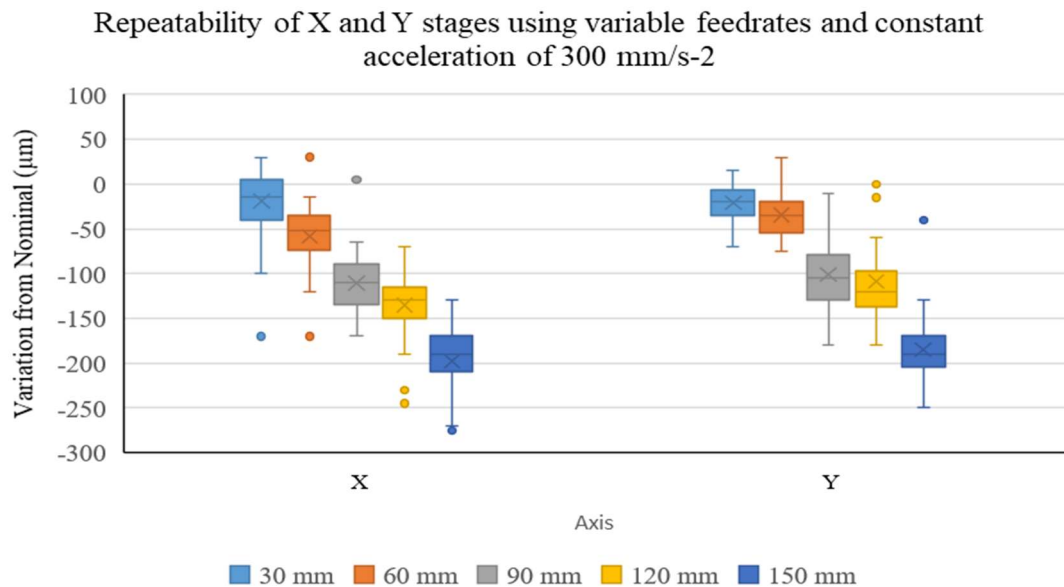


Figure 4-17 – Shows the deviation from the nominal for all of the data collected during the aforementioned tests

The data shows similar linear trends for both X and Y axes. The X-axis has an average spread of $179 \mu\text{m}$ with an average SD of $35.6 \mu\text{m}$ across all distances,

whilst the Y-axis has an average spread of 151 μm with an average SD of 32.8 μm . The linear trend of both axes indicates that manufacturing tolerances should be consistent during the fabrication of large or multiple parts (manufactured simultaneously). Both axes have a number of results that are classified as anomalous results, which are indicative of random errors within the system, which typically cannot be corrected for. Despite this, the repeatability of the X and Y stages using a maximum feedrate of 800 mm/min and a maximum acceleration 300 ms^{-2} was determined to be adequate to continue the development and validation of the hybrid manufacturing process. This was due to the limitations of the selected hardware such as the maximum material flowrate of the ecoPEN300 extruder and the behaviour of the feedstock material at faster speeds, which had a tendency to produce incomplete beads of material. Therefore, increasing the speed of the motion platform required a higher material flowrate and would necessitate the use of variable extrusion rates to account for higher speeds and accelerations. Furthermore, increasing the speed and acceleration of the motion platform, whilst using a constant extrusion rate increases the possibility of defects due to excess material deposits when changing direction and discontinuities in the material flow.

4.7 Component Toolpath generation

The lack of hybrid-specific toolpath generation software was an important limitation during the development of the hybrid manufacturing process due to the time-consuming and error-prone process of combining toolpath files for the individual processes into a single part file. The fabrication of precision 3D ceramic components requires the generation of toolpaths for the ceramic extruder, support extruder and the machining spindle. To enable the autonomous production of a part without operator intervention necessitates the amalgamation of the various toolpaths into a single part file. Commercial software vendors such as Autodesk are now combining AM software packages such as Netfabb within conventional manufacturing software packages such as PowerMill. However, this software is not yet publicly available and would be prohibitive in terms of cost as the PowerMill software package is commercial

software. Therefore, toolpath generation needed to be undertaken using separate, process specific software that were post-processed into a single file. A typical part file for the hybrid manufacture of a 3D ceramic part consists of the following operations:

- Substrate/raft toolpath
- Ceramic extruder toolpath
- Support toolpath
- Layer surfacing toolpath
- Feature creation toolpath
- Post processing/finishing operation

Components are designed using commercially available CAD software packages such as SolidWorks 2018 (Dassault Systèmes, France) and Fusion360 (AutoDesk, USA). Solidworks provides an extensive range of geometric modelling tools that can produce complex parts, which can be output as an STL file for use AM slicing software. CAM functionality is provided by SolidCAM (SolidCAM Ltd., Germany), which is a paid plugin within the SolidWorks software at an additional cost. SolidWorks provides users with the function to specify custom AM systems to aid the generation of STL files, although direct export to AM slicing software is not provided. Alternatively, Fusion360 provides both CAD modelling and CAM functionality as an all-in-one integrated package. Whilst Fusion360 provides less advanced functionality for 3D modelling than SolidWorks, it is capable of directly outputting to AM slicing software, thus reducing the likelihood of translational errors. Although, SolidWorks provided greater 3D modelling functionality, the requirement to purchase additional software largely mitigates the benefit of the additional functionality for this body of work. Therefore, Fusion360 was used to model part geometries that were produced during this work.

The generation of AM toolpaths was achieved using commercially available AM slicing software. Repetier Host 2.1.6 (Hot-World GmbH & Co., Germany) is open source slicing software that uses slicing algorithms such as Cura and Slic3r. These slicing algorithms provide extensive control over slicing and printing

parameter such as infill densities, infill patterns, variable layer thicknesses and post-processing scripts for both ceramic part and sacrificial support structures. Slic3R provided greater customisation over a broader range of manufacturing variables and was therefore used as the primary slicing algorithm with Repetier Host 2.1.6. Custom slicing profiles based on the intended machine parameters such as nozzle size were created within Slic3R and Repetier Host ensure continuity between the two software packages and streamline the generation of machine toolpaths. Adaptive slicing settings within Repetier Host slicing software were used to adjust the height of layers to ensure sufficient material could be removed during the interlayer machining to eliminate the defects and infill patterns mentioned previously. The oversizing function enables the controlled enlargement of the part's geometric dimensions in the X, Y and Z axes, ensuring that sufficient surplus material is available to achieve the required dimensional tolerances. Parts were scaled by +0.5mm, accounting for the repeatability of the stages and the selected nozzle diameter, whilst preventing excessive material waste during the subtractive processing.

Machining toolpaths were generated using the CAM functionality within Fusion360 by means of a custom machine configuration, which was based on the machine specification and the results from the system validation. Custom profiles for the cutting tools were created using the supplied tooling diagrams. Layer surfacing operations that were implemented after the drying of each layer were generated using the facing function using the top-down outline of the part to define the machining limits. Whilst this method is an inefficient method of machining the part, the generated toolpath was able to be implemented on all layers, which streamlined the amalgamation into final part file. Post-process and feature creation machining operations were generated separately using an appropriate machining function within the Fusion360 software, which were added to the single part file at a suitable point. Figure 4-18 shows the process of generating a manufacturing part file for the hybrid manufacturing platform. The CAD file is exported as an STL file into the AM (slicing) software, which generates the toolpath for the ceramic extrusion (*blue*) and the sacrificial support (*red*). The toolpaths for the subtractive elements are generated

separately in CAM software. Once generated, AM and subtractive toolpaths are amalgamated into a single manufacturing part file.

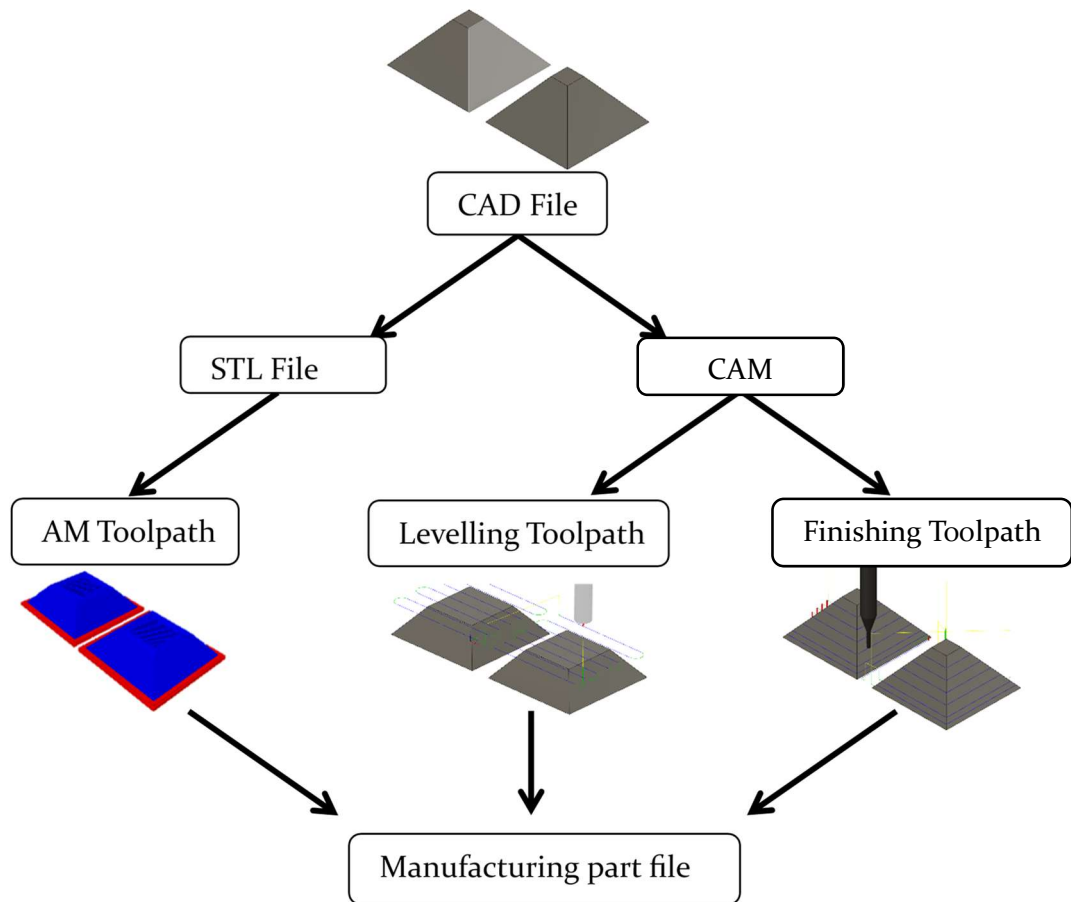


Figure 4-18 – Illustrates the process for generating manufacturing toolpaths for the various processes on the hybrid manufacturing process

Figure 4-19 shows a CAD rendering of the hybrid manufacturing process with photos of the key manufacturing processes highlighted. Figure 4-19a shows the ecoPEN 300 (Ceramic feedstock extruder) fixed centrally on the hybrid manufacturing platform. Figure 4-19b shows the E3D V6 FFF hotend (Sacrificial support extruder) mounted on the retraction mechanism. Figure 4-19c shows the machining spindle (1) with the automatic tool changer (2) that is rigidly mounted on the manufacturing platform. Figure 4-19d shows the heated forced convection drying unit that is mounted on the front of the spindle mounting bracket at an angle of 45°.

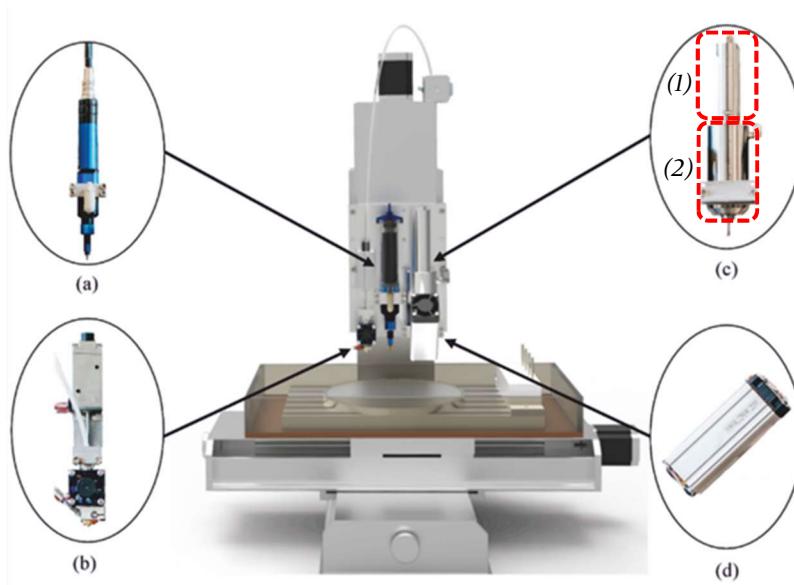


Figure 4-19 - Shows a) ecoPEN 300 PC extrusion system b) FFF hotend mounted on a linear solenoid c) Nakanishi Micromachining spindle (1) with ATC (2) d) enclosure heater for accelerated drying

4.8 Conclusion

The integration of suitable process hardware resulted in the creation of the hybrid manufacturing platform. The constituent elements were combined onto a non-branded 5-axis CNC stage system. To reduce the complexity of the system and increase the size of the build area the 4th and 5th axes were subsequently removed, although can be reimplemented should the need arise. A circular heated bed with a \varnothing 210 mm diameter was mounted centrally on the build plate. A bespoke mounting fixture was used to rigidly mount the process hardware onto the motion platform, with known offsets between adjacent tooling to simplify the commissioning the system.

The repeatability of the motion system was characterised over distances of 30 mm, 60 mm, 90 mm, 120 mm and 150mm at feedrates of 800 mm/min, 1,600 mm/min, 2,400 mm/min and 3,200 mm/min and accelerations of 300 ms⁻², 550 ms⁻² and 800 ms⁻². During these tests intermittent stalling of the motion stage was observed at speeds of 1,600 mm/min, 2,400 mm/min and 3,200 mm/min and accelerations of 550 ms⁻² and 800 ms⁻². This resulted in the motion platform being limited to a maximum feedrate of 800 mm/min and a

maximum acceleration 300 ms^{-2} . These parameters enable the X-axis to achieve an average spread of $179 \text{ }\mu\text{m}$ with an average SD of $35.6 \text{ }\mu\text{m}$ across all distances, whilst the Y-axis has an average spread of $151 \text{ }\mu\text{m}$ with an average SD of $32.8 \text{ }\mu\text{m}$.

A Preeflow ecoPEN 300 positive displacement extruder was implemented to extrude the ceramic feedstock, providing a minimum dispense volume of 0.12 ml/min through a range of luer lock compatible nozzles. The extruder was rigidly mounted on the centre of the fixture as this was used as the datum position for the other processes. The rationale being that the implementation of closed loop control and in-process metrology would enable subtractive machining operations to be undertaken only when necessary. This would further reduce fabrication times and waste generated by the process.

A commercially available FFF hotend and geared extruder was implemented to enable the production of sacrificial raft substrates and support structures. The sacrificial support is to be fabricated using standard 1.75mm PLA filament is extruded due to its low cost and availability. The extruder was setup in a Bowden configuration, enabling the extruder to be affixed to a static part of the platform, reducing the weight and bulk on the mounting fixture.

A precision micromachining spindle with an automatic tool changer was implemented as the subtractive machining systems. The system is compact and compatible with a range of tooling with shank diameters of $\text{Ø}2\text{-}6.35 \text{ mm}$, with a spindle speed of $1,000 - 50,000 \text{ RPM}$. The collet is mounted within the machining head as opposed to the tool, requiring the tooling to have the same shank diameter to function with the ATC.

Toolpaths for the various elements of the hybrid manufacturing process are generated separately using process specific software, which are then amalgamated into a single toolpath file. The additive elements of the process are generated simultaneously using commercially available software, utilising the oversizing function within this software to ensure that sufficient material is available to machine the parts into tolerance. Subtractive machining toolpaths are generated using commercially available CAM software, relying on custom

configuration files to ensure that the generated toolpath can be directly integrated with the AM toolpaths. The toolpaths are uploaded into the control software, which controls and monitors the various elements of the hybrid manufacturing system as illustrated by Figure 4-20.

Main Process Cycle

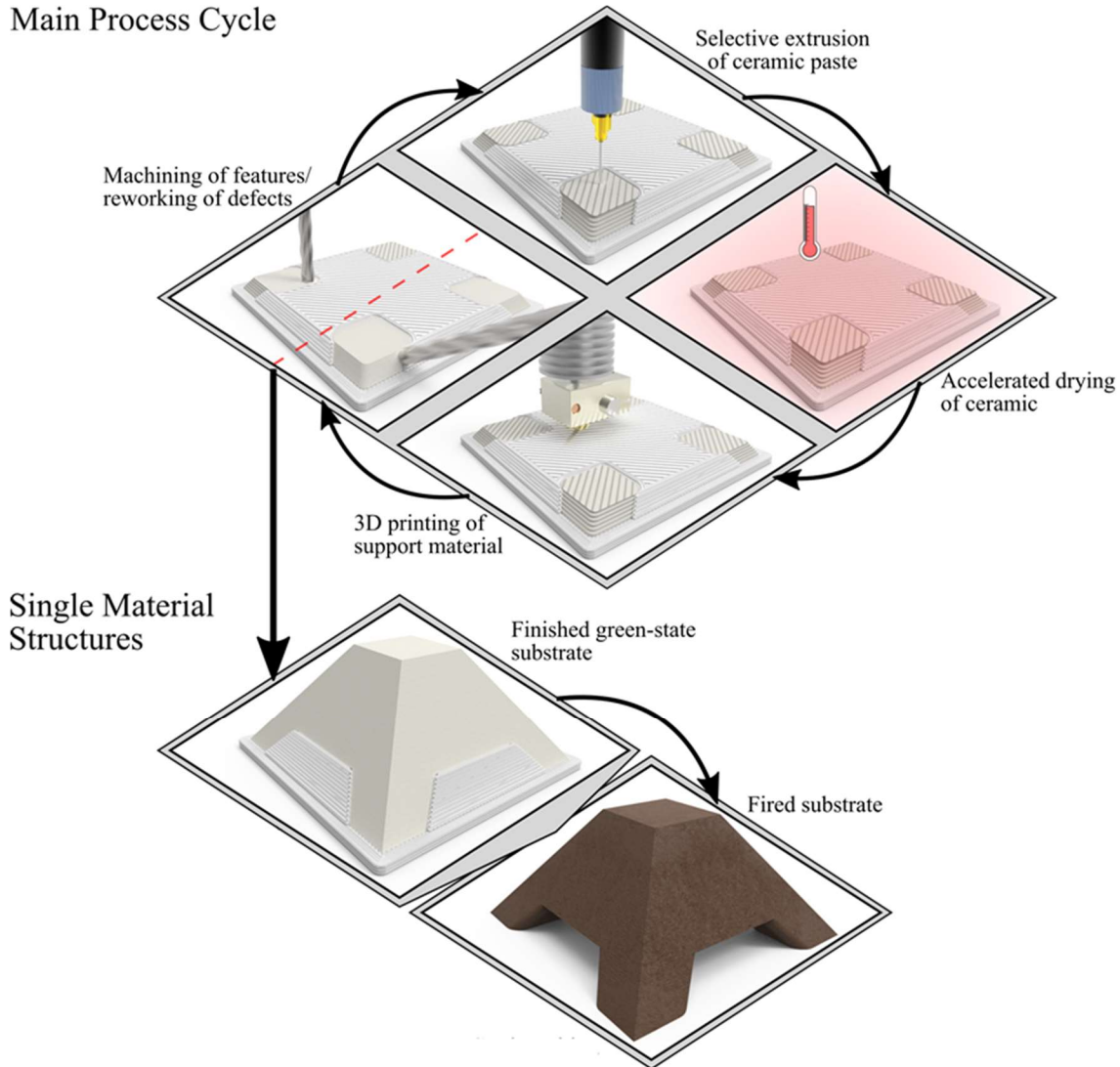


Figure 4-20 – Shows the hybrid manufacturing process to fabricate components from advanced ceramic materials. The part shown demonstrates all elements of the process including extrusion of the ceramic feedstock, accelerated drying, sacrificial support deposition and machining. Once the green state part is fabricated, the part is thermally processed (fired) by Morgan Advanced Materials.

The capabilities of the hybrid manufacturing platform were confirmed by the production of 3D ceramic parts, which demonstrated a range of geometric features and post-processing operations. The ceramic parts demonstrate the benefit of interleaving AM and subtractive manufacturing processes into an integrated process, demonstrating the production of overhanging features and internal cavities.

5 3D structures and characterization

5.1 3D ceramic Components

The production of 3D ceramic components that require the combined use of the ceramic paste extruder, PLA sacrificial support and machining spindle using different cutting tools provide validation of manufacturing capabilities and fabrication strategies. The design of the parts is intended to provide insight into the capability of producing 2.5D/3D filled geometries, closed cavities, spanning and overhanging geometries. A summary of the fabrication for each part shown in this chapter is documented in Appendix C.

5.2 Ceramic Feedstock Extrusion

The ceramic extrusion process is the primary mechanism to enable the fabrication of 3D ceramic components. Key parameters relating to the ceramic extrusion process are nozzle size, flowrate and printing speed (feedrate). The ceramic feedstock was deposited using the PC extrusion system using a 250 μm straight-profile nozzle and constant printing height of 125 μm onto standard printing paper. The print height was based on the recommended settings provided with the nozzles when used to dispense non-Newtonian, loaded materials such as solder paste, which was approximately half of the nozzle diameter. Standard printing paper substrates were used during this characterisation as the samples were not intended to undergo any thermal processing, meaning that there is no risk of contamination. 30 mm tracks were produced using each parameter, which were measured using non-contact profilometry (Talysurf CLI 2000, Taylor Hobson, USA). The initial deposit was produced using a flowrate of 40 $\mu\text{L}/\text{min}$ and a printing speed of 650 mm/min. Between sample sets the material flowrate was reduced in increments of 2 $\mu\text{L}/\text{min}$ whilst the printing speed was increased in increments of 5 mm/min, until non-continuous beads were produced.

Figure 5-1a shows profiles that were generated using non-contact profilometry of the tracks produced using a flowrate of 40 $\mu\text{L}/\text{min}$ and a print speed of 650 mm/min. This sample has a consistent edge profile with an average width of

347.15 μm and an average height of 168.52 μm . Figure 5-1b shows the profile of a track produced using a flowrate of 33 $\mu\text{L}/\text{min}$ and a print speed of 725 mm/min. This sample has a consistent edge profile with an average width of 369.95 μm and an average height of 68.68 μm . As these profiles were generated using optic methods, the inside of the tracks was unable to be imaged, however it should be noted that the tracks are solid. The full dataset for this test is shown in Appendix F.



Figure 5-1 – Shows the profiles generate for tracks produced with a 250 μm straight-profile nozzle and constant printing height of 125 μm on uncoated paper using a) Flowrate rate 40 $\mu\text{l}/\text{min}$, Printing speed 650mm/min b) Flow rate 33 $\mu\text{l}/\text{min}$, Printing speed 725mm/min w

Comparison of the two profiles, shows that Figure 5-1a has a more consistent edge profile, which reduces the likelihood of inter-bead porosity caused by insufficient coalescence from adjacent beads. The curved top may result in porosity caused by insufficient penetration of the material deposited during sequential layers as previously shown in Figure 3-2a, in Section 3.1. However, the profile shown by Figure 5-1b has a less consistent edge profile, which may result in porosity between adjacent beads of materials. This can be addressed by increasing the stepover distance between adjacent tracks, which may result in excess material deposits in these regions. The flatter top surface is less susceptible to the formation of porosity illustrated by Figure 3-2a, although there does appear to be a concave profile on the upper surface. A discernible difference between the two profiles is the height of the bead with a difference of ~ 100 μm , despite a constant print height of 125 μm . Within AM processes, thinner layer thicknesses are often associated with increased resolution and lower surface roughness, although fabrication times also increase. However, the thinner effective layers of this approach will increase fabrication times, although

this can be offset by the use of larger nozzles and thicker layers as the surface roughness and manufacturing resolution will be determined by the machining process.

The main criterion for selecting suitable deposition parameters was based on the uniformity of the edge of the bead profile and the width of the bead, enabling the production of cohesive, uniform layers. To ensure that porosity is not caused by the convex upper surface of the deposited tracks, sufficient material removal is required. The depth of the surface milling operation to remove the convex surface was determined by inspection of machined samples using optical microscopy (BX53M, Olympus, Japan). This resulted in a surface machining depth of ~25% of the layer thickness. For example, the deposition of material using a 25-gauge (437 μm) nozzle formed a layer with a thickness of ~400 μm , which was machined to ~300 μm as the discrete beads were no longer visible.

5.3 Fabrication of 3D ceramic structures

5.3.1 Square 2.5D geometries

The investigation of filled structures involved the production of 2.5/3D geometries, which were manufactured in batches of two or more to enable the direct comparison by ensuring consistent processing conditions. The generation of the toolpaths using the slicing and CAM software enables a scaling factor to be applied to account for the shrinkage/swelling during the fabrication process. These scaling factors were set to zero during the fabrication of the test samples. Two 2.5D tiles that measured $25 \times 25 \times 7$ mm were produced using a 25-gauge metal tapered nozzle using a flowrate of 67 $\mu\text{L}/\text{min}$ and a feedrate of 650mm/min. The parts were fabricated using a layer height of 300 μm , with the parts consisting of 23 layers each. Surface milling used a $\text{Ø}4$ mm end mill with a spindle speed of 10,000 rpm and a feedrate of 330 mm/min. Figure 5-2a shows the parts during the post-process machining of one of the parts, using a stepdown height of 1 mm, spindle speed of 10,000 RPM and feedrate of 330 mm/min. The part described as “non-machined” was machined on the top

surface only as this was part of the interlayer machining toolpath. The “machined” part, however, was machined on the top surface and on the side surfaces using the same $\text{Ø}4$ mm CVD end mill. The production of each layer including ceramic deposition, drying and surface machining took ~ 12 minutes, resulting in a total fabrication time of 4.5 hours for both parts. Measurement of the green and sintered parts with a 25 mm engineering micrometer (207-01, Hitec, Germany) with a resolution of 0.01 mm as this provided sufficient adequate resolution [241]. All specified measurements of the parts were obtained at Morgan Advanced Materials under the supervision of the technical staff. The green state non-machined part measured $25.74 \times 25.57 \times 7.01$ whilst the machined parts measured $24.73 \times 24.85 \times 6.98$ mm. Figure 5-2b shows the non-machined tile (*left*) which measures $21.85 \times 21.68 \times 5.29$ mm and the machined (*right*) which measures $20.85 \times 21.07 \times 5.27$ mm. The production of the parts on a PLA raft substrate resulted in a textured underside surface due to the infill pattern of the substrate.

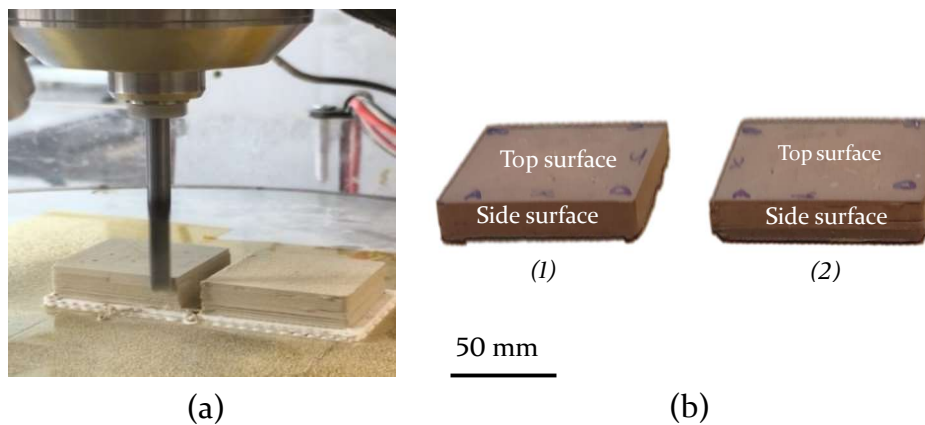


Figure 5-2 –a) shows the post-process machining of the green state tile using a $\text{Ø}4$ mm fluted CVD end mill b) shows the sintered tiles with (1) being machined on the top and side surfaces and (2) that was machined on the top surface only. Both tiles underwent a measure X-Y shrinkage of $\sim 16\%$

The density of all of the sintered samples was determined using an Archimedean technique under the supervision of the technical staff at Morgan Advanced Materials. The sintered part densities showed that the non-machined part had a calculated density of 99.19%, whereas the machined sample had a calculated density of 99.34%. Measurement of the sintered parts using non-contact profilometry (InfiniteFocus, Bruker/Alicona, Germany) with a 10x

objective showed that the top surface of the sintered machined and sintered non-machined tiles has an average surface roughness R_a of $1.3 \mu\text{m}$ and R_q of $1.9 \mu\text{m}$. Figure 5-3 shows a comparison of the height maps generated from the vertical sides of the sintered tile components. Figure 5-3a shows the height map for side C of the non-machined tile. Figure 5-3b shows the height map for side D of the machined sample. Additional height maps for the other side are shown in Appendix G.

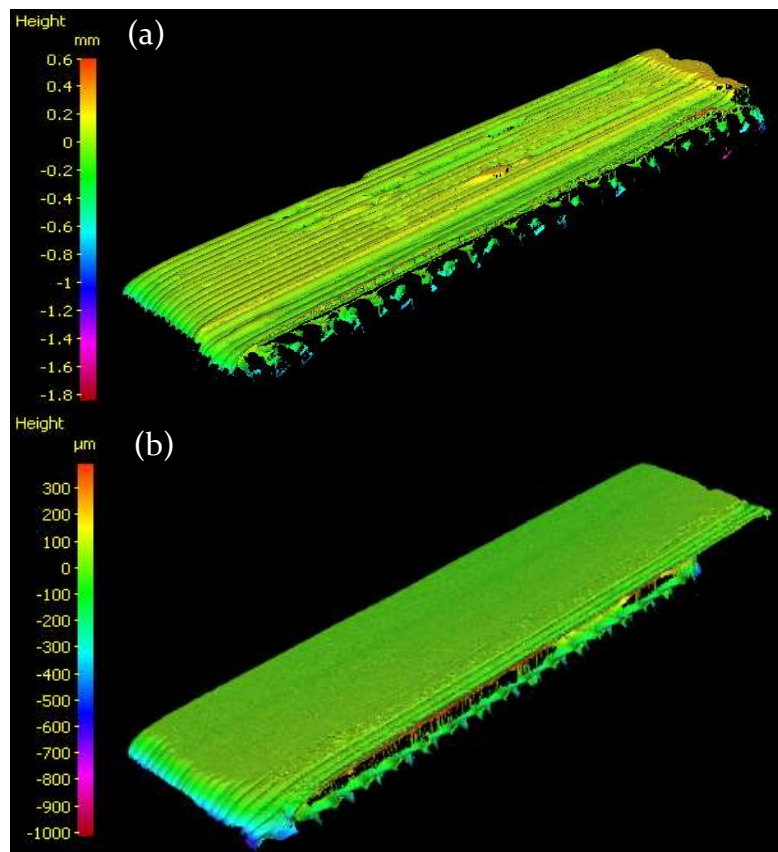


Figure 5-3 – Shows the profiles generated from the side surface of the parts. a) Shows side B of the non-machined tile b) shows side D of the machined sample. The machined sample shows a more consistent profile

The non-machined sample shows a height variation of between $\sim 400\text{-}600 \mu\text{m}$, whereas the machined sample shows a height variation of $\sim 150 \mu\text{m}$. The non-machined sample has an average surface roughness R_a of $17.9 \pm 13.4 \mu\text{m}$ and R_q of $24.6 \pm 19.2 \mu\text{m}$. The height maps from the machined samples indicate a more consistent profile compared to the non-machined sample, although some surface defects are still present on sides B and C (shown in Appendix G). The machined tile has an average surface roughness R_a of $1.0 \pm 0.5 \mu\text{m}$ and R_q of $1.4 \pm 0.7 \mu\text{m}$. Figure 5-4 shows the surface roughness data for the non-machined

and the machined parts. The inclusion of the side milling process results in lower surface roughness and more consistent edge profiles with fewer defects.

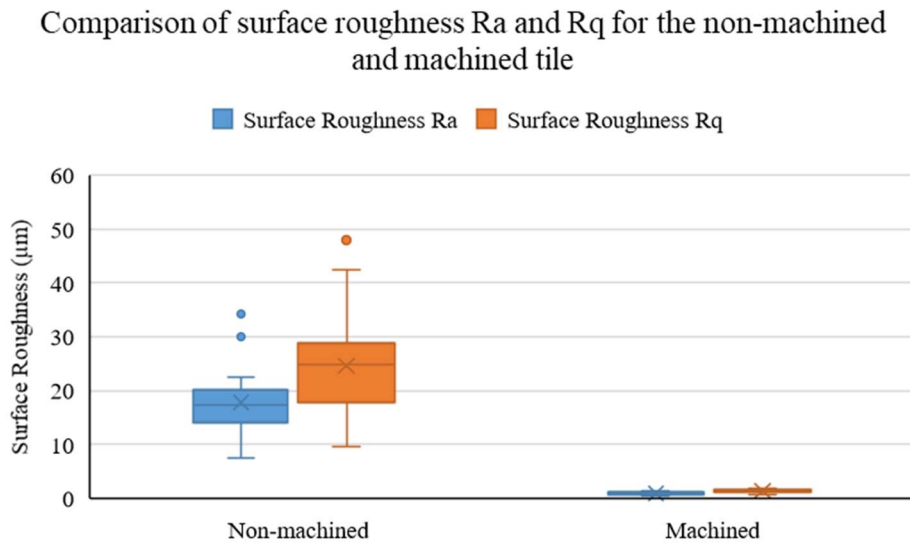


Figure 5-4 - illustrates the reduction in surface roughness R_a and R_q achieved by implementing a post-process machining operation

5.3.2 Tapered Tile Geometries

The fabrication of 3D filled geometries including tapered tiles and square-based pyramids require the use of alternative tooling during post-process machining. Figure 5-5 shows three green state tapered tile geometries, which measure $30 \times 30 \times 6$ mm with a 60° taper. The samples were fabricated onto a single PLA raft that was produced using the sacrificial support extruder. The ceramic extruder was fitted with a 25-gauge metal tapered nozzle and a flowrate of $70 \mu\text{L}/\text{min}$. The material flowrate was increased to reduce the presence of defects on the edges of the part, which were the result of insufficient material flow during fabrication. Surface milling of the dried layers used a $\varnothing 4$ mm end mill using a spindle speed of 10,000 RPM and a feedrate of 330 mm/min, using a concentric toolpath. Post-fabrication, two of the parts were machined using a $\varnothing 1$ mm ball nose cutter at a spindle speed of 10,000 RPM and feedrate of 330 mm/min. Figure 5-5b shows the machined sample that used a stepdown height of 1 mm. However, this part became detached from the substrate preventing the complete machining of the part. The green state part measured $29.75 \times 29.21 \times 5.30$ mm. Figure 5-5c shows the part that was machined using a defined stepdown height of 0.01 mm, which measured $29.50 \times 28.56 \times 5.33$ mm. The fabrication of these

parts took ~ 5 hours, with near-net shape of the samples being achieved after 4.5 hours. The post-process machining of sample *b* took 2 minutes whereas the post-process machining of sample *c* took 25 minutes.

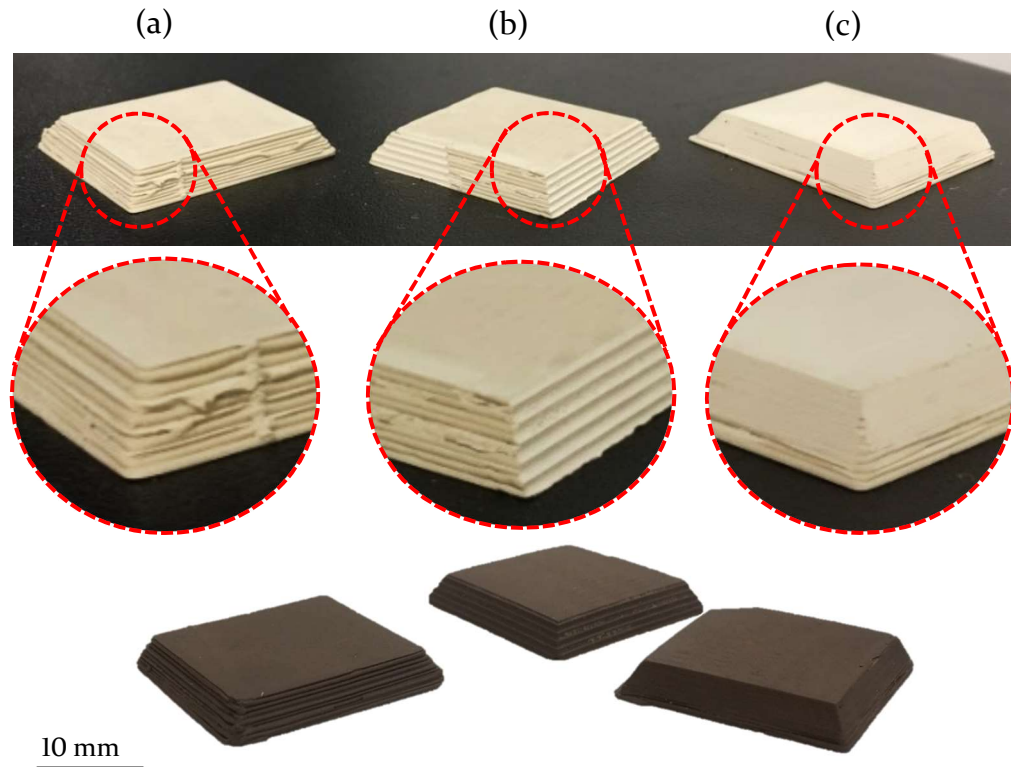


Figure 5-5 – (top) shows the taper tiles that were fabricated with different degrees of post processing. Sample *a* has undergone no post processing. Sample *b* was machined used a $\text{Ø}1$ mm ball nose cutter with a stepdown height of 1 mm. Sample *c* was machined used a $\text{Ø}1$ mm ball nose cutter with a stepdown height of 0.01 mm. (bottom) shows the sintered samples

Post sintering the part machined with a 1 mm stepdown height measured $24.77 \times 24.60 \times 4.00$ mm. The part machined with a 0.1 mm stepdown measured $25.01 \times 24.22 \times 4.02$ mm. Figure 5-6 shows the height maps that were generated using non-contact profilometry of samples *b* and *c*. The top surface of both parts has a number of open pores, which are exposed by the surface machining operation. Furthermore, the parts also exhibit signs of the infill pattern on the top surface, which is the result of inconsistent tool height caused by inadequate bed levelling prior to fabrication. Figure 5-6a shows the height map for sample Figure 5-5b, which has defined layers due to the large stepdown distance that is equivalent to diameter of the ball nose cutter. Alternatively, Figure 5-6b shows the height map for the part shown in Figure 5-5c, which has less defined layers along the edge of the part due to the thinner stepdown height used during the post-process machining. However, the machining passes are visible along the

edge of the part, which may be removed with smaller stepover heights or mechanical removal of machining debris.

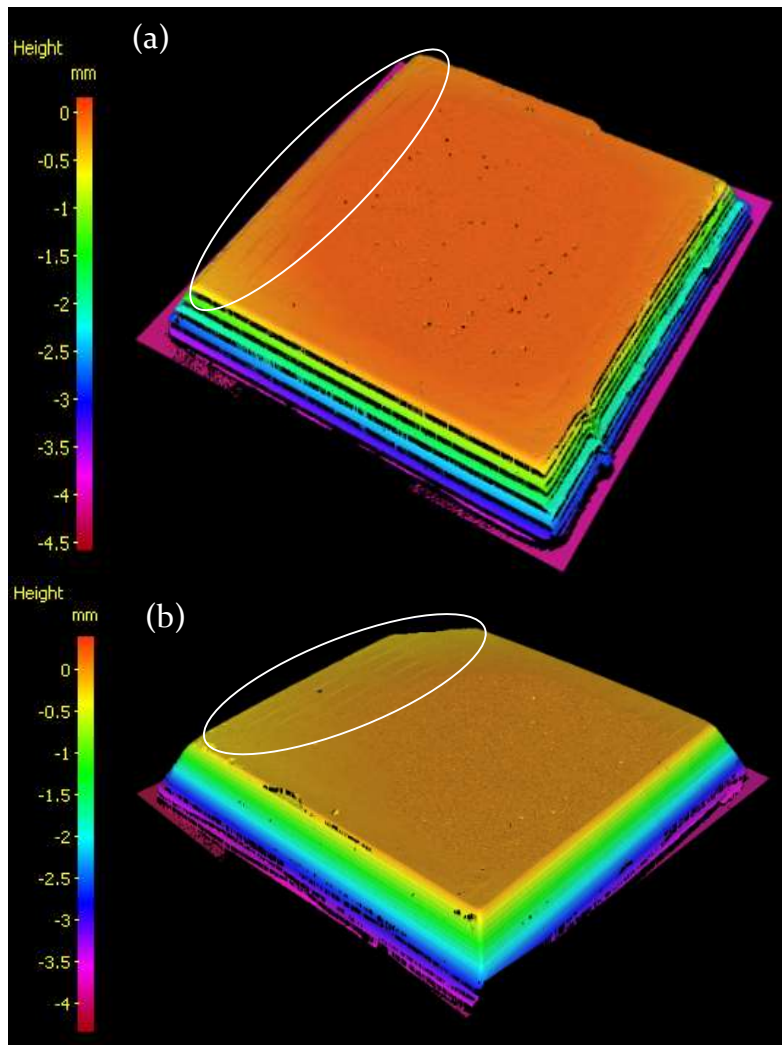


Figure 5-6 – Shows the height maps generated for a) sample b with a stepdown height of 1 mm and b) sample c with a stepdown height of 0.01 mm

Table 5-1 shows the measured surface roughness R_a and R_q values for the side surfaces of the sintered components. The non-machined part has the highest surface roughness, which are consistent with the measure values from the part shown in Figure 5-3.

Table 5-1 - average measured surface roughness of the tapered tile samples. Sample size $n = 5$.

	Surface Roughness R_a (μm)	Surface Roughness R_q (μm)
Sample a	15.0 ± 10.9	22.1 ± 12.3
Sample b	1.4 ± 0.6	2.7 ± 2.2
Sample c	1.2 ± 0.2	1.7 ± 0.5

Figure 5-7 shows the surface roughness R_a and R_q for the tapered tile geometries, which demonstrate a similar trend to the 2.5D tile geometries that are shown previously. Post-processing of the tapered samples demonstrates the benefit of implementing post-process machining on 3D geometries, although the time implication of machining using a stepdown height of 0.01mm is impractical due to the variation in surface roughness between samples b and c. The parts have an average calculated density of $98.04 \pm 0.635\%$, which is likely due to entrapped air throughout the layers of the part as illustrated on the top surface by Figure 5-6.

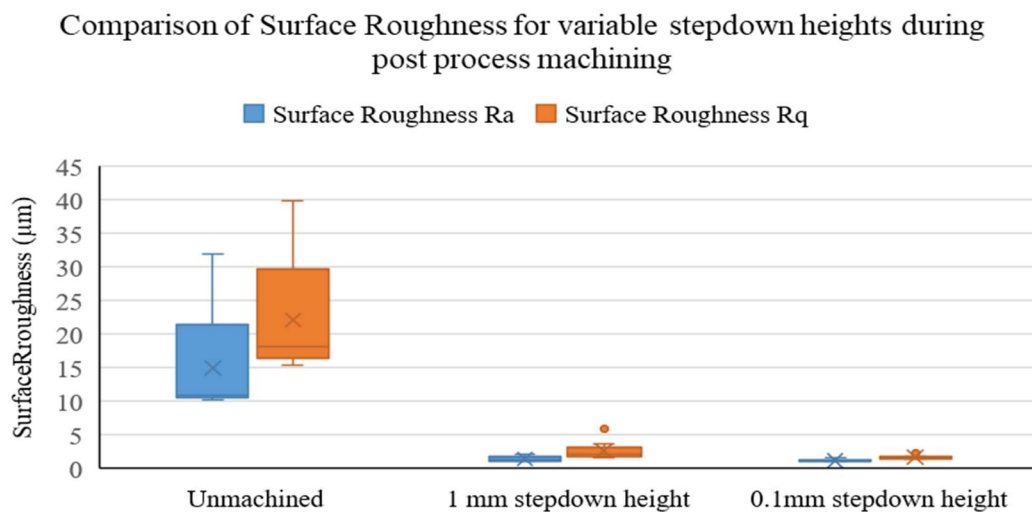


Figure 5-7 - Shows a comparison of the measured surface roughness of the samples following post process machining with a \varnothing 1 mm ball nose cutter using variable stepdown heights

5.3.3 Pyramid Geometries

Two pyramid structures, with a footprint of $25 \times 25 \times 20$ mm were fabricated using a 25-gauge metal tapered nozzle and a flowrate of $70 \mu\text{L}/\text{min}$. The tooling and parameter used for the interlayer surface milling operation are consistent with those used during the production of the aforementioned parts. Post-processing using the \varnothing 1 mm ball nose cutter using a stepdown height of 0.2 mm resulted in a post-processing time of 15 minutes. Figure 5-8a shows the pyramids during the fabrication process, with the PC pumping system depositing a layer of ceramic feedstock. The parts were fabricated using a concentric filling pattern, whereby the perimeter shell was formed and filled without disrupting the motion the ceramic extruder. The ceramic extruder was

not terminated during the transition between parts due to the potential of introducing defects due to insufficient material flow. The resultant connection was removed using during the post-process machining. Figure 5-8b shows the pyramid structures during the post process machining. During this stage a collision between the machining tool and the pyramid, which resulted in the top of the pyramid becoming detached. The non-machined pyramid measured $25.18 \times 25.14 \times 18.36$ mm. The machined pyramid measures $24.92 \times 24.99 \times 14.21$ mm.

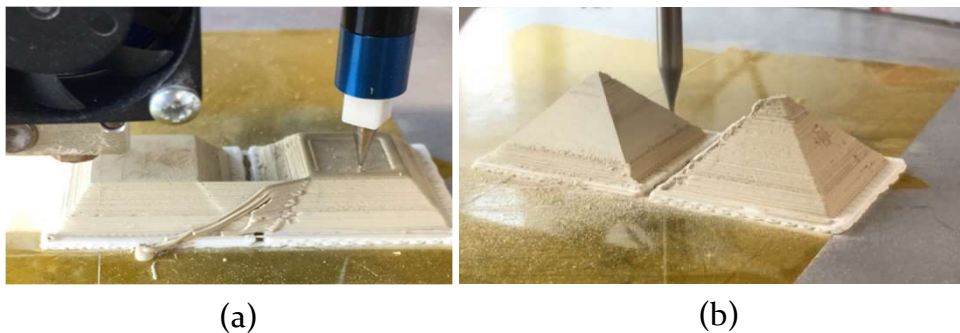


Figure 5-8 – a) shows the deposition of a new layer of ceramic during the fabrication of the pyramids b) shows the post process machining of the left hand pyramid using a $\text{Ø}1$ mm ball nose cutter and a stepdown height of 0.2 mm

Figure 5-9a shows the non-machined pyramid, which exhibits a number of surface defects. Figure 5-9b shows the machined pyramid, which exhibits a notch at the top of the part as a result of the collision with the machining spindle. The corner of the green state part became damaged during transit, which is also visible on the sintered part. The non-machined pyramid measured $21.35 \times 21.32 \times 12.41$ mm. The machined pyramid measures $21.13 \times 21.19 \times 10.73$ mm.



Figure 5-9 a) shows the sintered non-machined pyramid that exhibits a number of surface defects. b) shows the sintered machined pyramid

Figure 5-10 shows height maps of the non-machined pyramid and machined pyramid, additional surface maps from these parts are available in Appendix .

Figure 5-10a shows the non-machined pyramid, which has a number of surface defects that would have likely been removed if the part had been post-process machined. There are also a number of large defects that appear to be up to ~ 500 μm deep, which are unlikely to have been removed with additional processing due to insufficient material. Figure 5-10b shows an example of the machined pyramid, which has a more consistent profile with variations of ~ 100 μm .

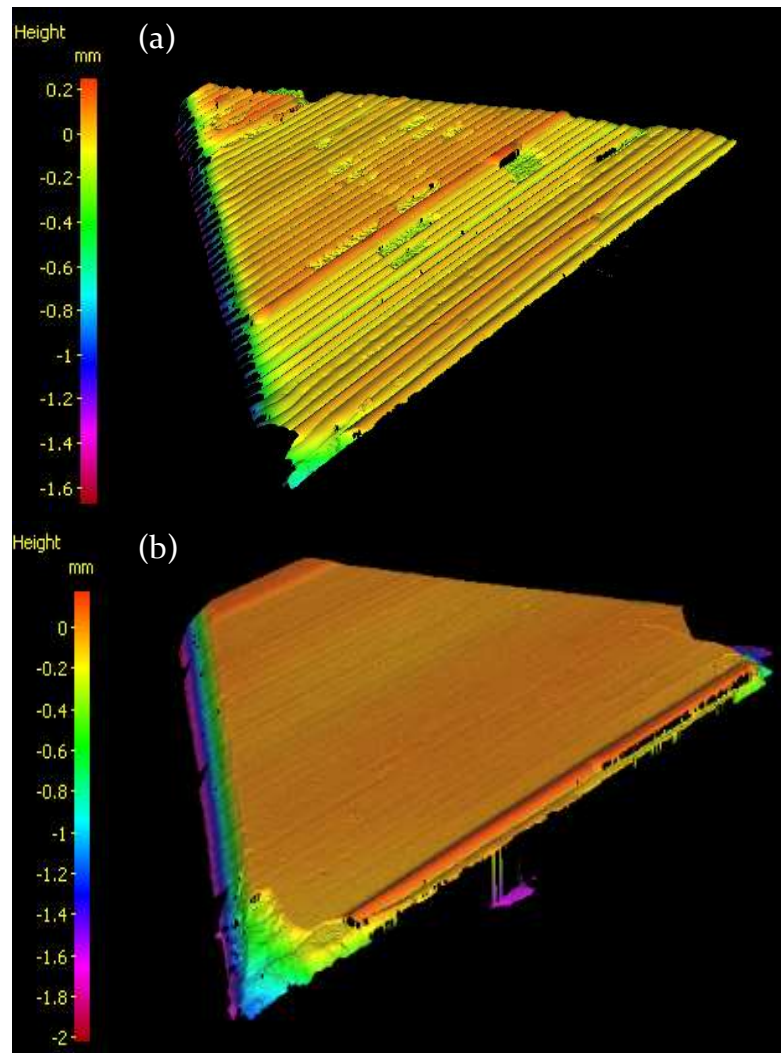


Figure 5-10 – a) shows the height map generated for Side C of the non-machined pyramid. b) shows the height map generated for Side D of the machined pyramid

The sintered non-machined pyramid has a measured surface roughness R_a of 37.0 ± 5.7 μm and R_q of 48.1 ± 7.7 μm with a calculated density of 99.76%. Alternatively, the machined pyramid has an average surface roughness R_a of 3.8 ± 2.0 μm and R_q of 5.0 ± 3.0 μm . However, two sides of the machined pyramid have surface roughness R_q values of 7.8 μm and 6.5 μm . The density of the sintered samples was determined under the supervision of the technical

staff at Morgan Advanced Materials. The machined part has a calculated density of 99.56% TD, which is lower than the non-machined part, though this is still comparable with conventional manufacturing processes. Figure 5-11 shows a plot of the surface roughness data for the two pyramids, which shows the machined part had a lower measured surface roughness with a narrower spread.

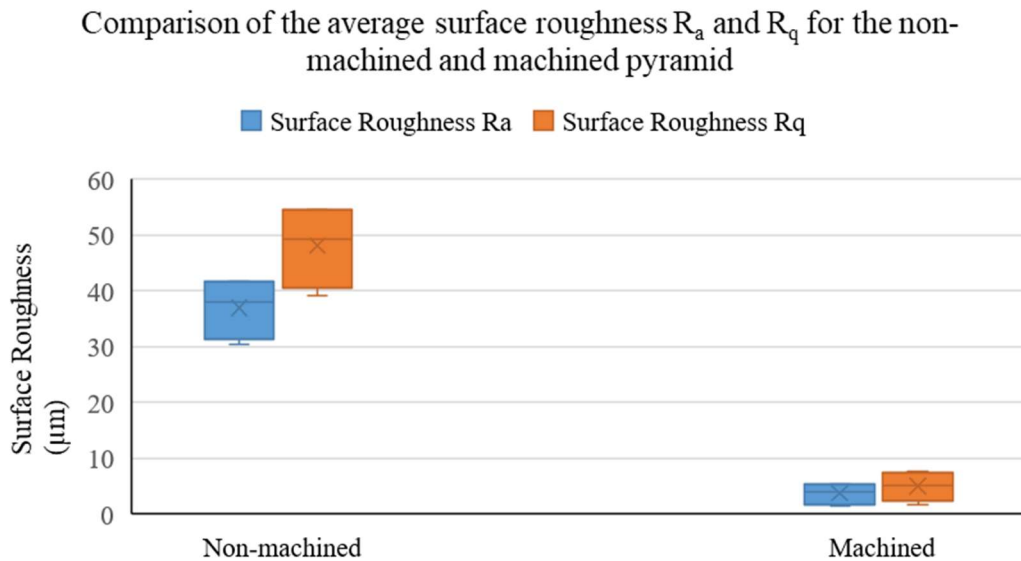


Figure 5-11 – Comparison of the surface roughness of the non-machined and machined pyramids

The fabrication of the aforementioned parts with densities of up to 99.76% and surface roughness R_a values of 0.5 μm and surface roughness R_q value of 0.6 μm validate the capabilities of the hybrid manufacturing platform for the production of filled 3D geometries.

5.3.4 Enclosed geometries

Investigation of parts with closed cavities was explored with the production of six cubes, which measured $15 \times 15 \times 10$ mm with a $9 \times 9 \times 2$ mm internal cavity. The parts were fabricated using the same manufacturing parameters as the aforementioned parts. To prevent the inclusion of machining debris within the cavity support structures, the PLA supports were fabricated externally using a commercial FFF system (Ultimaker 2+, Ultimaker, Netherlands) using white and grey PLA filaments (RS Pro, RS components, UK). The support structure was produced using a nozzle temperature of 210°C and a heated bed

temperature of 40°C to prevent warping of the support structures. The cavity support structures had varying levels of infill ranging from 0%, which consisted only of a shell structure with a specified thickness of 400 μm . Ventilation ports were not incorporated into the design of the parts as this would have resulted in the production of open cavities. Figure 5-12a shows the cavity support structures after being manually placed in the internal cavity of the part. Prior to this, the internal cavity was machined to ensure the correct internal dimensions. Machining debris was removed from the cavities using a handheld vacuum (V6, Dyson, UK) and foam tipped swabs. The deposition of material following the placement of the cavity support structures, confirmed the capability of fabricating green state parts with enclosed cavities. A \varnothing 1 mm ball nose cutter was used to engrave the top surface of the parts with the corresponding infill densities, with FL denoting the sample with 100% support structure.



Figure 5-12 a) shows the placement of the prefabricated PLA support structures within the internal cavities. b) shows the enclosed geometries with the corresponding infill densities engraved on the top surface

Thermal processing of the parts however, resulted in delamination of all of the parts regardless of the infill density of the cavity support structure. Figure 5-13 shows the samples post sintering, whereby parts 20, 40, 60 and 80 have delaminated, resulting in the two halves of the part becoming misaligned, which then sintered together. Parts 0 and FL delaminated but the two halves of the part did not sinter together. It is important to note that the parts delaminated at random location on the different parts. Figure 5-14 shows the internal cavities of the parts fabricated using support structures with 0% and 100% infill. Both cavities on these parts have retained the intended internal

profile of the cavity, although the base of the 100% infill part shows large material deposits.



Figure 5-13 – shows the delaminated samples post sintering where samples 20, 40, 60 and 80 sintered in the orientations shown. Samples 0 and FL split into two separated pieces.

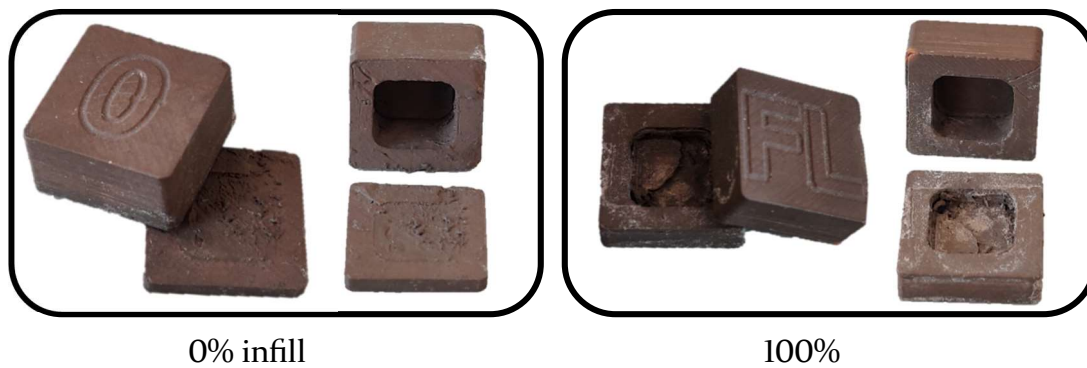


Figure 5-14 – Inspection of the internal cavities shows that both infill densities resulted in the formation of the internal cavity. Debris and other artefacts are visible in the base of the FL sample

This suggests that enclosed cavities using full encased support structures cannot be produced using PLA support materials without the inclusion of ventilation ports. This is due to the insufficient interlayer strength of the green state parts to withstand the pressure caused by the pyrolytic decomposition of the PLA support.

5.3.5 Conformal Geometries

The production of spanning geometries was previously demonstrated in section 3.5.2 Sacrificial Support during the feasibility testing of the PLA support. The feasibility of producing conformal geometries with overhanging features was investigated through the production of hollow hemisphere with an outer diameter of $\text{Ø}25$ mm and an internal cavity with a diameter of $\text{Ø}15$ mm. This

part required the use of sacrificial support structure that was attached directly to the PLA raft, shown by Figure 5-15a, which was required to support the overhanging internal face of the hemisphere. Four hemispheres were produced in two batches using the same parameters as the previous part. The ceramic extrusion process was not terminated during the transition between parts, resulting in the ridge structure that is evident of the non-machined part. Figure 5-15b shows the two hemispheres prior to post-process machining with the $\text{\O}1$ mm ball nose cutter. The parts exhibit a number of surface defects, which are similar to the defects on other non-machined parts show previously. Figure 5-15c shows the hemispheres after post-process machining using a $\text{\O}1$ mm ball nose cutter and a stepdown height of 0.2 mm. The green state parts were thermally processed whilst still attached to the sacrificial raft, in the orientation shown in Figure 5-15d, undergoing a calculated sintered density of 96.87 - 97.93%.

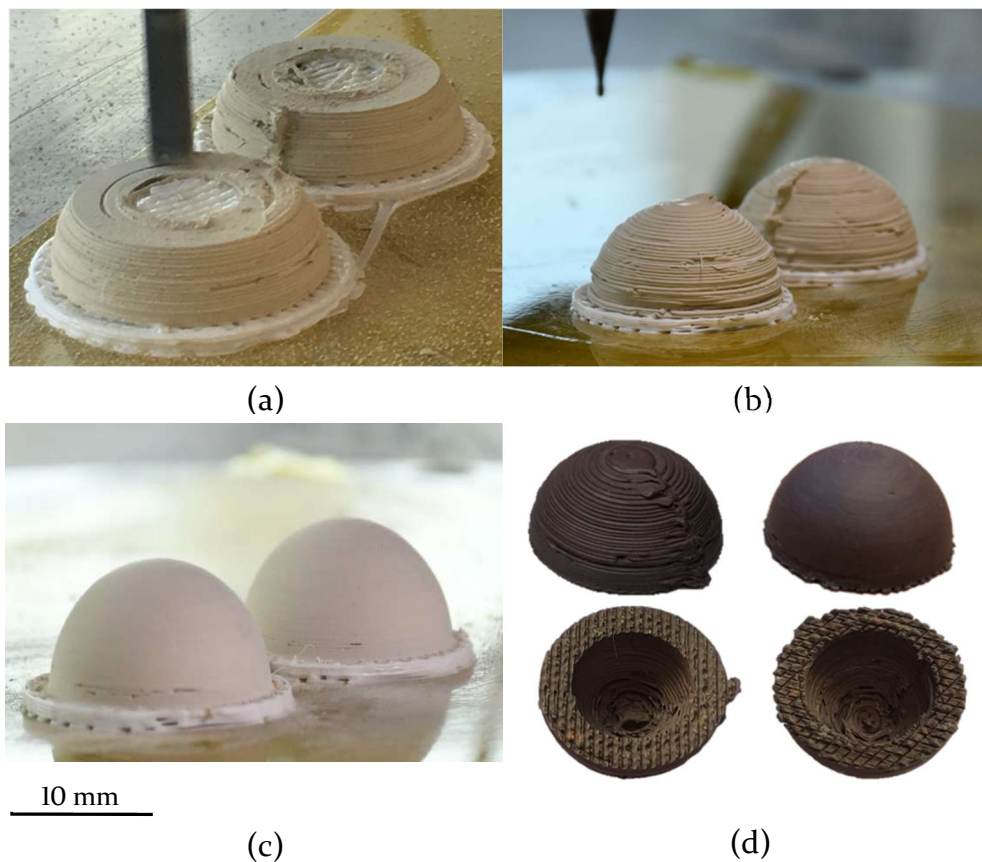


Figure 5-15 a) shows the support structure for the overhanging section of the conformal geometry during layer surface machining. b) shows the conformal geometries post fabrication before post process machining. c) shows the conformal after post process machining with a $\text{\O}1$ mm ball nose cutter and stepdown height of 0.2mm. d) shows a sintered non-machined and machined conformal geometry side-by-side with the internal structures shown below.

Imaging of the sintered parts using non-contact profilometry highlight the benefit of implementing post process machining of the conformal geometries. Figure 5-16a shows that the non-machined hemisphere is formed of discrete layers, resulting in the characteristic stair stepped AM appearance. Figure 5-16b shows the post processed geometry, which does not exhibit any significant stair stepping on the external surfaces of the part, although machining marks are visible. The ball nose cutter and 3 axis motion platform enabled the machining of the part down to the base of the part, including the near vertical edges at the base. Quantitative values of surface roughness are not possible due to the lack of suitable metrology software for determining the surface roughness of conformal geometries.

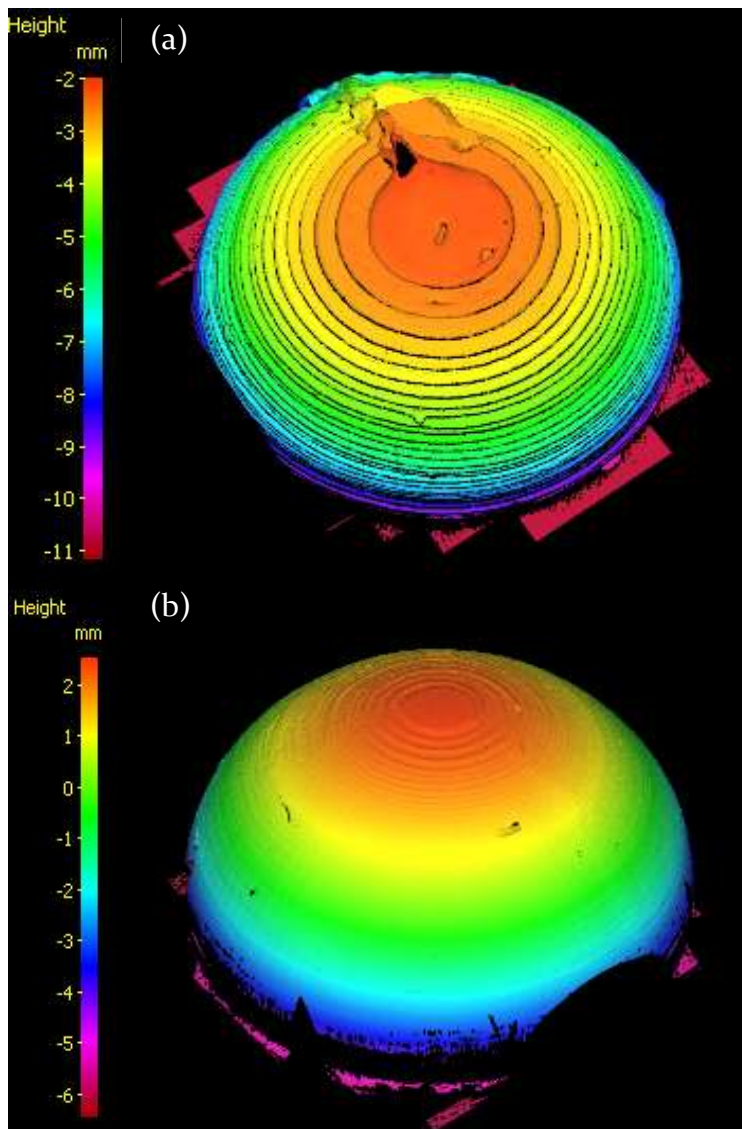


Figure 5-16 a) shows the height map generated for the non-machined dome. b) shows the height map for the machined dome with a stepdown height of 0.2 mm

The inside face of the internal cavity, however, does retain a stair-stepped appearance as the support structure and orientation of the part during fabrication prevents the in-situ machining of these surfaces. Removal of the PLA substrate and support prior to thermal process would facilitate the machining of this internal surface. However, this would require suitable tooling to hold the part, which is impractical for a templateless manufacturing process. Regardless, the fabrication of these parts validates the capability of producing overhanging, conformal structures. This part demonstrates the synergistic use of all elements of the hybrid manufacturing processing including the ceramic paste extruder, sacrificial PLA support and micromachining using multiple tools.

5.4 Mechanical Characterisation

Characterising the mechanical properties of parts fabricated using the hybrid manufacturing process required the use of destructive testing. Flexural testing, otherwise referred to as bend testing is used instead of tensile testing to determine the mechanical performance of non-ductile materials such as advanced ceramic materials. Two common methods of flexural testing are three-point (3-pt) and four-point (4-pt) testing. 3-pt bend testing requires the test sample to be placed on supports near its ends, and a central force is applied. Alternatively, 4-pt bend testing requires the test specimen to be placed on supports near its ends, with two equal forces are applied at two symmetrical positions between the supports. 3-pt bend testing is generally easier to setup and use, with it often implemented within industrial production for Quality Assurance purposes (QA). 4-pt testing is more complicated to setup and use, although the test specimen is subjected to a uniform stress and is used to obtain design data. The ASTM C1161 and ISO 14704 standards define the test parameters for determining the flexural strength of non-ductile materials with a strength > 50 MPa, such as advanced ceramic materials. These tests have been adapted for use within conventional manufacturing at Morgan Advanced materials. Therefore, test samples that measured $6 \times 6 \times 60$ mm were designed using the specification of the QA samples used within commercial production.

To enable the direct comparison of test results the bend test samples were manufactured in a single batch, requiring a minimum of 10 test specimens to determine the average strength. The build environment of the hybrid manufacturing platform enabled the production of 20 test specimens in a single batch. Figure 5-17 shows the 20 bend test samples being fabricated by the hybrid manufacturing platform on a single PLA raft structure. Figure 5-17a shows the deposition of the ceramic feedstock through a 25-gauge metal tapered nozzle using a flowrate of 67 $\mu\text{L}/\text{min}$ and a feedrate of 650mm/min. Figure 5-17b shows the samples being post processed using a $\text{\O}4$ mm end mill using a spindle speed of 10,000 RPM and a feedrate of 330 mm/min.

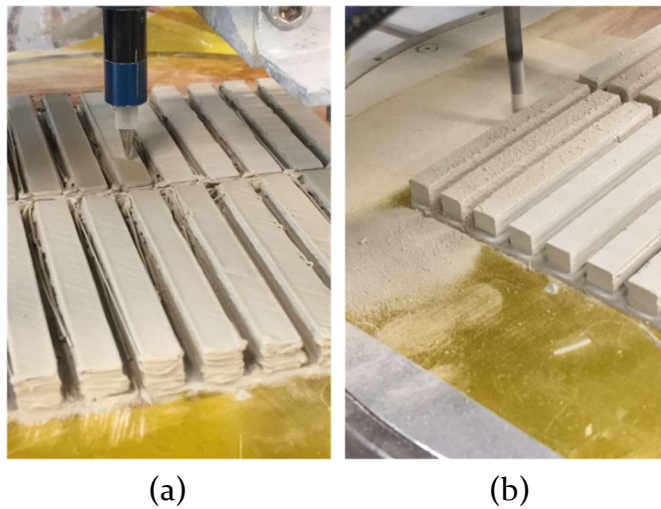


Figure 5-17 – a) shows the deposition of the ceramic feedstock during the production of the bend test samples. b) shows the post process machining of the bend test samples

The surface roughness of the green state specimens was measured with non-contact profilometry using a 10x objective along the 60 mm edge of the samples. Table 5-2 shows the average surface roughness of the bend test samples with the top and side values being determined using nine samples and the underside values being obtained using seven samples. Figure 5-18 shows the surface roughness of the samples sides has the lowest R_a and R_q values and lowest deviation.

Table 5-2 – Measured surface roughness of the bend test samples

	Surface Roughness R_a (μm)	Surface Roughness R_q (μm)
Top Surface	1.639 ± 0.663	2.593 ± 1.245
Side Surface	1.071 ± 0.289	1.554 ± 0.694
Underside	2.042 ± 1.678	3.773 ± 3.388

Measured surface roughness of the bend test samples

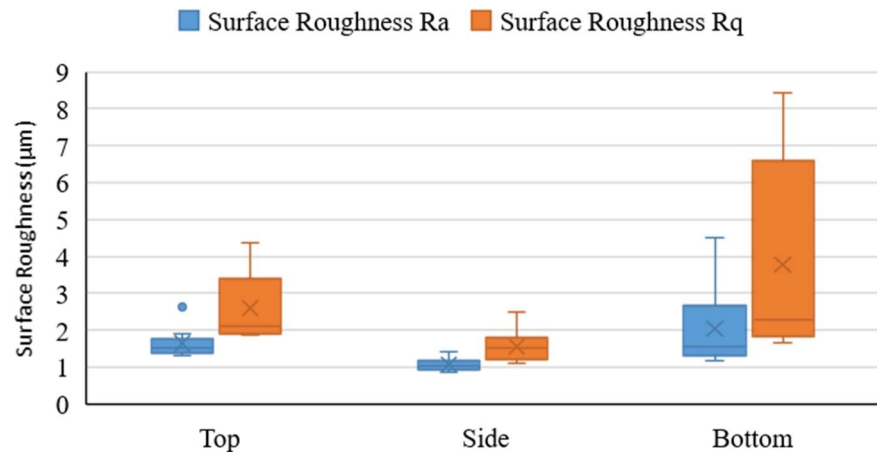


Figure 5-18 – Shows the measured surface roughnesses of the bend test samples. The bottom surface has a higher surface roughness due to the infill pattern of the substrate

The top surface has a higher surface roughness, which is possibly due to the final surface machining pass, which followed a toolpath that was perpendicular to the long edge of the samples. The base of the samples has the highest surface roughness, which is a result of the substrate infill pattern being transferred onto the parts. The flexural strength of the test specimens was determined using a table-top testing system (ProLine Z005, Zwick/Roell, Germany) with a maximum test load of 5 kN, using a 3-pt bending fixture with a span of 40 mm. The flexural strength of the samples was determined using the fixture shown in Figure 5-19a, applying the bending force perpendicular to the layer direction as indicated by Figure 5-19b.

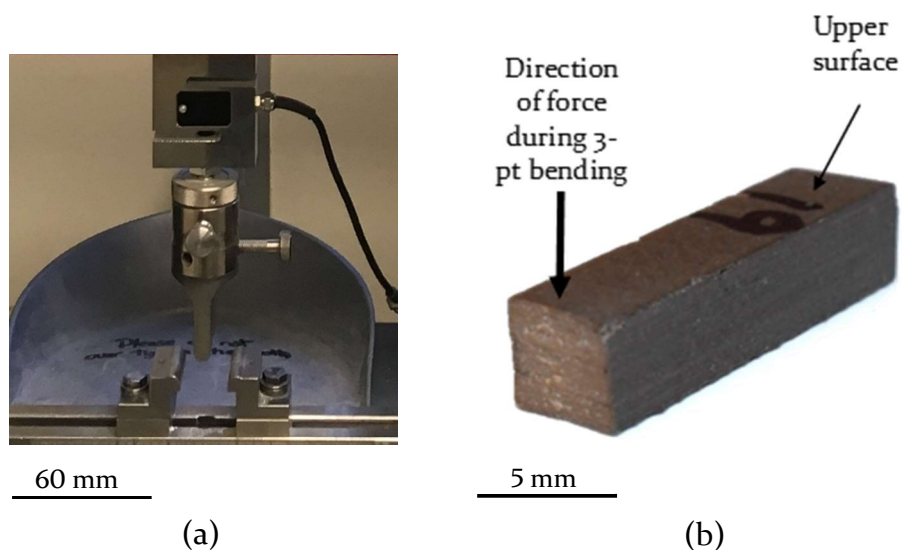


Figure 5-19 – Shows the orientation of the best test samples during the flexural strength testing

A preload force of 10 N was applied to the samples at a speed of 5 mm/min with the flexural strength being determined using a test speed of 1 mm/min, with a maximum deflection distance of 15 mm. The tests were terminated when a reading of 80 % F_{max} was registered with the F_{max} value being recorded. Table 5-3 shows the cross-section dimensions of the test specimens and the F_{max} values recorded during the flexural testing.

Table 5-3 – Cross sectional measurements of the bend test samples and the recorded F_{max} value output during the flexural tests

Sample	Width (mm)	Height One (mm)	Height Two (mm)	Average Height (mm)	Max Force (N)	Strength (MPa)
1	4.48	4.96	5.01	4.99	369	198.87
2	4.48	5.08	5.08	5.08	387	200.84
3	4.61	5.02	5.01	5.02	481	248.92
4	4.59	5.01	5.07	5.04	451	231.90
5	4.52	5.03	5.05	5.04	412	215.30
6	4.45	5.03	5.04	5.04	388	206.36
7	4.48	5.03	4.99	5.01	313	167.01
8	4.47	4.99	5.02	5.01	400	214.34
9	4.45	5.03	5.06	5.05	414	219.32
10	4.46	5.01	5.00	5.01	448	240.59
11	4.51	5.01	4.98	5.00	392	209.02
12	4.48	4.94	4.97	5.96	394	214.92
13	4.48	5.00	5.00	5.00	443	237.32
14	4.47	4.99	4.94	4.97	426	231.96
15	4.48	5.02	5.03	5.03	346	183.52
16	4.52	4.98	5.01	5.00	475	252.72
17	4.55	5.02	5.03	5.03	390	203.67
18	4.49	5.00	5.01	5.01	434	231.52
19	4.52	5.02	5.01	5.02	412	217.45
20	4.58	5.02	5.01	5.02	456	237.52
Average	4.50 ±0.08	-	-	5.08 ±0.13	411.55 ±84	218.15 ±42.86

Samples fabricated from the unmodified feedstock using isostatic pressing, which had been polished to a surface roughness R_a of 0.08 μm had an average flexural strength of 324.91 ± 5.23 MPa. Therefore, the hybrid manufactured samples exhibit a reduction in flexural strength of $\sim 70 - 160$ MPa. Calculation of flexural strength used the values shown in Table 5-3 with equation *H.1* shown in Appendix I. The twenty test samples had a flexural strength of 167.010 – 252.718 MPa with an average flexural strength of 221 MPa.

Examination of the break surfaces of the bend test specimens using scanning electron microscopy (SEM) confirm the production of monolithic ceramic parts with no discrete layers. A number of pores are visible throughout the cross sections indicating the presence of entrapped air within the feedstock materials. However, the sintered bend test specimens have an average density of $99.507 \pm 0.475\%$ TD, with the highest density measuring 99.93% TD, which are comparable to conventionally manufactured parts. The full dataset and equations for determining density are shown in Appendix J.

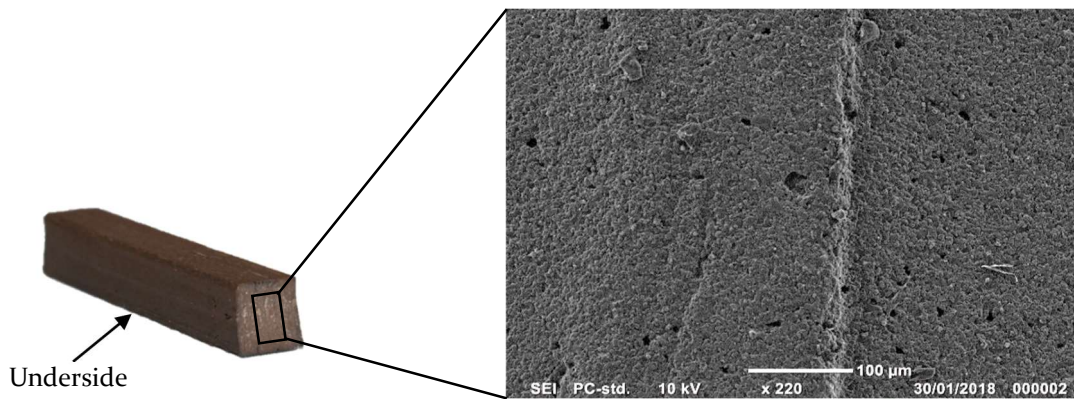


Figure 5-20 – shows the fracture surface of the bend test sample using SEM at 220 \times magnification

5.5 Process Summary

The fabrication of filled, spanning and overhanging geometries demonstrate the production of 3D ceramic components with reduced surface roughness and comparable resolution to existing ceramic manufacturing processes. The flexural strength and density of the fabricated parts are sufficient to be used within end user applications.

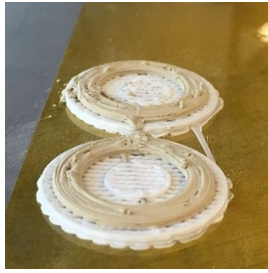
Figure 5-21 shows an overview of the various processing stages of fabricating the conformal geometry as shown in section 5.3.5. The process commences with the fabrication of the substrate using the sacrificial support extruder. The substrate consists of 5 layers of PLA that is deposited using a rectilinear infill pattern. Once the substrate is complete, the first layer of support structure is deposited, also using PLA deposited by the sacrificial support extruder. The solenoid that

the hotend is mounted to is de-energised, causing it to retract vertically, providing the necessary clearance between the inactive tooling and the workpiece.

The ceramic feedstock is then deposited by the ecoPEN-300 through a 437 μm metal tapered nozzle using a constant volumetric flowrate of 76 $\mu\text{L}/\text{min}$ following a concentric fill pattern. The material flow is not terminated when transitioning between parts due to the potential of creating defects as a result of delays in material flow when reinitiating extrusion. The resultant layer has a thickness of ~ 350 μm . The deposited material is then dried using the heated forced convection drying unit. During the drying process, the drying unit follows a raster pattern to uniformly heat the layer and prevent hotspots that may result in cracking or bubbling of the part as shown in chapter 3.4.

The tool change operation is then run, calling for the $\text{\O} 4$ mm CVD fluted end mill. The blanking adapter is firstly deposited in its corresponding slot within the toolholder before picking up the specified tool, in this instance the $\text{\O} 4$ mm CVD fluted end mill. The part is machined using a layer height of 300 μm using a spindle speed of 15,000 RPM and a feedrate of 330 mm/min. After the machining process is finished, the spindle is stopped and the tool change operation is once again run, the deposit the collecting tool and pick up the blanking adapter to provide clearance between the inactive tooling and the work piece. This process is repeated until a near net shape of the component is produced, after which the tool change operation is used to collect the specified tool, in this instance the $\text{\O} 1$ mm ball nose cutter. The external surface of the conformal geometry is machined using a spindle speed of 15,000 RPM, feedrate of 330 mm/min and step-down height of 0.2 mm.

The finished parts are then removed from the hybrid manufacturing platform, remaining attached to the PLA substrate and support throughout plus during shipping to Morgan Advanced Materials. Once received the parts were placed, inverted on the carriage that moves the parts through the tunnel kiln, alongside conventionally manufactured part. Post-firing the parts were determined to have a density of 97.93% and undergoing a linear shrinkage of $\sim 16\%$.



Substrate and sacrificial support

- Create a 2 mm (5 layers) sacrificial PLA rafter onto a metal bed covered in Kapton tape and heated to 60°C.
- Deposit a layer of sacrificial support material before depositing, drying and machining the ceramic material layer.



Ceramic Deposition

- Deposit a layer of ceramic feedstock with the ecoPEN-300 and a 437 μm tapered nozzle using a volumetric flow rate of 76 $\mu\text{L}/\text{min}$.
- After extrusion, the material is dried for 3 minutes. The convection drying unit is rastered across the parts to prevent hot spots.



Layer Machining

- The automatic tool changer deposits the blanking device in the tool holder and picks up the $\text{Ø}4$ mm end mill.
- The parts are machined using a spindle speed of 15,000 RPM and a feedrate of 330 mm/min.



Post-process Machining

- Once a net shape has been fabricated the automatic tool changer deposits the blanking device and picks up the $\text{Ø}1$ mm ball nose cutter.
- Machine the part using a spindle speed of 15,000 RPM and a feedrate of 330 mm/min. The net shape is deliberately oversized by +0.5 mm.



Part Removal

- The part is removed from the build plate of the hybrid manufacturing platform. The part is mechanically cleaned with a soft brush to remove machining debris before being sent to Morgan Advanced Materials for post-processing.



Post-processing

- The sample was placed into a ceramic processing tray in an inverted orientation before being loaded into an industrial tunnel furnace with the substrate and sacrificial support still attached.
- Debinding and sintering occurs as the part moves through the tunnel furnace, which has a peak temperature that exceeds 1,400°C.
- Visual inspection of the part shows no residue from the substrate/support material or distortion of the ceramic part.
- Calculation of part shrinkages and density were determined under the supervision of technical staff at Morgan Advanced Materials.

Figure 5-21 – Shows an overview of the various processing stages used to fabricate the hollow hemisphere using the hybrid manufacturing process.

6 Ceramic electronics

Harsh environments are described as any location or surrounding in which survival is arduous or outside the bounds of possibility [242]. Operations such as resource extraction and mining, power generation and transmission, transportation (automotive and aerospace) and chemical processing can expose components to harsh environments. These environments subject components to a number of factors including extremes of temperature and rapid temperature cycling plus chemical, radiative and mechanical stresses. Components within these environments are often high value, safety or mission critical elements that integrate electronics for sensing, actuation and control purposes. Consequently, these elements need to have stable and reliable operation over extended durations. However, silicon-based semiconductors and package materials such as thermoplastics cannot achieve the required performance or service life necessary for harsh environment applications [243].

Silicon-based electronics are designed to function at room temperature with an operational temperature range of -55°C to $+125^{\circ}\text{C}$ and relative humidity (RH) of between 40% and 60% [242]. At elevated temperatures $>125^{\circ}\text{C}$ the thermal energy of the electrons within silicon exceeds the bandgap energy, resulting in a breakdown of the material's semiconductor properties to that of a conductor. This subsequently causes the malfunction and potentially irreparable damage of the component. Rapid temperature cycling is also problematic due to mismatched coefficients of thermal expansion, resulting in fatigue and stress cracking of connection interfaces such as solder joints. The performance of conventional electronics is further exacerbated in conditions with $>80\%$ RH, which are classified as "very high" humidity environments. In these environments, water vapour readily condenses on the metal surfaces of the device can result in short circuits and ultimately premature failure of the device. Moisture is problematic for metallic elements of the device, which can corrode, resulting in an increase in the contact resistances.

Electronics components and devices such as integrated circuits (IC) are typically mounted within a package that streamlines manufacturing and provide

protection from environmental variables such as humidity. However, these packages are often manufactured using polymers that contain ultra-fine glass particles, which provides limited protection against high temperature and harsh environments. The integration of active or passive cooling solutions enables these devices to operate at elevated temperatures beyond those considered to be normal operating ranges. However, this approach is not without limitations, due to the additional weight, bulk and complexity of these systems. Consequently, thermal management solutions are often used with lower cost applications, where operating conditions do not warrant the use of materials such as advanced ceramics. However, for applications such as sensing within gas turbines, devices may be subjected to operating temperatures in excess of 1,000°C [244]. Within these high value, safety critical applications thermal management solutions may be incapable of achieving the required performance, particularly over extended periods. Furthermore, the added weight and complexity is undesirable, whilst increasing number of potential failure modes. In addition to the effects of temperature and humidity, harsh environments can also be exposed to corrosive media (other than humidity), nuclear and electro-magnetic radiation, vibration and mechanical shocks. Operations such as petrochemical exploration is striving to extract natural resources at increasingly remote and harsh environments, subjecting components to temperatures of >200°C, corrosive media plus shocks and mechanical vibrations at drill depths of up to 5km [242]. Operating within these environments necessitates the use of alternative materials including advanced ceramic materials.

Advanced ceramic materials are well established within the field of electronics, fulfilling a variety of functions such as substrate and package materials, electrical and thermal conductors, wideband gap semiconductors and passive components such as capacitors, inductors, and resistors. The use of advanced ceramic materials is as often necessitated by the need to operate within the aforementioned high temperature and harsh environments [245]. However, passive components such as ceramic capacitors are frequently used within conventional electronics. Wide bandgap semiconductors such as Silicon carbide

and Gallium nitride, enable devices to operate at temperatures, voltages and frequencies compared to conventional silicon-based semiconductors [242]. The manufacture of wideband gap semiconductor devices is beyond the resolution of the processes being discussed within this section. The remainder of this chapter will focus on the application of digital fabrication techniques for the production of ceramic electronics on substrates fabricated using the developed hybrid manufacturing platform.

Conventional manufacturing of ceramic electronics is reliant on template-based production methods to fabricate substrates and deposit materials such as conductive, resistive, capacitive and inductive materials [246]. This requires high volume production, limits design freedoms to 2.5D planar geometries and inhibits responsiveness to design modification. Digital fabrication of ceramic electronics has the potential to offer increased design freedom, that will contribute towards improved performance and reliability. The ability to dynamically alter material composition and internal structures of substrates and packages can help enable devices to withstand more extreme operating conditions [247]. This is complimented by the ability to produce components in low volumes without part specific manufacturing equipment.

Thick film production techniques are also referred to as “printed-and-fired” electronics; depositing conductive, resistive and dielectric pastes onto sintered ceramic substrates to form the electronic circuits [248]. The sintered substrates are often planar in design with low surface roughness, which are produced using conventional shaping and forming processes such as pressing and sheet lamination. The deposition of conductive and dielectric pastes onto these substrates uses processes such as screen-printing as shown by Figure 6-1a. Screen printing is a template-based fabrication technique that is widely used across the electronics manufacturing. Screen printing enables short manufacturing throughput times with the deposition of fine features down to 50 - 100 μm with a thickness of 5-20 μm at [249]. Once deposited, a secondary thermal process sinters the deposited conductive, resistive, and dielectric materials to achieve the required electrical performance and adhere it to the ceramic substrate. This typically requires temperatures less than 1,000°C,

which is below the melting points of the metals within the pastes, such as silver, which has a melting temperature of 961°C. and [250]. This second thermal process requires the thick film materials to exhibit anisotropic shrinkage rates, particularly in the X-Y plane as the sintered ceramic substrates do not shrink during these secondary thermal processes. This anisotropic shrinkage may be problematic when deposited onto digitally fabricated substrates, which may have non-planar geometries plus surface imperfections such as stair stepping. Non-planar geometries may be incompatible with existing thick film materials due to mismatched thermal expansion and shrinkages. This may result in breaks and discontinuities in the circuit following the firing process. The possibility of discontinuities is potentially exacerbated by the presence of stair stepping or surface textures caused by post-process machining, which can act as stress raisers. Figure 6-1b shows a planar thick film ceramic circuit, formed from the silver-Palladium conductor paste on a sintered alumina substrate. The dark rectangles on the circuit are thick film resistors that have been laser etched to have the required resistance.

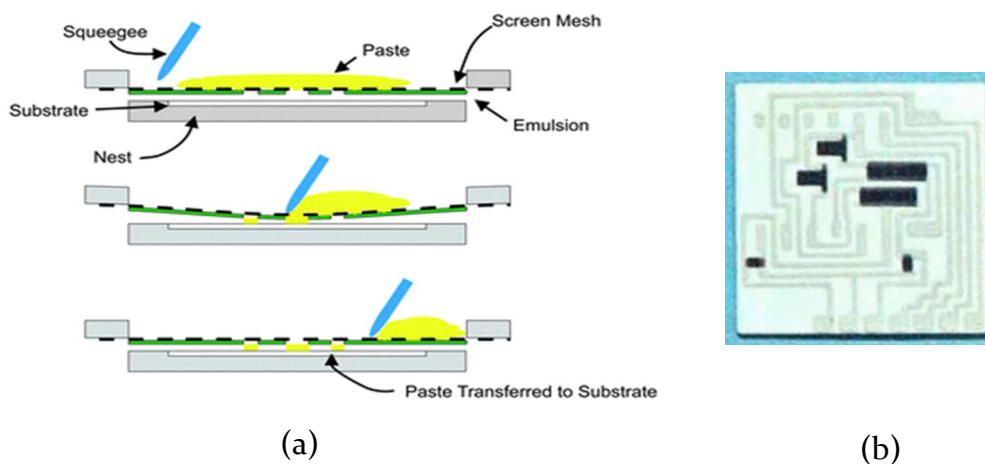


Figure 6-1 – (a) shows the screen printing process [251] (b) shows a planar circuit produced using screen-printed silver-Palladium conductor plus resistor materials [252]

Whilst thick film electronic production is technically an additive process, the reliance on templates is restrictive, particularly when attempting to functionalise 3D non-planar substrates produced using digital fabrication approaches. DIW has the potential to deposit thick-film materials onto 3D ceramic substrates, overcoming some of the limitations of conventional, template-based thick film manufacturing processes. This chapter demonstrates

the use of a commercially available pure silver (Ag) Co-fireable conductor paste (TC0306A, Heraeus, Germany) with a peak sintering temperature of 865 °C, to create ceramic electronics on substrates produced using the developed hybrid manufacturing platform as shown in chapter 5. DIW of a commercial conductor demonstrates the feasibility of digital fabricating thick film ceramic electronics, enabling low-volume production of harsh environment electronics with greater design freedoms [253]. A summary of the fabrication for each part shown in this chapter is documented in Appendix C.

6.1 Extrusion of LTCC Ag Paste

The Ag conductor paste is a single print co-fired surface conductor with 90 wt% ± 2 wt% solids loading. The conductor is intended to be deposited using a screen-printing process with a 250 – 325 (67 - 55 μm aperture) mesh. The material has a quoted viscosity of 170 – 200 Pas viscometer at 25°C [220], which is comparable to the measured viscosity of the alumina feedstock used in the production of the aforementioned ceramic parts. This indicates that the Ag paste should be extrudable using the previously investigated pneumatically actuated extrusion systems.

The Ag conductor paste was deposited directly from a material barrel using a pneumatic ram extrusion system (DC100 digital dispensing controller, Fisnar, USA) attached to a 3-axis robot (7400NVL, Fisnar, USA) with a repeatability of $\pm 8 \mu\text{m}$. The 3-axis robot was used to dispense the thick-film material and solder paste, used during a latter processing stage, instead of the developed hybrid manufacturing apparatus. The 3-axis robot is equipped with a laser profile scanner (IL-030, Keyence, Japan), CCD-camera vision system, and vacuum pick and place system (VPPE5II-LF, Fisnar, USA). These capabilities can be incorporated onto the hybrid manufacturing platform, although the use of the 3-axis robot was a matter of convenience. The laser profile scanner provides a topographical compensation capability, enabling the 3-axis robot to dispense onto 3D geometries with a constant nozzle height. The vision system enables the detection of reference features such as fiducial marks for alignment and programming purposes. This enables the parts to be removed and thermally

process the deposited thick-film materials before returning the part to the 3-axis robot to deposit the solder and place appropriate surface mount assembly (SMA) components. The deposition of solder utilises the vision system to identify the bond pad locations, depositing the solder using the pneumatic ram extrusion system. The vacuum pickup system was used to locate and deposit the circuit components. Figure 6-2 shows an overview of the process that was used to fabricate the ceramic electronics on the sintered alumina substrates.



Figure 6-2 – Shows a summary of process used to digitally fabricate electronic features on the sintered alumina substrates

The Ag thick-film conductor was designed to be deposited using a stencil-based manufacturing process. However, deposition using an extrusion-based process may alter the processing and material characteristics, such as the intended anisotropic shrinkage and final conductivity. Sheet resistance is a method of characterising the resistivity of a materials, specifically thin films, typically using four-point (4-pt) probe measurements. Four-point probe measurements are typically preferred over two-point probe measurements as errors caused by contact resistance can be compensated for. The probes of the measurement head are brought into contact with the material applying a constant current to two of the four probes whilst measuring the potential on the remainder using a high impedance voltmeter. Determining sheet resistance requires the fabrication of “thin, circular slice”, to which a correction factor is applied based on the ratio between the diameter of the test specimen and the probe spacing. During this work test specimens with a diameter of 30 mm were fabricated on sintered 96% alumina sheet that measured 50 × 50 × 0.250 mm (AL603026, Goodfellow, USA), applying a correction factor of 0.9895.

Sample 1 was fabricated using a 250 µm tapered polymer nozzle using a constant print height of 0.1 mm and extrusion pressure of 25 psi. Whilst the deposited material coalesced to form a cohesive circular specimen, the material extrusion rate was increased to 28 psi, which resulted in greater coalescing of the

deposited material. Figure 6-3a-c shows the samples after deposition but prior to debinding and sintering. Figure 6-3b exhibits a slight colour change as it was exposed to atmospheric conditions overnight, causing it to dry out. Drying of the deposited conductor material is often done during conventional manufacturing using a drying oven with temperature of 50 - 200°C. Figure 6-3d-f shows the samples post-sintering that was done using a chamber furnace following the recommended thermal profile shown by Figure 6-4.

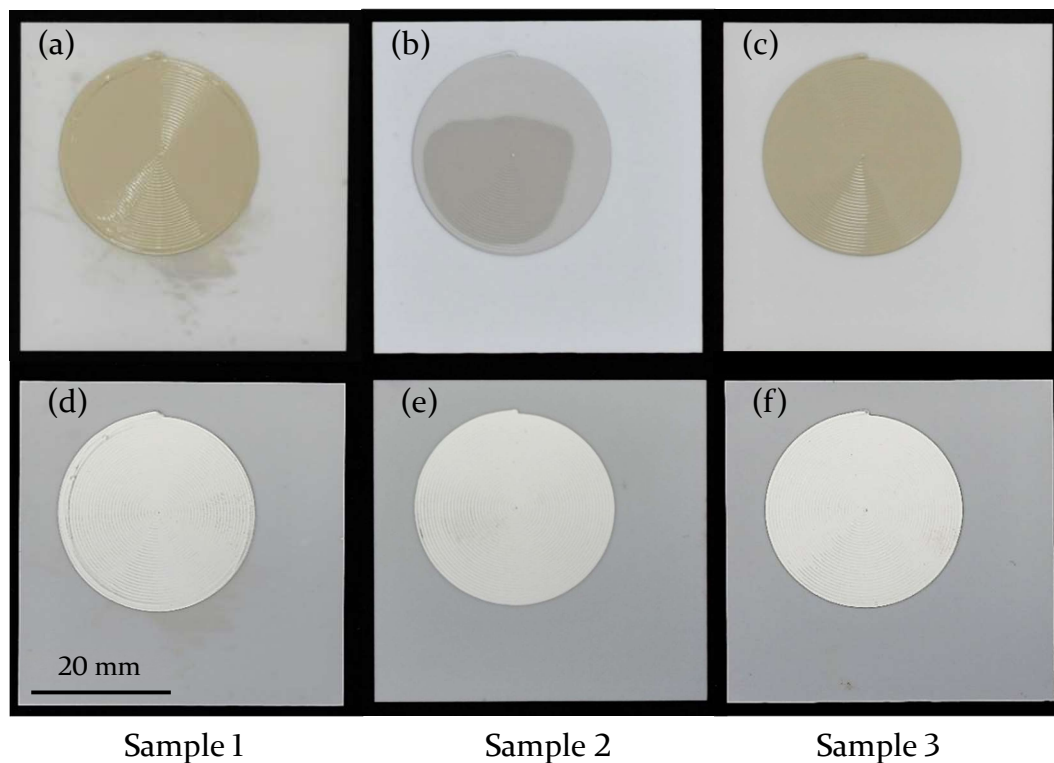


Figure 6-3 - (a-c) shows the unsintered Ag conductor deposited onto alumina substrates. (d-f) shows the sintered Ag conductor

The firing process was completed using a laboratory chamber furnace (RHF 16/3, Carbolite, UK) initially increasing the temperature ambient 100°C at 3 °C/min, after which it ramps to 450°C at 1°C/min. This pre-sintering stage decomposes the binder material and prevents thermal shock to the remaining inorganic material. The temperature ramp then increases to 865 °C at 8.0 to 10 °C/min, where it is maintained for 20 to 30 minutes to sinter and densify the ceramic material, after which it is cooled back to ambient conditions at 10 °C/min.

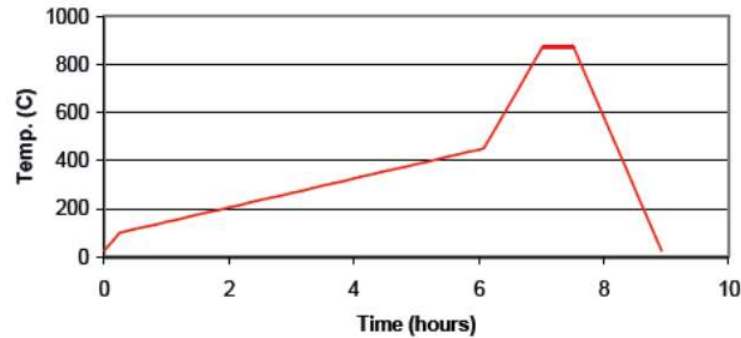


Figure 6-4 – Shows the manufacturers thermal profile for the Ag conductor paste (TC0306A, Heraeus, Germany)

Determining the volume resistivity of the specimen requires the sample thickness. The diameter and thickness of the samples were measured using optical metrology (InfiniteFocus, Bruker/Alicona, Germany) using a 10x objective, providing a vertical resolution of $< \pm 400$ nm and a lateral resolution ± 1.76 μm . Table 6-1 shows the measured diameters and thicknesses of the specimens' pre and post-sintering.

Table 6-1 – Measurement of the unsintered and sintered diameter and thickness with the calculated shrinkage

Sample	Unsintered Diameter (mm)	Unsintered Thickness (μm)	Sintered Diameter (mm)	Sintered Thickness (μm)	Diameter shrinkage (%)	Thickness shrinkage (%)
1	30.306	68.54	30.228	44.70	0.26%	34.78
2	29.767	57.68	29.69	39.39	0.23%	31.66
3	30.255	71.40	30.195	50.36	0.19%	29.47

The measured shrinkage values are consistent with the quoted values on the LTCC silver paste data sheet, which states an X-Y shrinkage of $0.20\% \pm 0.04\%$ ($\leq 0.35\%$) and a Z shrinkage of 32% . The Ag silver paste's resistivity was measured using a 4-pt probe (Cylinder four-point probe, Jandel, UK) with a 1 mm probe spacing. The 4-pt probe was used in conjunction with a source measurement unit (SMU) (2450 SourceMeter, Keithley, USA) outputting 100mA. Inputting the samples thickness into the SMU enables the direct output of volume resistivity. The samples were manually positioned underneath the 4-pt probe, which was positioned in the centre of the circular specimen. Five measurements were produced from each specimen, rotating the sample by 90° between each measurement. The aforementioned correction factor was applied to the average of the five measurements from each sample,

with the samples having an average volume resistivity of 8.49×10^{-8} - 1.14×10^{-7} Ωm . This is between ~ 5 and 8 times the resistivity of bulk silver, which has a bulk resistivity of 1.59×10^{-8} Ωm . Despite this, it is within the manufacturers specified limits and sufficient for demonstrating the feasibility of this approach to produce ceramic electronics. The full dataset for these samples is available in Appendix L. Figure 6-5 shows the volume resistivity data for the samples plotted, which shows comparable performance between all of the samples. However, sample 1 has a visually rougher surface compared to sample 3, which provides some explanation for the increased volume resistivity and deviation within measurements [254].

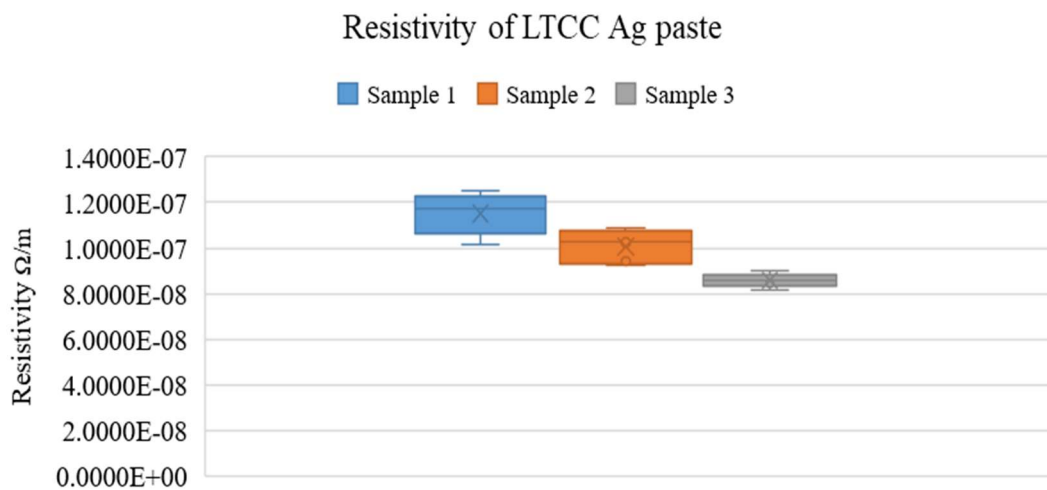


Figure 6-5 – shows the variation in conductivity across the three test samples post sintering.

Figure 6-6 shows an analysis of the surface roughness of the unsintered specimens. Figure 6-6a shows the surface roughness profile of sample one which has a surface roughness R_a of $14.4 \mu\text{m}$. Figure 6-6b shows sample two that has a visibly lower surface roughness, with a measured surface roughness R_a of $8.1 \mu\text{m}$. Figure 6-6c shows sample three, has the lowest measured surface roughness R_a of $6.2 \mu\text{m}$. The surface roughness on these samples is an artefact of the spiral motion and step over distance between adjacent tracks. This variable surface roughness is an artefact of extruding the LTCC silver paste, which might be removed with further process optimisation or by the modification of the paste pseudoplastic response.

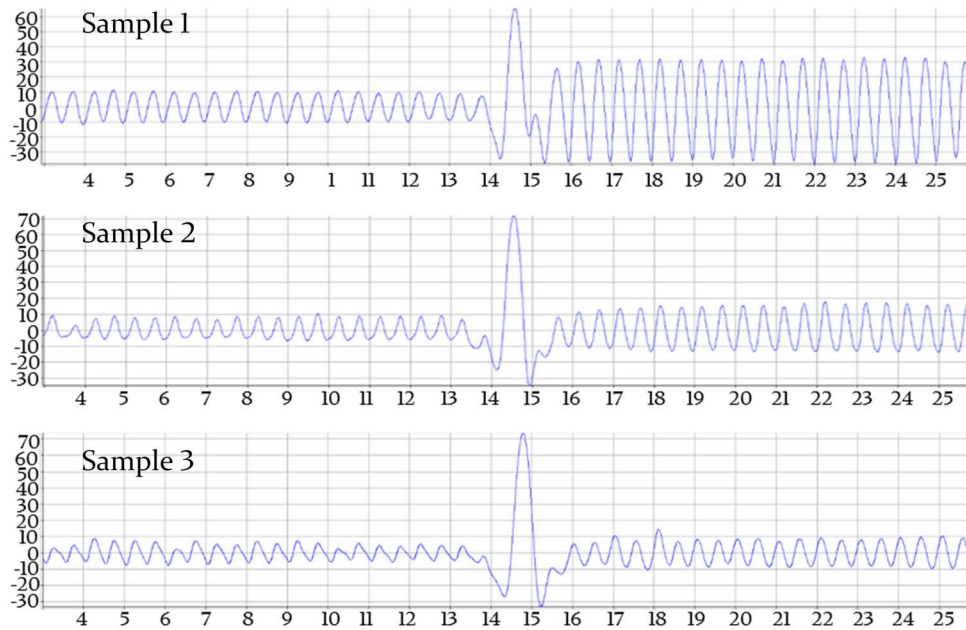


Figure 6-6 - shows the surface roughness of the 4-pt probs disks with sample 1 having an R_a of $14.4 \mu\text{m}$, sample 2 with a surface roughness R_a $8.1 \mu\text{m}$, sample 3 with a surface roughness R_a of $6.2 \mu\text{m}$

6.2 Ceramic electronic circuits

The compatibility of the thick-film conductor with the sintered alumina parts was investigated with the deposition of 12 tracks with pads for 0603 (1608 metric) components at either end. An additional 8 unconnected pads were also deposited to enable the placement of up to sixteen 0603 electronic components. The substrate underwent no further processing once sintered, with the LTCC silver conductor deposited onto the top surface of the part. The tracks were produced using a pneumatic ram extrusion system on the 3-axis dispensing robot using a $250 \mu\text{m}$ tapered polymer nozzle applying a pressure of 28 psi and a feedrate of 420 mm/min. Measurement of the sintered tracks was done using optical metrology (InfiniteFocus, Bruker/Alicona, Germany) using a 10x objective. The tracks were determined to have a track width of $199.36 - 341.9253 \mu\text{m}$ with an average width of $282.6569 \mu\text{m}$. The pads had measured diameters of $481.3343 - 611.4639 \mu\text{m}$ with an average diameter of $532.8568 \mu\text{m}$. Figure 6-7 shows profile of a deposited track, with the track being initiated on the left and terminated on the right, which has a minimum thickness of $70 \mu\text{m}$ with a maximum of $185 \mu\text{m}$.

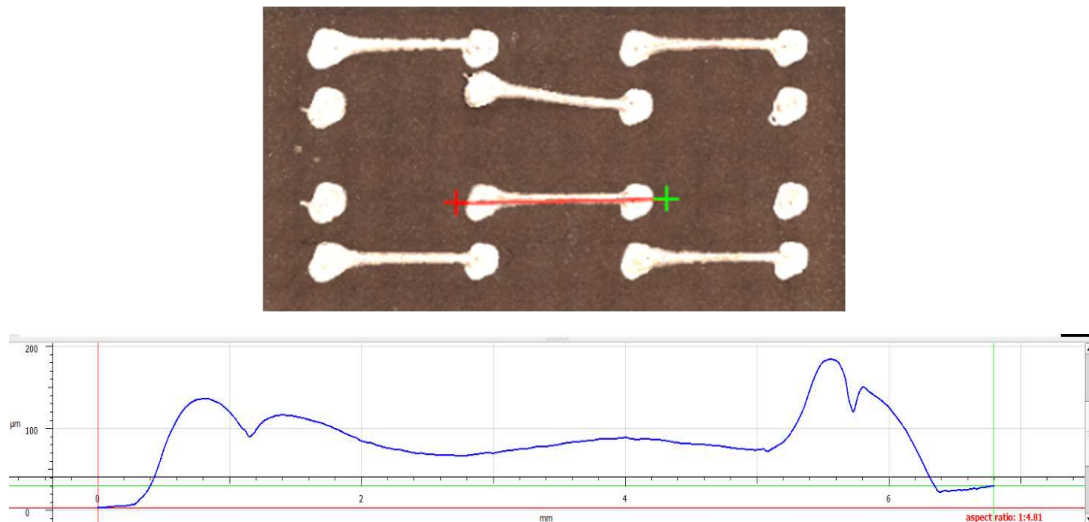


Figure 6-7 – Shows the profile of a sintered track on the alumina substrate

Adhesion of the tracks to the substrate was investigated using a tape test method using flatback tape (Scotch 250, 3M, USA). The sample was cleaned with Isopropanol alcohol (IPA) to remove contaminants such as flux and grease. The tape was applied to the sample, ensuring that the entire track was covered with no air pockets between the tape and the track. The tape was peeled back at 180° until it was no longer in contact with the track. This was carried out on all of the deposited tracks, using new tape for each track. All of the tracks remained attached to the substrate, confirming that there was sufficient adhesion to enable the fabrication of thick-film electronic circuits.

The solderability of sintered tracks was investigated by the deposition of Type-5 Tin-Silver-Copper (SAC) solder paste (SMD291SNLI0T5, Quikchip) onto 16 pads through a 250 µm tapered polymer nozzle using a pneumatic ram extruder. The solder paste is composed of 96.5 wt% Tin (Sn), 0.5wt% Silver (Ag) and 3.0wt% Copper (Cu) with a particle size distribution of 15 - 25 µm. Programming of the dispense locations involved the use of the CCD camera to locate the pads on the substrate, with the co-ordinates being subsequently recorded by the software. Once programmed, the robot completes a pre-dispense check to ensure the alignment of the part using the CCD camera, whilst the laser profile scanner ensures a consistent dispense height. Once the checks are complete, the solder is autonomously dispensed onto the designated pads. Eight 0603 passive components were subsequently placed onto the pads with

solder using a vacuum pickup system (VPPE511-LF, Fisnar, USA) that was mounted on 3-axis robot. For this application, the pick and place system was configured with a straight nozzle, with the components positioned in the same orientation as pads on the substrate prior to being picked up. The placement of the components was manually controlled by the operator, positioning the robot, and actuating the vacuum system using the user control interface. Once all of the components were placed, the solder was reflowed to form a permanent joint with the necessary electrical and mechanical properties. Reflowing the solder was done using a high temperature convection oven (LHT6/30, Carbolite, UK) with a temperature stability of $\pm 0.5^{\circ}\text{C}$ and a temperature uniformity of $\pm 5.0^{\circ}\text{C}$ at 250°C , following the manufacturers recommended reflow profile (shown in Appendix M) with a peak temperature of 249°C at 240s (four minutes). Figure 6-8 shows the sample with the deposited tracks and six 0603 components.



Figure 6-8 – Shows an alumina substrate with sintered LTCC Ag tracks and 1210 components that have been reflowed with SAC solder at a peak temperature of 249°C

The production of a functional circuit was demonstrated with a 555-timer circuit attached to a red LED on an alumina substrate that measures $20 \times 30 \times 3$ mm. Figure 6-9a shows the sintered LTCC conductor that was deposited using the dispensing robot and pneumatic extrusion system using a $250\ \mu\text{m}$ nozzle and a feedrate of 390 mm/min. Figure 6-9b shows the circuit with the LED illuminated, demonstrating that the circuit functions as intended. The circuit was produced using seven passive 1608 components, a leaded transistor and 555-time IC package, which are affixed to the circuit using type-5 SAC solder that was reflowed at a peak temperature of 249°C . Wire connectors were hand soldered to the connector pads to enable the circuit to be connected to a benchtop power supplier outputting 5V. To the author's knowledge, this is the

first example of a thick film ceramic circuit produced by DIW on a ceramic substrate that was manufacturing using an AM process.

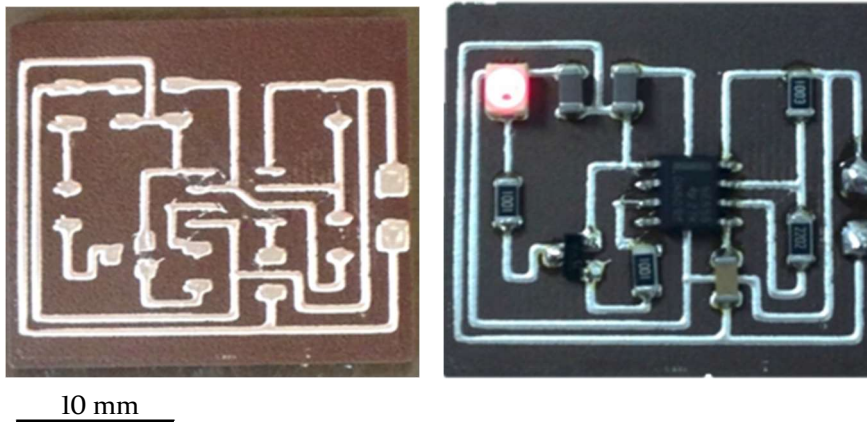


Figure 6-9 – Shows a functioning 555-timer circuit on a planar alumina substrate

Topographical compensation of the extruder on the 3 axis robot enabled by a laser profile scanner (IL-030, Keyence, Japan) enables the deposition onto non-planar 3D substrates. Depositing onto non-planar 3D substrates presents a number of challenges due to the potential for spreading due to the effect of gravity during the thixotropic relaxation period and distortion of features caused by the substrate and deposition nozzle not being perpendicular. Figure 6-10 shows the deposition of the LTCC silver conductor onto a flat top pyramid structure using a 200 μm nozzle. The thixotropic response of the LTCC paste resulted in no visible spreading of the deposited material with sufficient adhesion to enable vertical and horizontal depositions.

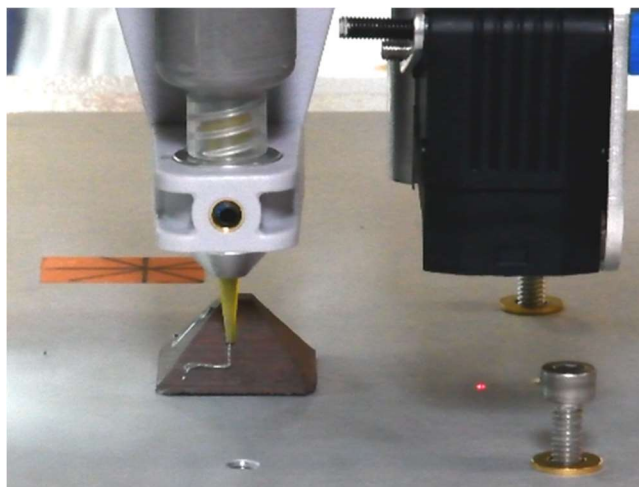


Figure 6-10 – Shows LTCC silver conductor being deposited onto a 3D geometry using topographical mapping generated by a Keyence

Figure 6-11a shows the pyramid with a non-planar 555-timer circuit post-sintering. Continuity testing of the circuit using a handheld multimeter (115 multimeter, Fluke, USA) confirmed that no breaks in the deposited tracks had occurred. Adhesion of the circuit was investigated using the aforementioned process, which resulted in none of the tracks becoming detached from the substrate. However, the tracks do have visually inconsistent track widths and heights due to the challenges of depositing onto 3D geometries using a 3-axis system. Deposition of SAC solder was achieved using a 200 μm straight profile nozzle. Placement of the 1210 components was achieved using a vacuum pick-up system using a straight pickup attachment for the LED and a 45° pickup attachment for the remaining components. The part was manually indexed through 90° to enable the parts to be placed. Reflow of the solder was done using the orientation shown by Figure 6-11b. Wires were manually soldered to the connection pads that were connected to a benchtop power supply outputting 5V, causing the LED to illuminate.

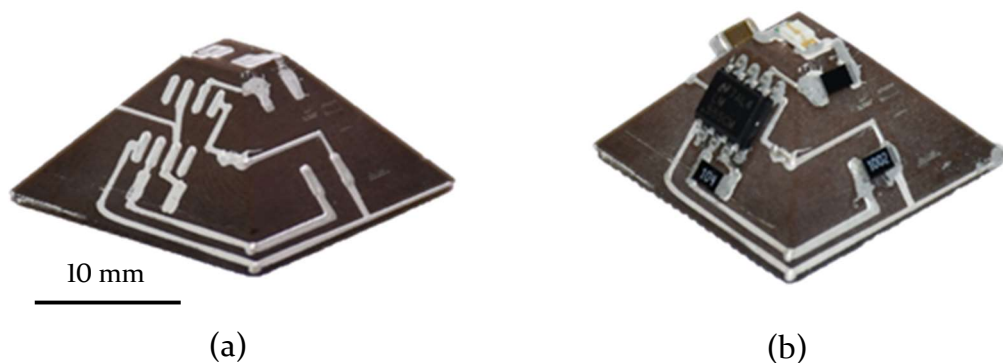


Figure 6-11 a) shows the sintered 3D thick film circuit produced using DIW of LTCC Ag conductor b) shows the circuit with the 1210

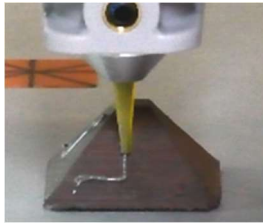
6.2.1 Process Summary

The creation of a non-planar 555-timer circuit on an alumina substrate demonstrates the feasibility of digitally fabricating a 3D thick-film electronic device. This has a number of benefits for harsh environment applications such as more compact device footprints and the incorporation of internal structures for thermal management and weight reduction purposes. Figure 6-12 shows a summary of the process steps used to create the non-planar thick-film ceramic electronics.



Substrate preparation

- Green state substrates produced using the developed hybrid manufacturing platform as shown in Chapter 5.3.3
- Thermally processed by Morgan Advanced Materials in an industrial tunnel kiln with a peak temperature in excess of 1,400°C.



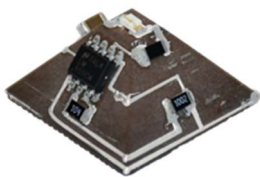
Deposition of Thick-film material

- Deposition of a pure silver (Ag) Co-fireable conductor (TC0306A, Heraeus, Germany) through a 250 μm tapered polymer nozzle using a pneumatic ram extruder.
- Topographical compensation is used to deposit the conductor onto a 3D geometry.



Thermal Processing of thick-film materials

- The thick-film material is sintered in a chamber furnace following the recommended thermal profile with a peak temperature of 865°C.



Deposition of solder and placement of components

- Deposition of Type-5 Tin-Silver-Copper solder (SAC) through a 250 μm nozzle using a pneumatic ram extruder.
- Placement of 555-timer chip and 1210 passive components using a vacuum pick and place mounted on a 3-axis robot. The robot was used as a tele-manipulator. The part was manually rotated by 90° to provide access to each side.
- The solder was reflowed in convection oven with a peak temperature of 249°C.

Figure 6-12 – Shows a summary of the process used to fabricate a 3D ceramic thick-film device on a sintered alumina substrate that was produced using the hybrid manufacturing platform

6.3 Co-fire Ceramics

The production of thick-film ceramic electronics on sintered alumina substrates requires multiple firing processes. This is due to the non-ceramic elements being incapable of withstanding the sintering temperature of the ceramic elements. Multiple thermal processes result in longer production times and increase manufacturing complexity as the coefficients of thermal expansion

need to be closely matched to prevent residual stresses and damage to the part and components. However, the most significant limitation of this approach is the inability to fabricate multilayer circuits, limiting the opportunity to miniaturise the device footprint as only dual sided circuits be produced. However, multilayer ceramic circuits can be produced using alternative material formulations referred to as High Temperature Co-fired Ceramic (HTCC) and Low Temperature Co-fired Ceramic (LTCC). These materials consist of advanced ceramic materials and metals that have been combined with a glass frit to formulate dielectric, conductive, resistive, capacitive and inductive feedstock materials that can be cofired simultaneously. Ceramic substrates are typically created by tape casting the dielectric materials to form uniform, stackable sheets of material, similar to those used in SL ceramic AM processes [255]. Shaping and forming of the substrates involves operations such as pressing, whilst vias between the different layers are created using drilling and more commonly punching. These cavities are subsequently filled with conductive paste to create the vertical interconnects. Conductive tracks and resistive materials are subsequently deposited onto the planar substrate, with fine-tuning of the electrical characteristics being achieved using laser ablation. The various layers of the circuit as subsequently stacked and laminated together to create a multilayer green-state part. Debinding and sintering of the part using a single thermal process at temperatures below 1,000°C for LTCC, results in the production of a monolithic structure containing multilayer electronic circuits [256]. Figure 6-13 shows a comparison between (a) “printed-and-fired” thick-film ceramic electronics and (b) HTCC and LTCC thick film ceramic electronics.



Figure 6-13 – a) shows the process of fabricating ceramic electronics when depositing thick-film materials onto sintered substrates b) shows the process of fabricating ceramic electronics using HTCC and LTCC materials

The use of HTCC and LTCC materials provide a number of advantages compared to other thick-film manufacturing techniques such as providing increased

protection by encasing the circuit within the ceramic plus fewer design restrictions. LTCC materials are extensively used for high-frequency RF [257] and harsh environment sensing [258] applications, due to the low dielectric losses and high conductivity metal.

A benefit of ceramic packages is the ability to create hermetic isolation of the electronic die. This is achieved by sealing the circuit within a cavity created using a “lid” that is typically formed from ceramic or vitreous glass which is sealed using a metal alloy or vitreous glass [259]. However, these additional processes add complexity during manufacture and increase the number of potential failure modes of the device. Interfacing with the encapsulated devices requires feedthroughs, which are typically produced using a metal connector surrounded by glass, commonly referred to a glass-to-metal seal (GTMS) [260]. However, the miniaturisation of devices and the increasingly complex routine of the feedthrough connections is resulting in GTMS becoming a limiting factor, particularly within communication applications. However, ceramic-to-metal seals produced using high-/low- temperature co-fire ceramics enable the design of feedthroughs with fewer design restrictions.

The ability to digitally fabricate multilayer ceramic electronics from LTCC materials with integrated feedthroughs presents a significant opportunity for further miniaturisation and enhanced performance. The feasibility of this approach was investigated by the extrusion of an alumina-based LTCC dielectric material (HeraLock HL2000, Heraeus, Germany) that was converted from a tape-cast sheet into a high viscosity paste. The paste was formulated by technicians at Morgan Advanced Material by thermally processing the tape cast sheets to remove the binder but without sintering the inorganic materials. These materials were subsequently combined with the same binder-matrix as the alumina feedstock used throughout the development of the hybrid manufacturing platform.

The material was deposited directly from a material barrel through a 200 μm straight profile nozzle using a pneumatic ram extruder onto a polyethylene sheet. During this preliminary work, machining of the part was not undertaken. The

material was formed into a rectangular substrate consisting of three layer and measures $12 \times 6 \times 1$ mm. Ag conductor (TC0306A, Heraeus, Germany) was deposited onto the green state substrate through a $250 \mu\text{m}$ polymer tapered nozzle using a pneumatic ram extruder mounted on the 3-axis robot (7400NVL, Fisnar, USA). The resultant tracks measured 10 mm in length. The substrate and conductive tracks were subsequently co-fired in a laboratory chamber furnace (RHF 16/3, Carbolite, UK) following the recommended thermal profile as shown in Figure 6-4. Figure 6-14 shows the sintered substrate and conductive tracks, that were successfully co-fired together.

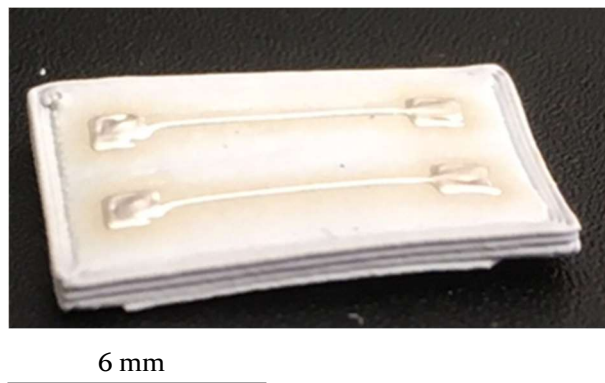


Figure 6-14 – shows the deposition of Ag conductor onto a substrate made from extruded LTCC dielectric material with Ag conductor that was co-fired at a peak temperature of 865°C

Visual analysis of the part shows warping and distortion of the substrate, which is likely due to the disruption of the particle orientation, which results in the anisotropic shrinkage of the material during conventional manufacture. The adhesion of the conductive tracks was investigated using a tape test method using flatback tape (Scotch 250, 3M, USA). The sample was cleaned with Isopropanol alcohol (IPA) to remove surface contaminants. The tape was applied to the sample, ensuring that the entire track was covered with no air pockets between the tape and the track. The tape was peeled back at 180° until it was no longer in contact with the track. The tracks remained attached to the substrate, with no signs of chipping or delamination from the substrate.

This part demonstrates the feasibility of digitally fabricating LTCC electronic devices, suggesting that this approach can be used in the low volume production of co-fired ceramic electronics. This can provide end-users with a method of overcoming the constraints imposed by existing manufacturing techniques.

7 Conclusion and Future Work

7.1 Conclusion

This thesis has presented the development of a hybrid manufacturing process for the production of full density, 3D ceramic components; presenting a new approach with which to fabricate high value, low volume advanced ceramic components. This has been achieved by:

- The development of a new hybrid manufacturing process combining high viscosity paste extrusion, sacrificial support extrusion, and micro-machining for fabricating components from advanced ceramic materials.
- Fabrication of parts from advanced ceramic materials demonstrating a range of geometries including solid, filled geometries, overhanging and conformal geometries.
- Processing of ceramic feedstock derived from conventional manufacturing lines enabling the use of the same front and backend processing.
- Analysis of the fabricated parts confirming the production of full density parts with calculated densities of up to 99.93% and measured shrinkages of ~17-19%.
- Functionalisation of ceramic substrates using DIW of LTCC silver paste and CNC pick and place of surface mount electronic components to create 3D ceramic thick film electronics.

This process has been developed using a modified commercial feedstock with a measured moisture content of between 18-22% enabling the production of parts with comparable densities to conventional manufacturing approaches. The use of commercial feedstocks aims to overcome the challenges associated with conventional ceramic AM and streamlining the integration of templateless manufacturing processes with existing ceramic processing chains.

Material extrusion of an aqueous-based feedstock is appropriate for this type of application as higher volumes of ceramic material can be dispersed within the binder matrix, which reduces the shrinkage during subsequent thermal

processing to form monolithic ceramic parts. Once deposited, the material forms a dilatant mass due to non-Newtonian pseudoplastic behaviour and the evaporation of volatile solvents. This solidification mechanism decouples the effects of colour and refractive index, which restrict the processability of certain materials such as silicon carbide using processes such as VP. Furthermore, the scalability of ME processes is not limited by the restrictive build volumes such as vats and heated build chambers that are required for VP and PBF processes.

The fabrication of substrate rafts and sacrificial support structures was achieved using FFF that was configured using a Bowden tube setup to deposit PLA filament. FFF is a low cost and small form factor AM process that was directly integrated into the hybrid manufacturing systems. The use of PLA, whilst not necessarily optimised, enabled the creation of spanning and overhanging geometries, which could not otherwise be produced. The PLA support remained attached to the green state ceramic parts during thermal processing, decomposing leaving minimal residues and preventing the deformation of the ceramic geometries. However, the use of PLA support within enclosed cavities resulted in the delamination of the parts, regardless of the infill density, preventing the creation of sintered ceramic parts within enclosed cavities.

The subtractive manufacturing capabilities were provided by a machining spindle fitted with an automatic tool changer capable of holding cutting tools with shank diameters of $\text{\O}2\text{-}6.35$ mm enabling the use of an appropriate range of tooling. Diamond cutting tools were found to be the most suitable compared to HSS cutting tools due to the rapid dulling of the cutting surfaces of the HSS tools. Investigation of coarse PCD diamond and fluted CVD diamond tooling, found fluted tooling resulted in better tool performance as the cutting surface did not become saturated with machining debris. Furthermore, the large material removal rates achieved by fluted cutting tools enables the creation of high-fidelity features using processes such as drilling and slot milling. Post process machining using alternative cutting tools such as ball nose cutter enhances the capability of the manufacturing platform by enabling the post-process machining of fabricated parts to remove surface defects and eliminate the stair-stepped appearance associated with AM.

Validation of the hybrid manufacturing platform was achieved through the production of filled (solid) 2.5D and 3D geometries with spanning, overhanging and conformal features. The inclusion of the post-process machining operation resulted in a reduction in surface roughness with average surface roughness R_a $17.9 \pm 13.4 \mu\text{m}$ and R_q $24.6 \pm 19.2 \mu\text{m}$ decreasing to R_a $1.0 \pm 0.5 \mu\text{m}$ and R_q $1.4 \pm 0.7 \mu\text{m}$ for 2.5 D samples. On 3D geometries post-processing using a $\varnothing 1 \text{ mm}$ ball nose cutter with a stepdown height of 0.2 mm result in surface roughness R_a of $37.0 \pm 5.7 \mu\text{m}$ and R_q of $48.1 \pm 7.7 \mu\text{m}$ decreasing to have an average surface roughness R_a of $3.745 \pm 2.020 \mu\text{m}$ and R_q of $5.0 \pm 3.0 \mu\text{m}$. Figure 7-1 shows a range of 3D ceramic parts after thermal processing at temperatures exceeding $1,400^\circ\text{C}$. The sintered fabricated parts achieved a maximum calculated density of 99.93% with an average 3-pt flexural strength of 221 MPa, which is $\sim 70\%$ of the strength of parts fabricated using isostatic pressing.



Figure 7-1 – Shows the range of parts that were fabricated as part of the validation of the hybrid manufacturing process

DIW of LTCC silver conductor paste onto the sintered alumina substrates demonstrated the templateless manufacture of thick film ceramic electronics. The extrusion of the silver paste resulted in measured volume resistivity down to $8.4937 \times 10^{-8} \Omega\text{m}$, which is comparable to bulk silver at $1.59 \times 10^{-8} \Omega\text{m}$. Topographical compensation of the 3-axis extrusion system enables the creation of 3D electronic circuits on the ceramic substrates. CNC controlled deposition of Sn96.5 Ag0.5 Cu3.0 (SAC) solder and pick and placement of 1608 electronic components demonstrate the feasibility of digitally fabricating thick film ceramic electronics. This was validated with the fabrication of a functioning

555-timer circuits that were produced. To the author's knowledge, this is the first example of ceramic electronics produced using digital fabrication techniques.

This work has also demonstrated the feasibility of formulating co-fireable dielectric materials into a high viscosity paste with pseudoplastic rheological characteristics to enable the fabrication of LTCC ceramic substrates. Co-firing with LTCC silver conductor demonstrates the future potential for fabricating multilayer, co-fire ceramic electronic devices. Figure 7-2 provides a visual representation of the hybrid manufacturing approach for digitally fabricating geometrically complex ceramic substrates with integrated, thick-film electronics.

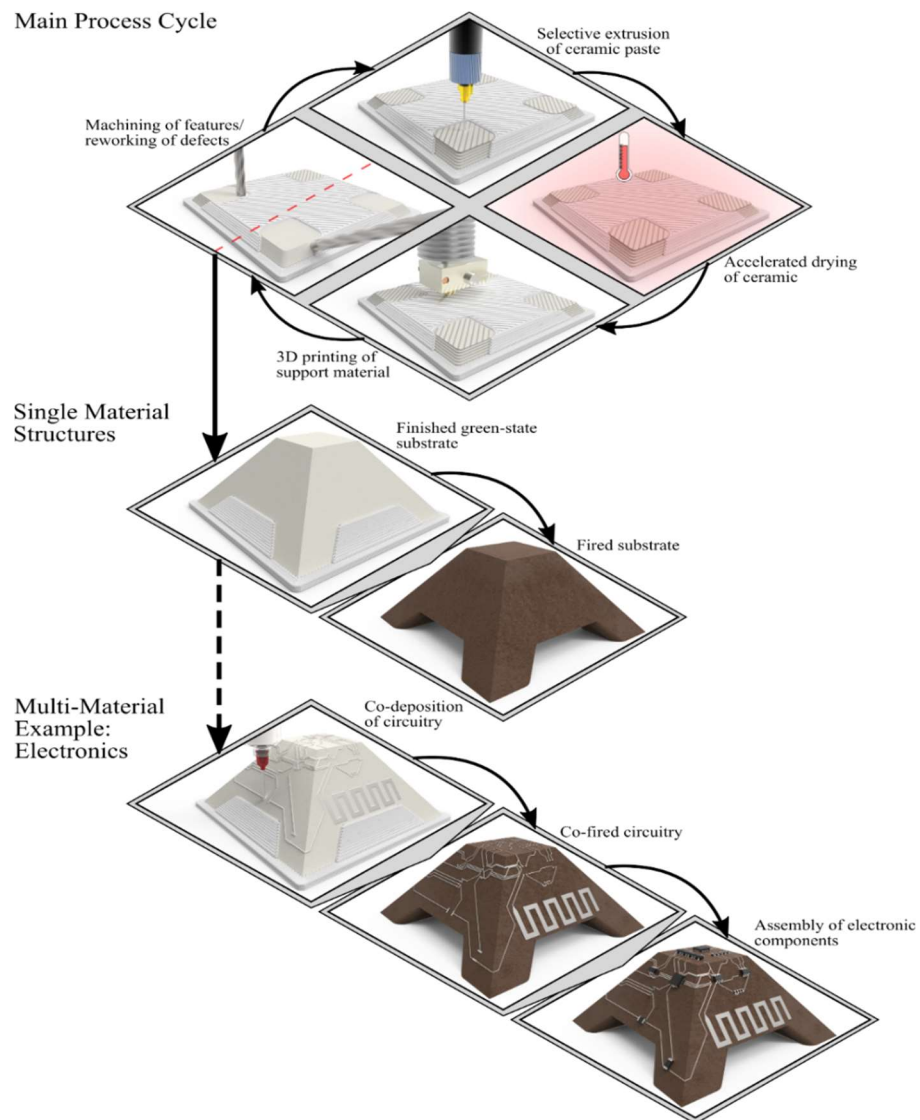


Figure 7-2 – Shows an overview of the hybrid manufacturing process with the incorporation of digitally-driven, 3D thick-film electronics.

7.2 Future work

7.2.1 Materials and feedstock development

Throughout this work raft substrates and sacrificial support were produced using PLA polymer as it had sufficient performance to enable the production of these initial components. However, the creation of parts with enclosed cavities proved unsuccessful due to the pressure increase caused by the decomposing PLA. Investigation of alternative filaments that are specifically designed for manufacturing applications such as investment casting may facilitate the creation of enclosed cavities without the need for ventilation ports. Moreover, the use of FFF substrates and supports resulted in the transfer of infill patterns to the ceramic part. Therefore, optimisation of the FFF process may enable the fabrication of support with lower surface roughness, resulting in lower resultant surface roughness on the ceramic part.

ME processes are capable of using a wide range of advanced ceramic materials due to the decoupling of refractive index and colour from the processability of feedstock materials. The use of aqueous feedstocks with an appropriate particle size distribution that exhibit non-Newtonian, pseudoplastic responses can increase the versatility of the process and expand the range of potential commercial end users. The feasibility of formulating LTCC materials into high viscosity paste as shown previously has the potential to enable templateless manufacturing of multilayer LTCC electronics. The samples produced demonstrate the feasibility of this approach, although a number of processing challenges remain.

Alternatively, SiC is an advanced ceramic material with numerous engineering applications including high temperature electronics [261], heating elements [262] and automotive components [263], [264]. SiC has proved challenging to process using existing AM approaches due to its high hardness, refractive index and thermal coefficients that result in insufficient resolutions and density. Figure 7-3 shows preliminary work using SiC pastes. Figure 7-3a shows a hollow hemisphere that was produced using the same toolpath file as shown previously.

Figure 7-3b shows a tube fabricated from SiC with the lower section post-processed machined and the top section being layer-machined only.

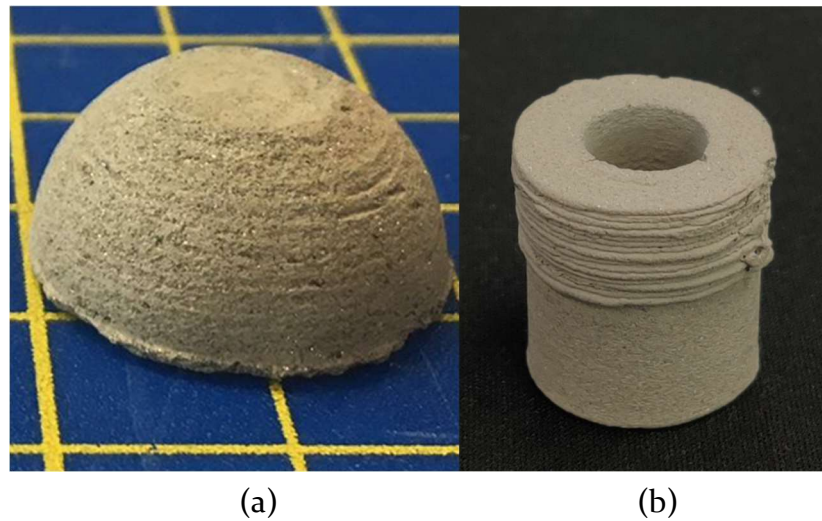


Figure 7-3 – a) shows a hollow hemisphere fabricated from silicon carbide using the hybrid manufacturing process. b) shows a tube geometry fabricated from silicon carbide. The base of the part was post-process machined whilst the top was not.

7.2.2 Process Optimisation

The current optimisation of the hybrid manufacturing platform was sufficient to enable the fabrication of demonstrator components using simple but inefficient manufacturing strategies. This is attributable to the limitations of generating toolpaths using separate, process specific software packages. These software packages had a number of incompatibilities that were overcome using rudimentary measures. The subsequent amalgamation of the various toolpaths was error prone and required manual inspection, which inhibited iterative design changes and manufacturing strategy updates. The application of hybrid software should enable better refinement of the generated toolpaths and enable iterative design changes.

The current motion platform has a number of shortcomings in terms of repeatability. Characterisation of the motion platform confirmed the occurrence of a systematic error that caused a deviation of up to $\sim 250 \mu\text{m}$ at distances of 150 mm. Optimisation of the existing motion stage could reduce this error, although the stage is limited by intermittent stalling of the motion stage at faster feedrates and accelerations. Furthermore, the lack of shrouding

of the transmission elements will likely result in the ingress of ceramic debris that will accelerate wear of the components, whilst reducing repeatability. Therefore, transitioning to stages that are shrouded and capable of operating at higher feedrates and accelerations could decrease throughput times and increase the resolution of fabricated parts. Additionally, the feasibility of this process has been demonstrated with the use of a 3-axis motion platform, which is adequate for creating a range of overhanging and conformal geometries. However, post process machining of the fabricated parts and feature creation are limited by the restrictions of using a 3-axis stage configuration. Implementing additional 4th and 5th axis would provide more versatility for the manufacturing process. These additional axes would also facilitate the deposition of tracks and features with better uniformity when fabricating 3D thick film electronics.

The current hardware configuration of the hybrid manufacturing platform results in a number of processes being “open loop” control, whereby there is no direct feedback from the manufacturing elements to the control software. This results in a number of limitations and challenges when operating the manufacturing platform. The identification and rectification of processing errors such as nozzle blockages is reliant on operator intervention. Whilst, the system operates autonomously in the fabrication part, it cannot be used unsupervised, requiring continuous supervision. Therefore, the implementation of additional sensing and feedback controls such as integrating a pressure sensor within the ceramic paste extruder would enable autonomous, unsupervised operation.

The implementation of in-process metrology equipment such as laser profile scanners would enhance the capability of the process by enabling automated defect detection and rework of components. Currently, the process requires the operator to visually identify defects on the fabricated part and instigate corrective measures. Furthermore, in-process metrology can be used to further reduce the waste generated by the subtractive manufacturing process. Currently, the machining process is applied every layer regardless of whether it is necessary. In-process metrology could be used to remove a sufficient amount

of material for the part to remain within tolerance but without generating excess waste.

The fabrication of a functioning 555-timer circuit demonstrates the feasibility of producing ceramic-thick film electronics on 3D ceramic substrates using the hybrid manufacturing process. The development of harsh environment sensing applications requires the use additional components and materials to achieve suitable sensing capabilities. Investigation of alternative materials for applications such as thermal measurement could be investigated. Furthermore, the devices fabricated in this work did not undergo reliability testing such as accelerated aging. Therefore, reliability testing of the samples would be advantageous for the design of next generation harsh environment electronic sensors. Finally, the production of substrates and packages for RF applications could be investigated due to the ability to dynamically alter the substrates and structures for next-generation RF applications.

8 References

- [1] S. J. Schneider, "Classification of Advanced Technical Ceramics," 1993.
- [2] E. C. Hammel, O. L.-R. Ighodaro, and O. I. Okoli, "Processing and properties of advanced porous ceramics: An application based review," *Ceram. Int.*, vol. 40, no. 10, Part A, pp. 15351–15370, 2014.
- [3] A. Shui, L. Zeng, and K. Uematsu, "Relationship between sintering shrinkage anisotropy and particle orientation for alumina powder compacts," *Scr. Mater.*, vol. 55, no. 9, pp. 831–834, 2006.
- [4] J. Allen, "An investigation into the comparative costs of additive manufacture vs. machine from solid for aero engine parts," ROLLS-ROYCE PLC DERBY (UNITED KINGDOM), 2006.
- [5] R. Sharma, "The Future Of 3D Printing And Manufacturing" [Online]. Available:
<https://www.forbes.com/sites/rakeshsharma/2014/01/15/1255/#52a9ae026a97>. [Accessed: 19-Oct-2018].
- [6] Frost & Sullivan, "Global Additive Manufacturing Market, Forecast to 2025," Mountain View, CA, 2016.
- [7] Grand View Research, "3D Printing Ceramics Market Size, Share & Trend Analysis Report 2019-2025," 2019.
- [8] SmarTech Markets Publishing LLC, "Ceramics Additive Manufacturing Markets 2017-2028," 2018.
- [9] V. K. Khanna, "Operating electronics beyond conventional limits," *Extreme-Temperature and Harsh-Environment Electronics*. IOP Publishing, pp. 2–24, 2017.
- [10] R. C. Buchanan, *Ceramic materials for electronics*. CRC press, 2018.
- [11] B. H. King, D. Dimos, P. Yang, and S. L. Morissette, "Direct-Write Fabrication of Integrated, Multilayer Ceramic Components," *J. Electroceramics*, vol. 3, no. 2, pp. 173–178, 1999.

- [12] D. Espalin, D. W. Muse, E. MacDonald, and R. B. Wicker, "3D Printing multifunctionality: structures with electronics," *Int. J. Adv. Manuf. Technol.*, vol. 72, no. 5–8, pp. 963–978, May 2014.
- [13] E. DeNava *et al.*, "Three-dimensional off-axis component placement and routing for electronics integration using solid freeform fabrication," in *Solid Freeform Fabrication Symposium, The University of Texas at Austin, Austin TX, Aug, 2008*, pp. 4–6.
- [14] New Venture Research, "The Worldwide Electronics Manufacturing Services Market - 2018 Edition," 2018.
- [15] I. Global Information, "The European EMS Industry - A Strategic Overview of the European Electronic Manufacturing Services Industry 2016-2021," 2018.
- [16] M. Wollschlaeger, T. Sauter, and J. Jasperneite, "The future of industrial communication: Automation networks in the era of the internet of things and industry 4.0," *IEEE Ind. Electron. Mag.*, vol. 11, no. 1, pp. 17–27, 2017.
- [17] J. Wan *et al.*, "Software-Defined Industrial Internet of Things in the Context of Industry 4.0," *IEEE Sens. J.*, vol. 16, no. 20, pp. 7373–7380, 2016.
- [18] Z. Zhu, V. G. Dhokia, A. Nassehi, and S. T. Newman, "A review of hybrid manufacturing processes—state of the art and future perspectives," *Int. J. Comput. Integr. Manuf.*, vol. 26, no. 7, pp. 596–615, 2013.
- [19] R. Merz, F. B. Prinz, K. Ramaswami, M. Terk, and L. E. Weiss, "Shape deposition manufacturing," in *International Solid Freeform Fabrication Symposium*, 1994.
- [20] Y.-A. Song, S. Park, D. Choi, and H. Jee, "3D welding and milling: Part I—a direct approach for freeform fabrication of metallic prototypes," *Int. J. Mach. Tools Manuf.*, vol. 45, no. 9, pp. 1057–1062, 2005.
- [21] J. Li *et al.*, "Hybrid additive manufacturing of 3D electronic systems," *J. Micromechanics Microengineering*, vol. 26, no. 10, p. 105005, 2016.
- [22] S. Martin and H. Johannes, "Additive Manufacturing of Dense Alumina

- Ceramics,” *Int. J. Appl. Ceram. Technol.*, vol. 12, no. 1, pp. 1–7, Sep. 2014.
- [23] T. Moritz and S. Maleksaeedi, “Additive manufacturing of ceramic components,” in *Additive Manufacturing*, Elsevier, 2018, pp. 105–161.
- [24] L. Yang and H. Miyanaji, “Ceramic additive manufacturing: a review of current status and challenges,” in *Solid Freeform Fabrication 2017: Proceedings of the 28th Annual International*, 2017, pp. 652–679.
- [25] E. Zanchetta *et al.*, “Stereolithography of SiOC Ceramic Microcomponents,” *Adv. Mater.*, vol. 28, no. 2, pp. 370–376, Jan. 2016.
- [26] D. Thomas-Vazquez, “3-D printing of polymer-derived CMCs for next-generation turbine blade manufacture,” *Am. Ceram. Soc. Bull.*, vol. 96, Jan. 2017.
- [27] M. Dehurtevent, L. Robberecht, J.-C. Hornez, A. Thuault, E. Deveaux, and P. Béhin, “Stereolithography: A new method for processing dental ceramics by additive computer-aided manufacturing,” *Dent. Mater.*, vol. 33, no. 5, pp. 477–485, 2017.
- [28] T. Chartier, C. Chaput, F. Doreau, and M. Loiseau, “Stereolithography of structural complex ceramic parts,” *J. Mater. Sci.*, vol. 37, no. 15, pp. 3141–3147, 2002.
- [29] M. L. Griffith and J. W. Halloran, “Freeform fabrication of ceramics via stereolithography,” 1996.
- [30] H. Wu *et al.*, “Fabrication of dense zirconia-toughened alumina ceramics through a stereolithography-based additive manufacturing,” *Ceram. Int.*, vol. 43, no. 1, Part B, pp. 968–972, 2017.
- [31] C. Hinczewski, S. Corbel, and T. Chartier, “Stereolithography for the fabrication of ceramic three-dimensional parts,” *Rapid Prototyp. J.*, vol. 4, no. 3, pp. 104–111, 1998.
- [32] A. de Blas Romero *et al.*, “Lithography-based additive manufacture of ceramic biodevices with design-controlled surface topographies,” *Int. J. Adv. Manuf. Technol.*, vol. 88, no. 5, pp. 1547–1555, 2017.

- [33] J.-C. Wang, "A novel fabrication method of high strength alumina ceramic parts based on solvent-based slurry stereolithography and sintering," *Int. J. Precis. Eng. Manuf.*, vol. 14, no. 3, pp. 485–491, 2013.
- [34] A. Zocca, P. Colombo, C. M. Gomes, and J. Günster, "Additive manufacturing of ceramics: issues, potentialities, and opportunities," *J. Am. Ceram. Soc.*, vol. 98, no. 7, pp. 1983–2001, 2015.
- [35] G. Varghese *et al.*, "Fabrication and characterisation of ceramics via low-cost DLP 3D printing," *Boletín la Soc. Española Cerámica y Vidr.*, vol. 57, no. 1, pp. 9–18, 2018.
- [36] T. Chartier *et al.*, "Fabrication of Millimeter Wave Components Via Ceramic Stereo- and Microstereolithography Processes," *J. Am. Ceram. Soc.*, vol. 91, no. 8, pp. 2469–2474, Aug. 2008.
- [37] W. Zhou, D. Li, and H. Wang, "A novel aqueous ceramic suspension for ceramic stereolithography," *Rapid Prototyp. J.*, vol. 16, no. 1, pp. 29–35, 2010.
- [38] M. Zhou *et al.*, "Preparation of a defect-free alumina cutting tool via additive manufacturing based on stereolithography – Optimization of the drying and debinding processes," *Ceram. Int.*, vol. 42, no. 10, pp. 11598–11602, 2016.
- [39] R. He *et al.*, "Fabrication of complex-shaped zirconia ceramic parts via a DLP- stereolithography-based 3D printing method," *Ceram. Int.*, vol. 44, no. 3, pp. 3412–3416, 2018.
- [40] E. Maines *et al.*, "Material Properties of Ceramic Slurries for Applications in Additive Manufacturing Using Stereolithography," Sandia National Lab.(SNL-NM), Albuquerque, NM (United States), 2018.
- [41] C.-J. Bae and J. W. Halloran, "Influence of Residual Monomer on Cracking in Ceramics Fabricated by Stereolithography," *Int. J. Appl. Ceram. Technol.*, vol. 8, no. 6, pp. 1289–1295, Nov. 2011.
- [42] V. Tomeckova and J. Halloran, "Cure Depth for Photopolymerization of

- Ceramic Suspensions,” *J. Eur. Ceram. Soc. - J EUR CERAM SOC*, vol. 30, pp. 3023–3033, Nov. 2010.
- [43] M. L. Griffith and J. W. Halloran, “Scattering of ultraviolet radiation in turbid suspensions,” *J. Appl. Phys.*, vol. 81, no. 6, pp. 2538–2546, 1997.
- [44] J. W. Halloran *et al.*, “Photopolymerization of powder suspensions for shaping ceramics,” *J. Eur. Ceram. Soc.*, vol. 31, no. 14, pp. 2613–2619, 2011.
- [45] G. Ding *et al.*, “Stereolithography-based additive manufacturing of gray-colored SiC ceramic green body,” *J. Am. Ceram. Soc.*, vol. 102, no. 12, pp. 7198–7209, Dec. 2019.
- [46] M. L. Griffith and J. W. Halloran, “Ultraviolet curable ceramic suspensions for stereolithography of ceramics,” in *The 1994 international mechanical engineering congress and exposition*, 1994, pp. 529–534.
- [47] G. Mitteramskogler *et al.*, “Light curing strategies for lithography-based additive manufacturing of customized ceramics,” *Addit. Manuf.*, vol. 1–4, pp. 110–118, 2014.
- [48] S. P. Gentry and J. W. Halloran, “Depth and width of cured lines in photopolymerizable ceramic suspensions,” *J. Eur. Ceram. Soc.*, vol. 33, no. 10, pp. 1981–1988, Sep. 2013.
- [49] E. Schwarzer, M. Götz, D. Markova, D. Stafford, U. Scheithauer, and T. Moritz, “Lithography-based ceramic manufacturing (LCM) – Viscosity and cleaning as two quality influencing steps in the process chain of printing green parts,” *J. Eur. Ceram. Soc.*, vol. 37, no. 16, pp. 5329–5338, 2017.
- [50] U. Scheithauer, E. Schwarzer, T. Moritz, and A. Michaelis, “Additive Manufacturing of Ceramic Heat Exchanger: Opportunities and Limits of the Lithography-Based Ceramic Manufacturing (LCM),” *J. Mater. Eng. Perform.*, vol. 27, no. 1, pp. 14–20, 2018.
- [51] X. Zhang, X. N. Jiang, and C. Sun, “Micro-stereolithography of polymeric and ceramic microstructures,” *Sensors Actuators A Phys.*, vol. 77, no. 2, pp.

149–156, 1999.

- [52] P. Colombo, G. Mera, R. Riedel, and G. D. Sorarù, “Polymer-Derived Ceramics: 40 Years of Research and Innovation in Advanced Ceramics,” *J. Am. Ceram. Soc.*, vol. 93, no. 7, p. no-no, Jun. 2010.
- [53] D. E. Yunus, R. He, W. Shi, O. Kaya, and Y. Liu, “Short fiber reinforced 3d printed ceramic composite with shear induced alignment,” *Ceram. Int.*, vol. 43, no. 15, pp. 11766–11772, 2017.
- [54] Z. C. Eckel, C. Zhou, J. H. Martin, A. J. Jacobsen, W. B. Carter, and T. A. Schaedler, “Additive manufacturing of polymer-derived ceramics,” *Science (80-.)*, vol. 351, no. 6268, pp. 58 LP – 62, Jan. 2016.
- [55] Y. de Hazan and D. Penner, “SiC and SiOC ceramic articles produced by stereolithography of acrylate modified polycarbosilane systems,” *J. Eur. Ceram. Soc.*, vol. 37, no. 16, pp. 5205–5212, 2017.
- [56] J. Schmidt and P. Colombo, “Digital light processing of ceramic components from polysiloxanes,” *J. Eur. Ceram. Soc.*, vol. 38, no. 1, pp. 57–66, 2018.
- [57] X. Wang, F. Schmidt, D. Hanaor, P. H. Kamm, S. Li, and A. Gurlo, “Additive manufacturing of ceramics from preceramic polymers: A versatile stereolithographic approach assisted by thiol-ene click chemistry,” *Addit. Manuf.*, vol. 27, pp. 80–90, 2019.
- [58] E. M. Sachs, J. S. Haggerty, M. J. Cima, and P. A. Williams, “Three-dimensional printing techniques.” Google Patents, 20-Apr-1993.
- [59] P. F. Blazdell, J. R. G. Evans, M. J. Edirisinghe, P. Shaw, and M. J. Binstead, “The computer aided manufacture of ceramics using multilayer jet printing,” *J. Mater. Sci. Lett.*, vol. 14, no. 22, pp. 1562–1565, 1995.
- [60] C. Ainsley, N. Reis, and B. Derby, “Freeform fabrication by controlled droplet deposition of powder filled melts,” *J. Mater. Sci.*, vol. 37, no. 15, pp. 3155–3161, 2002.
- [61] W. D. Teng and M. J. Edirisinghe, “Development of Ceramic Inks for Direct

- Continuous Jet Printing,” *J. Am. Ceram. Soc.*, vol. 81, no. 4, pp. 1033–1036, Apr. 1998.
- [62] X. Ding, Y. Li, D. Wang, and Q. Yin, “Fabrication of BaTiO₃ dielectric films by direct ink-jet printing,” *Ceram. Int.*, vol. 30, no. 7, pp. 1885–1887, Jan. 2004.
- [63] A. Şakar-Deliormanlı, E. Çelik, and M. Polat, “Rheological behavior of PMN gels for solid freeform fabrication,” *Colloids Surfaces A Physicochem. Eng. Asp.*, vol. 324, no. 1, pp. 159–166, 2008.
- [64] J. Windle and B. Derby, “Ink Jet Printing of PZT Aqueous Ceramic Suspensions,” *J. Mater. Sci. Lett.*, vol. 18, no. 2, pp. 87–90, 1999.
- [65] B. Cappi, E. Özkol, J. Ebert, and R. Telle, “Direct inkjet printing of Si₃N₄: Characterization of ink, green bodies and microstructure,” *J. Eur. Ceram. Soc.*, vol. 28, no. 13, pp. 2625–2628, 2008.
- [66] W. D. Teng, M. J. Edirisinghe, and J. R. G. Evans, “Optimization of Dispersion and Viscosity of a Ceramic Jet Printing Ink,” *J. Am. Ceram. Soc.*, vol. 80, no. 2, pp. 486–494, Feb. 1997.
- [67] B. Derby, “Additive manufacture of ceramics components by inkjet printing,” *Engineering*, vol. 1, no. 1, pp. 113–123, 2015.
- [68] Q. F. Xiang, J. R. G. Evans, M. J. Edirisinghe, and P. F. Blazdell, “Solid freeforming of ceramics using a drop-on-demand jet printer,” *Proc. Inst. Mech. Eng. Part B J. Eng. Manuf.*, vol. 211, no. 3, pp. 211–214, Mar. 1997.
- [69] E. Özkol, J. Ebert, and R. Telle, “An experimental analysis of the influence of the ink properties on the drop formation for direct thermal inkjet printing of high solid content aqueous 3Y-TZP suspensions,” *J. Eur. Ceram. Soc.*, vol. 30, no. 7, pp. 1669–1678, May 2010.
- [70] R. Noguera, M. Lejeune, and T. Chartier, “3D fine scale ceramic components formed by ink-jet prototyping process,” *J. Eur. Ceram. Soc.*, vol. 25, no. 12, pp. 2055–2059, Jan. 2005.
- [71] K. A. M. Seerden, N. Reis, J. R. G. Evans, P. S. Grant, J. W. Halloran, and B.

- Derby, "Ink-Jet Printing of Wax-Based Alumina Suspensions," *J. Am. Ceram. Soc.*, vol. 84, no. 11, pp. 2514–2520, Nov. 2001.
- [72] R. van Noort, "The future of dental devices is digital," *Dent. Mater.*, vol. 28, no. 1, pp. 3–12, Jan. 2012.
- [73] A. Kosmala, Q. Zhang, R. Wright, and P. Kirby, "Development of high concentrated aqueous silver nanofluid and inkjet printing on ceramic substrates," *Mater. Chem. Phys.*, vol. 132, no. 2, pp. 788–795, 2012.
- [74] K. A. M. Seerden, N. Reis, J. R. G. Evans, P. S. Grant, J. W. Halloran, and B. Derby, "Ink-Jet Printing of Wax-Based Alumina Suspensions," *J. Am. Ceram. Soc.*, vol. 84, no. 11, pp. 2514–2520, 2001.
- [75] R. Dou, T. Wang, Y. Guo, and B. Derby, "Ink-Jet Printing of Zirconia: Coffee Staining and Line Stability," *J. Am. Ceram. Soc.*, vol. 94, no. 11, pp. 3787–3792, Nov. 2011.
- [76] M. Mott, J.-H. Song, and J. R. G. Evans, "Microengineering of Ceramics by Direct Ink-Jet Printing," *J. Am. Ceram. Soc.*, vol. 82, no. 7, pp. 1653–1658, Jul. 1999.
- [77] R. Dou and B. Derby, "Formation of Coffee Stains on Porous Surfaces," *Langmuir*, vol. 28, no. 12, pp. 5331–5338, Mar. 2012.
- [78] A. Friederich, J. R. Binder, and W. Bauer, "Rheological Control of the Coffee Stain Effect for Inkjet Printing of Ceramics," *J. Am. Ceram. Soc.*, vol. 96, no. 7, pp. 2093–2099, Jul. 2013.
- [79] M. A. Sukeshini, R. Cummins, T. L. Reitz, and R. M. Miller, "Ink-Jet Printing: A Versatile Method for Multilayer Solid Oxide Fuel Cells Fabrication," *J. Am. Ceram. Soc.*, vol. 92, no. 12, pp. 2913–2919, Dec. 2009.
- [80] N. Yashiro, T. Usui, and K. Kikuta, "Application of a thin intermediate cathode layer prepared by inkjet printing for SOFCs," *J. Eur. Ceram. Soc.*, vol. 30, no. 10, pp. 2093–2098, 2010.
- [81] C. Li, H. Chen, H. Shi, M. O. Tade, and Z. Shao, "Green fabrication of composite cathode with attractive performance for solid oxide fuel cells

- through facile inkjet printing,” *J. Power Sources*, vol. 273, pp. 465–471, 2015.
- [82] M. M. Mohebi and J. R. G. Evans, “Combinatorial Ink-Jet Printer for Ceramics: Calibration,” *J. Am. Ceram. Soc.*, vol. 86, no. 10, pp. 1654–1661, Oct. 2003.
- [83] M. Rombouts, J. Deckers, I. Thijs, J. Deckx, and J.-P. Kruth, “Wax based binder for indirect selective laser sintering of alumina,” *Proceedings of the 5th International PMI Conference*. pp. 184–188, 2012.
- [84] K. Shahzad, J. Deckers, Z. Zhang, J.-P. Kruth, and J. Vleugels, “Additive manufacturing of zirconia parts by indirect selective laser sintering,” *J. Eur. Ceram. Soc.*, vol. 34, no. 1, pp. 81–89, 2014.
- [85] E. Sachs *et al.*, “Three-Dimensional Printing: The Physics and Implications of Additive Manufacturing,” *CIRP Ann.*, vol. 42, no. 1, pp. 257–260, 1993.
- [86] M. C. Leu, E. B. Adamek, T. Huang, G. E. Hilmas, and F. Dogan, “Freeform fabrication of zirconium diboride parts using selective laser sintering,” in *Proceedings of Solid Freeform Fabrication Symposium, Austin, TX, 2008*, pp. 194–205.
- [87] S. Meyers, L. De Leersnijder, J. Vleugels, and J.-P. Kruth, “Direct laser sintering of reaction bonded silicon carbide with low residual silicon content,” *J. Eur. Ceram. Soc.*, vol. 38, no. 11, pp. 3709–3717, Sep. 2018.
- [88] B. Y. Stevinson, D. L. Bourell, and J. J. Beaman, “Support free infiltration of selective laser sintered (SLS) silicon carbide preforms.” University of Texas at Austin, 2006.
- [89] H. Seitz, W. Rieder, S. Irsen, B. Leukers, and C. Tille, “Three-dimensional printing of porous ceramic scaffolds for bone tissue engineering,” *J. Biomed. Mater. Res. Part B Appl. Biomater.*, vol. 74, no. 2, pp. 782–788, 2005.
- [90] R. Detsch, S. Schaefer, U. Deisinger, G. Ziegler, H. Seitz, and B. Leukers,

“In vitro -Osteoclastic Activity Studies on Surfaces of 3D Printed Calcium Phosphate Scaffolds,” *J. Biomater. Appl.*, vol. 26, no. 3, pp. 359–380, Jul. 2010.

- [91] A. Spillmann, A. Sonnenfeld, and P. R. von Rohr, “Flowability Modification of Lactose Powder by Plasma Enhanced Chemical Vapor Deposition,” *Plasma Process. Polym.*, vol. 4, no. S1, pp. S16–S20, Apr. 2007.
- [92] P. Bertrand, F. Bayle, C. Combe, P. Goeuriot, and I. Smurov, “Ceramic components manufacturing by selective laser sintering,” *Appl. Surf. Sci.*, vol. 254, no. 4, pp. 989–992, 2007.
- [93] R. Chirone, D. Barletta, P. Lettieri, and M. Poletto, “Bulk flow properties of sieved samples of a ceramic powder at ambient and high temperature,” *Powder Technol.*, vol. 288, pp. 379–387, 2016.
- [94] D. Sofia, R. Chirone, P. Lettieri, D. Barletta, and M. Poletto, “Selective laser sintering of ceramic powders with bimodal particle size distribution,” *Chem. Eng. Res. Des.*, vol. 136, pp. 536–547, 2018.
- [95] P. BAI and W. WANG, “Selective laser sintering mechanism of polymer-coated molybdenum powder,” *Trans. Nonferrous Met. Soc. China*, vol. 17, no. 3, pp. 543–547, Jun. 2007.
- [96] H. Yves-Christian, W. Jan, M. Wilhelm, W. Konrad, and P. Reinhart, “Net shaped high performance oxide ceramic parts by selective laser melting,” *Phys. Procedia*, vol. 5, pp. 587–594, 2010.
- [97] I. Gibson and D. Shi, “Material properties and fabrication parameters in selective laser sintering process,” *Rapid Prototyp. J.*, vol. 3, no. 4, pp. 129–136, 1997.
- [98] J.-P. Kruth, X. Wang, T. Laoui, and L. Froyen, “Lasers and materials in selective laser sintering,” *Assem. Autom.*, vol. 23, no. 4, pp. 357–371, 2003.
- [99] U. Lakshminarayan, S. Ogrydziaik, and H. L. Marcus, “Selective laser sintering of ceramic materials,” in *1990 International Solid Freeform Fabrication Symposium*, 1990.

- [100] E. Juste, F. Petit, V. Lardot, and F. Cambier, "Shaping of ceramic parts by selective laser melting of powder bed," *J. Mater. Res.*, vol. 29, no. 17, pp. 2086–2094, Sep. 2014.
- [101] P. Bertrand, F. Bayle, C. Combe, P. Goeuriot, and I. Smurov, "Ceramic components manufacturing by selective laser sintering," *Appl. Surf. Sci.*, vol. 254, no. 4, pp. 989–992, 2007.
- [102] F. Klocke and C. Ader, "Direct laser sintering of ceramics," in *Solid freeform fabrication symposium*, 2003, pp. 447–455.
- [103] J. Wilkes, Y. Hagedorn, W. Meiners, and K. Wissenbach, "Additive manufacturing of ZrO₂-Al₂O₃ ceramic components by selective laser melting," *Rapid Prototyp. J.*, vol. 19, no. 1, pp. 51–57, Jan. 2013.
- [104] D. Hellrung, L.-Y. Yeh, F. Depiereux, A. Gillner, and R. Poprawe, "High-accuracy micromachining of ceramics by frequency-tripled Nd:YAG lasers," in *Proc.SPIE*, 1999, vol. 3618, pp. 348–356.
- [105] A.-N. Chen *et al.*, "High-performance ceramic parts with complex shape prepared by selective laser sintering: a review," *Adv. Appl. Ceram.*, vol. 117, no. 2, pp. 100–117, Feb. 2018.
- [106] A. T. Clare, P. R. Chalker, S. Davies, C. J. Sutcliffe, and S. Tsopanos, "Selective laser sintering of barium titanate–polymer composite films," *J. Mater. Sci.*, vol. 43, no. 9, pp. 3197–3202, 2008.
- [107] C. Gao, B. Yang, H. Hu, J. Liu, C. Shuai, and S. Peng, "Enhanced sintering ability of biphasic calcium phosphate by polymers used for bone scaffold fabrication," *Mater. Sci. Eng. C*, vol. 33, no. 7, pp. 3802–3810, 2013.
- [108] T. Hwa-Hsing, "Direct laser fusing to form ceramic parts," *Rapid Prototyp. J.*, vol. 8, no. 5, pp. 284–289, Jan. 2002.
- [109] Z. H. Liu, J. J. Nolte, J. I. Packard, G. Hilmas, F. Dogan, and M. C. Leu, "Selective Laser Sintering of High-density Alumina Ceramic Parts BT - Proceedings of the 35th International MATADOR Conference," 2007, pp. 351–354.

- [110] J. Deckers, S. Khuram, L. Cardon, M. Rombouts, J. Vleugels, and J.-P. Kruth, "Shaping ceramics through indirect Selective Laser Sintering," *Rapid Prototyping Journal*, vol. 22, no. 3. MCB University Press, pp. 544–558, 2016.
- [111] K. F. Leong, C. M. Cheah, and C. K. Chua, "Solid freeform fabrication of three-dimensional scaffolds for engineering replacement tissues and organs," *Biomaterials*, vol. 24, no. 13, pp. 2363–2378, Jun. 2003.
- [112] E. Sachs, M. Cima, and J. Cornie, "Three-dimensional printing: ceramic shells and cores for casting and other applications," in *Proceedings of 2nd international conference on rapid prototyping, Dayton, OH, 1991*, pp. 39–53.
- [113] G. A. Fielding, A. Bandyopadhyay, and S. Bose, "Effects of silica and zinc oxide doping on mechanical and biological properties of 3D printed tricalcium phosphate tissue engineering scaffolds," *Dent. Mater.*, vol. 28, no. 2, pp. 113–122, 2012.
- [114] R. Chumnanklang, T. Panyathanmaporn, K. Sitthiseripratip, and J. Suwanprateeb, "3D printing of hydroxyapatite: Effect of binder concentration in pre-coated particle on part strength," *Mater. Sci. Eng. C*, vol. 27, no. 4, pp. 914–921, 2007.
- [115] M. Hotta, A. Shimamura, N. Kondo, and T. Ohji, "Powder layer manufacturing of alumina ceramics using water spray bonding," *J. Ceram. Soc. Japan*, vol. 124, no. 6, pp. 750–752, 2016.
- [116] J. Will *et al.*, "Porous ceramic bone scaffolds for vascularized bone tissue regeneration," *J. Mater. Sci. Mater. Med.*, vol. 19, no. 8, pp. 2781–2790, Aug. 2008.
- [117] X. Lv, F. Ye, L. Cheng, S. Fan, and Y. Liu, "Binder jetting of ceramics: Powders, binders, printing parameters, equipment, and post-treatment," *Ceram. Int.*, vol. 45, no. 10, pp. 12609–12624, Jul. 2019.
- [118] A. Curodeau, E. Sachs, and S. Caldarise, "Design and fabrication of cast

- orthopedic implants with freeform surface textures from 3-D printed ceramic shell,” *J. Biomed. Mater. Res.*, vol. 53, no. 5, pp. 525–535, Sep. 2000.
- [119] B. Leukers *et al.*, “Hydroxyapatite scaffolds for bone tissue engineering made by 3D printing,” *J. Mater. Sci. Mater. Med.*, vol. 16, no. 12, pp. 1121–1124, Dec. 2005.
- [120] W. Du, X. Ren, C. Ma, and Z. Pei, “Binder jetting additive manufacturing of ceramics: a literature review,” in *ASME 2017 International Mechanical Engineering Congress and Exposition*, 2017.
- [121] A. Butscher *et al.*, “Printability of calcium phosphate powders for three-dimensional printing of tissue engineering scaffolds,” *Acta Biomater.*, vol. 8, no. 1, pp. 373–385, 2012.
- [122] A. Butscher, M. Bohner, S. Hofmann, L. Gauckler, and R. Müller, “Structural and material approaches to bone tissue engineering in powder-based three-dimensional printing,” *Acta Biomater.*, vol. 7, no. 3, pp. 907–920, 2011.
- [123] S. A. Uhland, R. K. Holman, S. Morissette, M. J. Cima, and E. M. Sachs, “Strength of Green Ceramics with Low Binder Content,” *J. Am. Ceram. Soc.*, vol. 84, no. 12, pp. 2809–2818, Dec. 2001.
- [124] E. Sachs, M. Cima, P. Williams, D. Brancazio, and J. Cornie, “Three Dimensional Printing: Rapid Tooling and Prototypes Directly from a CAD Model,” *J. Manuf. Sci. Eng.*, vol. 114, no. 4, pp. 481–488, Nov. 1992.
- [125] K. Shahzad, J. Deckers, J.-P. Kruth, and J. Vleugels, “Additive manufacturing of alumina parts by indirect selective laser sintering and post processing,” *J. Mater. Process. Technol.*, vol. 213, no. 9, pp. 1484–1494, 2013.
- [126] J. Deckers, “Selective Laser Sintering and Melting as Additive Manufacturing Methods to Produce Alumina Parts; 3D printing of Ceramics (Selectief laser sinteren en smelten als additieve vervaardigingsmethoden voor het produceren van alumina

voorwerpen; '3D printen' van ,” 2013.

- [127] K. Shahzad, J. Deckers, S. Boury, B. Neirinck, J.-P. Kruth, and J. Vleugels, “Preparation and indirect selective laser sintering of alumina/PA microspheres,” *Ceram. Int.*, vol. 38, no. 2, pp. 1241–1247, 2012.
- [128] B. Utela, R. L. Anderson, and H. Kuhn, “Advanced ceramic materials and processes for three-dimensional printing (3DP),” in *Solid Freeform Fabr. Symp. Proc.*, 2006, vol. 17, pp. 290–303.
- [129] J. A. Gonzalez, J. Mireles, Y. Lin, and R. B. Wicker, “Characterization of ceramic components fabricated using binder jetting additive manufacturing technology,” *Ceram. Int.*, vol. 42, no. 9, pp. 10559–10564, 2016.
- [130] R. Melcher, S. Martins, N. Travitzky, and P. Greil, “Fabrication of Al₂O₃-based composites by indirect 3D-printing,” *Mater. Lett.*, vol. 60, no. 4, pp. 572–575, 2006.
- [131] R. Melcher, N. Travitzky, C. Zollfrank, and P. Greil, “3D printing of Al₂O₃/Cu–O interpenetrating phase composite,” *J. Mater. Sci.*, vol. 46, no. 5, pp. 1203–1210, 2011.
- [132] J. Tomas, “Adhesion of ultrafine particles—A micromechanical approach,” *Chem. Eng. Sci.*, vol. 62, no. 7, pp. 1997–2010, 2007.
- [133] Z. Chen *et al.*, “3D printing of ceramics: A review,” *J. Eur. Ceram. Soc.*, vol. 39, no. 4, pp. 661–687, 2019.
- [134] B. Qian and Z. Shen, “Laser sintering of ceramics,” *J. Asian Ceram. Soc.*, vol. 1, no. 4, pp. 315–321, 2013.
- [135] D. Sofia, D. Barletta, and M. Poletto, “Laser sintering process of Ceramic powders: the effect of particle size on the mechanical properties of sintered layers,” vol. 23, Aug. 2018.
- [136] R. I. Campbell, M. Martorelli, and H. S. Lee, “Surface roughness visualisation for rapid prototyping models,” *Comput. Des.*, vol. 34, no. 10, pp. 717–725, 2002.

- [137] A. Butscher, M. Bohner, N. Doebelin, L. Galea, O. Loeffel, and R. Müller, "Moisture based three-dimensional printing of calcium phosphate structures for scaffold engineering," *Acta Biomater.*, vol. 9, no. 2, pp. 5369–5378, 2013.
- [138] C. Roth, Z. Künsch, A. Sonnenfeld, and P. Rudolf von Rohr, "Plasma surface modification of powders for pharmaceutical applications," *Surf. Coatings Technol.*, vol. 205, pp. S597–S600, 2011.
- [139] I. Zimmermann, M. Eber, and K. Meyer, "Nanomaterials as Flow Regulators in Dry Powders," *Zeitschrift für Phys. Chemie*, vol. 218, no. 1, pp. 51–102, 2004.
- [140] H. Zhao, C. Ye, Z. Fan, and C. Wang, "3D printing of CaO-based ceramic core using nanozirconia suspension as a binder," *J. Eur. Ceram. Soc.*, vol. 37, no. 15, pp. 5119–5125, 2017.
- [141] K. Liu *et al.*, "Additive manufacturing of traditional ceramic powder via selective laser sintering with cold isostatic pressing," *Int. J. Adv. Manuf. Technol.*, vol. 90, no. 1, pp. 945–952, 2017.
- [142] J. Yoo, M. J. Cima, and S. Khanuja, "Structural ceramic components by 3D printing," in *1993 International Solid Freeform Fabrication Symposium*, 1993.
- [143] S. Maleksaeedi, H. Eng, F. E. Wiria, T. M. H. Ha, and Z. He, "Property enhancement of 3D-printed alumina ceramics using vacuum infiltration," *J. Mater. Process. Technol.*, vol. 214, no. 7, pp. 1301–1306, 2014.
- [144] S. Kamatchi, "Selective laser sintering of alumina with polymer binders," *Rapid Prototyp. J.*, vol. 1, no. 2, pp. 24–35, Jan. 1995.
- [145] N. K. Vail and J. W. Barlow, "Ceramic structures by selective laser sintering of microencapsulated, finely divided ceramic materials," in *1992 International Solid Freeform Fabrication Symposium*, 1992.
- [146] K. Liu, Y. Shi, C. Li, L. Hao, J. Liu, and Q. Wei, "Indirect selective laser sintering of epoxy resin-Al₂O₃ ceramic powders combined with cold

isostatic pressing,” *Ceram. Int.*, vol. 40, no. 5, pp. 7099–7106, 2014.

- [147] A. Bellini, *Fused deposition of ceramics: a comprehensive experimental, analytical and computational study of material behavior, fabrication process and equipment design*. 2002.
- [148] J. Cesarano III, “Robocasting of ceramics and composites using fine particle suspensions,” Sandia National Labs., Albuquerque, NM (US); Sandia National Labs., Livermore, CA (US), 1999.
- [149] D. Owen *et al.*, “3D printing of ceramic components using a customized 3D ceramic printer,” *Prog. Addit. Manuf.*, pp. 1–7, 2018.
- [150] M. Youseffi, “Some aspects of the injection moulding of alumina and other engineering ceramics.” © M. Youseffi, 1992.
- [151] K. Rane and M. Strano, “A comprehensive review of extrusion-based additive manufacturing processes for rapid production of metallic and ceramic parts,” *Adv. Manuf.*, pp. 1–19, 2019.
- [152] P. Thomas-Vielma, A. Cervera, B. Levenfeld, and A. Várez, “Production of alumina parts by powder injection molding with a binder system based on high density polyethylene,” *J. Eur. Ceram. Soc.*, vol. 28, no. 4, pp. 763–771, 2008.
- [153] S. Danforth, “Fused deposition of ceramics: a new technique for the rapid fabrication of ceramic components,” *Mater. Technol.*, vol. 10, no. 7–8, pp. 144–146, 1995.
- [154] T. F. McNulty, D. J. Shanefield, S. C. Danforth, and A. Safari, “Dispersion of lead zirconate titanate for fused deposition of ceramics,” *J. Am. Ceram. Soc.*, vol. 82, no. 7, pp. 1757–1760, 1999.
- [155] M. K. Agarwala, R. van Weeren, A. Bandyopadhyay, A. Safari, S. C. Danforth, and W. R. Priedeman, “Filament feed materials for fused deposition processing of ceramics and metals,” in *1996 International Solid Freeform Fabrication Symposium*, 1996.
- [156] H. Valkenaers, F. Vogeler, E. Ferraris, A. Voet, and J.-P. Kruth, “A novel

- approach to additive manufacturing: screw extrusion 3D-printing,” in *Proceedings of the 10th International Conference on Multi-Material Micro Manufacture*, 2013, pp. 235–238.
- [157] E. A. Griffin and S. McMillin, “Selective laser sintering and fused deposition modeling processes for functional ceramic parts,” in *1995 International Solid Freeform Fabrication Symposium*, 1995.
- [158] S. Onagoruwa, S. Bose, and A. Bandyopadhyay, “Fused deposition of ceramics (FDC) and composites,” *Pro SFF, Texas*, pp. 224–231, 2001.
- [159] M. K. Agarwala, “Structural quality of parts processed by fused deposition,” *Rapid Prototyp. J.*, vol. 2, no. 4, pp. 4–19, Jan. 1996.
- [160] S. Iyer *et al.*, “Microstructural Characterization and Mechanical Properties of Si₃N₄ Formed by Fused Deposition of Ceramics,” *Int. J. Appl. Ceram. Technol.*, vol. 5, no. 2, pp. 127–137, Mar. 2008.
- [161] J. L. Lombardi, R. A. Hoffinan, J. A. Waters, and D. Popovich, “Issues associated with EFF & FDM ceramic filled feedstock formulation,” in *1997 International Solid Freeform Fabrication Symposium*, 1997.
- [162] A. Ghazanfari, W. Li, M. C. Leu, and G. E. Hilmas, “A novel extrusion-based additive manufacturing process for ceramic parts,” in *Solid Free. Fabr. Symp., Austin, TX, USA*, 2016, pp. 1509–1529.
- [163] J. M.A., “A novel system for fused deposition of advanced multiple ceramics,” *Rapid Prototyp. J.*, vol. 6, no. 3, pp. 161–175, Jan. 2000.
- [164] J. McIntosh, S. C. Danforth, and V. Jamalabad, “Shrinkage and Deformation in Components Manufactured by Fused Deposition of Ceramics,” Jan. 1997.
- [165] J. Cesarano III and P. D. Calvert, “Freeforming objects with low-binder slurry,” *United States Pat.*, vol. 6027326, 1997.
- [166] J. Cesarano, “A Review of Robocasting Technology,” *MRS Proc.*, vol. 542, p. 133, 1998.

- [167] A. Ghazanfari, W. Li, M. C. Leu, and G. E. Hilmas, "A novel freeform extrusion fabrication process for producing solid ceramic components with uniform layered radiation drying," *Addit. Manuf.*, vol. 15, pp. 102–112, 2017.
- [168] H. B. Denham, J. Cesarano III, B. H. King, and P. Calvert, "Mechanical behavior of robocast alumina," in *Solid Free. Fabr. Symp., Austin, TX, USA*, 1998, pp. 589–596.
- [169] M. C. Leu, B. K. Deuser, L. Tang, R. G. Landers, G. E. Hilmas, and J. L. Watts, "Freeze-form extrusion fabrication of functionally graded materials," *CIRP Ann.*, vol. 61, no. 1, pp. 223–226, 2012.
- [170] J. J. Benbow, E. W. Oxley, and J. Bridgwater, "The extrusion mechanics of pastes—the influence of paste formulation on extrusion parameters," *Chem. Eng. Sci.*, vol. 42, no. 9, pp. 2151–2162, 1987.
- [171] W. Li, A. Ghazanfari, D. McMillen, M. C. Leu, G. E. Hilmas, and J. Watts, "Fabricating ceramic components with water dissolvable support structures by the Ceramic On-Demand Extrusion process," *CIRP Ann.*, vol. 66, no. 1, pp. 225–228, 2017.
- [172] W. Li, A. Ghazanfari, M. C. Leu, and R. G. Landers, "Methods of extrusion on demand for high solids loading ceramic paste in freeform extrusion fabrication," in *Solid Freeform Fabrication Symposium, Austin, TX*, 2015.
- [173] H. Tieshu, "Aqueous-based freeze-form extrusion fabrication of alumina components," *Rapid Prototyp. J.*, vol. 15, no. 2, pp. 88–95, Jan. 2009.
- [174] R. Liu, T. Xu, and C. Wang, "A review of fabrication strategies and applications of porous ceramics prepared by freeze-casting method," *Ceram. Int.*, vol. 42, no. 2, Part B, pp. 2907–2925, 2016.
- [175] N. O. Shanti, K. Araki, and J. W. Halloran, "Particle Redistribution During Dendritic Solidification of Particle Suspensions," *J. Am. Ceram. Soc.*, vol. 89, no. 8, pp. 2444–2447, Aug. 2006.
- [176] K. Stuffle, A. Mulligan, J. Lombardi, P. Calvert, and B. Fabes, "Solid

- freebody forming of ceramics from polymerizable slurry,” *MRS Online Proc. Libr. Arch.*, vol. 346, 1994.
- [177] J. A. Lewis, J. E. Smay, J. Stuecker, and J. Cesarano, “Direct ink writing of three-dimensional ceramic structures,” *J. Am. Ceram. Soc.*, vol. 89, no. 12, pp. 3599–3609, 2006.
- [178] W. Gao *et al.*, “The status, challenges, and future of additive manufacturing in engineering,” *Comput. Des.*, vol. 69, pp. 65–89, 2015.
- [179] B. N. Turner, R. Strong, and S. A. Gold, “A review of melt extrusion additive manufacturing processes: I. Process design and modeling,” *Rapid Prototyp. J.*, vol. 20, no. 3, pp. 192–204, Apr. 2014.
- [180] B. . . Turner and S. A. Gold, “A review of melt extrusion additive manufacturing processes: II. Materials, dimensional accuracy, and surface roughness,” *Rapid Prototyp. J.*, vol. 21, no. 3, pp. 250–261, Apr. 2015.
- [181] H. W. Stetson, “Method of making multilayer circuits.” Google Patents, 22-Jun-1965.
- [182] A. R. Rodriguez and A. B. Wallace, “Ceramic capacitor and method of making it.” Google Patents, 10-Oct-1961.
- [183] B. Schwartz, “Review of multilayer ceramics for microelectronic packaging,” *J. Phys. Chem. Solids*, vol. 45, no. 10, pp. 1051–1068, 1984.
- [184] C. B. Williams, “Design and development of a layer-based additive manufacturing process for the realization of metal parts of designed mesostructure.” Georgia Institute of Technology, 2008.
- [185] J. D. Cawley, P. Wei, Z. E. Liu, W. S. Newman, B. B. Mathewson, and A. H. Heuer, “Al₂O₃ Ceramics Made by CAM-LEM (Computer-Aided Manufacturing Engineering Materials) Technology,” in *1995 International Solid Freeform Fabrication Symposium*, 1995.
- [186] Y. Zhang, X. He, S. Du, and J. Zhang, “Al₂O₃ Ceramics Preparation by LOM (Laminated Object Manufacturing),” *Int. J. Adv. Manuf. Technol.*, vol. 17, no. 7, pp. 531–534, 2001.

- [187] M. Agarwala, D. Klosterman, N. Osborne, and A. Lightman, "Hard metal tooling via SFF of ceramics and powder metallurgy," in *Proceedings of the SFF Symposium, 1999*, pp. 759–766.
- [188] Z. Liu, N. Suppakarn, J. Cawley, and S. Levine, "Coated Feedstock for Fabrication of Ceramic Parts by CAM-LEM," Feb. 2000.
- [189] B. A. Bender, R. J. Rayne, and T. L. Jessen, "Laminated Object Manufacturing of Functional Ceramics," *25th Annual Conference on Composites, Advanced Ceramics, Materials, and Structures: B: Ceramic Engineering and Science Proceedings*. pp. 127–134, 01-Jan-2001.
- [190] C. Griffin, J. Daufenbach, and S. McMillin, "Desktop manufacturing: LOM vs. pressing," *Am. Ceram. Soc. Bull.*, vol. 73, no. 8, pp. 109–113, 1994.
- [191] C. Griffin, J. Daufenbach, and S. McMillin, "Solid freeform fabrication of functional ceramic components using a laminated object manufacturing technique," in *1994 International Solid Freeform Fabrication Symposium, 1994*.
- [192] E. A. Griffin, D. R. Mumm, and D. B. Marshall, "Rapid prototyping of functional ceramic composites," *Am. Ceram. Soc. Bull.*, vol. 75, no. 7, pp. 65–68, 1996.
- [193] T. C. Ko, J. Bes, J. D. Cawley, and A. H. Heuer, "CAM-LEM processing: materials flexibility," in *1997 International Solid Freeform Fabrication Symposium, 1997*.
- [194] M. J. Pope, M. C. L. Patterson, W. Zimbeck, and M. Fehrenbacher, "Laminated object manufacturing of Si₃N₄ with enhanced properties," in *1997 International Solid Freeform Fabrication Symposium, 1997*.
- [195] B. A. Bender, R. J. Rayne, and C. C. M. Wu, "Solid Freeform Fabrication of a Telescoping Actuator Via Laminated Object Manufacturing," *24th Annual Conference on Composites, Advanced Ceramics, Materials, and Structures: B: Ceramic Engineering and Science Proceedings*. pp. 143–150, 01-Jan-2000.

- [196] D. Klosterman, R. Chartoff, N. Osborne, and G. Graves, "Automated Fabrication of Monolithic and Ceramic Matrix Composites via Laminated Object Manufacturing (LaM)," in *1997 International Solid Freeform Fabrication Symposium*, 1997.
- [197] D. Klosterman *et al.*, "Automated Fabrication of Monolithic Ceramics and Ceramic Matrix Composites (CMCs) Using a Novel Rapid Prototyping Method," in *22nd Annual Conference on Composites, Advanced Ceramics, Materials, and Structures: A: Ceramic Engineering and Science Proceedings*, 1988, pp. 291–301.
- [198] H. Zhong *et al.*, "Preparation of SiC ceramics by laminated object manufacturing and pressureless sintering," *J Ceram Sci Technol*, vol. 6, pp. 133–140, 2015.
- [199] J. D. Cawley, A. H. Heuer, W. S. Newman, and B. B. Mathewson, "Computer-aided manufacturing of laminated engineering materials," *Am. Ceram. Soc. Bull.*, vol. 75, no. 5, 1996.
- [200] J. W. Halloran, "Freeform fabrication of ceramics," *Br. Ceram. Trans.*, vol. 98, no. 6, pp. 299–303, Jun. 1999.
- [201] D. T. Pham and R. S. Gault, "A comparison of rapid prototyping technologies," *Int. J. Mach. Tools Manuf.*, vol. 38, no. 10, pp. 1257–1287, 1998.
- [202] B. Y. Tay, J. R. G. Evans, and M. J. Edirisinghe, "Solid freeform fabrication of ceramics," *Int. Mater. Rev.*, vol. 48, no. 6, pp. 341–370, Dec. 2003.
- [203] A. Das, G. Madras, N. Dasgupta, and A. M. Umarji, "Binder removal studies in ceramic thick shapes made by laminated object manufacturing," *J. Eur. Ceram. Soc.*, vol. 23, no. 7, pp. 1013–1017, 2003.
- [204] D. A. Klosterman *et al.*, *Development of a curved layer LOM process for monolithic ceramics and ceramic matrix composites*, vol. 5. 1999.
- [205] F. Zhang *et al.*, "3D printing technologies for electrochemical energy storage," *Nano Energy*, vol. 40, pp. 418–431, 2017.

- [206] N. Travitzky *et al.*, “Additive Manufacturing of Ceramic-Based Materials,” *Adv. Eng. Mater.*, vol. 16, no. 6, pp. 729–754, Jun. 2014.
- [207] Johnson Matthey, “Ceramic 3D printing: additive manufacturing,” *Products and Services*, 2019. .
- [208] E. Feilden, “Additive manufacturing of ceramics and ceramic composites via robocasting,” Imperial College London, 2017.
- [209] J.-Y. Lee, J. An, and C. K. Chua, “Fundamentals and applications of 3D printing for novel materials,” *Appl. Mater. Today*, vol. 7, pp. 120–133, 2017.
- [210] T. Chartier *et al.*, “Additive manufacturing to produce complex 3D ceramic parts,” *J. Ceram. Sci. Tech*, vol. 6, no. 2, pp. 95–104, 2015.
- [211] M. Lasgorceix, “Mise en forme par microstéréolithographie et frittage de céramiques macro-micro-poreuses en hydroxyapatite silicatée et évaluation biologique,” 2014.
- [212] J. Gonzalez-Gutierrez, S. Cano, S. Schuschnigg, C. Kukla, J. Sapkota, and C. Holzer, “Additive manufacturing of metallic and ceramic components by the material extrusion of highly-filled polymers: a review and future perspectives,” *Materials (Basel)*, vol. 11, no. 5, p. 840, 2018.
- [213] E. Ferraris, J. Vleugels, Y. Guo, D. Bourell, J. P. Kruth, and B. Lauwers, “Shaping of engineering ceramics by electro, chemical and physical processes,” *CIRP Ann.*, vol. 65, no. 2, pp. 761–784, 2016.
- [214] T. Lieneke *et al.*, “Systematical determination of tolerances for additive manufacturing by measuring linear dimensions,” in *Solid Freeform Fabrication Symposium—An Additive Manufacturing Conference, Austin, TX, Aug, 2015*, pp. 10–15.
- [215] R. Soares *et al.*, “Large-area Ceramic Tooling Production through Hybrid Manufacturing,” in *Direct Digital Manufacturing Conference, 2018*, no. March, pp. 3–8.
- [216] T. Yamazaki, “Development of A Hybrid Multi-tasking Machine Tool: Integration of Additive Manufacturing Technology with CNC Machining,”

in *Procedia CIRP*, 2016.

- [217] R. Soares *et al.*, “Large-area Ceramic Tooling Production through Hybrid Manufacturing,” in *Direct Digital Manufacturing Conference*, 2018, no. March, pp. 27–32.
- [218] J. Shular, “The Emission Factor Documentation for AP-42 Section 11.7: Ceramic Products Manufacturing for US Environmental,” *EPA Contract*, pp. 68-D2, 1996.
- [219] S. Somiya, *Handbook of advanced ceramics: materials, applications, processing, and properties*. Academic press, 2013.
- [220] Heraeus, “TC0306A Data Sheet.” Heraeus.
- [221] M. C. Leu *et al.*, “Freeze-form extrusion fabrication of composite structures,” in *Proceedings of the Solid Freeform Fabrication Symposium*. Austin, TX, 2011, pp. III-124.
- [222] L. F. G. Setz, L. Koshimizu, S. R. H. de Mello-Castanho, and M. R. Morelli, “Rheological Analysis of Ceramics Suspensions with High Solids Loading,” *Mater. Sci. Forum*, vol. 727–728, pp. 646–651, 2012.
- [223] D. M. Devine, *Polymer-Based Additive Manufacturing: Biomedical Applications*. Springer International Publishing, 2019.
- [224] N. Holzman and L. Francis, “Pneumatic System Design for Direct Write 3D Printing,” *Res. Gate*, 2017.
- [225] F. Händle, *Extrusion in Ceramics*. Springer Berlin Heidelberg, 2009.
- [226] A. Perrot, D. Rangeard, V. N. Nerella, and V. Mechtcherine, “Extrusion of cement-based materials-an overview,” *RILEM Tech. Lett.*, vol. 3, pp. 91–97, 2018.
- [227] S. Derakhshanfar, R. Mbeleck, K. Xu, X. Zhang, W. Zhong, and M. Xing, “3D bioprinting for biomedical devices and tissue engineering: A review of recent trends and advances,” *Bioact. Mater.*, vol. 3, pp. 144–156, Feb. 2018.

- [228] “Moineau Pumps | Progressing Cavity Crude Oil Transfer Pumps | PCM.” [Online]. Available: <https://www.pcm.eu/en/oil-and-gas/pcm-solutions/surface-transfer-technologies/moineau-progressing-cavity-crude-oil-transfer-pumps>. [Accessed: 13-Jun-2019].
- [229] M. S. Mason, T. S. Huang, R. G. Landers, M. C. Leu, and G. E. Hilmas, “Freeform extrusion of high solids loading ceramic slurries, part I: extrusion process modeling,” in *17th Annual Solid Freeform Fabrication Symposium, Austin, TX, Aug, 2006*, pp. 14–16.
- [230] Pump School, “When to Use a Positive Displacement Pump,” *PumpSchool.com*, 2007. [Online]. Available: [http://www.pumpschool.com/intro/pd vs centrif.pdf](http://www.pumpschool.com/intro/pd%20vs%20centrif.pdf).
- [231] W. M. Bundy and J. N. Ishley, “Kaolin in paper filling and coating,” *Appl. Clay Sci.*, vol. 5, no. 5–6, pp. 397–420, Mar. 1991.
- [232] Ceresana, “Bioplastics Market Report,” 2016.
- [233] M. Deans, “4-climb convention,” *Fusion 360 Blog*, 2018. [Online]. Available: <https://www.autodesk.com/products/fusion-360/blog/top-8-milling-tools-new-cnc-machinists/4-climb-conventional/>. [Accessed: 26-Jan-2020].
- [234] S. Dhara and B. Su, “Green Machining to Net Shape Alumina Ceramics Prepared Using Different Processing Routes,” *Int. J. Appl. Ceram. Technol.*, vol. 2, no. 3, pp. 262–270, May 2005.
- [235] S. Mohanty, A. P. Rameshbabu, and S. Dhara, “Net shape forming of green alumina via CNC machining using diamond embedded tool,” *Ceram. Int.*, vol. 39, no. 8, pp. 8985–8993, 2013.
- [236] M. Asif *et al.*, “A new photopolymer extrusion 5-axis 3D printer,” *Addit. Manuf.*, vol. 23, pp. 355–361, Oct. 2018.
- [237] HAGE3D GmbH, “HAGE3D 3D Printer I75X– LARGEST 5-AXIS GANTRY MATERIAL EXTRUSION PRINTER,” 2020. [Online]. Available: <https://hage3d.com/index.php/en/hage3d-3d-printer-175-x/>. [Accessed:

14-Jan-2020].

- [238] J. M. Flynn, A. Shokrani, S. T. Newman, and V. Dhokia, “Hybrid additive and subtractive machine tools – Research and industrial developments,” *Int. J. Mach. Tools Manuf.*, vol. 101, pp. 79–101, Feb. 2016.
- [239] Inkbord Tech Co. Ltd, “PID Temperature Controller ITC-100.” 2020.
- [240] V. S. Bagad, *Mechatronics*. Technical Publications, 2009.
- [241] R. Morrell, “Flexural strength testing of ceramics and hardmetals.” 2007.
- [242] V. K. Khanna, “Extreme-Temperature and Harsh-Environment Electronics,” *Physics, technology and applications*. IOP Publishing, 2017.
- [243] M. R. Werner and W. R. Fahrner, “Review on materials, microsensors, systems and devices for high-temperature and harsh-environment applications,” *IEEE Trans. Ind. Electron.*, vol. 48, no. 2, pp. 249–257, 2001.
- [244] N. Ulerich, G. Kidane, C. Spiegelberg, and N. Tevs, “Condition Based Monitoring of Gas Turbine Combustion Components,” Siemens Energy, Incorporated, Pittsburgh, PA, and Morgantown, WV (United States), Sep. 2012.
- [245] E. H. Amalu, N. N. Ekere, and R. S. Bhatti, “High temperature electronics: R&D challenges and trends in materials, packaging and interconnection technology,” in *2009 2nd International Conference on Adaptive Science & Technology (ICAST)*, 2009, pp. 146–153.
- [246] F. Bechtold, “A comprehensive overview on today’s ceramic substrate technologies,” in *2009 European Microelectronics and Packaging Conference*, 2009, pp. 1–12.
- [247] M. Ohadi and J. Qi, “Thermal management of harsh-environment electronics,” in *Twentieth Annual IEEE Semiconductor Thermal Measurement and Management Symposium (IEEE Cat. No.04CH37545)*, 2004, pp. 231–240.
- [248] J. J. Licari and L. R. B. T.-H. M. T. H. (Second E. Enlow, Eds., “4 - Thick

Film Processes,” Westwood, NJ: William Andrew Publishing, 1998, pp. 104–171.

- [249] S. Khan, L. Lorenzelli, and R. S. Dahiya, “Technologies for printing sensors and electronics over large flexible substrates: a review,” *IEEE Sens. J.*, vol. 15, no. 6, pp. 3164–3185, 2014.
- [250] N. White, “Thick Films BT - Springer Handbook of Electronic and Photonic Materials,” S. Kasap and P. Capper, Eds. Cham: Springer International Publishing, 2017, p. 1.
- [251] J. P. Metters, R. O. Kadara, and C. E. Banks, “New directions in screen printed electroanalytical sensors: an overview of recent developments,” *Analyst*, vol. 136, no. 6, pp. 1067–1076, 2011.
- [252] T. H. Lemon and L. TH, “High tensile strength thick-film silver-palladium metallisations. Improved compositions for screen-printed circuits,” 1975.
- [253] D. Espalin, D. W. Muse, E. MacDonald, and R. B. Wicker, “3D Printing multifunctionality: structures with electronics,” *Int. J. Adv. Manuf. Technol.*, vol. 72, no. 5–8, pp. 963–978, May 2014.
- [254] A. Javidjam, M. H. Hekmatshoar, L. Hedayatifar, and S. N. K. Abad, “Effect of surface roughness on electrical conductivity and hardness of silver plated copper,” *Mater. Res. Express*, vol. 6, no. 3, p. 36407, 2018.
- [255] L. Cheng *et al.*, “Structure design, fabrication, properties of laminated ceramics: A review,” *Int. J. Light. Mater. Manuf.*, vol. 1, no. 3, pp. 126–141, 2018.
- [256] Y. Imanaka, *Multilayered Low Temperature Cofired Ceramics (LTCC) Technology*. Springer US, 2006.
- [257] K.-L. Wu, “Low Temperature Co-Fired Ceramic (LTCC) Technology in RF and Microwave Engineering,” *Encycl. RF Microw. Eng.*, 2005.
- [258] P. Sturesson, Z. Khaji, S. Knaust, L. Klintberg, and G. Thornell, “Thermomechanical properties and performance of ceramic resonators for wireless pressure reading at high temperatures,” *J. Micromechanics*

Microengineering, vol. 25, no. 9, p. 95016, 2015.

- [259] M. L. Minges and A. S. M. I. H. Committee, *Electronic Materials Handbook: Packaging*. Taylor & Francis, 1989.
- [260] W. H. Kohl, "Ceramics and ceramic-to-metal sealing," *Vacuum*, vol. 14, no. 9, pp. 333–354, 1964.
- [261] M. Bhatnagar and B. J. Baliga, "Comparison of 6H-SiC, 3C-SiC, and Si for power devices," *IEEE Trans. Electron Devices*, vol. 40, no. 3, pp. 645–655, Mar. 1993.
- [262] Y. V. Deshmukh, *Industrial heating: principles, techniques, materials, applications, and design*. CRC Press, 2005.
- [263] D. O'Sullivan, M. J. Pomeroy, S. Hampshire, and M. J. Murtagh, "Degradation resistance of silicon carbide diesel particulate filters to diesel fuel ash deposits," *J. Mater. Res.*, vol. 19, no. 10, pp. 2913–2921, 2004.
- [264] S. Fan *et al.*, "Microstructure and properties of 3D needle-punched carbon/silicon carbide brake materials," *Compos. Sci. Technol.*, vol. 67, no. 11–12, pp. 2390–2398, Sep. 2007.
- [265] Y. Liang and S. P. Dutta, "Application trend in advanced ceramic technologies," *Technovation*, vol. 21, no. 1, pp. 61–65, 2001.

Appendix A

An overview of applications that use advanced ceramic materials categorised by industrial segment [213], [265]

INDUSTRY	APPLICATION
Mechanical engineering	<ul style="list-style-type: none"> • Cutting tools and dies • Precise instrument parts • Molten metal filter • Low weight, rotary components • Bearings • Seals • Solid lubricants
Aerospace	<ul style="list-style-type: none"> • Fuel systems and valves • Low weight components • Fuel cells • Thermal protection • Turbine engine components
Automotive	<ul style="list-style-type: none"> • Catalytic converter • Drive chain components • Fuel injector components • Turbocharger rotors
Biological, chemical processing	<ul style="list-style-type: none"> • Artificial bones, teeth and joints • Heart valves • Heat exchanger • Reformers • Refractories
Electrical, magnetic engineering	<ul style="list-style-type: none"> • Resistance heating element • IC substrate • Advanced multilayer integrated packages
Electrical power generation	<ul style="list-style-type: none"> • High temperature components • Fuel cells (Solid oxide) • Filters
Thermal engineering	<ul style="list-style-type: none"> • Electrode material • Heat sinks for electronics • Refractory components • Heating elements

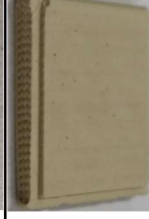
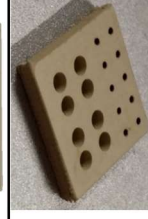
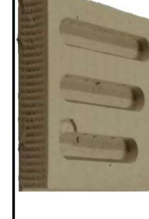
Appendix B

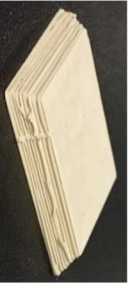
IT classes chart

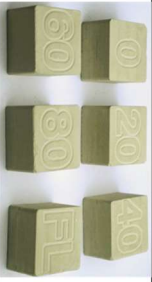
Basic size mm	Standard tolerance grades																	
	IT1(2)	IT2(2)	IT3(2)	IT4(2)	IT5(2)	IT6	IT7	IT8	IT9	IT10	IT11	IT12	IT13	IT14(3)	IT15(3)	IT16(3)	IT17(3)	IT18(3)
Above	Tolerances																	
	µm									mm								
—	0,8	1,2	2	3	4	6	10	14	25	40	60	0,1	0,14	0,25	0,4	0,6	1	1,4
3	1	1,5	2,5	4	5	8	12	18	30	48	75	0,12	0,18	0,3	0,48	0,75	1,2	1,8
6	1	1,5	2,5	4	6	9	15	22	36	58	90	0,15	0,22	0,36	0,58	0,9	1,5	2,2
10	1,2	2	3	5	8	11	18	27	43	70	110	0,18	0,27	0,43	0,7	1,1	1,8	2,7
18	1,5	2,5	4	6	9	13	21	33	52	84	130	0,21	0,33	0,52	0,84	1,3	2,1	3,3
30	1,5	2,5	4	7	11	16	25	39	62	100	160	0,25	0,39	0,62	1	1,6	2,5	3,9
50	2	3	5	8	13	19	30	46	74	120	190	0,3	0,46	0,74	1,2	1,9	3	4,6
80	2,5	4	6	10	15	22	35	54	87	140	220	0,35	0,54	0,87	1,4	2,2	3,5	5,4
120	3,5	5	8	12	18	25	40	63	100	160	250	0,4	0,63	1	1,6	2,5	4	6,3
180	4,5	7	10	14	20	29	46	72	115	185	290	0,46	0,72	1,15	1,85	2,9	4,6	7,2
250	6	8	12	16	23	32	52	81	130	210	320	0,52	0,81	1,3	2,1	3,2	5,2	8,1
315	7	9	13	18	25	36	57	89	140	230	360	0,57	0,89	1,4	2,3	3,6	5,7	8,9
400	8	10	15	20	27	40	63	97	155	250	400	0,63	0,97	1,55	2,5	4	6,3	9,7
500	9	11	16	22	32	44	70	110	175	280	440	0,7	1,1	1,75	2,8	4,4	7	11
630	10	13	18	25	36	50	80	125	200	320	500	0,8	1,25	2	3,2	5	8	12,5
800	11	15	21	28	40	56	90	140	230	360	560	0,9	1,4	2,3	3,6	5,6	9	14
1000	13	18	24	33	47	66	105	165	260	420	660	1,05	1,65	2,6	4,2	6,6	10,5	16,5
1250	15	21	29	39	55	78	125	195	310	500	780	1,25	1,95	3,1	5	7,8	12,5	19,5
1600	18	25	35	46	65	92	150	230	370	600	920	1,5	2,3	3,7	6	9,2	15	23
2000	22	30	41	55	78	110	175	280	440	700	1100	1,75	2,8	4,4	7	11	17,5	28
2500	26	36	50	68	96	135	210	330	540	860	1350	2,1	3,3	5,4	8,6	13,5	21	33

Appendix C

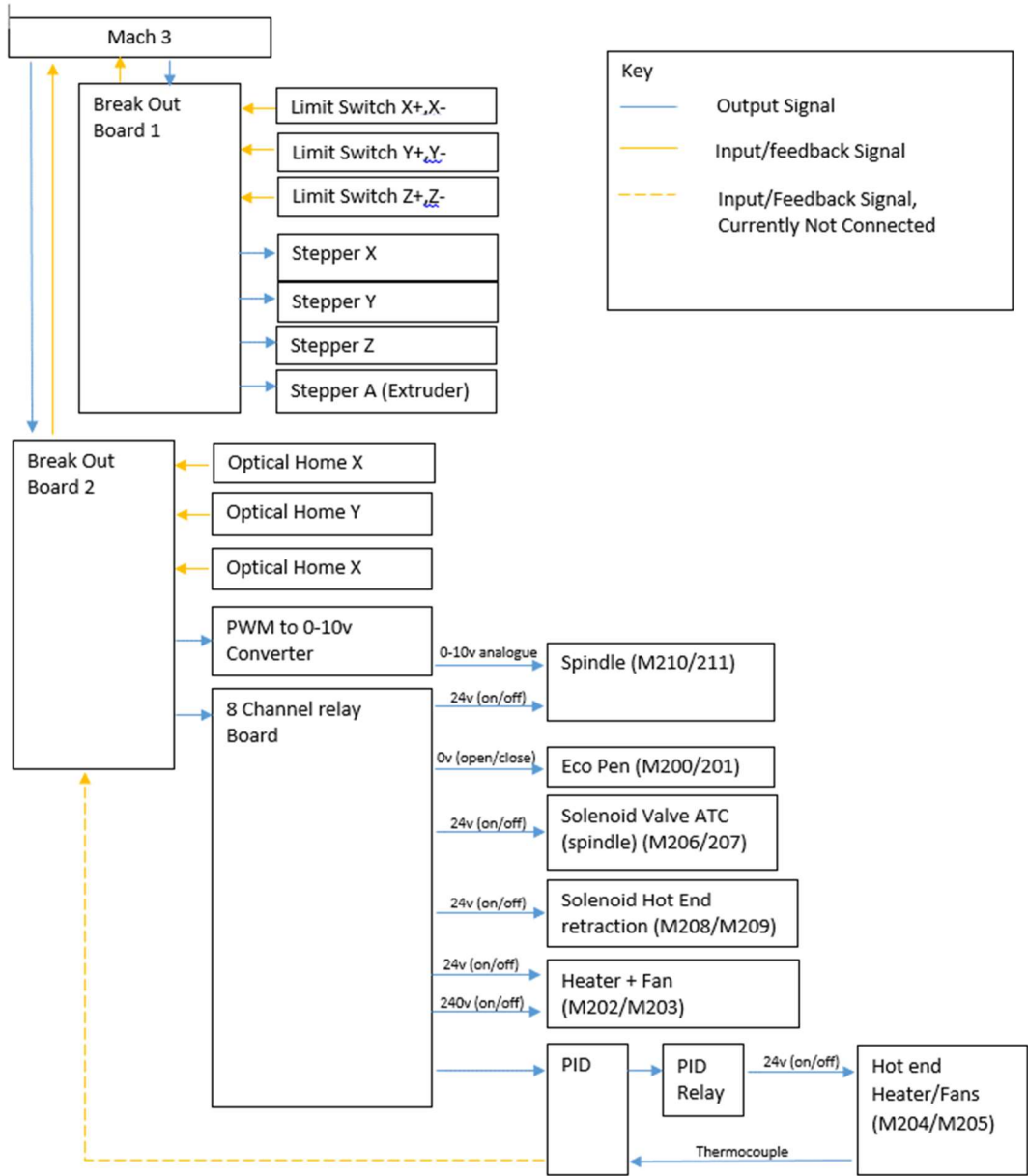
Part	Figures	Additive			Subtractive			Thermal Processing
		Substrate	Support	Deposition	Layer	Post-processing		
	Figure 3-15a	Cellulose sheet on a non-heated bed	No support material was required	ecOPEN 300 mounted on the developed platform using 223 µm metal tapered nozzle using a flowrate of 43 µL/min	Ø 4 mm PCD straight sided end mill	No post-process machining was carried out	Thermal processes at production facility at Morgan Advanced Materials using a commercial tunnel kiln with a peak temperature of 1,400°C	
	Figure 3-15b and Figure 3-30 sample 2	Polyethylene sheet on a non-heated bed	No support material was required	ecOPEN 300 mounted on the developed platform using 223 µm metal tapered nozzle using a flowrate of 43 µL/min	Ø 4 mm PCD straight sided end mill	Post-processed using a Ø 4 mm fluted CVD end mill. Table 3-1 Sample 1 shows the parameters that were used.	Thermal processes at production facility at Morgan Advanced Materials using a commercial tunnel kiln with a peak temperature of 1,400°C	
	Figure 3-15c	Standard printing paper on a non-heated bed	No support material was required	ecOPEN 300 mounted on the developed platform using 223 µm metal tapered nozzle using a flowrate of 43 µL/min	Ø 4 mm PCD straight sided end mill a spindle speed of 15,000RPM feedrate 30 mm/min	No post-process machining was carried out	Thermal processes at production facility at Morgan Advanced Materials using a commercial tunnel kiln with a peak temperature of 1,400°C	
	Figure 3-15d	White PLA deposited using the sacrificial support extruder	No support material was required	ecOPEN 300 mounted on the developed platform using 427 µm metal tapered nozzle using a flowrate of 79 µL/min	Ø 4 mm fluted CVD end mill using a spindle speed of 15,000RPM feedrate 30 mm/min	Ø 1 mm fluted CVD end mill using a spindle speed of 15,000RPM feedrate 30 mm/min 0.2 mm step down height	Thermal processes at production facility at Morgan Advanced Materials using a commercial tunnel kiln with a peak temperature of 1,400°C	
	Figure 3-18	Fabricated directly onto aluminium plate	Produced separately on an Ultimaker 2 using Ultimaker PLA. Manually placed during the build.	ecOPEN 300 mounted on the developed platform using 220 µm metal straight nozzle using a flowrate of 79 µL/min	No inter-layer machining	No post-process machining was carried out	Thermal processes at production facility at Morgan Advanced Materials using a commercial tunnel kiln with a peak temperature of 1,400°C. Support structure attached	

Part	Figures	Additive			Subtractive			Thermal Processing
		Substrate	Support	Deposition	Layer	Post-processing		
	Figure 3-19	SLA casting mould	N/A	Deposition of material using a manually controlled syringe	No inter-layer machining	Used to determine the suitability of machining operations	Not thermally processed	
	Figure 3-25b	Fabricated directly onto aluminium plate	No support material was required	ecopEN 300 mounted on the developed platform using 223 µm metal tapered nozzle using a flowrate of 43 µL/min	Ø 4 mm PCD straight sided end mill using a spindle speed of 15,000RPM feedrate 300 mm/min	Ø 4 mm PCD straight sided end mill using a spindle speed of 15,000RPM feedrate 300 mm/min	Not thermally processed	
	Figure 3-30 sample 2	Standard printing paper on a non-heated bed	No support material was required	ecopEN 300 mounted on the developed platform using 223 µm metal tapered nozzle using a flowrate of 43 µL/min	Ø 4 mm PCD straight sided end mill using a spindle speed of 15,000RPM feedrate 300 mm/min	Post-processed using a Ø 4 mm fluted CVD end mill. Table 3-1 Sample 2 shows the parameters that were used.	Thermal processes at production facility at Morgan Advanced Materials using a commercial tunnel kiln with a peak temperature of 1,400°C	
	Figure 3-30 sample 3	Standard printing paper on a non-heated bed	No support material was required	ecopEN 300 mounted on the developed platform using 223 µm metal tapered nozzle using a flowrate of 43 µL/min	Ø 4 mm PCD straight sided end mill using a spindle speed of 15,000RPM feedrate 300 mm/min	Post-processed using a Ø 4 mm fluted CVD end mill. Table 3-1 Sample 3 shows the parameters that were used.	Thermal processes at production facility at Morgan Advanced Materials using a commercial tunnel kiln with a peak temperature of 1,400°C	
	Figure 3-33	Standard printing paper on a non-heated bed	No support material was required	ecopEN 300 mounted on the developed platform using 223 µm metal tapered nozzle using a flowrate of 43 µL/min	Ø 4 mm PCD straight sided end mill using a spindle speed of 15,000RPM feedrate 300 mm/min	Holes drilled using 0.7 and 2 mm drill bits using the parameter specified in table 3-2	Thermal processes at production facility at Morgan Advanced Materials using a commercial tunnel kiln with a peak temperature of 1,400°C	
	Figure 3-34	Standard printing paper on a non-heated bed	No support material was required	ecopEN 300 mounted on the developed platform using 223 µm metal tapered nozzle using a flowrate of 43 µL/min	Ø 4 mm PCD straight sided end mill using a spindle speed of 15,000RPM feedrate 300 mm/min	Holes drilled using 0.7 and 2 mm drill bits using the parameter specified in table 3-3.	Thermal processes at production facility at Morgan Advanced Materials using a commercial tunnel kiln with a peak temperature of 1,400°C	

Part	Figures	Additive		Deposition	Subtractive			Thermal Processing
		Substrate	Support		Layer	Post-processing		
	Figure 5-2b(2)	White PLA deposited using the sacrificial support extruder	No support material was required	ecopEN 300 mounted on the developed platform using 223 μm metal tapered nozzle using a flowrate of 43 $\mu\text{L}/\text{min}$	\varnothing 4 mm fluted CVD end mill \varnothing 4 mm fluted CVD end mill spindle speed of 15,000RPM feedrate 30 mm/min/min	Top surface machined using \varnothing 4 mm fluted CVD end mill spindle speed of 15,000RPM feedrate 30 mm/min/min	Thermal processes at production facility at Morgan Advanced Materials using a commercial tunnel kiln with a peak temperature of 1,400°C	
	Figure 5-2b(1)	White PLA deposited using the sacrificial support extruder	No support material was required	ecopEN 300 mounted on the developed platform using 223 μm metal tapered nozzle using a flowrate of 43 $\mu\text{L}/\text{min}$	\varnothing 4 mm fluted CVD end mill using a spindle speed of 15,000RPM feedrate 30 mm/min	Top and side surface machined using \varnothing 4 mm fluted CVD end mill spindle speed of 15,000RPM feedrate 30 mm/min	Thermal processes at production facility at Morgan Advanced Materials using a commercial tunnel kiln with a peak temperature of 1,400°C	
	Figure 5-5a	White PLA deposited using the sacrificial support extruder	No support material was required	ecopEN 300 mounted on the developed platform using 223 μm metal tapered nozzle using a flowrate of 43 $\mu\text{L}/\text{min}$	\varnothing 4 mm fluted CVD end mill using a spindle speed of 15,000RPM feedrate 30 mm/min	No post-process machining was carried out	Thermal processes at production facility at Morgan Advanced Materials using a commercial tunnel kiln with a peak temperature of 1,400°C	
	Figure 5-5b	White PLA deposited using the sacrificial support extruder	No support material was required	ecopEN 300 mounted on the developed platform using 223 μm metal tapered nozzle using a flowrate of 43 $\mu\text{L}/\text{min}$	\varnothing 4 mm fluted CVD end mill using a spindle speed of 15,000RPM feedrate 30 mm/min	\varnothing 1 mm fluted CVD end mill using a spindle speed of 15,000RPM feedrate 30 mm/min, 1 mm step down height	Thermal processes at production facility at Morgan Advanced Materials using a commercial tunnel kiln with a peak temperature of 1,400°C	
	Figure 5-5c	White PLA deposited using the sacrificial support extruder	No support material was required	ecopEN 300 mounted on the developed platform using 223 μm metal tapered nozzle using a flowrate of 43 $\mu\text{L}/\text{min}$	\varnothing 4 mm fluted CVD end mill using a spindle speed of 15,000RPM feedrate 30 mm/min	\varnothing 1 mm fluted CVD end mill using a spindle speed of 15,000RPM feedrate 30 mm/min, 0.2 mm step down height	Thermal processes at production facility at Morgan Advanced Materials using a commercial tunnel kiln with a peak temperature of 1,400°C	
	Figure 5-8 and 5-9a	White PLA deposited using the sacrificial support extruder	No support material was required	ecopEN 300 mounted on the developed platform using 223 μm metal tapered nozzle using a flowrate of 43 $\mu\text{L}/\text{min}$	\varnothing 4 mm fluted CVD end mill using a spindle speed of 15,000RPM feedrate 30 mm/min/min	No post-process machining was carried out	Thermal processes at production facility at Morgan Advanced Materials using a commercial tunnel kiln with a peak temperature of 1,400°C	
	Figure 5-8 and 5-9b	White PLA deposited using the sacrificial support extruder	No support material was required	ecopEN 300 mounted on the developed platform using 223 μm metal tapered nozzle using a flowrate of 43 $\mu\text{L}/\text{min}$	\varnothing 4 mm fluted CVD end mill using a spindle speed of 15,000RPM feedrate 30 mm/min	\varnothing 1 mm fluted CVD end mill using a spindle speed of 15,000RPM feedrate 30 mm/min, 0.2 mm step down height	Thermal processes at production facility at Morgan Advanced Materials using a commercial tunnel kiln with a peak temperature of 1,400°C	

Part	Figures	Additive			Subtractive		Thermal Processing
		Substrate	Support	Deposition	Layer	Post-processing	
	Figure 5-12 Figure 5-13 and Figure 5-14	White PLA deposited using the sacrificial support extruder	Produced separately on an Ultimaker 2 with Ultimaker PLA using different infill densities. Manually placed during the build.	ecopEN 300 mounted on the developed platform using 223 μm metal tapered nozzle using a flowrate of 43 $\mu\text{L}/\text{min}$	\varnothing 4 mm fluted CVD end mill using a spindle speed of 15,000RPM feedrate 300 mm/min	Top and side surface machined using \varnothing 4 mm fluted CVD end mill spindle speed of 15,000RPM feedrate 300 mm/min Surface engraved with the infill values	Thermal processes at production facility at Morgan Advanced Materials using a commercial tunnel kiln with a peak temperature of 1,400°C Support structure attached
	Figure 5-15	White PLA deposited using the sacrificial support extruder	Support structure created using the in-situ support extruder using PLA filament using a layer height of 0.3 mm and rectilinear infill pattern.	ecopEN 300 mounted on the developed platform using 223 μm metal tapered nozzle using a flowrate of 43 $\mu\text{L}/\text{min}$	\varnothing 4 mm fluted CVD end mill using a spindle speed of 15,000RPM feedrate 300 mm/min	No post-process machining was carried out	Thermal processes at production facility at Morgan Advanced Materials using a commercial tunnel kiln with a peak temperature of 1,400°C Support structure attached
	Figure 5-14	White PLA deposited using the sacrificial support extruder	Support structure created using the in-situ support extruder using PLA filament using a layer height of 0.3 mm and rectilinear infill pattern.	ecopEN 300 mounted on the developed platform using 223 μm metal tapered nozzle using a flowrate of 43 $\mu\text{L}/\text{min}$	\varnothing 4 mm fluted CVD end mill using a spindle speed of 15,000RPM feedrate 300 mm/min	\varnothing 1 mm fluted CVD end mill using a spindle speed of 15,000RPM feedrate 300 mm/m 0.2 mm step down height	Thermal processes at production facility at Morgan Advanced Materials using a commercial tunnel kiln with a peak temperature of 1,400°C Support structure attached

Appendix D



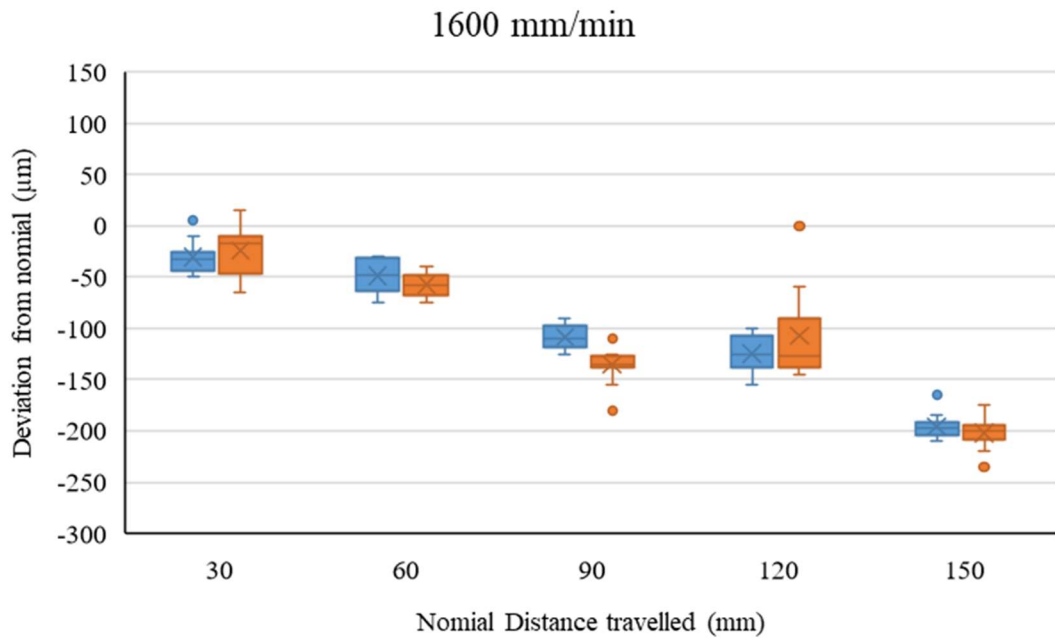
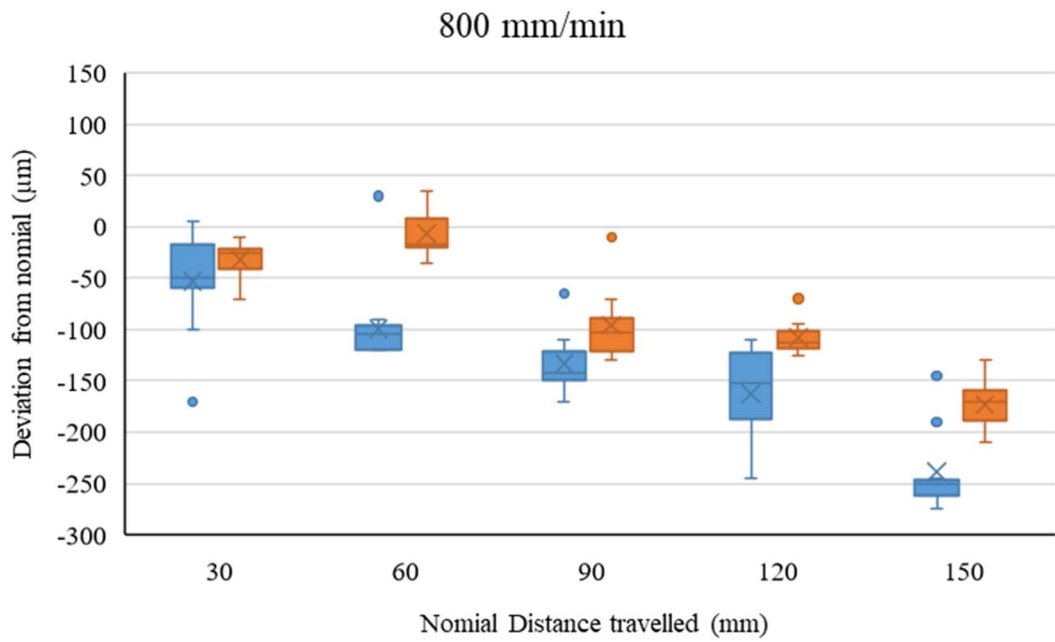
X-Axis

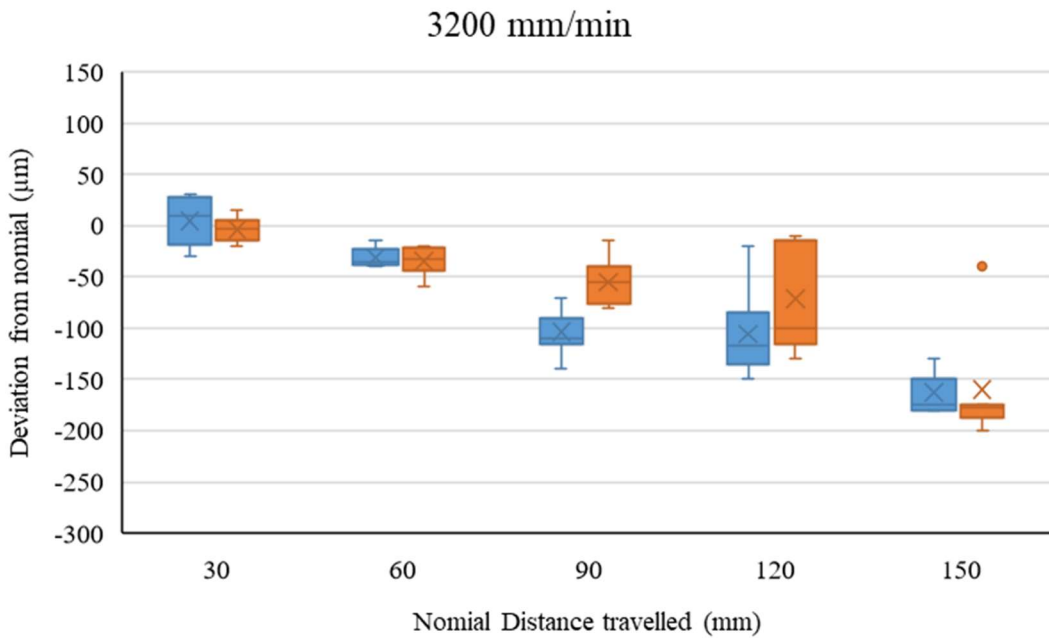
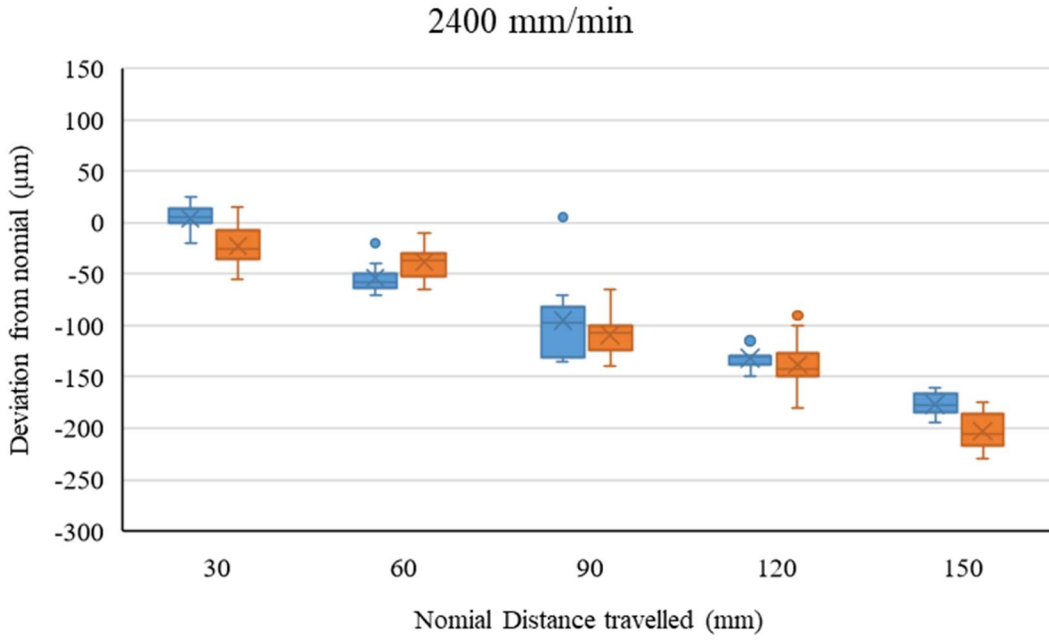
Distance travelled (mm)	Feedrate (mm/min)	Acceleration (m/s ²)	Measurement (µm)										Average distance from nom (µm)	Data spread +/- (µm)	Standard Deviation (µm)		
			1	2	3	4	5	6	7	8	9	10				Max	Min
30	800	300	-170	-60	-50	-100	-50	-60	5	5	-10	-40	-170	-53	175	49.759	
60	800	300	30	-170	-120	-120	-120	-110	-100	-100	-100	-100	-170	-100	100	48.19	
90	800	300	-140	-120	-170	-160	-160	-125	-150	-130	-110	-65	-170	-134	52.5	28.727	
120	800	300	-180	-155	-115	-230	-150	-130	-120	-110	-190	-245	-110	-245	67.5	45.291	
150	800	300	-250	-275	-250	-250	-250	-270	-265	-245	-145	-190	-145	-275	65	38.328	
30	1600	300	-50	-10	-45	-30	-30	-45	-25	-30	5	-40	-50	-31	25	16.194	
60	1600	300	-65	-75	-70	-30	-30	-30	-40	-55	-30	-35	-75	-49	22.5	17	
90	1600	300	-125	-115	-125	-110	-120	-110	-105	-95	-90	-90	-125	-109	17.5	12.659	
120	1600	300	-155	-135	-100	-140	-130	-100	-115	-110	-120	-105	-155	-125	25	19.105	
150	1600	300	-200	-210	-190	-195	-195	-205	-200	-165	-210	-185	-165	-210	22.5	12.738	
30	2400	300	-20	5	0	15	0	25	0	25	10	15	25	4	20	13	
60	2400	300	-60	-20	-50	-60	-60	-65	-65	-70	-55	-40	-70	-54	25	13.973	
90	2400	300	-105	-135	-80	5	-120	-135	-90	-90	-85	-70	-135	-95	70	40.62	
120	2400	300	-150	-130	-135	-110	-145	-130	-140	-140	-115	-130	-150	-132	17.5	11.63	
150	2400	300	-185	-195	-190	-170	-160	-185	-185	-165	-170	-185	-165	-177	17.5	11.662	
30	3200	300	5	-15	30	-30	-30	30	20	15	30	-20	-30	5	30	22.522	
60	3200	300	-35	-35	-40	-40	-40	-15	-30	-40	-20	-35	-15	-40	-31	12.5	8.888
90	3200	300	-140	-70	-70	-110	-110	-115	-120	-90	-110	-70	-140	-104	25	21.83	
120	3200	300	-70	-70	-150	-150	-150	-110	-130	-130	-90	-125	-70	-150	40	27.756	
150	3200	300	-180	-150	-180	-175	-180	-180	-180	-175	-175	-130	-180	-163	25	19.9	
30	1600	550	25	20	-55	35	25	25	-10	15	25	10	-55	8	45	25.715	
60	1600	550	-50	-65	-70	-35	-60	-65	-60	-55	-60	-75	-75	-58	20	12.093	
90	1600	550	-120	-160	-150	-110	-145	-160	-160	-125	-150	-135	-160	-138	25	17.066	
120	1600	550	-160	-190	-190	-185	-185	-160	-165	-160	-185	-140	-190	-169	25	16.401	
150	1600	550	-225	-210	-210	-190	-230	-235	-235	-195	-220	-215	-235	-216	22.5	14.229	
30	1600	800	-10	20	20	-10	-25	-20	-20	10	15	15	20	-25	1	22.5	16.292
60	1600	800	-85	-50	-65	-65	-65	-100	-90	-110	-75	-80	-110	-77	30	19	
90	1600	800	-160	-130	-140	-180	-145	-135	-135	-120	-135	-130	-180	-141	30	16.401	
120	1600	800	-235	-245	-230	-240	-240	-215	-210	-230	-230	-225	-190	-245	27.5	16.063	
150	1600	800	-250	-250	-265	-265	-245	-245	-245	-270	-270	-190	-270	-238	40	28.964	
30	3200	550	-35	-20	-50	-30	-30	-25	-25	-20	-15	-15	-50	-28	17.5	10.308	
60	3200	550	-110	-80	-90	-90	-90	-120	-70	-85	-115	-70	-120	-95	25	15.166	
90	3200	550	-45	-120	-110	-115	-130	-140	-140	-115	-130	-105	-45	-114	17.5	25.179	
120	3200	550	-160	-145	-140	-155	-110	-170	-170	-140	-100	-140	-170	-137	35	23.214	
150	3200	550	-220	-220	-200	-200	-235	-220	-220	-225	-190	-225	-190	-235	22.5	14.671	
30	3200	800	-35	-15	-15	-20	-20	-30	-30	-30	0	-15	-20	-35	15	9.487	
60	3200	800	-70	-100	-140	-85	-70	-80	-80	-60	-65	-100	-75	-85	40	22.522	
90	3200	800	-140	-155	-160	-110	-110	-120	-120	-140	-125	-135	-110	-160	25	17.015	
120	3200	800	-190	-190	-190	-110	-135	-180	-180	-210	-200	-125	-110	-210	50	37.074	
150	3200	800	-235	-255	-270	-270	-270	-270	-270	-270	-170	-220	-170	-227	50	32.361	

Y-Axis

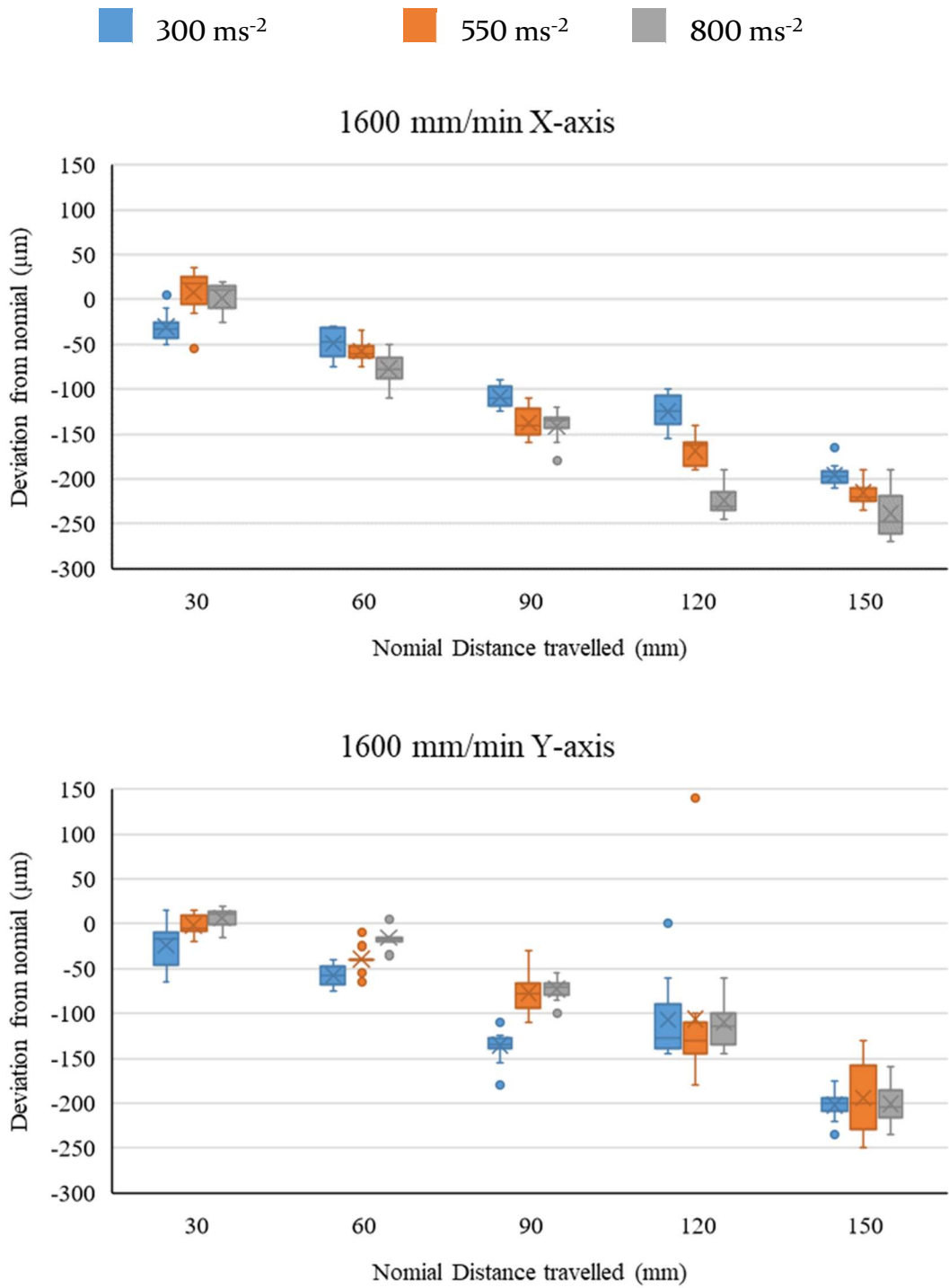
Distance travelled (mm)	Feedrate (mm/min)	Acceleration (m/s ²)	Measurement (µm)										Average distance from nom (µm)	Data spread +/-	Standard Deviation				
			1	2	3	4	5	6	7	8	9	10				Max	Min		
30	800	300	-50	-45	-70	-20	-25	-25	-25	-25	-25	-30	-10	-20	-10	-70	-32	30	16.91153
60	800	300	30	35	-20	-20	-35	10	-15	-15	-130	-20	-35	-20	35	-35	-6.5	35	23.87991
90	800	300	-70	-100	-10	-125	-85	-110	-125	-100	-100	-105	-10	-130	-96	-96	60	33.67492	
120	800	300	-125	-115	-115	-110	-70	-95	-100	-120	-125	-105	-70	-125	-108	-108	27.5	15.84298	
150	800	300	-150	-170	-170	-155	-130	-200	-210	-190	-170	-185	-130	-210	-173	-210	40	22.93469	
30	1600	300	-50	-60	-10	-15	-20	-35	-65	10	-10	15	15	15	65	-24	40	26.34388	
60	1600	300	-70	-55	-60	-45	-55	-45	-70	-75	-60	-40	-40	-75	-57.5	-24	17.5	11.2361	
90	1600	300	-105	-135	-125	-135	-135	-135	-180	-110	-140	-155	-105	-180	-135.5	-107	37.5	20.18044	
120	1600	300	-145	-105	-140	-85	-60	0	-145	-120	-135	-135	0	-145	-107	-107	72.5	44.56456	
150	1600	300	-195	-200	-235	-185	-220	-205	-210	-195	-200	-175	-175	-235	-202	-202	30	16.15549	
30	2400	300	-30	-20	-35	-50	-55	-15	-15	5	-5	15	15	-35	-55	-22.5	35	21.70829	
60	2400	300	-45	-30	-30	-30	-10	-15	-45	-60	-65	-55	-10	-65	-38.5	-38.5	27.5	17.61391	
90	2400	300	-65	-105	-95	-110	-125	-120	-140	-100	-130	-100	-65	-140	-109	-109	37.5	20.22375	
120	2400	300	-145	-100	-165	-180	-125	-90	-140	-150	-135	-150	-90	-180	-138	-138	45	26	
150	2400	300	-180	-190	-200	-185	-220	-225	-210	-230	-175	-210	-175	-230	-230	-202.5	27.5	18.47295	
30	3200	300	5	15	-10	10	-15	-20	5	-15	-20	5	15	-20	-4	-4	17.5	12.60952	
60	3200	300	-25	-20	-30	-40	-35	-45	-20	-55	-60	-20	-20	-60	-35	-35	20	13.96424	
90	3200	300	45	-40	-10	-15	-15	-65	-80	-75	-80	-15	-80	-80	-55	-55	32.5	22.0794	
120	3200	300	300	-10	-15	-15	-100	-105	-105	-125	-130	-10	-130	-130	-71.4286	-71.4286	60	51.24969	
150	3200	300	-200	-40	-190	-175	-180	-175	-180	-175	-175	-40	-200	-160	-160	-160	80	54.39056	
30	1600	550	10	5	10	15	-15	-20	-5	-5	-10	-5	15	15	-20	-2	17.5	11	
60	1600	550	-25	-40	-40	-40	-40	-10	-55	-40	-40	-40	-65	-65	-39.5	-39.5	27.5	14.04457	
90	1600	550	-65	-70	-100	-110	-90	-60	-30	-70	-85	-30	-110	-77.5	-77.5	40	22.16416		
120	1600	550	-110	-160	-140	-145	-180	-180	-100	-130	-125	-100	-180	-137.222	-137.222	40	23.10737		
150	1600	550	-150	-130	-235	-205	-240	-210	-195	-150	-180	-250	-130	-250	-194.5	-194.5	60	39.3351	
30	1600	800	15	20	10	10	-5	10	15	10	15	20	15	15	6.5	6.5	17.5	10.5	
60	1600	800	-20	-15	-35	5	-20	-15	-15	10	-30	-20	10	-35	-15.5	-15.5	22.5	13.1244	
90	1600	800	-65	-70	-70	-75	-55	-80	-100	-70	-60	-85	-55	-100	-73	-73	22.5	12.28821	
120	1600	800	-100	-75	-115	-145	-60	-115	-135	-135	-110	-60	-145	-110	-110	-110	42.5	26.5623	
150	1600	800	-200	-210	-235	-160	-190	-175	-220	-215	-160	-215	-160	-235	-200.625	-200.625	37.5	23.1081	
30	3200	550	-25	-30	-5	5	-15	-80	-10	-5	-20	-20	5	-30	-13.8889	-13.8889	17.5	10.4822	
60	3200	550	-45	-30	-30	-30	-75	-80	-40	-40	-10	-10	-80	-38	-38	-38	35	22.38303	
90	3200	550	-90	-100	-85	-110	-110	-120	-110	-60	-65	-60	-120	-92.5	-92.5	30	20.3101		
120	3200	550	-150	-150	-150	-115	-130	-160	-160	-100	-105	-90	-160	-131	-131	-131	35	25.17936	
150	3200	550	-200	-220	-190	-85	-195	-195	-210	-85	-110	-110	-85	-220	-161.875	-161.875	67.5	54.25274	
30	3200	800	5	10	5	5	-20	-35	-35	-10	-15	10	-35	-8.5	-8.5	22.5	16.2865		
60	3200	800	-35	-20	-15	-30	-65	-60	-70	-40	-15	-35	-15	-70	-38.5	-38.5	27.5	19.24188	
90	3200	800	-100	-100	-80	-65	-110	-110	-125	-70	-85	-65	-125	-93.5714	-93.5714	30	19.94891		
120	3200	800	-165	-80	-60	-185	-65	-165	-125	-190	-175	-60	-190	-134.444	-134.444	65	50.08018		
150	3200	800	-80	-80	-80	-210	-220	-220	-255	-235	-240	-80	-255	-206.667	-206.667	87.5	58.42849		

Repeatability for X and Y axes at a constant acceleration of 300ms^{-2}

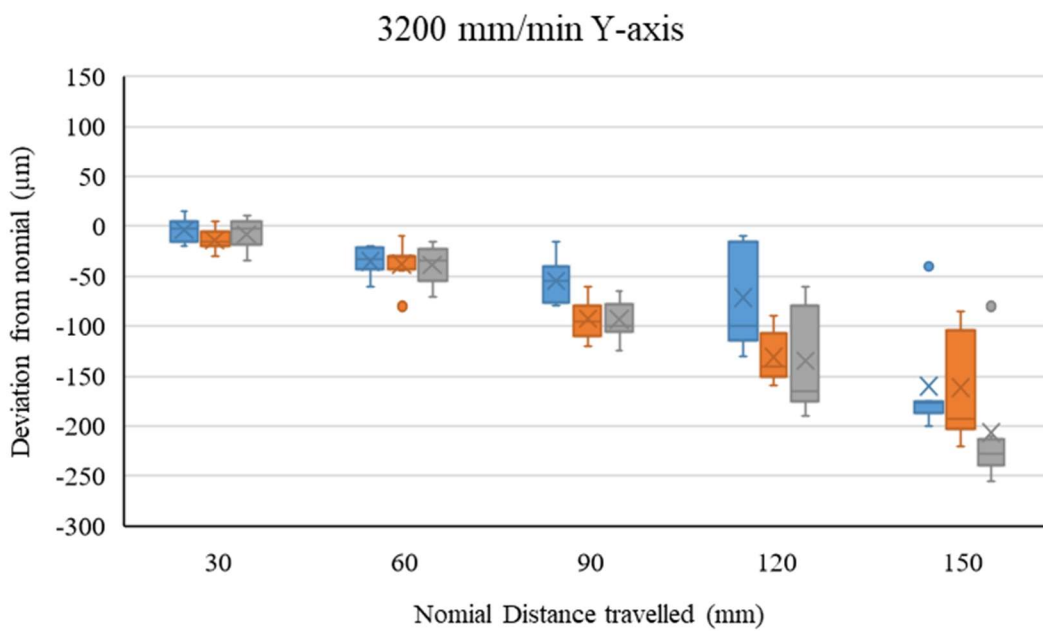
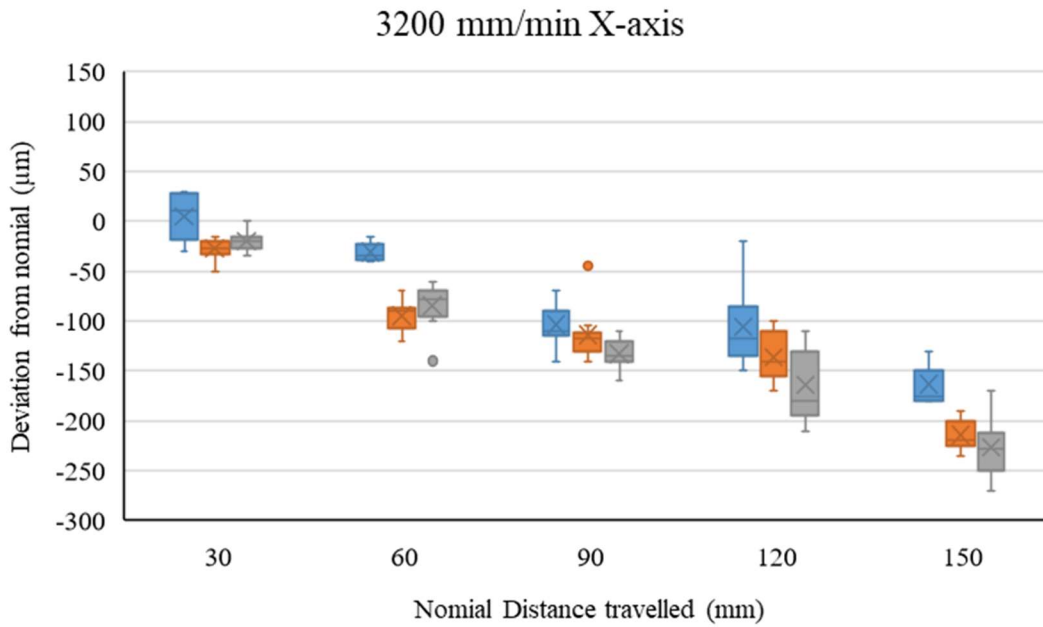




9.1 Variable Acceleration at target feedrate of 1,600 mm/min



9.2 Variable Acceleration at target feedrate of 3,200 mm/min



Appendix F

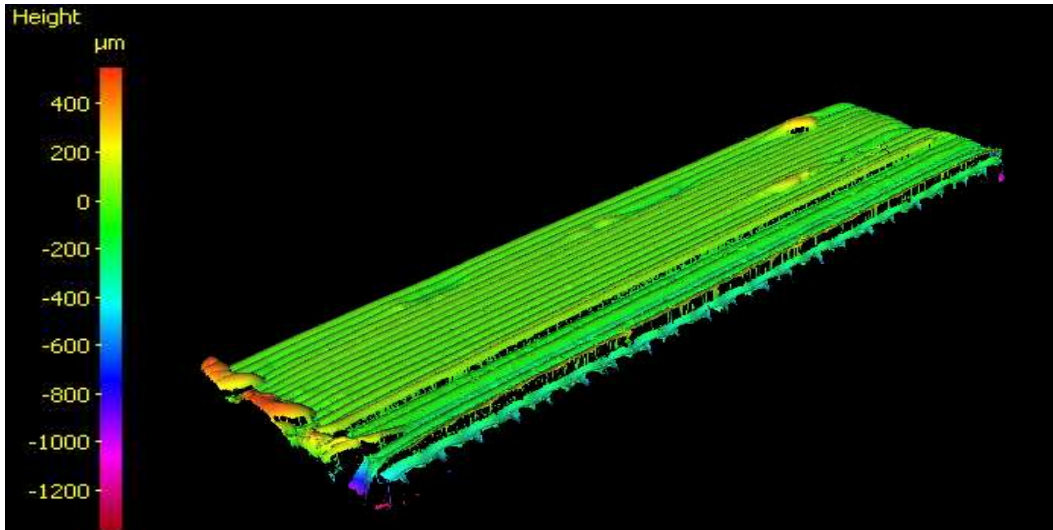
Measurement of deposited tracks using ceramic feedstock

Line	Flow Rate ($\mu\text{l}/\text{min}$)	Printing Speed (mm/min)	Line width (μm)				Line height (μm)				
			Left	Centre	Right	Average	Left	Centre	Right	Average	
1	40	650	343	330	369	347	166	165	175	169	
2	39	655	283	297	301	294	157	159	157	158	
3	38	660	300	512	540	451	139	129	143	137	
4	37	665	530	538	531	533	145	145	140	143	
5	36	670	648	616	617	627	140	143	147	143	
6	35	675	745	706	706	719	150	141	141	144	
7	34	680	547	572	613	577	138	135	144	139	
8	33	685	723	727	719	723	133	135	137	135	
9	32	690	No Continuous Line								
10	33	695	777	727	688	731	122	118	114	118	
11	33	700	699	708	696	701	135	126	126	129	
12	33	705	379	365	365	370	110	113	119	114	
13	33	710	277	322	326	308	126	120	118	121	
14	33	715	439	431	396	422	89	95	102	95	
15	33	720	342	373	380	365	117	109	113	113	
16	33	725	337	408	365	370	70	77	59	69	
17	33	730	443	458	453	451	99	94	80	91	
18	33	735	379	379	424	394	57	52	61	56	
19	33	740	452	439	434	442	88	90	100	93	
20	33	745	381	404	425	403	57	65	78	66	
21	33	750	397	414	400	403	97	89	86	91	
22	33	755	435	435	441	437	76	65	72	71	
23	33	760	380	431	318	377	65	65	36	55	
24	33	765	447	353	302	367	76	53	35	55	
25	33	770	425	314	248	329	69	35	19	41	

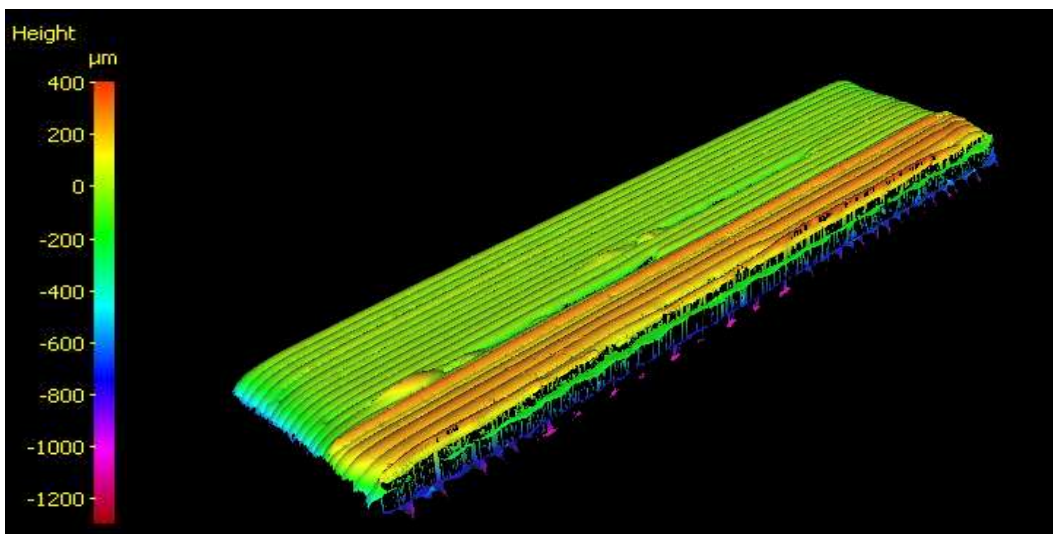
Appendix G

9.3 Non-machined Sample

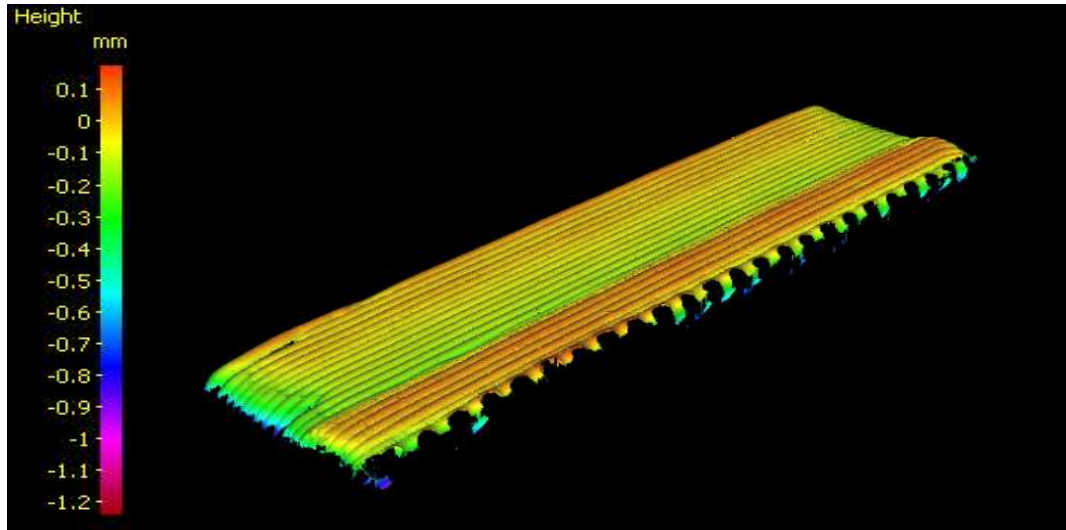
Side A



Side C



Side D

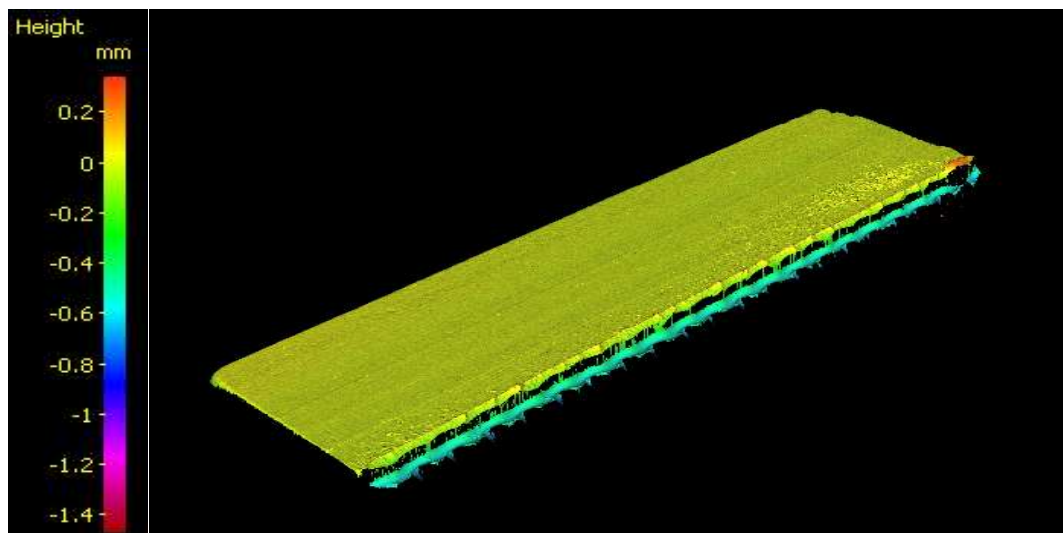


Surface roughness measurements for the non-machined tile

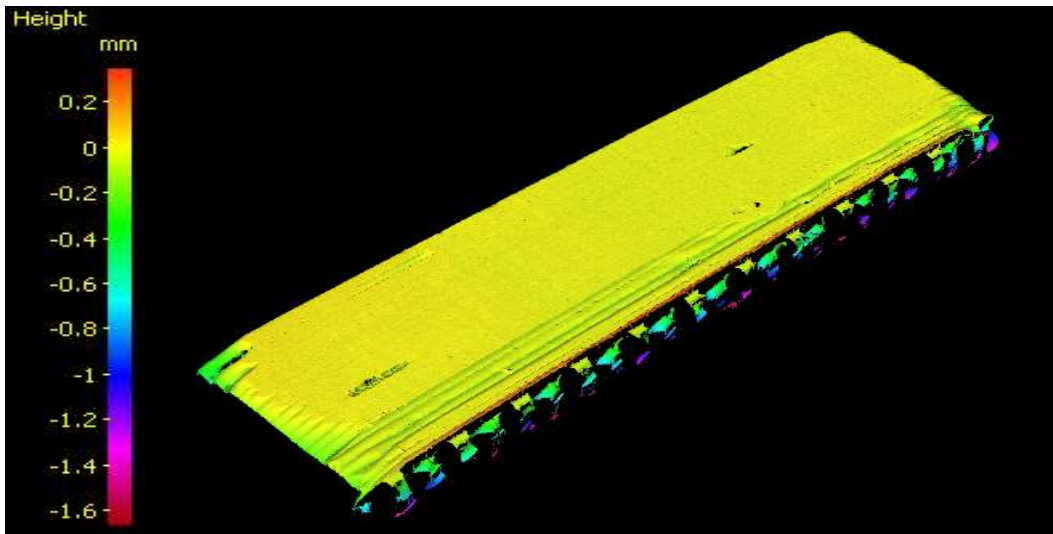
	Surface Roughness R_a (μm)	Surface Roughness R_q (μm)
Side A	17.0 ± 7.0	23.3 ± 10.1
Side B	18.5 ± 12.9	24.2 ± 15.0
Side C	21.5 ± 13.3	32.2 ± 11.8
Side D	14.5 ± 2.3	18.9 ± 4.3
Average	17.9 ± 13.3	24.6 ± 19.2

9.4 Machined Sample

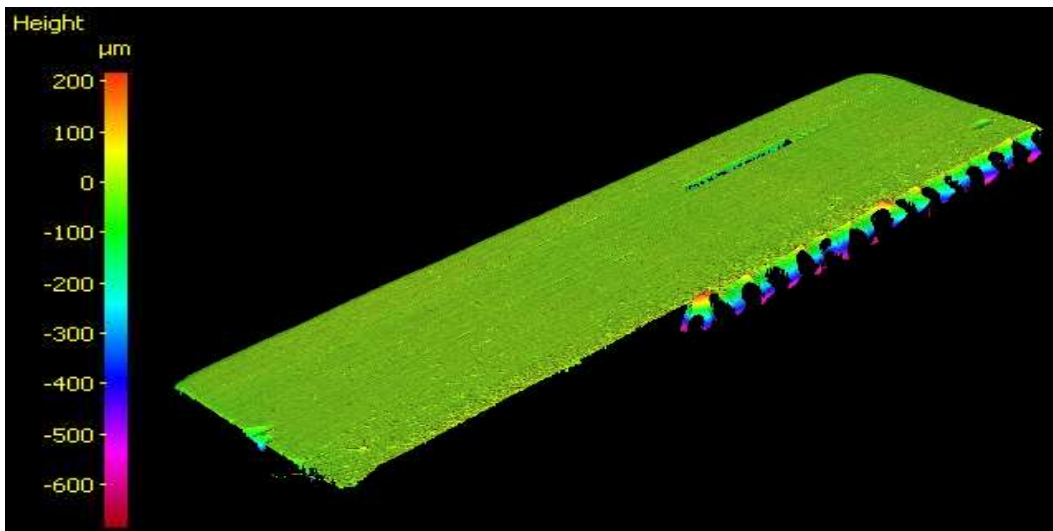
Side A



Side B



Side C



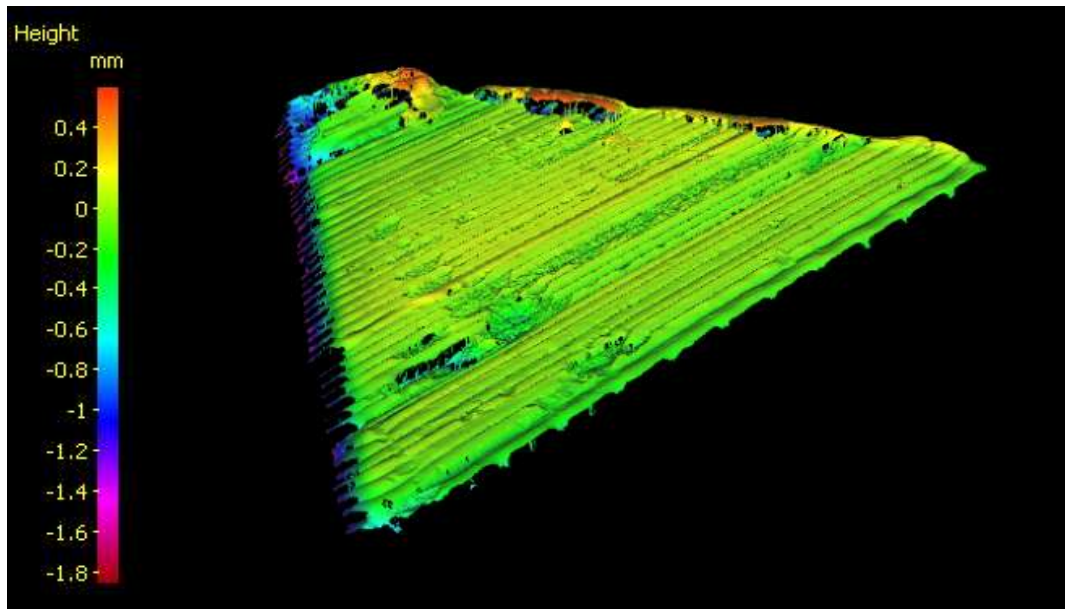
Surface roughness measurements for the machined tile

	Surface Roughness R_a (μM)	Surface Roughness R_q (μM)
Side A	0.7 ± 0.3	1.0 ± 0.6
Side B	1.2 ± 0.1	1.7 ± 0.3
Side C	1.1 ± 0.1	1.6 ± 0.2
Side D	0.9 ± 0.3	1.3 ± 0.4
Average	0.99 ± 0.5	1.4 ± 0.7

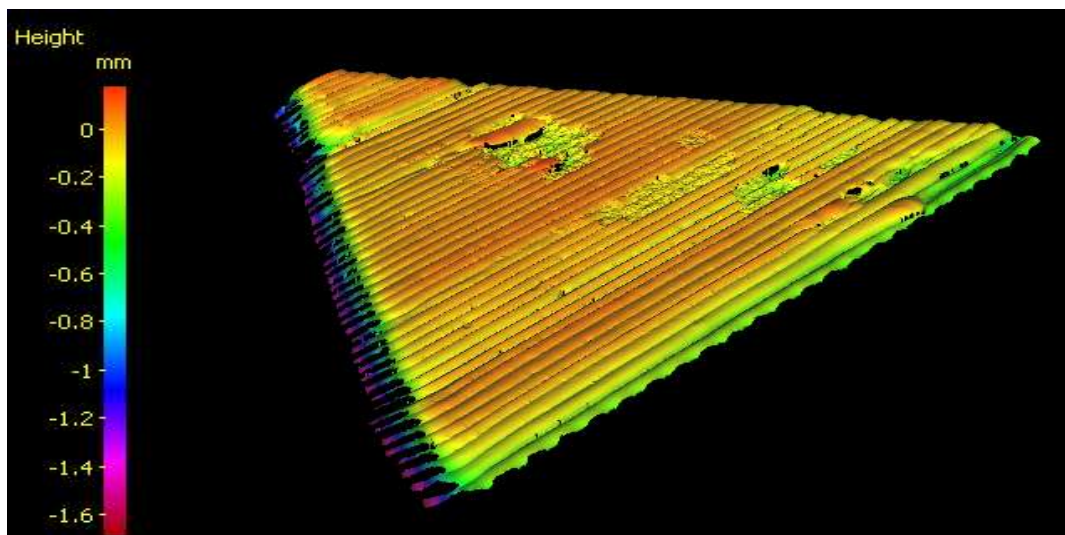
Appendix H

9.5 Non-machined Sample

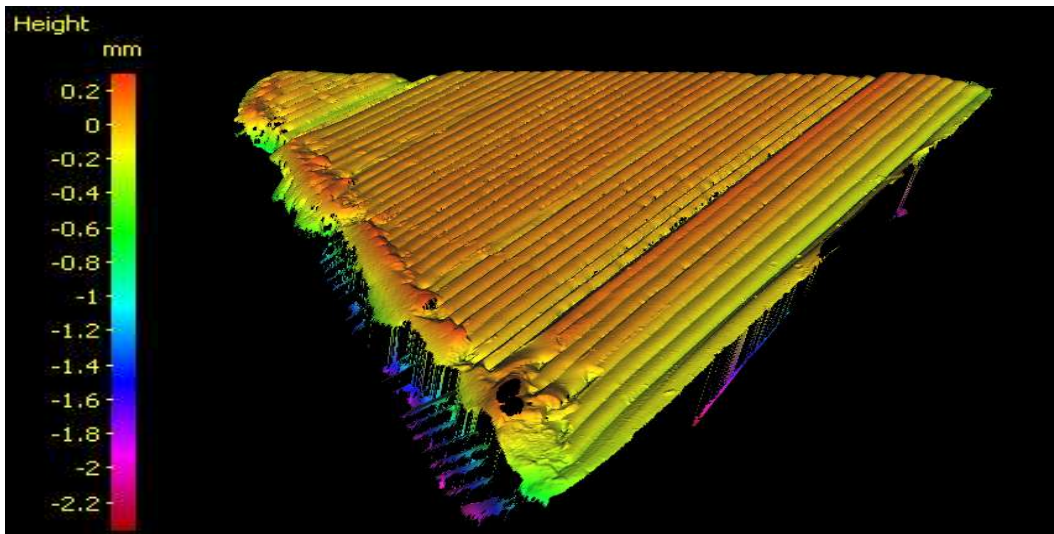
Side A



Side B

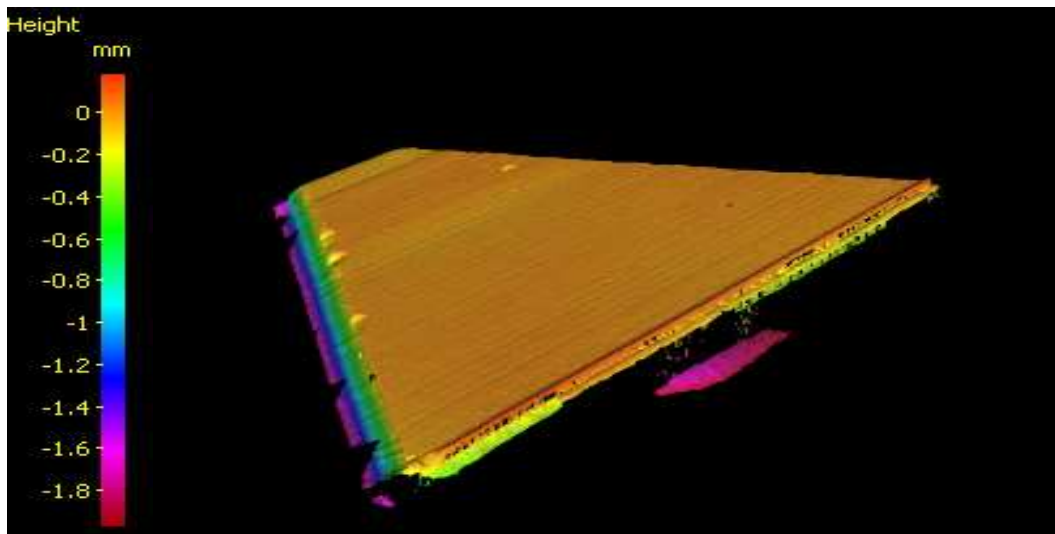


Side D

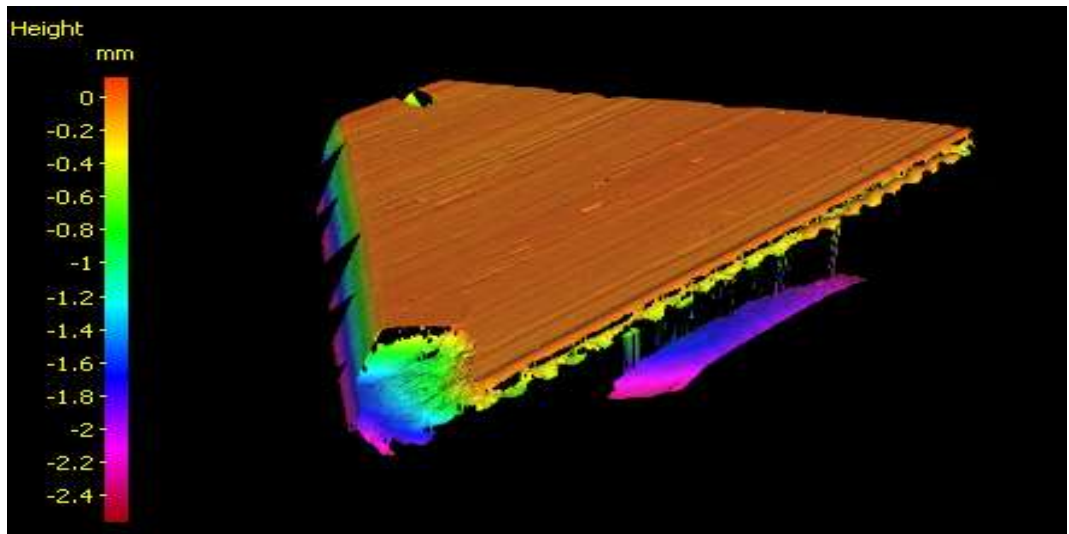


9.6 Machined Sample

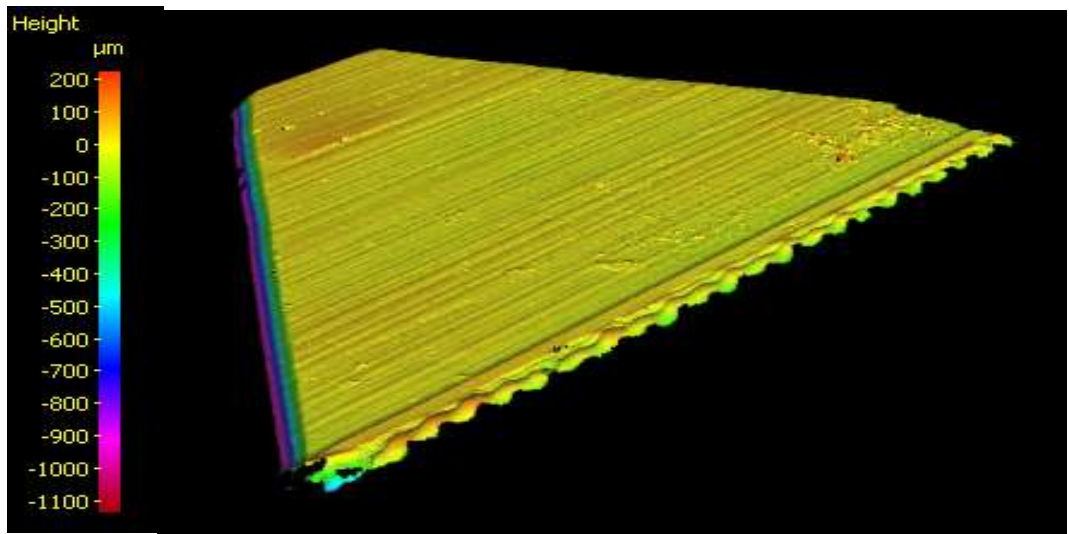
Side A



Side B



Side C



Appendix I

$$\sigma = \frac{3F_m l}{2bh^2} \quad (H.1)$$

Where:

F_m = Maximum force applied

l = Support span

b = Width of test-piece

h = Thickness of test-piece in direction of bending

Appendix J

$$\text{Bulk Density} = \frac{M_1}{(M_3 - M_2)}$$

$$\text{Apparent Solid Density} = \frac{M_1}{(M_1 - M_2)}$$

$$\text{Porosity} = 100 \times \frac{(M_1 - M_1)}{(M_3 - M_2)}$$

Where:

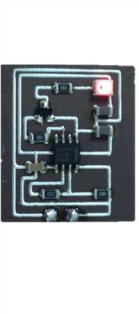
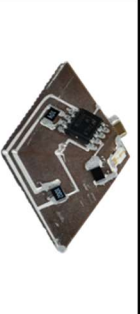
M_1 = Dry Weight

M_2 = Suspended Weight

M_3 = Soaked Weight

Part	Dry Mass (g)	Suspended Mass (g)	Soaked Mass (g)	Bulk Density (g/cm ³)	Solid Density (g/cm ³)	Porosity (%)	Density (%)
1	3.9035	2.8354	3.9083	3.64	3.65	0.45	99.55
2	3.7992	2.7514	3.8044	3.61	3.63	0.49	99.51
3	3.9819	2.8915	3.9827	3.65	3.65	0.07	99.93
4	4.0094	2.9055	4.0112	3.63	3.63	0.16	99.84
5	3.9613	2.8715	3.9667	3.62	3.63	0.49	99.51
6	3.982	2.8916	3.9861	3.64	3.65	0.37	99.63
7	3.9934	2.9006	3.9969	3.64	3.65	0.32	99.68
8	4.0338	2.9313	4.041	3.64	3.66	0.65	99.35
9	3.9864	2.8923	3.993	3.62	3.64	0.6	99.4
10	3.9049	2.8346	3.9107	3.63	3.65	0.54	99.46
11	4.0159	2.918	4.0237	3.63	3.66	0.71	99.29
12	3.9579	2.8737	3.9626	3.63	3.65	0.43	99.57
13	4.015	2.9175	4.0191	3.64	3.66	0.37	99.63
14	3.8987	2.8308	3.9034	3.63	3.65	0.44	99.56
15	3.827	2.7787	3.8342	3.63	3.65	0.68	99.32
16	3.9755	2.8899	3.9792	3.65	3.66	0.34	99.66
17	3.9973	2.9033	4.003	3.63	3.65	0.52	99.48
18	3.8936	2.8207	3.9047	3.59	3.63	1.02	98.98
19	3.9732	2.8862	3.9785	3.64	3.66	0.49	99.51
20	4.0187	2.9222	4.0267	3.64	3.67	0.72	99.28
Tile	8.8392	6.3716	8.8593	3.55	3.58	0.81	99.19
Machined Tile	8.5146	6.1534	8.5302	3.58	3.61	0.66	99.34
Tapered Square 1 mm	5.3852	3.9023	5.2775	2.97	3.02	1.78	98.22
Tapered Square 0.1 mm	4.7912	3.4469	4.8104	3.51	3.56	1.41	98.59
Tapered square	4.1882	3.0281	4.2202	3.51	3.61	2.68	97.32
Pyramid	7.4807	5.3928	7.4858	3.57	3.58	0.24	99.76
Machined Pyramid	7.0338	5.0719	7.0424	3.57	3.59	0.44	99.56
Dome	2.3139	1.6737	2.3274	3.54	3.61	2.07	97.93
Dome	3.222	2.2866	3.2522	3.34	3.44	3.13	96.87
machined dome	2.7781	1.9606	2.8027	3.3	3.4	2.92	97.08

Appendix K

Part	Figures	Substrate	Conductor deposition	Conductor sintering	Solder deposition and component placement	Solder Reflow
	Figure 6-2	50 x 50 x 0.250 mm sintered alumina substrates (AL603026, Goodfellow, USA)	Deposited using a pneumatic ram extruder mounted on 3-axis robot (7400NVL, Fisar, USA) using a 250 µm polymer tapered nozzle	Carbolite RHF 16/3 chamber furnace following the manufacturers recommended profile as shown by Figure 2-10	No Components were placed on this part.	No solder was deposited on this part.
	Figure 6-6	Alumina substrate fabricated using the developed hybrid manufacturing hardware and thermally process by Morgan Advanced Materials using a tunnel kiln.	Deposited using a pneumatic ram extruder mounted on 3-axis robot (7400NVL, Fisar, USA) using a 250 µm polymer tapered nozzle	Carbolite RHF 16/3 chamber furnace following the manufacturers recommended profile as shown by Figure 2-10	Deposition of Type-5 Sn96.5 Ag0.5 Cu3.0 using a pneumatic ram extruder through a 250 µm tapered polymer nozzle. Remote controlled placement of 0603 components.	Reflowed using a Carbolite LHT6/30 high temperature convection oven, following the manufacturers recommended profile.
	Figure 6-7	Alumina substrate fabricated using the developed hybrid manufacturing hardware and thermally process by Morgan Advanced Materials using a tunnel kiln.	Deposited using a pneumatic ram extruder mounted on 3-axis robot (7400NVL, Fisar, USA) using a 250 µm polymer tapered nozzle	Carbolite RHF 16/3 chamber furnace following the manufacturers recommended profile as shown by Figure 2-10	Deposition of Type-5 Sn96.5 Ag0.5 Cu3.0 using a pneumatic ram extruder through a 250 µm tapered polymer nozzle. Manual placement of 0603 components.	Reflowed using a Carbolite LHT6/30 high temperature convection oven, following the manufacturers recommended profile.
	Figure 6-9	Alumina substrate fabricated using the developed hybrid manufacturing hardware and thermally process by Morgan Advanced Materials using a tunnel kiln.	Deposited using a pneumatic ram extruder mounted on 3-axis robot (7400NVL, Fisar, USA) using a 250 µm polymer tapered nozzle	Carbolite RHF 16/3 chamber furnace following the manufacturers recommended profile as shown by Figure 2-10	Deposition of Type-5 Sn96.5 Ag0.5 Cu3.0 using a pneumatic ram extruder through a 250 µm tapered polymer nozzle. Remote controlled placement of 0603 components.	Reflowed using a Carbolite LHT6/30 high temperature convection oven, following the manufacturers recommended profile.
	Figure 6-10	Alumina substrate fabricated using the developed hybrid manufacturing hardware. Substrate co-fired in a chamber furnace at University of Leeds	Deposited using a pneumatic ram extruder mounted on 3-axis robot (7400NVL, Fisar, USA) using a 250 µm polymer tapered nozzle	Co-fired with the substrate in Carbolite RHF 16/3 chamber furnace following the manufacturers recommended profile as shown by Figure 2-10	No Components were placed on this part.	No solder was deposited on this part.

Appendix L

Measurement	Sample 1 Ω/m	Sample 2 Ω/m	Sample 3 Ω/m
1	1.2030E-07	9.4430E-08	8.4630E-08
2	1.0150E-07	9.2260E-08	8.6850E-08
3	1.1130E-07	1.0880E-07	8.1670E-08
4	1.2490E-07	1.0250E-07	8.6010E-08
5	1.1720E-07	1.0590E-07	9.0030E-08
Average	1.1383E-07	1.0078E-07	8.5838E-08
Correction factor applied	1.1383E-07	9.9720E-08	8.4937E-08

Appendix M

